Doctoral Dissertation
博士論文

Modeling and Searching for Stochastic Gravitational-waves Backgrounds from Ultralight Boson Particles

(極低質量ボゾン粒子からの背景重力波のモデリングおよび探査)

A Dissertation Submitted for
the Degree of Doctor of Philosophy

December 2020
令和2年12月博士(理学)申請

Department of Physics Graduate School of Science
The University of Tokyo

東京大学大学院理学系研究科
物理学専攻

Leo Tsukada
塚田怜央

Abstract

Since the first detection of gravitational waves (GWs) in 2015, the field of GW astronomy has been successfully flourished with many subsequent observations. One of the next targets of GW signals is a stochastic gravitational-wave background (SGWB), superposed GW signals from distant unresolvable sources in the Universe. Recently, it was proposed that a search for a SGWB using current ground-based GW detectors, e.g. the Laser Interferometer Gravitational-wave Observatory (LIGO), can be used to probe the existence of exotic boson particles with extremely small mass $m_b \sim 10^{-13}\,\mathrm{eV}$ via a phenomenon called *superradinace instability* around a rotating black hole (BH). Such particles are predicted by beyond-Standard-Model scenarios and are expected, if present, to provide a solution to the strong CP problem in the particle physics as well as serve as a dark-matter candidate in the cosmological context. The gravitational dynamics involved in the BH superradiance yields a means of probing such particles complementary to the conventional model assuming the boson-photon coupling. Therefore, whether or not one detects the signal from the bosons, the GW search would be able to provide a meaningful implication from the perspective of the particle physics and cosmology. This thesis describes modeling of the predicted SGWB spectrum for each model of the minimally-coupled massive scalar and vector bosons and the search results of such a signal using LIGO's observation data.

The superrandiant instability is a unstable system caused by massive bosonic fields extracting energy and angular momentum from a rotating BH, and forming quasi-bound states with a successive energy amplification. While the bosonic field starts to grow exponentially with the timescale of τ_{inst}, the BH loses its mass and angular momentum accordingly. This instability continues until the BH spins down to the point where the superradiance condition starts to be saturated. By that time, the bosonic field would become boson condensate, which we call macroscopic "cloud", and its energy scale can be typically $\sim 10\%$ of the BH mass. Eventually, the quadrupole moment of the cloud induces characteristic gravitational radiation. The BH perturbation theory predicts the GW emission with the nearly monochromatic frequency that depends on the boson mass over the timescale of $\tau_{\mathrm{GW}}(\gg \tau_{\mathrm{inst}})$, during which the gravitational emission dissipates the energy of the boson cloud until its energy becomes negligible.

Based on the unstable behavior of the two types of bosonic fields, which is discussed

in Chapter 3, we note that whole dynamical timescale for the vector field is several order-of-magnitude shorter than that for the scalar field. In chapter 4, we calculate the SGWB spectra predicted from these boson cloud models and find that the significant difference in the GW emission timescale leads to the enhancement of the background amplitude for the vector model with the mass $\sim 10^{-13}$ eV. Interestingly, assuming the isolated BHs and binary black hole (BBH) merger remnant as the entire BH population, we identify a certain range of the boson masses that yields potentially detectable SGWB signal even with the current sensitivity of advanced LIGO, which implies our capability to place a meaningful constraint on the boson masses using a null result of the SGWB search.

Chapter 6 provides the results of our studies using a Bayesian-based search pipeline to look for the SGWB signal of the superradiant instability. Our injection test suggests that the search pipeline can be sensitive to scalar mass of around 1.8×10^{-13} eV to 7.5×10^{-13} eV and to vector mass of 0.4×10^{-13} eV to 9.4×10^{-13} eV, respectively. Considering a more realistic situation where SGWBs from a population of compact binary coalescences and from a boson cloud model both are present in data, we perform a model-selection test with injections simulated from the both models and show that we can distinguish the boson cloud SGWB even from a modestly spinning BH population at around 3×10^{-13} eV(1×10^{-13} eV) for the scalar (vector) cloud model.

Lastly, we conduct a search for this kind of SGWB from each scalar and vector cloud model using the data from advanced LIGO's first and second observing runs. We do not find any strong evidence of such SGWB signal . This allows us to place the following constraints on each boson mass: for the pessimistic case, at $\chi_{\rm ul} = 0.8$ we exclude scalar mass of 2.0×10^{-13} eV to 4.0×10^{-13} eV and similarly vector mass of 0.9×10^{-13} eV to 5.1×10^{-13} eV (see Figs. 6.11 and 6.13). On the other hand, for the optimistic case, scalar mass of $m_b = 2.4 \times 10^{-13}$ eV to 5.2×10^{-13} eV and vector bosons mass of $m_b = 0.8 \times 10^{-13}$ eV to 6.5×10^{-13} eV are disfavored regardless of spin lower bound $\chi_{\rm ll}$ at a 95% confidence level. We highlight that these are the first constraints made on the boson masses based on a rigorous SGWB search.

Contents

List of Figures

Glossary

Constants

c	the speed of light	$299\,792\,458\,\mathrm{m/s}$
G	gravitational constant	$6.67408 \times 10^{-11}\,\mathrm{m^3/kg/s^2}$
$\hbar$	reduced Planck constant	$1.05457 \times 10^{-34}\,\mathrm{m^2 kg/s}$

Abbreviations

ALP	Axion-like particle
BBH	Binary black hole
BH	Black hole
BNS	Binary neutron star
CBC	Compact binary coalescence
CDM	Cold dark matter
CGWB	Cosmic gravitational-wave background
CMB	Cosmic microwave background
CW	Continous gravitational wave
DM	Dark matter
GW	Gravitational wave
LIGO	The Laser Interferometer Gravitational-wave Observatory

LISA	Laser Interferometer Space Antenna
LVC	the LIGO & Virgo Scientific Collaboration
NP scalar	Newman-Penrose scalar
O1	The first observing run
O2	The second observing run
O3	The third observing run
O3a	The first half of the third observing run
O4	The fourth observing run
O5	The fifth observing run
QCD	Quantum chromodynamics
SFR	Star formation rate
SGWB	Stochastic gravitational-wave background
SNR	Signal-to-noise ratio
TT-gauge	Transverse traceless gauge
ULV	Ultra-light vector field

Chapter 1

Introduction

This chapter provides theoretical introduction and detection technique of gravitational waves (GWs) and the background context of the current GW astronomy. Also, we describe the theoretical overview and motivations to search for ultra-light boson particle from the perspective of particle physics and dark matter (DM) searches.

1.1 Gravitational wave radiation in general relativity

Einstein's general theory of relativity provides the unified description of gravity as a geometric structure of space and time. While an earlier formalism of gravity such as Newton's law of universal gravitation describes gravity as an attractive force that exerts instantaneously and remotely between objects, the general relativity treats it as a result of the interaction between energy and spacetime. Not only can the general relativity reduce to Newton's law of gravity in the weak field limit, but also it has yielded new predictions that have been proven correct by various experiments [1], [2]. One of the prediction is a phenomenon called *gravitational waves*, namely space-time perturbation which propagates at the speed of light.

Here we review the derivation and some properties of GWs. The geometrical structure of the four dimensional spacetime is characterized by the metric tensor, $g_{\alpha\beta}$, which constructs the line element $\mathrm{d}s$, the proper distance given between two points in spacetime, yielding

$$\mathrm{d}s = g_{\alpha\beta}\,\mathrm{d}x^{\alpha}\,\mathrm{d}x^{\beta}, \tag{1.1}$$

where the indices $\alpha, \beta = \{t, x, y, z\}$ represent each dimension of spacetime and $\mathrm{d}x^{\alpha}$ is the interval between the two points in α's dimension, i.e. (ct, x, y, z). The metric tensor $g_{\alpha\beta}$ can be interpreted as a set of coefficients that convert the displacement in every dimension to the line element and fully encodes the geometric information of the spacetime. Building upon this tensor, the general relativity formulates the master equations, called

the Einstein equations, which read

$$G_{\alpha\beta} = \frac{8\pi G}{c^4} T_{\alpha\beta}, \tag{1.2}$$

$$\text{where} \qquad G_{\alpha\beta} \equiv R_{\alpha\beta} - \frac{1}{2} g_{\alpha\beta} R. \tag{1.3}$$

In the equation above, $G_{\alpha\beta}$ is called the Einstein tensor and contains the geometrical information given by the Ricci tensor ($R_{\alpha\beta}$) and the Ricci scalar (R) respectively as a function of $g_{\alpha\beta}$. The both quantities are related through $g_{\alpha\beta}$ such that $R = g_{\alpha\beta} R^{\alpha\beta}$ and can be evaluated at every point x^α in spacetime. Also, the Ricci tensor is defined by contracting another geometry-related tensor called the Riemann tensor, which essentially quantifies the curvature along a cyclic path on a surface in spacetime, yielding $R_{\alpha\beta} = g^{\gamma\delta} R_{\alpha\gamma\beta\delta}$. In contrast, the tensor on the right hand side of Eq. (1.2) is called the stress-energy tensor, which characterizes the distribution of matter, energy and momentum. Since the Riemann tensor involves the covariant derivatives, mathematically speaking, Eq. (1.2) is a set of non-linear differential equations in terms of x^α. This physically implies that the spacetime metric and its curvature interact with the energy distribution and they co-evolve until they reach an equilibrium. The equilibrium configuration can be derived by solving the Einstein equations (1.2).

1.1.1 Derivation of gravitational waves

Now we consider a nearly flat spacetime where the deviation from a flat spacetime is approximated with a linear perturbation such that

$$g_{\alpha\beta} = \eta_{\alpha\beta} + h_{\alpha\beta}. \tag{1.4}$$

Here $\eta_{\alpha\beta}$ is the Minkowski metric defined as $\mathrm{diag}(-1, 1, 1, 1)$ and $h_{\alpha\beta}$ is an infinitesimal perturbation, which satisfies $|h_{\alpha\beta}| \ll 1$. Substituting of Eq. (1.4) into the left hand side of Eq. (1.2), and introducing a new perturbed parameter, i.e. the *trace-reversed metric perturbation*, defined as

$$\bar{h}_{\alpha\beta} = h_{\alpha\beta} - \frac{1}{2} \eta_{\alpha\beta} h^\mu_\mu, \tag{1.5}$$

The Einstein tensor in Eq. (1.2) can be reduced to

$$G_{\alpha\beta} = \frac{1}{2} \left(\frac{\partial^2 \bar{h}^\mu_\beta}{\partial x^\alpha \partial x^\mu} + \frac{\partial^2 \bar{h}^\mu_\alpha}{\partial x^\mu \partial x^\beta} - \eta^{\mu\nu} \frac{\partial^2 \bar{h}_{\alpha\beta}}{\partial x^\mu \partial x^\nu} - \eta_{\alpha\beta} \frac{\partial^2 \bar{h}^{\mu\nu}}{\partial x^\mu \partial x^\nu} \right) + O\left(h^2\right) \tag{1.6}$$

to leading order of h.

To further simplify this expression, one needs to apply a gauge fixing. Just like electric and magnetic fields, one can measure the Riemann tensor by observing the physical tidal acceleration. Furthermore, it can be shown that the linearized Riemann

tensor is gauge invariant to linear order of h, i.e. the components of the tensor do not change in any gauge one chooses. Therefore, without inconsistency in experiments, one can apply *any* gauge transformation for $h_{\alpha\beta}$, in analogy to the vector potential in electromagnetism. Here we impose the following condition:

$$\frac{\partial \bar{h}^{\alpha\beta}}{\partial x^{\alpha}} = 0, \tag{1.7}$$

which is called the *Lorenz gauge* given a similarity to the Lorenz gauge condition in electromagnetism. With this gauge in place, only the third term in Eq. (1.6) remains and hence the Einstein equations (1.2) reduce to

$$\eta^{\mu\nu}\partial_{\mu}\partial_{\nu}\bar{h}_{\alpha\beta} = -\frac{16\pi G}{c^4}T_{\alpha\beta}. \tag{1.8}$$

Particularly in a vacuum where $T_{\alpha\beta} = 0$,

$$\eta^{\mu\nu}\partial_{\mu}\partial_{\nu}\bar{h}_{\alpha\beta} = 0. \tag{1.9}$$

This wave equation implies that the metric perturbation propagates in a vacuum at the speed of light in the same way as electromagnetic waves do, which led to the prediction of the existence of GWs by Albert Einstein in 1915 [3].

In fact, the Lorenz gauge condition (1.7) does not uniquely determine a new coordinate system, in other words, one can choose a different Lorenz gauge without breaking the condition of Eq. (1.7). Also, one can find that the Riemann tensor has the two independent degree of freedom due to its symmetry. From the fact that the Riemann tensor is observable quantities, it is expected that accordingly a GW solution should have two physical degrees of freedom and one can further remove artificial degrees of freedom through the appropriate gauge transformation. To illustrate additional gauge conditions to impose, given the wave equation (1.9), we consider a monochromatic plane-wave solution, namely

$$\bar{h}_{\alpha\beta} = A_{\alpha\beta}\cos(k_{\mu}x^{\mu}), \tag{1.10}$$

where the amplitude $A_{\alpha\beta}$ is a constant and symmetric tensor, and k_{μ} is a constant null-vector (i.e. $k_{\mu}k^{\mu} = 0$). Here we introduce a uniquely-fixed gauge called *transverse traceless gauge* (TT-gauge), $h^{\mathrm{TT}}_{\alpha\beta}$, which satisfies the following three conditions:

- The transverse condition

$$\frac{\partial \bar{h}^{\alpha\beta}_{\mathrm{TT}}}{\partial x^{\alpha}} = -k_{\mu}A^{\mu\alpha}_{\mathrm{TT}}\sin(k_{\nu}x^{\nu}) = 0 \tag{1.11}$$

This is equivalent to the Lorenz gauge imposed to obtain the wave equation (1.9).

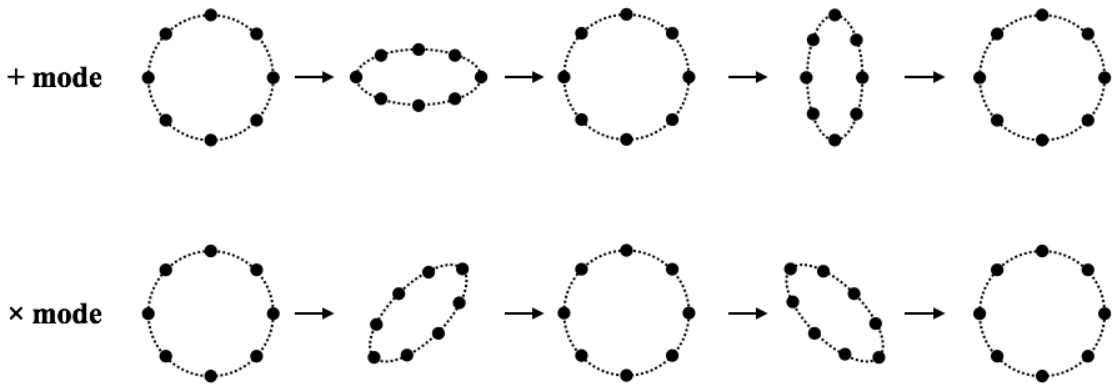

Figure 1.1: The schematic picture of time evolution for the two GW polarization modes.

- The spatial condition
  Given a time like vector $\boldsymbol{u} = \mathrm{d}/\mathrm{d}t$, we require that

$$A^{\mathrm{TT}}_{\alpha\beta} u^{\alpha} = 0. \tag{1.12}$$

- The traceless condition
  Given the requirement that $\eta^{\alpha\beta} h^{\mathrm{TT}}_{\alpha\beta} = 0$, it follows that

$$\eta^{\alpha\beta} A^{\mathrm{TT}}_{\alpha\beta} = 0. \tag{1.13}$$

It can be found that now the degrees of freedom of the metric perturbation, which is originally ten due to the symmetry of $h_{\mu\nu}$, reduces to two. This is consistent with the physical degree of freedom in the Riemann tensor, $R_{\alpha\gamma\beta\delta}$. Thus, the components of $h^{\mathrm{TT}}_{\alpha\beta}$ can be explicitly written as

$$h^{\mathrm{TT}}_{\alpha\beta} = \begin{pmatrix} 0 & 0 & 0 & 0 \\ 0 & -h_{+} & h_{\times} & 0 \\ 0 & h_{\times} & h_{+} & 0 \\ 0 & 0 & 0 & 0 \end{pmatrix}. \tag{1.14}$$

h_{+} and $h_{\times}$ are referred to as the plus and cross polarization mode, respectively, and their schematic time evolution is illustrated in Fig. 1.1.

1.1.2 Energy density of gravitational waves

As noted previously, there exists interaction between the energy distribution and the spacetime metric, meaning that the linear metric perturbation, $h_{\alpha\beta}$ derived from Eq. (1.8) in turn acts as energy source by itself, which induces second-order metric perturbation. Here we calculate the energy density associated with radiated GWs, although one should note that GW energy cannot be defined in a local frame, i.e. according to the equivalence principle one can always perform a coordinate transformation where the metric

perturbation is canceled out and hence there is no local GW energy. Therefore, as will be shown below, we will define it as integral average of an effective stress-energy tensor.

To better understand the effective stress-energy tensor, the Einstein equations in vacuum can be expanded such that

$$G_{\alpha\beta} = G^{[0]}_{\alpha\beta}(h_{\alpha\beta}) + G^{[1]}_{\alpha\beta}(h_{\alpha\beta}) + G^{[2]}_{\alpha\beta}(h_{\alpha\beta}) + \cdots \tag{1.15}$$

$$= 0, \tag{1.16}$$

where $G^{[n]}_{\alpha\beta}(h_{\alpha\beta})$ is the Einstein tensor constructed from n-th order of the perturbation, $O(h^n)$, e.g. $G^{[1]}_{\alpha\beta}(h_{\alpha\beta})$ is given by Eq. (1.6). We also expand the metric perturbation in Eq. (1.4) in powers of a formal order parameter λ, which reads

$$g_{\alpha\beta} = \eta_{\alpha\beta} + h_{\alpha\beta} \tag{1.17}$$

$$= \eta_{\alpha\beta} + \lambda h^{[1]}_{\alpha\beta} + \lambda^2 h^{[2]}_{\alpha\beta} + \cdots . \tag{1.18}$$

Substituting Eq. (1.17) into the Einstein tensor Eq. (1.15), one obtains an identity in terms of λ

$$0 = G_{\alpha\beta} = \lambda G^{[1]}_{\alpha\beta}\left(h_{\mu\nu}\right) + \lambda^2 \left\{G^{[1]}_{\alpha\beta}\left(h_{\mu\nu}\right) + G^{[2]}_{\alpha\beta}\left(h_{\mu\nu}\right)\right\} + O\left(\lambda^3\right), \tag{1.19}$$

which leads to the following equations by orders in λ,

$$G^{[1]}_{\alpha\beta}\left(h^{[1]}_{\mu\nu}\right) = 0, \tag{1.20}$$

$$G^{[1]}_{\alpha\beta}\left(h^{[2]}_{\mu\nu}\right) = -G^{[2]}_{\alpha\beta}\left(h^{[1]}_{\mu\nu}\right), \tag{1.21}$$

$$\cdots$$

and so on. Note that Eq. (1.20) is equivalent to Eq. (1.9) and Eq. (1.21) can be interpreted as the second-order Einstein equations. Therefore, from Eq. (1.21) that the right hand side given by the first-order perturbation, $h^{[1]}_{\alpha\beta}$, can be treated as an effective stress-energy tensor,

$$T^{\mathrm{GW}}_{\alpha\beta} \equiv -\frac{c^4}{8\pi G} G^{[2]}_{\alpha\beta}\left(h^{[1]}_{\mu\nu}\right) \tag{1.22}$$

which induces the second-order perturbation $h^{[2]}_{\alpha\beta}$. As mentioned above, we define the GW energy tensor by taking an integral average over a region of spacetime so that it contains several GW wavelengths, yielding

$$\bar{T}^{\mathrm{GW}}_{\alpha\beta} \equiv \left\langle T^{\mathrm{GW}}_{\alpha\beta} \right\rangle \tag{1.23}$$

$$= -\frac{c^4}{8\pi G}\left\langle R^{[2]}_{\alpha\beta} - \frac{1}{2}\eta_{\alpha\beta} R^{[2]} \right\rangle. \tag{1.24}$$

$R^{[2]}_{\alpha\beta}$ and $R^{[2]}$ are the Ricci tensor and scalar that appear in the second-order Einstein tensor, $G^{[2]}_{\alpha\beta}$. Although we skip the further derivation, expressing $R^{[2]}_{\alpha\beta}$ with the Christoffel symbols and applying some gauge conditions, Eq. (1.23) reduces to

$$\bar{T}^{\mathrm{GW}}_{\alpha\beta} = \frac{c^4}{32\pi G}\left\langle \frac{\partial h^{\alpha\beta}_{\mathrm{TT}}}{\partial x^\alpha} \frac{\partial h^{\mathrm{TT}}_{\alpha\beta}}{\partial x^\beta} \right\rangle. \tag{1.25}$$

In particular, taking $\alpha = \beta = t$, the GW energy density takes the form of

$$\rho_{\rm GW} \equiv \bar{T}^{\rm GW}_{tt} \tag{1.26}$$

$$= \frac{c^2}{32\pi G}\left\langle \dot{h}^{\alpha\beta}_{\rm TT}\, \dot{h}^{\rm TT}_{\alpha\beta}\right\rangle = \frac{c^2}{16\pi G}\left\langle |\dot{h}_+|^2 + |\dot{h}_\times|^2\right\rangle. \tag{1.27}$$

This expression will be useful later when we formulate a SGWB.

1.1.3 Quadrupole formula

So far we have considered the situation where there is no matter or energy except GWs themselves by setting the right hand side of the Einstein equation (1.2) to be zero. Here we deal with the GW generation from a given energy source especially in far-field zone where the distance to the source, r, is much longer than typical wavelength of the radiated GWs. We also assume that the size of the GW source is much smaller than the GW wavelength so that one can ignore the relative time shift between one region of the source relative to another, in which case a GW solution of Eq. (1.2) at spatial infinity ($r \to \infty$) takes the form of

$$\bar{h}^{\alpha\beta}(t,x) \simeq \frac{4G}{c^4 r}\int \tau^{\alpha\beta}\left(t - r/c, x'\right)\, {\rm d}^3x'. \tag{1.28}$$

In this expression, we introduce the effective stress-energy tensor including the contribution from GWs such that

$$\tau^{\alpha\beta} \equiv T^{\alpha\beta} + T^{\alpha\beta}_{\rm GW} + \cdots. \tag{1.29}$$

As we will be computing a GW solution in the TT-gauge, it is sufficient to have the spatial components of the trace-reversed metric perturbation $\bar{h}^{ij}$. Making use of the conservation law that holds between temporal and spatial components of $\tau^{\alpha\beta}$, one finds

$$\bar{h}^{ij}(t,x) \simeq \frac{2G}{c^4 r}\frac{\partial^2}{\partial t^2}\int x'^i x'^j \tau^{00}\left(t - r/c, x'\right)\, {\rm d}^3x' \tag{1.30}$$

$$=: \frac{2G}{c^4 r}\ddot{I}^{\rm ij}(t - r/c), \tag{1.31}$$

where the quadrupole tensor of the effective stress-energy tensor is defined as

$$I^{ij}(t) = \int x^i x^j \tau^{00}(t - r/c, x)\, {\rm d}^3x. \tag{1.32}$$

It is important to highlight that $\bar{h}^{\alpha\beta}(t,x)$ is inversely proportional to r, which is the radiative functional form just like the dipole radiation of electromagnetic waves. Transforming to the TT-gauge with a projection operator

$$I^{\rm TT}_{ij} = \left(P_{ik}P_{lj} - \frac{1}{2}P_{ij}P_{kl}\right)I^{kl}, \tag{1.33}$$

$$\text{where} \quad P_{ij} \equiv \delta_{ij} - \hat{n}_i \hat{n}_j \quad \text{and} \quad \hat{n}^i \equiv \frac{x^i}{r}, \tag{1.34}$$

it follows that

$$h_{ij}^{\mathrm{TT}}(t) \simeq \frac{2G}{c^4 r} \ddot{I}_{ij}^{\mathrm{TT}}(t - r/c). \tag{1.35}$$

Eventually, one can calculate the GW flux per unit source-frame time t and area A by inserting Eq. (1.35) into Eq. (1.25) with $(\alpha, \beta) = (t, z)$:

$$\frac{\mathrm{d}\rho_{\mathrm{GW}}}{\mathrm{d}t\,\mathrm{d}A} = T_{tz}^{\mathrm{GW}} = -c^{-1} T_{tt}^{\mathrm{GW}} = -\frac{G}{8\pi c^5 r^2} \left\langle \ddot{\dot{I}}_{ij}^{\mathrm{TT}} \ddot{\dot{I}}_{\mathrm{TT}}^{ij} \right\rangle. \tag{1.36}$$

After integrating over all solid angles in source frame, one finds the GW luminosity given by

$$\frac{\mathrm{d}\rho_{\mathrm{GW}}}{\mathrm{d}t} = -\frac{G}{5c^5} \left\langle \dddot{I}_{ij} \dddot{I}^{ij} \right\rangle. \tag{1.37}$$

We note that this expression is valid to leading order and only in the limit where the size of a GW source is much smaller than the GW wavelength. Also, the negative sign indicates the energy dissipation through the GW radiation. To understand how tiny effect GWs can only have in terms of energy, it is important to point out that the numerical factor G/c^5 is extremely small even for typical stellar objects, e.g. the Earth-Moon system can radiate GWs with only $\sim \mathcal{O}(10^{-6})$W. Nevertheless, given the triple time derivative of the quadrupole moment, the GW luminosity can be amplified significantly when objects are massive and highly accelerating. From this order-of-magnitude argument, one can expect substantial GW radiation from compact binary coalescence (CBC) systems.

1.2 Gravitational-wave astronomy

1.2.1 History of gravitational-wave observations

In 1915, Einstein's theory of general relativity was first published [4] and in the following year he predicted the existence of GWs [3]. Since then tremendous efforts to search for GWs had been made but the first observational evidence of their existence had not been found until Russell Hulse and Joseph Tayler discovered a binary neutron star (BNS) known as PSR1913+16 [5]. They detected pulse signals from one of the neutron stars using a radio telescope and the data analysis by Taylor and Joel Weisberg confirmed that the decay rate of the binary orbit is consistent with the prediction based on the GW emission in the general relativity, which suggested the indirect observation of GWs. This historical milestone led Hulse and Taylor to the 1993 Novel Prize in Physics and inspired many of the subsequent direct searches for GWs from CBC systems.

Since the discovery by Hulse and Taylor, there have been extensive studies on different mechanisms for direct measurements of the GW effect, which includes the pioneer

GW bar-detector designed by J. Weber [6]. After decades of null detections in their searches, the revolutionary breakthrough was eventually made by the Laser Interferometer Gravitational-wave Observatory (LIGO), a pair of km-scale interferometers located in the USA. Given a number of exquisite techniques to suppress the detector noise, LIGO is now able to detect sub-atomic scale of mirror displacements. On September 14th 2015, LIGO detected unambiguous strain waveform (GW150914) consistent with GWs from a coalescence of BBH predicted in the general relativity [7]. Along with this first-ever detection of GWs, it revealed the existence of a BBH system as massive as $30M_{\odot}$ for each component. Theorists proposed many scenarios that might produce such heavy BHs, e.g. pop 3 progenitor stars [8], [9], dynamical formation in a stellar cluster [10] and primordial BHs [11]. Given the considerable sensation caused by the LIGO's detection, it is no wonder that it took only one and half years for the three pioneers of the LIGO & Virgo Scientific Collaboration (LVC) to receive the 2017 Novel prize in Physics for their discovery. Without any doubt, this was indeed the dawn of a brand-new field of astronomy, *gravitational-wave astronomy*.

The next milestone arrived only two years later, on August 17th 2017, when advanced LIGO & Virgo detected GW signal consistent with a BNS, named as GW170817, [12] in coincidence with the detection of the short γ-ray burst by Fermi [13]. After a detection alert of GW170817 was sent out with a localization of the GW source within 31 deg^2, extensive follow-up by electromagnetic telescopes were conducted. Subsequently, optical and infrared emissions (known as kilonova [14]–[16]) as well as radio afterglow were detected from the consistent host galaxy, which provided some insight on the characteristic nuclear process, called *r*-process, and the models of a relativistic jet [17]. Furthermore, this event brought many more implications than GW150914, such as the constraints on the equation of state for high-density nuclear matter [18], GW propagation speed [19], and independent measurement of the hubble constant [20]. This is one of the greatest success of the multi-messenger astronomy in the history of science.

So far advanced LIGO & Virgo continued to detect GW signals during the first and second observing runs (O1 and O2), producing catalogs of their GW detections from CBC systems [21], [22]. Recently, LVC published the latest[1] GW transient catalog (GWTC-2 [23]) using the data up to the first half of the third observing run (O3a), which contains 39 new GW candidates, amounting to 50 candidates in total throughout O1-O3a. Some of those candidates are known to have unusual characteristics: relatively higher mass-ratio [24], the total mass heavier than $150M_{\odot}$ [25] and potential neutron-star black-hole binary [26]. Moreover, given the 50 candidates, now it is possible to perform more statistical population inference, e.g. the observed samples of BBH systems prefer the distribution of the primary component mass with a power-law and a local peak [27].

[1] As of December 2020.

After LVC finished O3, there has been an upgrade commissioning phase to prepare for upcoming next observing run (O4) and beyond. As future proposals, not only are ground-based interferometers with even larger scale being planed, e.g. Einstein telescope [28] and Cosmic Explorer [29], but also space interferometric observation projects such as Laser Interferometer Space Antenna (LISA) [30] and DECIGO [31], [32] are waiting to be realized in 2030s or later. In particular, the LISA pathfinder has already made a great achievement on its target performance [33], which is a promising sign of future GW observations. Apart from interferometric experiments, there exist other GW detection projects with different principles such as Pulsar Timing Array [34]–[36], which claimed potential detection of a SGWB (though not yet to be confirmed) [37], and cosmic microwave background (CMB) B-mode polarization measurement by BICEP and KECK Array [38]. In summary, the field of GW astronomy is still in its infancy and will keep growing in the future, and given an expanding detector network on Earth and in space the next excitement is likely to be just around the corner.

1.2.2 Interferometric gravitational-wave detector

As mentioned above, an interferometric GW detector is the only instruments that have made direct GW detections successfully so far. Here we briefly show how one can measure the GW effect using a Michelson interferometer. For the purpose of demonstration, we consider only the simplest configuration where two test masses sit on the end of the two arms in an interferometer. An input laser is first split by a beam splitter sitting on the center of apparatus into two paths, each of which is incident toward the end of each arm and travels along the arm until it reflects back off the test mass at the end. The two beams return back to the beam splitter and merge together and eventually go into the other port where a photodetector measures the beam intensity. The general concept of interferometry is to read off information from beating signals of multiple beams which create interference. Particularly, in the following we mathematically show how to extract information of GW strain from a phase shift between interfered two lasers.

Each laser diverged at a beam splitter has an electric field, which is approximated to be monochromatic as follows

$$E_{x/y}(t) = E_0 \exp(-i\omega t), \tag{1.38}$$

where the subscript "x/y" indicates a field in X and Y arm, respectively. Now suppose that two test masses originally sit at the end of the two arms respectively, being L_0 away from the beam splitter in the absence of GW effect or noise disturbance. After a round trip along each arm, taking time of Δt, the fields gain a phase term, $\Phi_{x/y}$, namely

$$E_{x/y}(t + \Delta t) = E_0 \exp(-i(\omega t + \Phi_{x/y})). \tag{1.39}$$

Here referring to the metric perturbation in the TT-gauge (1.14),

$$\Phi_{x/y} = \frac{2\pi}{\lambda} 2 \times \int_0^{L_0} \sqrt{g_{xx/yy}}\, \mathrm{d}x/y \tag{1.40}$$

$$\approx \frac{4\pi}{\lambda} \int_0^{L_0} \left(1 \pm \frac{1}{2} h_+(t - z/c)\right) \mathrm{d}x/y \tag{1.41}$$

$$= \frac{4\pi}{\lambda} \left(1 \pm \frac{1}{2} h_+(t - z/c)\right) L_0 \tag{1.42}$$

where the (+) sign in (1.41) is for x component, while the (−) sign is for y component. Here we assume that the wavelength λ is much longer than the arm length L_0, i.e. the period of GW oscillation is much longer than the round trip time in the arm so that h_+ can be approximated to be stationary during the light's travel. These fields add up again at the beam splitter and the electric field reaching a photodetector reads

$$E_{PD}(t) = \frac{1}{\sqrt{2}} E_x + \frac{1}{\sqrt{2}} E_y \tag{1.43}$$

$$= \frac{1}{\sqrt{2}} E_0 \left\{ \exp(-i(\omega t + \Phi_x)) + \exp(-i(\omega t + \Phi_y)) \right\}. \tag{1.44}$$

The photodetector senses power of this field, so one can measure

$$P_{PD}(t) = |E(t)|^2 \tag{1.45}$$

$$\propto E_0^2 \left(1 + \cos((\Phi_x - \Phi_y))\right) = E_0^2 \left\{ 1 + \cos\left(\frac{4\pi h_+}{\lambda} L_0\right) \right\}. \tag{1.46}$$

This indicates that one can detect the GW effect as an amplitude modulation measured by the photo detector and that magnitude of the effect is proportional to the arm length. Please note that this discussion is largely simplified and a number of complex components, such as a Fabry-Perot cavity, will be discussed below taking an example of advanced LIGO [39].

1.2.3 LIGO

LIGO is a US-funded interferometric GW observatory consisting of two identical facilities located at Hanford, Washington and Livingston, Lousiana respectively. After the intermittent hardware upgrades since their first operation in 2002, LIGO improved their sensitivity approximately ten times better than its initial phase, which corresponds to the improvement of its sensitive volume by a factor of 1000. Fig. 1.2 illustrates the apparatus of advanced LIGO upgraded from the basic configuration of a Michelson interferometer. As explained in the previous subsection, the GW train is encoded in the phase shift between the two beams:

$$\Delta\Phi = \frac{4\pi h L}{\lambda}. \tag{1.47}$$

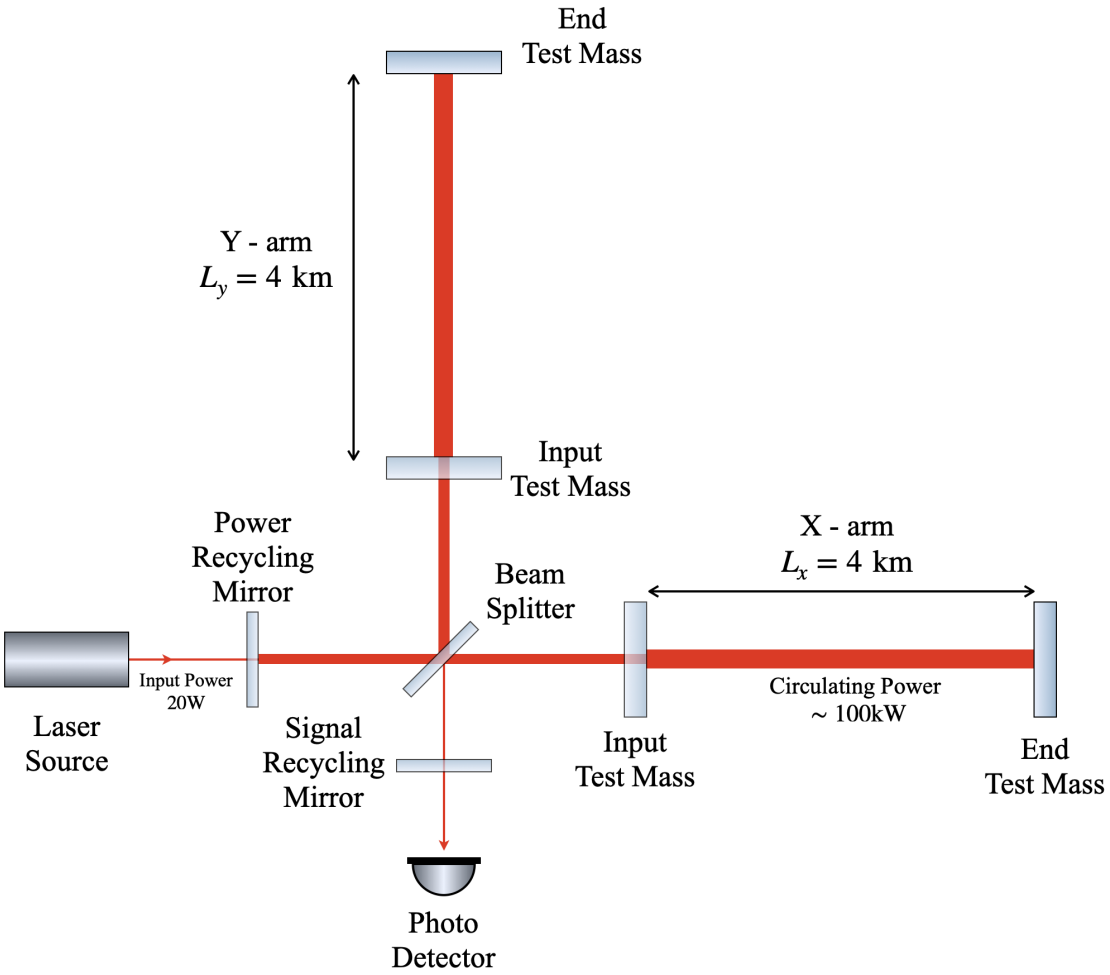

Figure 1.2: Schematic diagram of advanced LIGO. An input laser is first split by a beam splitter sitting on the center of apparatus into two paths, each of which is incident toward the end of each arm and travels along the arm until it reflects back off the test mass at the end. The two beams return back to the beam splitter and this time merge together and eventually go into the other port where a photodetector measures beam intensity.

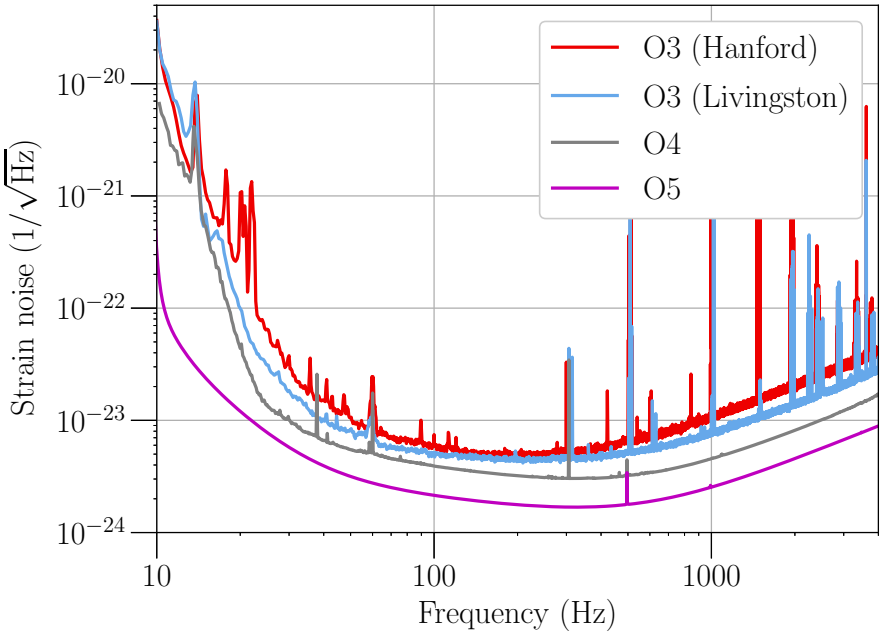

Figure 1.3: Amplitude spectral density of Advance LIGO for different commissioning phases from the third observing run (O3) to the fifth observing run (O5). Each observation phase is depicted with different colors. This is reproduced from the data products publicly available in Ref. [40]

This expression implies that the arm length L serves as amplification factor of the strain signal and a longer arm length yields larger phase shift, leading stronger amplitude modulation at a photodetector. Building upon this insight, LIGO was designed to have kilometer-scale arms to enhance the sensitivity to the GW strain. Additionally, another test mass is installed inside each arm to form a 4-kilometer Fabry-Perot optical cavities. Inside the cavities, an incident beam keeps reflecting by the inner side of the test masses and accumulate its circulating power. This power circulation effectively increases the arm length by a factor of ~ 300 for advanced LIGO [39]. To further improve the sensitivity, two more mirrors, called power-recycling and signal-recycling mirror respectively, are placed at the input and output port of the interferometer. They reflect lights back to the arm cavity with tuned configuration so that they effectively increase circulating beam power inside cavity without hardware defect caused by excessive heat.

Fig. 1.3 shows the amplitude spectral density of advanced LIGO's instrumental noise for different observing phase from O3 to O5. To gauge the detector's sensitivity, it is conventional to use the maximum distance at which a $1.4M_\odot + 1.4M_\odot$ BNS system with the optimal orientation can be detected with SNR ≥ 8. One can see during O3 the Livingson site tends to have slightly better sensitivity (130 Mpc) than the Hanford site (110 Mpc). O4 and O5 are expected to reach the sensitivity of 160–190 Mpc and 330 Mpc respectively [41]. Overall, at the lower frequency band $f \lesssim 30\,\text{Hz}$ the sensitivity is limited by seismic noise, whereas at higher frequencies $f \gtrsim 1000\,\text{Hz}$ photon shot noise

is the dominant factor.

1.3 Ultra-light boson particles

Ultra-light boson particles, which refer to masses $\ll$ eV, have drawn a broad attention in the perspectives of particle physics and cosmology. Specifically, some of the light scalar and vector fields motivated by beyond-the-Standard-Model or the superstring theories are promising candidates of the dark matter alternative to the weakly-coupled cold dark matter (CDM) scenario, e.g. WIMPs [42]. In what follows, we briefly review the theoretical background of these boson particles from the both viewpoints and provide motivations to search for such particles.

In particle physics, one of the plausible examples of light boson particles is axion [43] (see Refs. [44]–[46] for technical review), which is a pseudoscalar proposed as a potential solution to the strong CP problem in the quantum chromodynamics (QCD) [43]. In this model, the QCD axion acquires its mass through QCD symmetry breaking (i.e. instanton effects), being inversely proportional to its decay constant, f_a:

$$m_a \approx 6 \times 10^{-12}\,\mathrm{eV}\left(\frac{10^{18}\,\mathrm{GeV}}{f_a}\right), \tag{1.48}$$

which implies that for a relatively high decay constant the axion can be substantially light. There is also somewhat generalized model of such scalar bosons, called axion-like particles (ALPs). These particles are naturally emerged in string-inspired theories such as axiverse [47] and have been predicted to be a potential signature of extra dimensions [47], [48]. In particular, in the axiverse scenario the ALPs are predicted to have a wider range of masses, down to 10^{-33} eV. The constraints on the masses of these scalar fields are derived typically from mechanisms based on their coupling to photons characterized by the following term in the Lagrangian:

$$\mathcal{L}_{a\gamma} = g_{a\gamma} a F^{\mu\nu} F_{\mu\nu}, \tag{1.49}$$

where $g_{a\gamma}$ is the mixing parameter between the scalar field a and the photon γ, and $F^{\mu\nu}$ is the electromagnetic field tensor. This produces constraints on the two-dimensional parameter space of $(m_a, g_{a\gamma})$. The axion mass is currently bound from the direct search [49]–[52], overproduction in the early Universe, negative searches in accelerators and astrophysical considerations [53], [54]. And similarly the constraints on ALP's mass can be derived, although they are far less stringent than those for axions due to no relation between their mass and decay constant. See Ref. [55] for a review of these constraints. Furthermore, there have been models of ultra-light vector fields (ULVs), e.g. dark photons, predicted by string theories [56]. This scenario considers a ULV, γ', in a hidden $U(1)$ sector weakly coupling to the visible photon field via the mixing term

as follows:

$$\mathcal{L}_{\gamma\gamma'} = \frac{\sin\chi}{2} X_{\mu\nu} F^{\mu\nu}, \tag{1.50}$$

where χ is the mixing parameter between a ULV and the visible photon field and $X^{\mu\nu}$ is the field-strength tensor of the ULV. The constraints on such a vector field is given in the $(m_{\gamma'}, \chi)$ plane. See Ref. [57] for the details.

In the context of the cosmological DM, naively speaking, if such light boson particles are in thermal equilibrium in the early Universe, they would have decoupled at very early phase and acted as relativistic radiation, which leads to mass density too low to become the DM. Nevertheless, it has been found that at a large scale they coherently oscillate and can be interpreted as a Bose condensate of bosons [58]–[60], which implies the some of the CDM-like features. More importantly, their characteristic behaviors due to the extremely small masses would help to solve some long-standing puzzles of the large-scale structure, such as small scale problem (i.e. the apparent inconsistency of the DM density at the scale $\leq 10\,\mathrm{kpc}$ between the current observations and the prediction based on the standard CDM model) [61] and the cusp-core problem (i.e. the disagreement in the halo's density profile near its center between the observations and the diverging behavior, $\rho(r) \propto r^{-1}$, predicted by the simulation) [62]. For example, in the Fuzzy dark matter model, scalar boson particles behave like a classical field at the scale smaller than their de Broglie wavelength given by

$$\frac{\lambda}{2\pi} = \frac{\hbar}{mv} = 1.92\,\mathrm{kpc}\left(\frac{10^{-22}\,\mathrm{eV}}{m}\right)\left(\frac{10\,\mathrm{km\,s^{-1}}}{v}\right), \tag{1.51}$$

and hence the boson mass of the order of $10^{-22} \sim 10^{-21}$ eV can naturally explain the inconsistency in the small scale problem. Also, several simulations suggest that there exists a stationary solution of the field's configuration that minimizes the energy, called a "soliton" [63]–[66]. Thus, such a model predicts core-like profile in the center that smoothly transitions to normal density profile in outskirts of halos and could solve the cusp-core problem.

In summary, current yet-unsolved problems in the particle physics and standard cosmology bring a strong motivation to probe the existence of exotic ultra-light boson particles. Most importantly for this thesis, it is known that these particles can form macroscopic Bose condensate around a rotating BH via superradiance [67]–[74]. As will be shown in the subsequent chapter, this phenomenon can be searched using its GW signature produced from the macroscopic bosons and the sensitive frequency band of advanced LIGO could target the bosons with mass $\sim 10^{-12}\,\mathrm{eV}$ (see Eq. (4.2.3)), which can be obtained by QCD axion model shown in Eq. (1.48). Additionally, we note that there are several models that assume that ultra-light bosons could couple directly to Standard-Model matter. Interestingly, in some models where such particles couple to

baryons, they could also produce different (but characteristic) signals in GW interferometers by inducing displacements of optical mirrors [75]–[78]. Since the superradince is purely gravitational effect and hence our results in this thesis apply to massive bosons for which non-gravitational interactions are negligible, it can provide an approach to place constraints on the boson masses, being independent of those searches as well as other models assuming the boson-photon coupling. (see Ref. [79] for more discussion in the DM context).

Chapter 2

Stochastic Gravitaional-wave Background

We briefly review the statistical properties and the possible sources of a SGWB. Putting an emphasis on the context of the current ground-based GW detectors, we also provide the conventional method to detect the background signal. For more thorough review, see [80]–[82].

2.1 Statistical properties

A SGWB is the incoherent superposition of GW signals produced from a large number of sources in the Universe, which is too faint or closely overlapped to detect individually. In contrast to deterministic strain signals from astrophysical sources such as CBCs, a SGWB is by definition probabilistic, and hence, can be treated as random variables just like intrinsic detector noise. Therefore, it should be characterized only in a statistical way.

Apart from the probabilistic nature of a SGWB, it is different from transient signals in several aspects. Typically we assume a SGWB to be: (a) isotropic, (b) unpolarized, (c) stationary and (d) Gaussian. These assumptions are the ground for the discussion in the rest of this thesis. In what follows, we will describe the details of these assumptions and explain why each of them can be justified in our analysis.

(a) The isotropy of the background is not always the case for an astrophysical GW sources unlike its electromagnetic equivalent, that is, a CMB. For example, if a large number of binary white dwarf systems in our galaxy make a significant contribution to a SGWB, the background would have an anisotropic distribution just like the Milky Way for electromagnetic waves. Therefore, practically speaking, a search for a SGWB is performed in two ways, isotropic [83], [84] and directional search [85], [86]. Our pipeline that builds up on this assumption is sensitive to only the isotropic component of the spatial distribution.

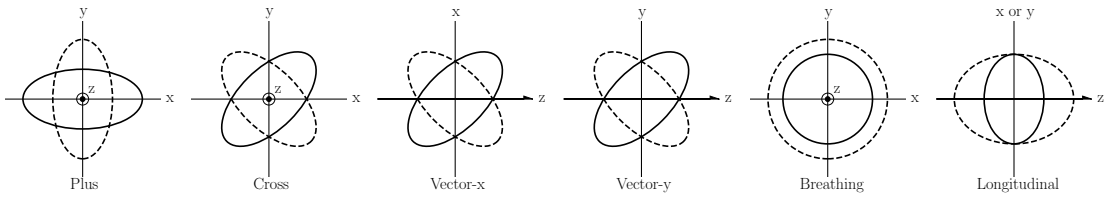

Figure 2.1: Illustration of test particles under the six generalized GW polarizations.

(b) As mentioned in Chapter 1.1, general relativity predicts GWs with only two degrees of freedom. These modes, referred to as plus and cross polarizations, are geometrically equivalent to each other through rotation by 90°. Thus, as an ensemble of individual signals, a SGWB is expected to have statistically equal amount of energy in either mode. Although different theories of gravity may include other polarizations such as the x/y vector and the breathing/longitudinal scalar modes (See Fig. 2.1), a search for such polarizations is beyond the scope of this thesis.

(c) The stationarity of a SGWB means that any statistical quantity obtained from data depends only on the time interval between samples, not the choice of absolute time. This can be quite likely satisfied because most of the astronomical timescale such as stellar lifetime and merger timescale of compact binaries is sufficiently longer than the characteristic period of the waves that ground-based detectors can detect ($\sim 1/100$ second), or the observation times ($\sim$ years).

(d) The statement that signal $h(t_i)$ in each detector is Gaussian means that the joint probability density function of GW strains $h_i(t_i), h_j(t_j)$, ... in detectors i, j, ... is a multivariate Gaussian distribution. Since a SGWB is defined here as the superposition of a extremely large number of sources, the central limit theorem ensures Gaussianity of the superposed signals regardless of intrinsic probability distributions which individual strain samples obey.

In the context of a SGWB, motivated by standard cosmology, it has been customary to consider the energy density of GWs in the Universe, $\rho_{\rm GW}$, instead of a spectrum of the GW strain. In particular, the energy density is described relative to the critical energy density,

$$\rho_c \equiv \frac{3c^2 H_0^2}{8\pi G} \approx 1.6 \times 10^{-8} h_{100}^2 \ \mathrm{erg/cm^3}, \tag{2.1}$$

and the background spectrum is defined as the fractional GW energy density per logarithmic frequency interval. Therefore, the energy density spectrum is defined as

$$\Omega_{\rm GW}(f) \equiv \frac{1}{\rho_c} \frac{\mathrm{d}\rho_{\rm GW}}{\mathrm{d}\ln(f)}, \tag{2.2}$$

where $\mathrm{d}\rho_{\rm GW}(f)$ is the energy density of the stochastic GW field in the logarithmic frequency interval between $\ln(f)$ and $\ln(f + \Delta f)$. Under the assumptions described above, a SGWB can be fully described by this quantity.

Here we provide some statistical properties of a SGWB, which will be necessary to describe the detection method in the subsequent chapter. Eventually, we wil show the relation between a GW strain and the energy density spectrum. First of all, gravitational metric perturbation at the time of t and spatial coordinate of $\vec{x}$ generally can be expanded in terms of plane waves in a TT-gauge such that

$$h_{ab}(t,\vec{x}) = \sum_A \int_{-\infty}^{\infty} \mathrm{d}f \int \mathrm{d}\hat{\Omega}\, h_A(f,\hat{\Omega}) \mathrm{e}^{i2\pi f(t-\hat{\Omega}\cdot\hat{x}/c)} e^A_{ab}(\hat{\Omega}) \tag{2.3}$$

Here $e^A_{ab}(\hat{\Omega})$ are the polarization tensors for the plus and cross modes $A = +, \times$. Also, $\hat{\Omega}$ is a unit vector pointing a direction on the two-dimensional sphere. Explicitly,

$$e^+_{ab}(\hat{\Omega}) = \hat{m}_a\hat{m}_b - \hat{n}_a\hat{n}_b \tag{2.4}$$

$$e^\times_{ab}(\hat{\Omega}) = \hat{m}_a\hat{m}_b + \hat{n}_a\hat{n}_b \tag{2.5}$$

where

$$\hat{\Omega} = \cos\phi\sin\theta\,\hat{x} + \sin\phi\sin\theta\,\hat{y} + \cos\theta\,\hat{z}, \tag{2.6}$$

$$\hat{m} = \sin\phi\,\hat{x} - \cos\phi\,\hat{y}, \tag{2.7}$$

$$\hat{n} = \cos\phi\cos\theta\,\hat{x} + \sin\phi\cos\theta\,\hat{y} - \sin\theta\,\hat{z}, \tag{2.8}$$

and (θ,ϕ) are the polar and azimuthal angles on the two-dimensional sphere. The Fourier amplitudes $h_A(f,\hat{\Omega})$ is the amplitude of the Fourier component for a given f and $\hat{\Omega}$. Note that $h_A(f,\hat{\Omega})$ is an arbitrary complex function on the condition that $h_A(-f,\hat{\Omega}) = h^*_A(f,\hat{\Omega})$.

Using the four assumptions above, the correlation function for pairs of modes reads

$$\langle h^*_A(f,\hat{\Omega}) h_{A'}(f',\hat{\Omega}')\rangle = \delta^2(\hat{\Omega},\hat{\Omega}')\delta_{AA'}\delta(f-f')H(f), \tag{2.9}$$

where $H(f)$ is a real, non-negative even function, that is, $H(f) = H(-f)$[1]. Since a stochastic background has zero mean, i.e.

$$\langle h_A(f,\hat{\Omega})\rangle = 0. \tag{2.10}$$

and it is assumed that the SGWB is Gaussian, Eq. (2.9) completely specifies its statistical properties.

As shown in Section 1.1.2, the energy density of GW can be derived from an ensemble average of time derivative's product of the GW strain (see Eq. (1.27)),

$$\rho_{\mathrm{GW}} = \frac{c^2}{32\pi G}\langle \dot{h}_{ab}(t,\vec{x})\dot{h}^{ab}(t,\vec{x})\rangle. \tag{2.11}$$

[1]Note that if the SGWB is anisotropic or polarized, $H(f)$ becomes $H(f,\hat{\Omega},A)$, which depends on $\hat{\Omega}$ and A too.

Substituting Eq. (2.3) into Eq. (2.11) and making use of Eq. (2.9), one can find

$$\rho_{\rm GW} = \frac{4\pi^2 c^2}{G}\int_0^\infty {\rm d}f\ f^2 H(f)\ \left(=: \int {\rm d}f \frac{1}{f}\frac{{\rm d}\rho_{\rm GW}}{{\rm d}\ln f}\right). \tag{2.12}$$

From the definition of $\Omega_{\rm GW}$ Eq. (2.2), Eq. (2.12) yields

$$H(f) = \frac{3H_0^2}{32\pi^3}|f|^{-3}\Omega_{\rm GW}(|f|). \tag{2.13}$$

Therefore, one can obtain the relation between $h_A(f,\hat{\Omega})$ and $\Omega_{\rm GW}$ as follows [80]

$$\langle h_A^*(f,\hat{\Omega})h_{A'}(f',\hat{\Omega}')\rangle = \frac{3H_0^2}{32\pi^3}\delta^2(\hat{\Omega},\hat{\Omega}')\delta_{AA'}\delta(f-f')|f|^{-3}\Omega_{\rm GW}(|f|). \tag{2.14}$$

2.2 Possible sources

There exists a variety of sources which contribute to a SGWB. They can be categorized into the cosmological and astrophysical sources . This section provides the basic explanation for each of them based on [80], [82], [87].

2.2.1 Cosmological backgrounds

Inflation

Since the discovery of the CMB [88] and the precise measurement of its temperature fluctuations in various angular scales [89]–[91], it has become possible to infer the cosmological parameters that describe the Universe. As we have obtained more observational data and established the standard cosmology (i.e. ΛCDM model), there have been several puzzling questions such as *Horizon problem* and *Flatness problem*, which theories need to account for.

The theory of inflation was proposed to solve these problems [92], stating that exponential growth of the scale factor a in the early Universe naturally leads to the curvature being negligible without the fine tuning of the initial condition and makes our observable Universe at present being originally in causal contact. This theory is formulated in the presence of quantum scalar field, called *inflaton*. Just like any other quantum fields, this scalar field would have had vacuum fluctuation at the beginning, which is believed to serve as the initial seeds of the subsequent matter distribution of the Universe. Although the inflation is the promising theory so far, we have not yet found the smoking gun that proves it.

In the context of the GW physics, along with the scalar fluctuation, there would have existed the tensor fluctuation in the density of the early Universe, which in turn induces fluctuations in the spacetime geometry leading to GW generation. This GW

signal remains even at present in the background, which is often referred to as a cosmic gravitational-wave background (CGWB). Just as the observation of CMB indicates the existence of freeing photons, CGWB can be interpreted as gravitons decoupled from photons and matter. Since gravitation could have decoupled at the Plank time ($= \sqrt{\hbar G/c^5} \sim 10^{-43}$ s after the Big Bang), CGWB in principle provides one of possible ways to probe the Universe much earlier than CMB does ($\sim 10^{13}$ s after the Big Bang).

A toy model of a quantum pendulum is often used to illustrate the amplification of the quantum fluctuation during inflation [80], [87]. This pendulum, which analogizes a quantum field acting as a harmonic oscillator, undergoes an adiabatic expansion and eventually gain some expectation value of energy. In other words, the number of quanta would increase through inflation. In the case of the gravitational field, these quanta correspond to gravitons. As inflation and subsequent cosmic expansion proceed, the gravitons are created and their wavelength get lengthened until they become classical GWs.

Under a simple model of harmonic oscillators and the standard cosmology, one can approximately calculate the amplitude of energy density spectrum $\Omega_{\rm GW}$ for CGWB. After taking into account the number density and energy levels of each harmonic mode and so on, one can eventually obtain the expression of $\Omega_{\rm GW}$ as follows [87]

$$\Omega_{\rm GW} = \frac{\hbar}{4\pi^2 c^5} \frac{H_0^2 H_{\rm inf}^2}{\rho_c} \tag{2.15}$$

where H_0 and $H_{\rm inf}$ are the Hubble parameter today and during the inflationary epoch respectively and ρ_c is the critical density of the Universe. What is noticeable in Eq. (2.15) is that the energy density spectrum is constant over the frequency range of our interest, specifically frequencies above 10^{-17} Hz, which is the horizon crossing scale. Also, more crucially, due to the exponential expansion during the inflationary era, the amplitude of CGWB is supposed to be largely suppressed and it is not effective to survey with the current or planned GW detectors. Depending on the value of $H_{\rm inf}$ or the detail of the inflation model, $\Omega_{\rm GW}$ can be inferred as $\sim [10^{-12} - 10^{-15}]$.

Cosmic Strings

Cosmic strings are one-dimensional topological defects believed to have been formed during a phase transition in the early Universe. This phase transition can be characterized by a spontaneous symmetry breaking [93] within a wide range of field theories such as Grand Unified Theories in the early Universe [94]. Apart from classical cosmic strings, so-called cosmic superstrings have been proposed as quantum objects in the superstring cosmologies [95].

Theoretically, the both types of cosmic strings have several remarkable aspects [82], [87]. First, there always exist some strings in the form of loops. When a cosmic string

self-intersects, it swaps its partner and separates from the rest of the string with some probability, p (the intercommutation probability), eventually forming a cosmic string loop. While classical cosmic strings always form a loop upon their self-intersection (i.e. $p \approx 1$) , cosmic superstrings can have a variety of p, predicted to be in the range from 10^{-3} or 10^{-1} to 1 depending on the model [96]. As such a self-intersection happens over time within a network of strings, along the loops they can have points with discontinuities on the tangent vectors, which are called "kinks" shown in Fig. 2.2 and there will be a large number of string loops with different sizes up to Hubble scale. It turns out that the energy density of cosmic superstrings is proportional to the inverse of intercommutation probability $\propto p^{-1}$ [95], and hence this probability plays an important role in the production of SGWB from cosmic superstrings. Second, a cosmic string is characterized by its mass-per-unit-length μ, by which one can define an effective length of the loop. More importantly, they have a tension equal to μc^2, so they oscillate highly relativistically at the points where the strings double-back on themselves called "cusp" (see Fig. 2.2 for the illustration). Thus, a circular loop of a cosmic string, initially at rest, collapses subject to its own tension, which takes a timescale comparable to the time it takes a light ray to move a distance equal to the radius of loop [80]. Lastly, once the strings reach the stable trajectory resulting from successive loop formations, the loops dissipate through gravitational radiation. In particular, a cusp or kink formed in a string causes a burst of GWs, by which a loop of a cosmic string eventually loses its energy and shrink to zero size. These individual signals produced from cosmic strings throughout the history of the Universe could be superposed and contribute to a SGWB.

Three types of GW bursts, originated from cusps, kinks and kink-kinks collisions on string loops have been studied [97]–[99] and are expected to follow the characteristic power-law spectra

$$\tilde{h}_i(f) = \begin{cases} A_i(\ell, \mu, z) f^{-\alpha_i} & (f_1 < f < f_2) \\ 0 & \text{otherwise,} \end{cases} \tag{2.16}$$

where $i = \{\mathrm{c}, \mathrm{k}, \mathrm{kk}\}$ indicates cusp, kink and kink-kinks collision cases respectively, and each source type has a different power-law index: $q_\mathrm{c} = 4/3, q_\mathrm{k} = 5/4$ and $q_\mathrm{kk} = 2$. $A_i(\ell, \mu, z)$ is an undetermined amplitude factor that depends on a loop size, ℓ, and the dimensionless string tension, $G\mu/c^2$. f_1 is practically set by the frequency band cutoff by a GW detector, and f_2 depends on a viewing angle of an observer with respect to the cusp. The energy density spectrum of the SGWB, $\Omega_\mathrm{GW}(f)$ contributed from these burst types can be constructed by weighting individual energy spectra of the burst signals (2.16) with the burst rate density $\mathrm{d}R_i/\,\mathrm{d}z$, yielding

$$\Omega_\mathrm{GW}(f) = \frac{4\pi^2}{3H_0^2} f^3 \sum_i \int_0^\infty \mathrm{d}z \frac{\mathrm{d}R_i}{\mathrm{d}z} \times h_i^2(z). \tag{2.17}$$

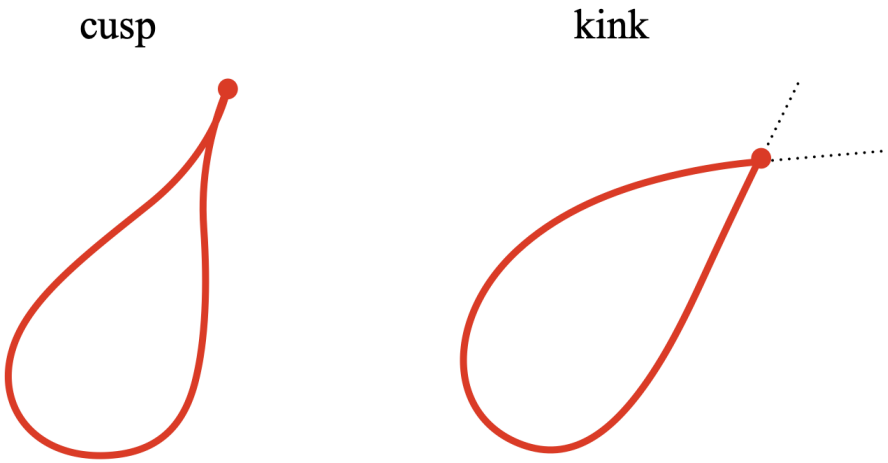

Figure 2.2: Cartoon illustration of cosmic string's cusp and kink.

In the above expression, the contribution from each burst type is summed up independently and the burst rate density depends on the population model of cosmic strings.

Recently, several experiments have been used to place constraints on the string tension, $G\mu/c^2$. Ref. [100] combined the results from different cosmological surveys such as CMB temperature anisotropies, baryon acoustic oscillations and gravitational lensing data and derived the join constraints of $\Omega_{\rm GW}h_0 < 3.8 \times 10^{-6}$ at a 90% confidence level, which is translated to the upper limit $G\mu/c^2 \leq 4 \times 10^{-9}$ for the intercommutation probability of $p = 10^{-3}$. This constraint assumes the size of the loops are derived by gravitational back-reaction. Also, LVC considered two analytical models for the cosmic string population and published the results of their analysis using the data from O1 and O2 [84], [101]. The first model adopts the numerical calculations to compute the loop size at its creation, whereas the second one incorporates the distribution of strings without self-interaction, as well as the back-reaction on the loops. The burst search was not sensitive enough to place constraints for the first model but for the second model derived the limit of $G\mu/c^2 \leq 4.2 \times 10^{-10}$ with a 95% confidence level [101]. On the other hand, the SGWB search produced the limits of $G\mu/c^2 \leq 1.1 \times 10^{-6}$ for the first model and $G\mu/c^2 \leq 2.1 \times 10^{-14}$ for the second model, respectively [84].

First-order Phase Transition

Another cosmological origin of a SGWB is a first-order phase transition in the early Universe. In general, a first-order phase transition involves the discontinuity in a thermodynamic variable. Consider a system in thermal equilibrium with the temperature T and the pressure p and for this system the Gibbs free energy can be given by

$$G(p, T) = U + pV - TS, \tag{2.18}$$

$$\text{where} \qquad S \equiv -\left.\frac{\partial G}{\partial T}\right|_p, \quad V \equiv \left.\frac{\partial G}{\partial p}\right|_T \tag{2.19}$$

are the entropy and the volume of the system respectively. A first-order phase transition happens when the entropy and volume are discontinuous. In the context of the quantum field theory, phase transitions can be explained by spontaneous symmetry breaking of a scalar field. In particular, the electroweak phase transition in the early Universe, which separated electromagnetic and weak-nuclear interactions, can be studied based on a symmetry breaking of a Higgs field, so-called "Higgs mechanism". Although the standard electroweak phase transition is believed to be a cross-over (i.e. smooth) transition between the two phases, which happened at a temperature of $T_c = 159.5 \pm 1.5\,\mathrm{GeV}$ [102], some modification to the Standard Model could alter the nature of the phase transition and yield a first-order electroweak phase transition [103]. More importantly, the first-order electroweak phase transition has been expected to address baryon asymmetry [104], which is one of the unsolved puzzles within the standard cosmology. This is based on mechanisms that would have produced an symmetry in baryon density during the electroweak first-order transition, and hence could possibly explain the observed abundance of matter over anti-matter in the Universe, which is known as "electroweak baryogenesis". Therefore, detecting a GW signature from this kind of a phase transition would be a smoking gun of a potential extension to the Standard Model as well as a solution to the baryon asymmetry problem.

Here we provide the basic description of how a phase transition occurs. Before the symmetry of a scalar field (e.g. the Higgs fields in the electroweak theory) broke, the effective potential of the field had obtained the only global minimum, where all the fields should have been in the lowest energy state, being $\phi = 0$. However, as the temperature in the Universe decreased the shape of the effective potential changed, and at some point there would have appeared a lower energy state, referred to as the true vacuum where the fields obtain non-zero value, $\phi = \phi_c$. Then, the field configuration transitioned to the true vacuum as the Universe continues the expansion. This kind of a phase transition typically do not proceed uniformly, but rather create nuclei at particular places and they expand, forming bubbles of one phase within a domain of the other phase (See Fig. 2.3). The transition from one vacuum to the other provides energy, so-called a latent heat, which is determined by the difference in the potential energy between the two states, ΔV and is initially stored in the effective wall of the bubble. Around this wall, the field drastically transitions from the old vacuum into the new one and hence it would release the latent heat of $\approx \Delta V R^2 \Delta l$, letting $R, \Delta l$ be the typical size and width of a spherical wall. This freed energy exponentially accelerates the rate of expansion of the bubble until the bubble wall expand at relativistic speeds.

Despite the relativistic dynamics of the bubbles described above, a single expanding bubble should not produce GWs because of its spherical symmetry. However, the walls of neighboring bubbles start colliding and the bubbles could merge within Hubble time, which is expected to contribute to GW radiation based on several different

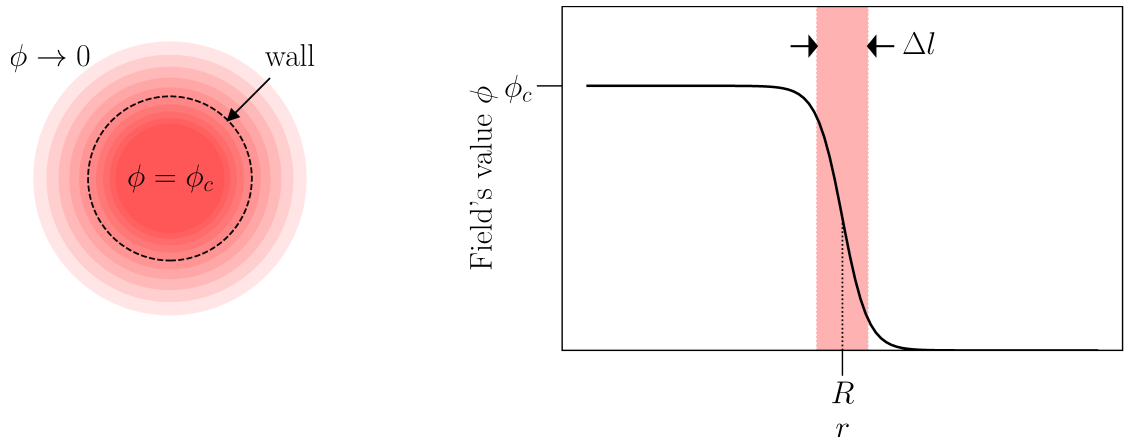

Figure 2.3: (Left) Schematic picture of a bubble of one phase expanding into the surrounding domain. The gradation of red color indicates the field's value that has non-zero value (say, $\phi = \phi_c$) in the true vacuum. While it expands, an field's wall is effectively formed, which determines the size of the bubble. (Right) the field's value as a function of distance from the bubble's center. An effective wall with the width of Δl can be formed at the point where the field's value drops rapidly.

mechanisms. Firstly, the bubble collisions deform the spherical symmetry of the bubble walls, creating anisotropic stresses with quadrupole moments that emit GWs. Secondly, the bubble collision creates shock waves propagating inside the plasma (arbitrary matter fields), which generates GWs [105]–[107]. Lastly, the movement of charges during the phase transition amplifies the magnetic fields in the plasma with a large magnetic Reynolds [108], which enhances the magnetohydrodynamic turbulence, creating additional anisotropic stress as an additional source of GW emission.

Unlike the previous two examples of the cosmological origins, the GW spectrum from the bubble mergers has a peak around a particular frequency, f_*. This frequency depends on the duration of the phase transition or the typical size of the colliding bubbles. Also, the spectral shape depends on the detailed mechanism of the phase transition such as the speed of the expanding bubbles, the latent heat being freed during the transition and so on. To a leading order $\Omega_{\rm GW} \propto f^{2\sim3}$ ($f < f_*$). For ($f > f_*$), on the other hand, $\Omega_{\rm GW}$ decreases as $\propto f^{-1\sim-5/3}$ depending on the GW generation mechanism. Specifically, some modification to the Standard Model yields a SGWB with the peaked frequency of about 260 mHz [109], which is within the observing band of LISA [30]. The projected sensitivity of LISA with regard to a SGWB is expected to be of order $\Omega_{\rm GW} \sim 5 \times 10^{-13}$ at 10^{-3} Hz [110] and many of the modifications to the Standard Model that would realize the first-order electroweak phase transition can be probed by LISA. One can find that the SGWB spectra predicted from different mechanisms as well as LISA's sensitivity for comparison in Ref. [105].

2.2.2 Astrophysical backgrounds

Compact binary coalescence : BBH and BNS

The most probable source of a SGWB, whether astrophysical or cosmological origin, so far is a population of CBCs, in particular those of BBH and BNS. Many CBC systems observed in O1 and O2 by advanced LIGO and Virgo have suggested that there exists a population of compact binary systems in the Universe. Recently, LVC published their latest catalog of transient GW signals (GWTC-2 [23]) using observational data up to the first half of the third Observing run (O3), which contains 50 new CBC candidates. Among the new candidates, the farthest event, GW190413_134308, is estimated to have the redshift $z = 0.80^{+0.30}_{-0.31}$ along with several others with the redshift around 0.7. This clearly implies that we have already started observing sources at nearly cosmological distances ($z \sim 1$), from which most of contribution for a SGWB is expected to originate.

In order to estimate the energy density spectrum $\Omega_{\rm GW}$ from a source population described by a set of source parameters $\{\theta_k\}$, one needs to compute a GW energy spectrum per individual source, $\mathrm{d}E_{\rm GW}/\,\mathrm{d}f$, weighted by the merger rate density as a function of the redshift, $R_m(z)$. Therefore, the energy density spectrum can be generally formulated as

$$\Omega_{\rm GW}(f;\theta_k) = \frac{f}{\rho_c H_0}\int_0^{z_{\rm max}} \mathrm{d}z\, R_m(z;\theta_k)\frac{\mathrm{d}t}{\mathrm{d}z}\frac{\mathrm{d}E_{\rm GW}}{\mathrm{d}f_s}(f_s;\theta_k), \tag{2.20}$$

where the factor $\mathrm{d}t/\,\mathrm{d}z$ encodes the cosmological effect, typically given by the standard ΛCDM cosmology. Regarding $\mathrm{d}E_{\rm GW}/\,\mathrm{d}f$, according to previous studies of a binary population synthesis [111]–[113], a single event of such a coalescence consists of three stages: the inspiral phase, the merger phase and the ringdown phase. Since all of these binaries spend most their lifetime in the inspiral phase, most of the contribution to a SGWB comes from their inspiral phase. Given the strain spectrum for the inspiral phase $h(f) \propto f^{-7/6}$ under the stationary phase approximation [114]–[116], together with Eqs. (2.9) and (2.13), the energy density spectrum for a CBC population can be approximated as the power-law model, $\Omega_{\rm GW} \propto f^3 \times \left(f^{-7/6}\right)^2 = f^{2/3}$.

The merge rate density $R_m(z;\theta_k)$ depends on the formation scenario of CBC systems. The mainstream is isolated field binaries of compact objects [111]–[113]. In this scenario, relatively heavy binaries with component masses in the range of [$40M_\odot$ – $100M_\odot$] is likely to be formed in a low metallicity environment, typically lower than 10% of the solar metallicity [113]. The other possible scenario particularly for BBHs is dynamical binary formation in dense stellar environments such as globular clusters [117]–[119]. While in the isolated binary scenario the common envelop phase aligns the components' spin angular momentum with their orbital angular momentum and circularizes a binary orbit, the dynamical binary formation predicts isotropic distribution of the misaligned angle between the two angular momentum [117], [120] and tend to

have large eccentricities [121]–[125]. Therefore, the observations of the spins and orbital eccentricities for CBC systems can be used as a probe of the binary's formation scenarios [120], [126]–[130].

Previous analyses of a SGWB from a CBC population relies on the population model of isolated field binaries [83], [131], [132], by assuming the binary formation rate is proportional to the cosmic star formation rate. Also, $R_m(z)$ is calibrated by the merger rate at the local Universe ($z \approx 0$) estimated by advanced LIGO and Virgo's observations. Using the local merger rate of BBH and BNS estimated from the first observing run (O1) and O2 [22], Ref. [132] predicted the SGWB magnitude of $\Omega_{\rm GW} = 1.1^{+1.2}_{-0.2} \times 10^{-9}$ ($0.7^{+1.5}_{-0.6} \times 10^{-9}$) for BBH (BNS) at 25 Hz, leading to the total SGWB of $\Omega_{\rm GW} = 1.8^{+2.7}_{-1.3} \times 10^{-9}$. Given this SGWB prediction, it was expected that the median background from the combined BBH and BNS population is possibly detected with a signal-to-noise ratio (SNR)=3 after 40 months of observation. However, one should note that the latest population inference performed in GWTC-2 [27] yields the estimate of the local merger rate around twice lower than that in O2, which leads to a SGWB prediction lowered by the same factor and implies that the prospect at the time of O2 turns out to be optimistic.

Compact binary coalescence : white dwarf binary

While binaries of compact objects we observe with GWs are mostly extragalactic, there exist thousands of binary systems, most of which consist of white dwarfs, in our galaxy. They have orbital frequencies of typically a few minutes or hours, which correspond to the GW frequencies of $[10^{-4}$–$10^{-2}]$ Hz within the sensitive band of LISA. Detecting these GW signals would be beneficial in order to infer the distribution of white dwarfs inside the Milky way.

However, some of the signals that are not individually resolvable (including extragalactic binaries) would form a SGWB and the galactic and extragalactic binaries both have been predicted to produce an background amplitude of $\Omega_{\rm GW} \sim 10^{-12}$ Hz [133]–[136]. It is anticipated that this would mask a potential SGWB from a cosmological origin and ultimately act as noise, which would make LISA's cosmological observation challenging. In order to mitigate such a contamination, in analogy with the foreground removal in the CMB observation [137], [138], there have been some attempts to model these signal components and remove it from the foreground and possibly reach a cosmologically produced SGWB [133], [136], [139]–[143]. In particular, Refs. [133], [136] conclude that it would be possible to detect a scale-invariant SGWB with the energy density of $\Omega_{\rm GW} \sim [2-5] \times 10^{-13}$.

Furthermore, prior knowledge about those galactic white dwarf binaries can be used to predict the galactic GW foreground more accurately. Specifically, a mass model or a three-dimensional maps of the Milky way assessed by Gaia's observation will be helpful to construct a distribution of those binaries [144]–[148].

Rotating neutron stars

Since it is natural that neutron stars rotating as fast as a period of $\sim$ millisecond are not perfectly axisymmetric, time-independent quadrupole moment they create act as a source of gravitational radiation. There are believed to be several mechanisms that induce the non-axisymmetry of neutron stars: a mountain on the neutron star surface due to cracking of a crust through thermal effect, toroidal magnetic fields inside the neutron star that causes its deformation and mechanical oscillation mode being internally excited, which is the so-called *r*–mode. Across these different mechanisms, the ellipticity ϵ of a neutron star determines the amplitude of time-dependent quadrupole moment, equivalently the amplitude of gravitational radiation. Also, its frequency is nearly constant over time and twice the rotation frequency of the neutron stars, so they are categorized into continuous gravitational wave (CW). Precisely speaking, however, the neutron stars lose their rotational energy through GW emission itself, or dipole radiation. Therefore, the GW signals also are expected to have decreasing frequency over time. Using such a signal model, several searches for individual rotating neutron stars have been conducted to place constraints on the ellipticity of targeted neutron star. See Ref. [149] for the results of a targeted search for several known pulsar, which put constraints of their equatorial ellipticity being less than 10^{-8}. The upper limits on the ellipticity can be converted to intrinsic properties of the neutron stars such as the crust strain or internal magnetic field strength depending on deformation mechanisms one assumes.

Since a large number of neutron stars are expected to exist in the Universe, there would also exist a SGWB contributed from a population of such neutron stars. For example, Ref. [150] considers relatively young neutron stars, assuming the *r*–mode as a deformation mechanism and predict the energy density of $\Omega_{\rm GW} \sim (2.2 - 3.3) \times 10^{-8}$ in the frequency band of [500–1700] Hz. Additionally, Refs. [151], [152] studied a SGWB from magnetars, namely neutron stars with significantly large magnetic fields ~[10^{15}-10^{17} G], yielding the predictions of $\Omega_{\rm GW} \sim 10^{-10}$ at 100 Hz. Many neutron stars are known to be located in the Galactic plane of the Milky way and have been investigated to provide constraints on the average neutron star ellipticity based on the upper limit on the SGWB derived from the co-located initial LIGO detectors. Ref. [153] predicted that, assuming [10^8–10^9] neutron stars exist in our galaxy, advanced LIGO and Virgo detector network should be able to constrain the ellipticity less than 2×10^{-7} and third generation detector like the Einstein Telescope [28] could achieve the upper limit of $\epsilon \sim 6 \times 10^{-10}$. These constraints can be compared to the largest possible ellipticity for a neutron star that is theoretically predicted being $\epsilon \sim 10^{-5}$.

2.3 Detection

Here one will see the detailed explanation of how to detect a SGWB based on [80], [81]. In particular, one takes a cross-correlation of the data stream, $s_1(t)s_2(t')$, to extract a SGWB component correlated among multiple detectors. Along with the four assumptions about a SGWB, we also follow some assumptions about the noise intrinsic to the detectors: the detector noise is stationary, Gaussian, statistically independent of one another and of the stochastic background. Furthermore, the analysis can be simplified by assuming the noise has a much larger magnitude than a SGWB. Firstly, we start with the simplest situation where detectors are coincident and coaligned. Subsequently, the discussion will be extended to a more realistic case in which detectors are not necessarily coincident or coaligned.

2.3.1 Coincident and coaligned detectors

We consider coincident and coaligned detectors, meaning that they have the identical location and arm orientations. Each of them outputs time series of strain data consisting of signal $h(t)$ and noise $n(t)$ components such that

$$s_1(t) \equiv h_1(t) + n_1(t), \tag{2.21}$$

$$s_2(t) \equiv h_2(t) + n_2(t), \tag{2.22}$$

where we label each detector with the subscript and

$$h_1(t) = h_2(t) \equiv h(t) \tag{2.23}$$

because of the coincident and coaligned detectors. For these outputs, one defines an estimator $\hat{Y}$ by integrating their product over time, namely

$$\hat{Y} \equiv \int_{-T/2}^{T/2} \mathrm{d}t\; s_1(t)s_2(t). \tag{2.24}$$

This is nothing but the cross-correlation of $s_1(t)$ and $s_2(t)$ during a given observation time T. Essentially, this estimator is a random variable which can estimate a statistical quantity of interest. This has the mean $\mu \equiv \langle \hat{Y} \rangle$ and the variance $\sigma^2 \equiv \langle \hat{Y}^2 \rangle - \langle \hat{Y} \rangle^2$. Once one defines an estimator and derives its mean and variance, it is possible to construct a SNR

$$\mathrm{SNR} \equiv \frac{\mu}{\sigma}. \tag{2.25}$$

In this prescription, one can use this as the detection statistics for a SGWB signal.

In order to show the expression of the SNR, in what follows we will derive μ and σ^2. Using the expressions Eqs. (2.21) and (2.22), the mean μ reduces to

$$\mu = \int_{-T/2}^{T/2} \mathrm{d}t\; \langle s_1(t)s_2(t) \rangle \tag{2.26}$$

$$= \int_{-T/2}^{T/2} \mathrm{d}t \, \langle h^2(t) + h(t)n_2(t) + n_1(t)h(t) + n_1(t)n_2(t) \rangle \tag{2.27}$$

$$= \int_{-T/2}^{T/2} \mathrm{d}t \, \langle h^2(t) \rangle \tag{2.28}$$

$$= T\langle h^2(t) \rangle. \tag{2.29}$$

Here we adopt the assumption that $n_1(t), n_2(t)$ and $h(t)$ are statistically independent of one another and stationary when deriving Eq. (2.28) and Eq. (2.29) respectively. One should note that from the plane wave expansion Eq. (2.3) and its zero mean Eq. (2.10), $\langle h^2(t) \rangle$ is equivalent to the variance of $h(t)$, namely $\sigma_h^2 = \langle h^2(t) \rangle$. In order to express σ_h^2 with respect to the energy density spectrum $\Omega_{\mathrm{GW}}(f)$, recall that the GW strain in detector frame $h(t)$ is related to the metric perturbation tensor $h_{\mu\nu}(t, \vec{x})$ via a detector response factor

$$h(t) \equiv h_{ab}(t, \vec{x_0}) \frac{1}{2} \left(\hat{X}^a \hat{X}^b - \hat{Y}^a \hat{Y}^b \right). \tag{2.30}$$

Here $\vec{x}_0$ is the identical position vector of the two coincident and coaligned detectors, and $\hat{X}^a$ and $\hat{Y}^a$ are unit vectors indicating the directions of those detector's arms. Making use of Eq. (2.3), one can obtain

$$\begin{aligned} \sigma_h^2 = \sum_A \sum_{A'} \int_{S^2} \mathrm{d}\hat{\Omega} \int_{S'^2} \mathrm{d}\hat{\Omega}' \int_{-\infty}^{\infty} \mathrm{d}f \int_{-\infty}^{\infty} \mathrm{d}f' \, \langle h_A^*(f, \hat{\Omega}) h_{A'}(f', \hat{\Omega}') \rangle \\ \times \mathrm{e}^{-i2\pi f'(t - \hat{\Omega}' \cdot \vec{x}_0/c)} \mathrm{e}^{i2\pi f(t - \hat{\Omega} \cdot \vec{x}_0/c)} F^A(\hat{\Omega}) F^{A'}(\hat{\Omega}') \end{aligned} \tag{2.31}$$

where

$$F^A(\hat{\Omega}) \equiv e^A_{ab}(\hat{\Omega}) \frac{1}{2} \left(\hat{X}^a \hat{X}^b - \hat{Y}^a \hat{Y}^b \right) \tag{2.32}$$

is the response of either detector to a zero frequency[2], unit amplitude, $A = +, \times$ polarized gravitational wave. Using Eq. (2.9), Eq. (2.31) reduces to

$$\sigma_h^2 = \frac{3H_0^2}{32\pi^3} \int_{-\infty}^{\infty} \mathrm{d}f |f|^{-3} \Omega_{\mathrm{GW}}(|f|) \sum_A \int_{S^2} \mathrm{d}\hat{\Omega} F^A(\hat{\Omega}) F_A(\hat{\Omega}) \tag{2.33}$$

$$= \frac{3H_0^2}{20\pi^2} \int_{-\infty}^{\infty} \mathrm{d}f |f|^{-3} \Omega_{\mathrm{GW}}(|f|) \tag{2.34}$$

where

$$\sum_A \int_{S^2} \mathrm{d}\hat{\Omega} F^A(\hat{\Omega}) F^A(\hat{\Omega}) = \frac{8\pi}{5} \tag{2.35}$$

is used to derive Eq. (2.34). It follows that the mean of the cross-correlation estimator $\hat{Y}$ reads

$$\mu = \frac{3H_0^2}{20\pi^2} T \int_{\infty}^{-\infty} \mathrm{d}f \, |f|^{-3} \Omega_{\mathrm{GW}}(|f|). \tag{2.36}$$

[2]Precisely speaking, Eq. (2.32) uses the long-wavelength approximation where $\lambda_{\mathrm{GW}} \gg L_{\mathrm{arm}}$. More generally, $F^A(\hat{\Omega})$ depends on f too. See Section. 7.9 of [87] for the detailed discussion.

On the other hand, to derive the variance σ^2, we use the assumption that the magnitude of the noise intrinsic to the detectors are much larger than that of the gravitational strain, i.e. $\langle n_1(t)n_2(t)\rangle \gg \langle h^2(t)\rangle$. It follows that

$$\begin{aligned}
\sigma^2 &\equiv \langle \hat{Y}^2\rangle - \langle \hat{Y}\rangle^2 \approx \langle \hat{Y}^2\rangle && (2.37)\\
&= \int_{-T/2}^{T/2} \mathrm{d}t \int_{-T/2}^{T/2} \mathrm{d}t' \ \langle s_1(t)s_2(t)s_1(t')s_2(t')\rangle && (2.38)\\
&\approx \int_{-T/2}^{T/2} \mathrm{d}t \int_{-T/2}^{T/2} \mathrm{d}t' \ \langle n_1(t)n_2(t)n_1(t')n_2(t')\rangle && (2.39)\\
&= \int_{-T/2}^{T/2} \mathrm{d}t \int_{-T/2}^{T/2} \mathrm{d}t' \ \langle n_1(t)n_1(t')\rangle\langle n_2(t)n_2(t')\rangle. && (2.40)
\end{aligned}$$

We introduce the (one-sided) power spectral density of the i-th detector's noise ($i = 1, 2$) as follows,

$$\langle n_i(t)n_i(t')\rangle \equiv \frac{1}{2}\int_{-\infty}^{\infty} \mathrm{d}f \ \mathrm{e}^{i2\pi f(t-t')} P_i(|f|). \tag{2.41}$$

Fig. 1.3 shows evolution of the measured (proposed) amplitude spectrum density, defined as $\sqrt{P(|f|)}$, of advanced LIGO. Inserting Eq. (2.66) into Eq. (2.65) to obtain

$$\begin{aligned}
\sigma^2 \approx \frac{1}{4}\int_{-T/2}^{T/2} \mathrm{d}t \int_{-T/2}^{T/2} \mathrm{d}t' \int_{-\infty}^{\infty} \mathrm{d}f \int_{-\infty}^{\infty} \mathrm{d}f' \\
\times \mathrm{e}^{i2\pi f(t-t')}\mathrm{e}^{-i2\pi f'(t-t')} P_1(|f|)P_2(|f|),
\end{aligned} \tag{2.42}$$

one can integrate the two exponentials over t and t'

$$\begin{aligned}
\text{Eq. (2.42)} = \frac{1}{4}\int_{-\infty}^{\infty} \mathrm{d}f \int_{-\infty}^{\infty} \mathrm{d}f' \ P_1(|f|)P_2(|f|) \\
\times \left\{\int_{-T/2}^{T/2} \mathrm{d}t \ \mathrm{e}^{i2\pi(f-f')t}\right\}\left\{\int_{-T/2}^{T/2} \mathrm{d}t' \ \mathrm{e}^{-i2\pi(f-f')t'}\right\}.
\end{aligned} \tag{2.43}$$

Here for simplicity one can replace either of the two finite-time integration by t or t' with the infinite-time integration over $-\infty < t < \infty$ [3], yielding

$$\begin{aligned}
\sigma^2 &\approx \frac{1}{4}\int_{-\infty}^{\infty} \mathrm{d}f \int_{-\infty}^{\infty} \mathrm{d}f' \ P_1(|f|)P_2(|f|) \\
&\quad \times \left\{\int_{-\infty}^{\infty} \mathrm{d}t \ \mathrm{e}^{i2\pi(f-f')t}\right\}\left\{\int_{-T/2}^{T/2} \mathrm{d}t' \ \mathrm{e}^{-i2\pi(f-f')t'}\right\} && (2.44)\\
&= \frac{1}{4}\int_{-\infty}^{\infty} \mathrm{d}f \int_{-\infty}^{\infty} \mathrm{d}f' \ \delta(f-f')\delta_T(f-f')P_1(|f|)P_2(|f|) && (2.45)\\
&= \frac{T}{4}\int_{-\infty}^{\infty} \mathrm{d}f \ P_1(|f|)P_2(|f|). && (2.46)
\end{aligned}$$

[3] In reality, the observation time T is long enough that $\delta_T(f-f')$ is sharply peaked over a region in $f-f'$ whose size $\approx 1/T$ is sufficiently small compared to the timescale of the functions $P_1(|f|)$ and $P_2(|f|)$ varying.

Here $\delta_T(f-f')$ is a finite-time approximation to the Dirac delta function $\delta(t)$

$$\delta_T(f-f') \equiv \int_{-T/2}^{T/2} \mathrm{d}t' \; \mathrm{e}^{-i2\pi(f-f')t'} \tag{2.47}$$

and the factor of T comes from $\delta_T(0) = T$.

From Eqs. (2.36) and (2.46), the explicit expression of SNR reads [80], [81]

$$\mathrm{SNR} \equiv \frac{\mu}{\sigma} \approx \frac{3H_0^2}{10\pi^2}\sqrt{T}\frac{\int_{-\infty}^{\infty}\mathrm{d}f\;|f|^{-3}\Omega_{\mathrm{GW}}(|f|)}{\left[\int_{-\infty}^{\infty}\mathrm{d}f\;P_1(|f|)P_2(|f|)\right]^{1/2}}. \tag{2.48}$$

Although these colocated and coaligned detectors are a hypothetical situation, the resultant expression Eq. (2.48) provides a meaningful implication. For example, the factor of $\sqrt{T}$ indicates that no matter how conservative threshold one sets for detection, in principle SNR can surpass it within a finite observation time. In what follows, we will consider a more realistic configuration.

2.3.2 Optimal filtering

In reality, two detectors are not necessarily either colocated or coaligned. This chapter deals with this realistic case, based on [80], [81], and provides the formalism to maximize a SNR for a given signal spectrum $\Omega_{\mathrm{GW}}(f)$, by introducing what we call "optimal filter".

Firstly, one re-defines an estimator $\hat{Y}$ as

$$\hat{Y} \equiv \int_{-T/2}^{T/2}\mathrm{d}t\int_{-T/2}^{T/2}\mathrm{d}t'\; s_1(t)s_2(t')Q(t,t'), \tag{2.49}$$

where $Q(t,t')$ is a linear filter function, which corresponds to a delta function $\delta(t-t')$ in Eq. (2.24). The statistical assumption that a SGWB signal and detector noise are both stationary implies the filter function can depend only on the time difference $\Delta t = t - t'$. Secondly, for simplicity one can take one of the finite-time integration to be infinite similarly to Eq. (2.44), which leads to

$$\hat{Y} = \int_{-T/2}^{T/2}\mathrm{d}t\int_{-\infty}^{\infty}\mathrm{d}t'\; s_1(t)s_2(t')Q(t-t'). \tag{2.50}$$

Introducing the Fourier transform of $s_1(t)$ and $\int_{-\infty}^{\infty}\mathrm{d}t' s_2(t')Q(t-t')$ such that

$$s_1(t) \equiv \int_{-\infty}^{\infty}\mathrm{d}f\;\mathrm{e}^{-i2\pi ft}\tilde{s}_1^*(f) \tag{2.51}$$

$$\int_{-\infty}^{\infty}\mathrm{d}t' s_2(t')Q(t-t') \equiv \int_{-\infty}^{\infty}\mathrm{d}f'\;\mathrm{e}^{i2\pi f't}\tilde{s}_2(f')\tilde{Q}(f'), \tag{2.52}$$

it follows that

$$\text{Eq. (2.50)} = \int_{-\infty}^{\infty}\mathrm{d}f\int_{-\infty}^{\infty}\mathrm{d}f'\;\tilde{s}_1^*(f)\tilde{s}_2(f')\tilde{Q}(f')\left\{\int_{-T/2}^{T/2}\mathrm{d}t\;\mathrm{e}^{-i2\pi(f-f')t}\right\} \tag{2.53}$$

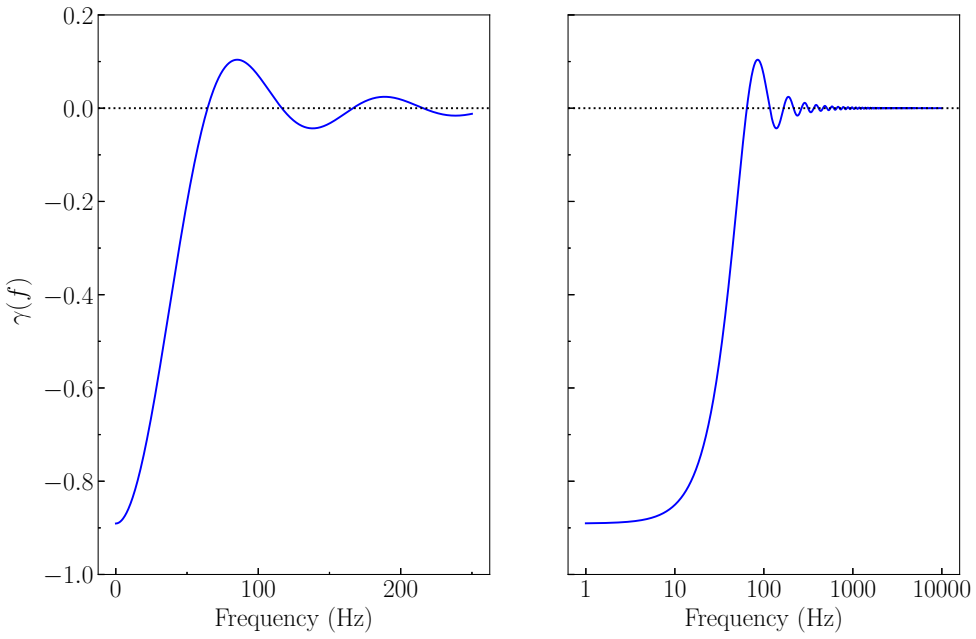

Figure 2.4: The overlap reduction function $\gamma(f)$ for the Hanford, WA and Livingston, LA LIGO detector pair.

$$= \int_{-\infty}^{\infty} \mathrm{d}f \int_{-\infty}^{\infty} \mathrm{d}f' \; \delta_T(f - f')\tilde{s}_1^*(f)\tilde{s}_2(f')\tilde{Q}(f'). \tag{2.54}$$

Since we take the SNR as the detection statistics, the optimal filter should be determined by maximizing the SNR

$$\mathrm{SNR} \equiv \frac{\mu}{\sigma} = \frac{\langle \hat{Y} \rangle}{\sqrt{\langle \hat{Y}^2 \rangle - \langle \hat{Y} \rangle^2}}. \tag{2.55}$$

The evaluation of μ and σ is quite similar to Eqs. (2.36) and (2.46), respectively except for geometrical separation and misalignment between the two detectors, which will be addressed in the following discussion. Under the assumption about the statistical independence between both signal $h(t)$ and intrinsic noise $n(t)$, the calculation of the mean μ can be simplified as follows

$$\mu = \langle \hat{Y} \rangle = \int_{-\infty}^{\infty} df \int_{-\infty}^{\infty} df' \; \delta_T(f - f')\langle \tilde{h}_1^*(f)\tilde{h}_2(f') \rangle \tilde{Q}(f'). \tag{2.56}$$

Making use of the plane wave expansion Eq. (2.3) and the antenna pattern response of each detector Eq. (2.32), one can obtain the GW strain of i-th detector

$$\tilde{h}(f) = \sum_A \int_{S^2} \mathrm{d}\hat{\Omega} h_A(f, \hat{\Omega}) \mathrm{e}^{-i2\pi f \hat{\Omega} \cdot \vec{x}_i / c} F_i^A(\hat{\Omega}). \tag{2.57}$$

Substituting this expression for $i = 1, 2$ into Eq. (2.56), it follows that

$$\langle \tilde{h}_1^*(f)\tilde{h}_2(f') \rangle = \sum_A \sum_{A'} \int_{S^2} \mathrm{d}\hat{\Omega} \int_{S^2} \mathrm{d}\hat{\Omega}' \; \langle \tilde{h}_A^*(f, \hat{\Omega})\tilde{h}_{A'}(f', \hat{\Omega}') \rangle$$

$$\times e^{i2\pi f\hat{\Omega}\cdot\vec{x}_1/c} e^{-i2\pi f\hat{\Omega}'\cdot\vec{x}_2/c} F_1^A(\hat{\Omega}) F_2^{A'}(\hat{\Omega}') \tag{2.58}$$

$$= \frac{3H_0^2}{32\pi^3}\delta(f-f')|f|^{-3}\Omega_{\rm GW}(|f|) \times \sum_A \int_{S^2} d\hat{\Omega}\, e^{i2\pi f\hat{\Omega}\cdot\Delta\vec{x}/c} F_1^A(\hat{\Omega}) F_2^A(\hat{\Omega}) \tag{2.59}$$

$$= \frac{3H_0^2}{20\pi^3}\delta(f-f')|f|^{-3}\Omega_{\rm GW}(|f|)\gamma(|f|) \tag{2.60}$$

where Eq. (2.14) is used and $\Delta\vec{x} \equiv \vec{x}_1 - \vec{x}_2$ is the spatial separation between the two detector sites. $\gamma(f)$ is the so-called overlap reduction function defined as

$$\gamma(f) \equiv \frac{5}{8\pi}\sum_A \int_{S^2} d\hat{\Omega}\, e^{i2\pi f\hat{\Omega}\cdot\Delta\vec{x}/c} F_1^A(\hat{\Omega}) F_2^A(\hat{\Omega}). \tag{2.61}$$

In general, this is the factor that encodes the effect of the geometrical separation and misaligned orientation between two detectors under the assumptions about an isotropic and unpolarized SGWB. In particular, $\gamma(f)$ is equal to unity for a pair of colocated and coaligned detectors. Separation between detectors creates a phase shift between potential signals in output data, and the misaligned arm orientation makes a detector network sensitive to different polarizations. Thus, the overlap reduction function decreases below unity for separated and misaligned detectors. Fig. 2.4 shows the overlap reduction function $\gamma(f)$ for the Hanford, WA and Livingston, LA LIGO detector pair[4]. Note that $\gamma(f)$ for the LIGO detector pair is negative for $f \to 0\,\mathrm{Hz}$. This is because the arm orientations of the two LIGO detectors are rotated by approximately 90°, in other words, two output stream from the detectors are anti-correlated. However, they are misaligned by not exactly 90°, so the function does not converge to -1 even at $f = 0\,\mathrm{Hz}$. Additionally, for a given separation between two detectors, the two outputs from the detectors are getting out of phase as a signal contains higher frequency components. Eventually, $\gamma(f)$ has its first zero at 64 Hz, at which the phase shift between the LIGO detectors completely cancels out the correlation in the data. (See Fig. 2.4.) In conclusion, the detectability of a stohcastic GW background depends not only on the sensitivity of each single detector alone but also significantly on the overlap reduction function $\gamma(f)$. Using Eq. (2.60), Eq. (2.56) reduces to

$$\mu = \frac{3H_0^2}{20\pi^2} T \int_{-\infty}^{\infty} df |f|^{-3}\Omega_{\rm GW}(|f|)\gamma(|f|)\tilde{Q}(f) \tag{2.62}$$

Next, one can evaluate the variance σ^2 assuming that the noise intrinsic to the two detectors are much larger in magnitude than the SGWB and that $n_1(t)$ and $n_2(t)$ are

[4]This function $\gamma(f)$ can be evaluated for any detector pair and the behavior of the function strongly depends on the choice of a detector pair. For example, since the separation between Virgo and either LIGO detector is longer than that for LIGO detector pair and that would make the function more rapidly oscillating, which would make a negative impact on the sensitivity to a SGWB.

statistically independent. It follows that

$$\sigma^2 \equiv \langle \hat{Y}^2 \rangle - \langle \hat{Y} \rangle^2 \approx \langle \hat{Y}^2 \rangle \tag{2.63}$$

$$\approx \int_{-\infty}^{\infty} \mathrm{d}f \int_{-\infty}^{\infty} \mathrm{d}f' \int_{-\infty}^{\infty} \mathrm{d}\hat{k} \int_{-\infty}^{\infty} \mathrm{d}\hat{k}' \times \delta_T(f - f')\delta_T(k - k')\langle \tilde{n}_1^*(f)\tilde{n}_2(f')\tilde{n}_1^*(k)\tilde{n}_2(k')\rangle \tilde{Q}(f')\tilde{Q}(k') \tag{2.64}$$

$$= \int_{-\infty}^{\infty} \mathrm{d}f \int_{-\infty}^{\infty} \mathrm{d}f' \int_{-\infty}^{\infty} \mathrm{d}\hat{k} \int_{-\infty}^{\infty} \mathrm{d}\hat{k}' \times \delta_T(f - f')\delta_T(k - k')\langle \tilde{n}_1^*(f)\tilde{n}_1^*(-k)\rangle\langle \tilde{n}_2(-f')\tilde{n}_2(k')\rangle \tilde{Q}(f')\tilde{Q}(k') \tag{2.65}$$

Now one defines the power spectral density $P_i(|f|)$ of detector noise in the frequency domain similar to the definition on time domain, Eq. (2.41).

$$\langle \tilde{n}_i^*(f)\tilde{n}_i(f')\rangle =: \frac{1}{2}\delta(f - f')P_i(|f|). \tag{2.66}$$

Substituting this result into Eq. (2.65), it reduces to

$$\sigma^2 \approx \frac{1}{4} \int_{-\infty}^{\infty} \mathrm{d}f \int_{-\infty}^{\infty} \mathrm{d}f'\ \delta_T^2(f - f')P_1(|f|)P_2(|f|)\tilde{Q}(f')\tilde{Q}^*(f') \tag{2.67}$$

$$\approx \frac{T}{4} \int_{-\infty}^{\infty} \mathrm{d}f\ P_1(|f|)P_2(|f|)|\tilde{Q}(f)|^2, \tag{2.68}$$

where the approximation to the time integration is made in the same way as Eq. (2.44). In summary,

$$\mu = \frac{3H_0^2}{20\pi^2} T \int_{-\infty}^{\infty} \mathrm{d}f |f|^{-3}\Omega_{\mathrm{GW}}(|f|)\gamma(|f|)\tilde{Q}(f) \tag{2.69}$$

$$\sigma^2 \approx \frac{T}{4} \int_{-\infty}^{\infty} \mathrm{d}f\ P_1(|f|)P_2(|f|)|\tilde{Q}(f)|^2. \tag{2.70}$$

Now we aim to identify the expression of the filter function $\tilde{Q}(f)$ which maximizes SNR defined by Eq. (2.55) for a given $\Omega_{\mathrm{GW}}(f)$ and a given detector pair. To find it, one introduces an inner product (A, B) for any pair of complex functions $A(f)$ and $B(f)$. Let (A, B) be a complex number defined by

$$(A, B) \equiv \int_{-\infty}^{\infty} \mathrm{d}f\ A^*(f)B(f)P_1(|f|)P_2(|f|). \tag{2.71}$$

From the fact that $P_i(|f|) > 0$, one can see that $(A, A) \geq 0$, and $(A, A) = 0$ if and only if $A(f) = 0$. Also, $(A, B) = (B, A)^*$ and $(A, B + \lambda C) = (A, B) + \lambda(A, C)$ for any complex number λ. In other word, (A, B) is positive-definite inner product which satisfies all of the properties of an ordinary dot product.

Using this inner product, the mean value μ and variance σ^2 can be expressed as

$$\mu = \frac{3H_0^2}{20\pi^2} T \left(\tilde{Q}, \frac{\gamma(|f|)\Omega_{\mathrm{GW}}(|f|)}{|f|^3 P_1(|f|)P_2(|f|)} \right) \tag{2.72}$$

$$\sigma^2 \approx \frac{T}{4}\left(\tilde{Q}, \tilde{Q}\right). \tag{2.73}$$

The optimization of $\tilde{Q}(f)$ can be formulated so that it takes the maximum value of the signal-to-noise ratio (2.55), explicitly

$$\mathrm{SNR} \propto \frac{\left(\tilde{Q}, \frac{\gamma(|f|)\Omega_{\mathrm{GW}}(|f|)}{|f|^3 P_1(|f|)P_2(|f|)}\right)}{\left(\tilde{Q}, \tilde{Q}\right)^{1/2}} =: \frac{\left(\tilde{Q}, \tilde{A}(f)\right)}{\left(\tilde{Q}, \tilde{Q}\right)^{1/2}} \tag{2.74}$$

Solving this optimization problem is actually straightforward from the viewpoint of geometry. Let the frequency range be divided into N bins and any function $G(f)$ defined on the range can be treated as a N-dimensional complex vector. Since the norm of $\tilde{Q}(f)$ does not affect the value of SNR Eq. (2.74), this ratio is proportional to only the relative orientation between $\tilde{Q}(f)$ and $\tilde{A}(f)$. Therefore, SNR can be maximized with $\tilde{Q}(f)$ in parallel to $\tilde{A}(f)$, that is

$$\tilde{Q}(f) = \lambda \frac{\gamma(|f|)\Omega_{\mathrm{GW}}(|f|)}{|f|^3 P_1(|f|)P_2(|f|)} \tag{2.75}$$

where λ is an arbitrary normalization constant. Substituting Eq. (2.75) into Eq. (2.74), one can obtain the desired form of SNR (see [80], [81])

$$\mathrm{SNR} \approx \frac{3H_0^2}{20\pi^2}\sqrt{T}\left[\int_{-\infty}^{\infty} \mathrm{d}f \, \frac{\gamma(|f|)\Omega_{\mathrm{GW}}(|f|)}{|f|^3 P_1(|f|)P_2(|f|)}\right]^{\frac{1}{2}}. \tag{2.76}$$

Chapter 3

Superrandiant Instability

3.1 Overview

Superradiance is general phenomena in which radiation is amplified through the interaction with its ambient environment [67]. This thesis particularly focuses on the superrandiant instability caused by massive bosonic fields extracting energy and angular momentum from a rotating BH. In the context of energy extraction from BHs, the Penrose process [154] first demonstrated the possibility of energy and angular momentum loss within the ergoregion of a rotating BH. Although this process deals with a classical point particle, the similar conclusion can be made for radiation carrying energy [67], [155]. It can be shown that waves, with constant frequency ω, incoming to a rotating BH is scattered off having a larger amplitude under a certain condition such that

$$0 < \omega < m\Omega_H, \tag{3.1}$$

where m is the azimuthal index of the wave function and Ω_H is the horizon angular velocity of the BH. Motivated by this implication, Press and Teukolsky [156] introduced the concept of the so-called "BH bomb", where a rotating BH is enclosed by a hypothetical spherical mirror and oscillating fields bounce off the mirror and undergo the repeated amplification through superradiance, leading to an exponential instability.

Furthermore, it has been found that massive bosonic fields[1] can form quasi-bound states around a rotating BH and undergoes the successive amplification, which implies that the spherical mirror hypothesized previously can be naturally realized unlike massless fields. Fig. 3.1 shows a cartoon picture of the superradiant instability induced by massive bosonic fields. A small amount (even a level of quantum fluctuation) of a bosonic field with the rest mass of m_b, oscillating around a rotating BH yields a flux across the event horizon, by which energy and angular momentum exchange between the BH and the surrounding bosons. If the superradiance condition Eq. (3.1) is satisfied, the boundary condition at the horizon becomes outgoing and hence the energy and

[1] It is known that massive fermionic fields do not induce superradiant instabilities [157].

angular momentum are extracted from the BH. While the bosonic field starts to grow exponentially with the timescale of $\tau_{\rm inst}$, the BH loses its mass and angular momentum accordingly. This instability continues until the BH spins down to the point where the superradiance condition becomes saturated (i.e. $\omega \approx m\Omega_H$). By that time, the bosonic field would become condensates, which we call macroscopic "cloud", and its energy scale can be typically $\sim 10\%$ of the BH mass [67], [158], [159] (see Fig. 3.3).

The presence of such a boson cloud would yield several potentially observable signatures. The BH spin down as a consequence of superradiant instability leads to a prohibitive region in the BH mass-spin parameter space (i.e. the Regge plane) and it can be assessed with individual measurements or population inferences of BH masses and spins [68], [79], [160]–[163]. Also, the boson clouds could affect the dynamics of binary BHs, leaving its imprints in their inspiral phase or tidal effects [164]–[167]. Most importantly to this thesis, the quadrupole moment of the cloud induces characteristic gravitational radiation. The BH perturbation theory predicts the GW emission with the nearly monochromatic frequency

$$f_{\rm GW} \approx \frac{\omega}{\pi} \sim 500\,{\rm Hz} \times \left(\frac{m_b c^2}{10^{-12}\,{\rm eV}}\right) \tag{3.2}$$

over the timescale of $\tau_{\rm GW} (\gg \tau_{\rm inst})$, during which the gravitational emission dissipates the energy of the bosonic field until its energy becomes negligible.

The dynamics of the instability and the subsequent GW emission are governed by the coupling strength between a BH and a bosonic field characterized by

$$\frac{GM_{\rm BH}}{c^2}\frac{m_b c}{\hbar}\left(= \frac{r_g}{\lambda\!\!\!^{-}_{\mu}}\right), \tag{3.3}$$

which we call "coupling parameter". In the above expression, $r_g \equiv GM_{\rm BH}/c^2$ is the characteristic length of the BH mass of $M_{\rm BH}$ and $\lambda\!\!\!^{-}$ is the reduced Compton wavelength of the bosonic field. Numerical and analytical studies found that the superradiance is the most unstable (i.e. the smallest $\tau_{\rm inst.}$) when $r_g/\lambda\!\!\!^{-} \sim O(1)$ [68], [168]–[172], in other words, the Compton wavelength of the bosonic field is comparable to the spatial scale of a BH. Therefore, one yields the relation between masses of the bosonic field and a strongly-coupled BH

$$m_b c^2 \sim \frac{\hbar c^3}{GM_{\rm BH}} \sim 10^{-12}\,{\rm eV} \times \left(\frac{M_{\rm BH}}{30M_\odot}\right)^{-1}. \tag{3.4}$$

This implies, together with Eq. (3.2), that advanced LIGO is sensitive to the GW signals originated from the superradiant instability by the bosonic fields with the mass $\sim 10^{-12}\,{\rm eV}$ vias their coupling with stellar mass BHs $\sim 30M_\odot$, whose existence have been confirmed by advanced LIGO's observing runs.

There are two types of GWs emitted from superradiant instability. On the one hand, resolvable sources, which are close to Earth enough that their GW emission can be detected individually, contribute to CWs [47], [68], [69], [74], [173]–[179]. Searches for

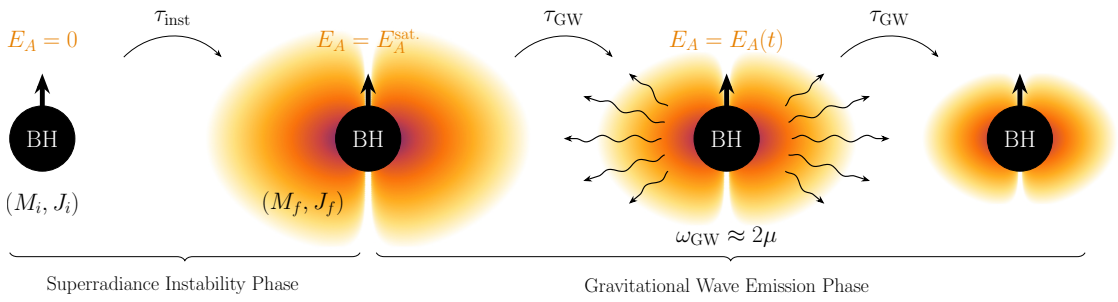

Figure 3.1: Cartoon picture of superradiant instability shown in Ref. [182]. A small amount (even a level of quantum fluctuation) of a bosonic field ($E_A = 0$) with mass of $\mu(\equiv m_b c^2/\hbar)$, where m_b is the rest mass of a boson particle in the SI unit, oscillating around a rotating BH yields a flux across the event horizon, by which energy and angular momentum exchange between the BH and the surrounding bosons. If the superradiance condition Eq. (3.1) is satisfied, the boundary condition at the horizon becomes outgoing and hence the energy and angular momentum are extracted from the BH. While the bosonic field starts to grow exponentially with the timescale of $\tau_{\rm inst}$, the BH loses its mass and angular momentum accordingly. This instability continues until the BH spins down to the point where the superradiance condition starts to be saturated ($E_A = E_A^{\rm max}$). The quadrupole moment of the cloud induces characteristic gravitational radiation with the nearly monochromatic frequency $\omega_{\rm GW} \approx 2\mu$ over the timescale of $\tau_{\rm GW}$, during which the gravitational emission dissipates the energy of the bosonic field until its energy becomes negligible.

this kind of signals require the semi-coherent search [175], [177] that circumvents extensive computational cost necessary to fit numerous parameters and several searches dedicated to CW signals from ultralight scalar clouds have been conducted. In particular, Ref. [176] performed an all-sky search for such a signal using the data from advanced LIGO's O2 and place constraints on the existence of the scalar fields within a certain volume around the Earth, whereas the directional CW search described in Ref. [178] targeted the location of Cygnus X-1, a X-ray binary that possesses a BH candidate, and searched for a CW signal from a scalar cloud that potentially exists in the binary system. Additionally, Ref. [179] constructed the CW signal model from the ultralight scalar fields based on the Galactic BH population and assessed its detectability with advanced LIGO's data. None of the searches above detected such a signal, and hence they placed the constraints on the mass of scalar fields in a similar range $\sim [10^{-13} - 10^{-12}]$ eV.

On the other hand, the rest of the sources in the Universe at higher redshifts provides superposed signals which contribute to a SGWB [70], [180]–[182]. Complementary to the CW searches mentioned above, this thesis focuses on the SGWB signal accumulated by a population of BH-cloud systems in the distant Universe. Ref. [70] first estimated the SGWB spectra predicted from ultralight scalar fields and suggested the possibility of excluding the scalar masses $\sim 10^{-13}$ eV.

3.2 Ultralight bosons on a Kerr background

The phenomenology discussed in the previous subsection is applied to all types of massive bosonic fields, namely scalar [67], [73], [168], vector [74], [158], [169], [183], [184] and tensor [185], [186] fields associated with the spin-0,1,2 boson respectively, as long as the condition Eq. (3.1) is satisfied [67]. Starting with the basics of metric around a rotating BH, this subsection describes how the field equation can be solved for massive bosonic fields and consequently the superradiant instability takes place and turns into GW emission. In particular, scalar and vector fields will be discussed here because the SGWB signal from these types of fields are the main target in this thesis and recently there have been extensive studies and substantial advancement in the theoretical understanding of these fields' dynamics.

Instability involving either massive scalar or vector fields has a several features in common. The dynamics of a bosonic field in a BH-cloud system leads to solving eigenvalue problems in terms of complex frequency of the field,

$$\omega = \omega_R + i\omega_I. \tag{3.5}$$

It will be shown that the superradiance condition,

$$0 < \omega_R < m\Omega_H \tag{3.6}$$

ensures that the imaginary part of the complex frequencies is positive, equivalent to the exponential growth of the field. Also, the superradiance condition realizes the outgoing boundary flux at the BH horizon, leading to the energy extraction from the BH. Therefore, the condition (3.6) plays a central role in inducing the superradiant instability.

It is important to note that a fully nonlinear evolution of this system is incredibly difficult to trace. This is due to the four different timescales to consider: (a) the dynamics of a rotating BH, which is equivalent to the light-crossing time, $\tau_{\rm BH}$, (b) the oscillation period of the bosonic field, (c) the instability timescale and (d) the GW emission timescale. As shown *a posteriori*, generally the BH-cloud possesses the hierarchical relation among these timescales such that (a) $\ll$ (b) $\ll$ (c) $\ll$ (d). The fact that (a) $\ll$ (b) suggests that during the dynamical timescale of the metric around a BH, the oscillating fields can be treated as almost stationary. Additionally, despite the possible backreaction of the field to the background metric, we ignore this backreaction since the energy density of the boson cloud is smaller than that of a BH by orders of magnitude. This approximation turns out to reasonable even at the time of instability saturation, when the total mass of a bosonic cloud can amount to $\sim$ 10% of the BH mass. Given this justification, it can be assumed that the BH-cloud system evolves along a sequence of Kerr background spacetimes, which is referred to as a quasi-adiabatic approximation. Also, from (b) $\ll$ (c) $\ll$ (d) the time dependence of the field's amplitude (e.g. its growth

or decay) can be neglected when analyzing its evolution based on the field equations. In these regards, the treatment we apply below is substantially simplified compared to the exact situation without crucial inconsistency [71].

In what follows of this chapter, we use units $G = c = 1$ unless otherwise stated.

3.2.1 Kerr spacetime

The geometry around a rotating BH in a vacuum is described by the Kerr spacetime, which is characterized purely by the BH mass M and angular momentum J.[2] Here we provide a brief review for the basics of the Kerr spacetime and more thorough descriptions can be found in Ref. [187]. Typically the Kerr spacetime is formulated using Boyer-Lindquist coordinates, given by

$$\begin{aligned} \mathrm{d}s^2 = &-\left(1-\frac{2Mr}{\Sigma}\right)\mathrm{d}t^2 - \frac{4Mar\sin^2\theta}{\Sigma}\,\mathrm{d}t\,\mathrm{d}\phi + \frac{\Sigma}{\Delta}\,\mathrm{d}r^2 \\ &+ \Sigma\,\mathrm{d}\theta^2 + \left[r^2 + a^2 + \frac{2Mra^2\sin^2\theta}{\Sigma}\right]\sin^2\theta\,\mathrm{d}\phi^2, \end{aligned} \tag{3.7}$$

where

$$\Delta \equiv r^2 + a^2 - 2Mr, \qquad \Sigma \equiv r^2 + a^2\cos^2\theta, \qquad a \equiv \frac{J}{M}. \tag{3.8}$$

Hereafter, we label the roots of $\Delta = 0$ as $r_\pm = M \pm \sqrt{M^2 - a^2}$ and r_+ is known as the event horizon for Kerr BHs. Also, one of the roots of $g_{tt} = 0$ determines so-called the ergosurface, $r_{\mathrm{ergo}} = M + \sqrt{M^2 - a^2\cos^2\theta}$. The region between the event horizon and the ergosurface is called the ergoregion. The ergoregion plays the most crucial role in the context of energy extraction from a BH since the classical Penrose process is possible only inside of the ergoregion.

The geodesic equations of a free pointlike particle can be explicitly written down for t, ϕ components as follows

$$\dot{t} = \frac{1}{\Delta}\left[\left(r^2 + a^2 + \frac{2a^2M}{r}\right)E - \frac{2aM}{r}L\right], \tag{3.9}$$

$$\dot{\phi} = \frac{1}{\Delta}\left[\frac{2aM}{r}E + \left(1 + \frac{2M}{r}\right)L\right], \tag{3.10}$$

where $\dot{x}$ represents the derivative of a variable x in terms of the affine parameter. E and L are the conserved energy and angular momentum of the particle per unit rest mass respectively, given by

$$E = -\frac{\partial\mathcal{L}}{\partial\dot{t}} = \text{Const.}, \tag{3.11}$$

[2] The no hair theorem states that BHs could have charge as another parameter, but from the astrophysical viewpoint we consider only neutral BHs.

$$L = \frac{\partial \mathcal{L}}{\partial \dot{\phi}} = \text{Const.}, \tag{3.12}$$

where $\mathcal{L} = g_{\mu\nu}\dot{x}^\mu \dot{x}^\nu$. As can be seen from the geodesic equations above, unlike the Newtonian gravity, in the general relativity the rotation of a BH, a, can affect the equation of motion, referred to as the frame-dragging effect. The strength of dragging, namely the angular velocity of the geometry itself around the BH, can be derived by considering an free-falling observer with $L = 0$, physically meaning that azimuthal component of the observer's position is attached to the metric. Using Eqs. (3.9) and (3.10) in the case of $L = 0$, the angular velocity of the metric at arbitrary r outside the event horizon reads

$$\Omega(r) \equiv \frac{\dot{\phi}}{\dot{t}} = \frac{2Ma}{r^3 + ra^2 + 2a^2M}. \tag{3.13}$$

In particular, at the event horizon ($r = r_+$) this reduces to

$$\Omega_H = \frac{a}{2Mr_+}, \tag{3.14}$$

which can be interpreted as the angular velocity of the BH and appears in the superradiant condition through Eq. (3.1).

3.2.2 Instability of massive scalar fields

Suppose a real scalar field[3], $\Psi(x^\alpha)$ with the mass $\mu(\equiv m_b c^2/\hbar$ in the SI unit), which is minimally coupled only with gravity around a rotating BH. The action describing this system is

$$S = \int \mathrm{d}^4x \sqrt{-g}\left(\frac{R}{16\pi} - \frac{1}{2}g^{\alpha\beta}\Psi_{,\alpha}\Psi_{,\beta} - \frac{\mu^2}{2}\Psi^2\right), \tag{3.15}$$

where R is the Ricci scalar and the metric is given by Eq. (3.7). In the expression of Eq. (3.15), one can ignore nonlinear self-interaction terms because the self-interaction effect is negligible unless the amplitude of the bosonic field turns to be large after the onset of the superradiant instability[4] [73]. Applying the variational method with regard to the scalar field, Ψ, one obtains the Klein-Gordon equation

$$\nabla_\alpha \nabla^\alpha \Psi = \mu^2 \Psi. \tag{3.16}$$

Eq. (3.16) on the Kerr background can be solved in the Teukolsky formalism, which provides the unified way to describe field perturbations on the Schwarzschild or Kerr background. It shows that linearized perturbation of bosonic fields (whether they are

[3] A complex scalar field ends up with a stationary stress-energy tensor, which does not induce GW emission [73]. Since this section is interested in GW emission in the end, complex scalar fields are out of the scope here.

[4] Nonlinear self-interaction is a phenomenon of great interest such as a bosenova. See [72], [73] for further details.

massless or massive) obeys a single master equation with different spin parameter, s [188], [189]. In particular, the master equation for massive scalar fields on the Kerr background, which can be derived from Eq. (3.16), reads

$$\left[\frac{(r^2+a^2)^2}{\Delta}-a^2\sin^2\theta\right]\frac{\partial^2\Psi}{\partial t^2}+\frac{4Mar}{\Delta}\frac{\partial^2\Psi}{\partial t\partial\phi}+\left[\frac{a^2}{\Delta}-\frac{1}{\sin^2\theta}\right]\frac{\partial^2\Psi}{\partial\phi^2} -\frac{\partial}{\partial r}\left(\Delta\frac{\partial\Psi}{\partial r}\right)-\frac{1}{\sin\theta}\frac{\partial}{\partial\theta}\left(\sin\theta\frac{\partial\Psi}{\partial\theta}\right)+\mu^2\Sigma^2\Psi=0, \tag{3.17}$$

where Δ, Σ and a are defined in Eq. (3.8). Furthermore, Ref. [190] found that Eq. (3.17) is separable using spin-weighted spheroidal functions with $s=0$, ${}_0S_{\ell m}(\theta)$. More generally, this argument can be extended to other types of *massless* bosonic fields such as vector and tensor fields. Spin-s spheroidal harmonics are applied for fields with the spin equal to s. The general solution of Eq. (3.17) can be expressed in a separable form:

$$\Psi=\mathrm{Re}\left[\int \mathrm{d}\omega\sum_{\ell m} \mathrm{e}^{-i\omega t+im\phi}\,{}_0S_{\ell m}(\theta)R_{\ell m}(r)\right]. \tag{3.18}$$

Substitution of Eq. (3.18) into the partial differential equation Eq. (3.17) provides two separated ordinary differential equations for the radial and angular function respectively as follows

$$\Delta\left(\Delta\frac{\mathrm{d}R_{\ell m}}{\mathrm{d}r}\right)+\left[\omega^2(r^2+a^2)^2-4aMrm\omega +a^2m^2-\Delta(\mu^2r^2+a^2\omega^2+\lambda_{\ell m})\right]R_{\ell m}=0, \tag{3.19}$$

$$\frac{1}{\sin\theta}\frac{\mathrm{d}}{\mathrm{d}\theta}\left(\sin\theta\frac{\mathrm{d}\,{}_0S_{\ell m}}{\mathrm{d}\theta}\right)+\left[a^2(\omega^2-\mu^2)\cos^2\theta-\frac{m^2}{\sin^2\theta}+\lambda_{\ell m}\right]{}_0S_{\ell m}=0. \tag{3.20}$$

In $a\to 0$ limit, ${}_0S_{\ell m}$ reduces to the spherical harmonics with the eigenvalue $\lambda=l(l+1)$.

Here, one can study the qualitative behavior of the radial function $R_{\ell m}(r)$ around a rotating BH. Introducing the tortoise coordinate r^* defined as

$$r_*(r)\equiv r+\frac{2Mr_+}{r_+-r_-}\ln\frac{r-r_+}{2M}-\frac{2Mr_-}{r_+-r_-}\ln\frac{r-r_-}{2M} \tag{3.21}$$

$$r^*\to-\infty \quad \text{for } r\to r_+, \qquad r^*\to\infty \quad \text{for } r\to\infty \tag{3.22}$$

and altering the wave function by $u_{\ell m}(r)=\sqrt{r^2+a^2}R_{\ell m}(r)$, Eq. (3.67) reduces to

$$\frac{\mathrm{d}^2u_{\ell m}(r^*)}{\mathrm{d}^2r^*}+(\omega^2-V_{\ell m}(\omega))u_{\ell m}(r^*)=0, \tag{3.23}$$

with the effective potential

$$V_{\ell m}(\omega)=\frac{\Delta\mu^2}{r^2+a^2}+\frac{4Marm\omega-a^2m^2+\Delta(\lambda_{\ell m}+(\omega^2-\mu^2)a^2)}{(r^2+a^2)^2} +\frac{\Delta(3r^2-4Mr+a^2)}{(r^2+a^2)^3}-\frac{3\Delta^2r^2}{(r^2+a^2)^4}. \tag{3.24}$$

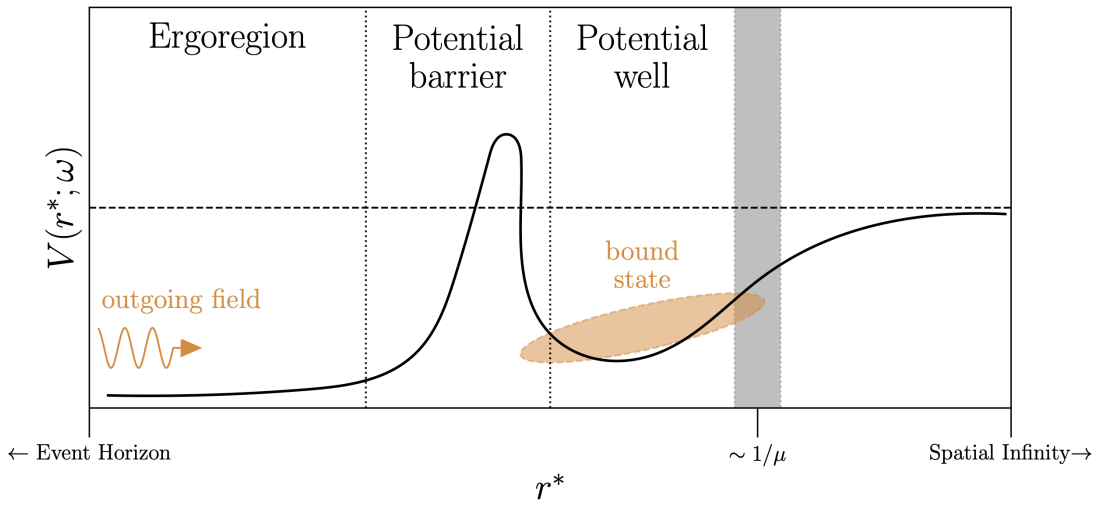

Figure 3.2: Schematic picture of the effective potential as a function of the tortoise coordinate r^*.

Fig. 3.2 is a schematic picture of the effective potential $V(\omega)$ as a function of the tortoise coordinate r^*. With respect to asymptotic properties, the potential approaches $V \to \mu^2$ at spatial infinity ($r \to \infty, r^* \to \infty$) and $V \to 2m\Omega_H\omega - m^2\Omega_H^2$ at the event horizon ($r \to r_+, r^* \to -\infty$). The shape of this potential shows that there is the centrifugal barrier at around $r^* \simeq M$, within which there exists the ergoregion. Also, outside the barrier it bears a potential well, which presents potential values of $V < \mu^2$. Therefore, once the superradiance sets in and energy becomes extracted from a rotating BH beyond the centrifugal barrier, outgoing waves from the BH will bounce off the outer edge of the well, experience successive superradiant scattering and gain more and more energy and angular momentum. This results in the exponential growth of the scalar field, which is natural demonstration of BH bombs. In conclusion, the presence of the potential well is the most crucial characteristic of this unstable mechanism.

To derive the superradiance condition, one considers the boundary conditions of $R_{\ell m}$. Because of the asymptotic behavior of the effective potential, at the infinity Eq. (3.23) reduces to

$$\frac{\mathrm{d}^2 u_{\ell m}(r^*)}{\mathrm{d}r^*} - (\mu^2 - \omega^2) u_{\ell m}(r^*) = 0. \tag{3.25}$$

Here, since we seek for the bound states, the decaying mode of $u_{\ell m}$ at the infinity should be chosen, which is

$$u_{\ell m} \propto \mathrm{e}^{-\sqrt{\mu^2-\omega^2}r^*}. \tag{3.26}$$

Near the event horizon, on the other hand, Eq. (3.23) reads

$$\frac{\mathrm{d}^2 u_{\ell m}(r^*)}{\mathrm{d}r^*} + (\omega - m\Omega_H)^2 u_{\ell m}(r^*) = 0. \tag{3.27}$$

Then, one should choose an ingoing boundary condition with regard to a comoving observer, being

$$u_{\ell m} \propto \mathrm{e}^{-ik_+ r^*}, \tag{3.28}$$

where $k_+ = \omega - m\Omega_H$. The other sign $\mathrm{e}^{ik_+ r^*}$ is excluded because of the requirement that the solution has to be regular in ingoing-Kerr coordinates. In this coordinate system, ingoing geodesics pass through the outer horizon in a finite coordinate time. See Ref. [172] for further detail.

Once these boundary conditions are imposed, in analogy with quasi-normal modes, general solutions of Eq. (3.23) are characterized by a set of discrete complex frequencies $\omega_{\ell mn}$, which depend on the set of mode numbers (ℓ, m, n). The total wavefunction at the infinity reads

$$\Psi \propto \mathrm{Re}\left\{\mathrm{e}^{-ik_+ r^* - i\omega_{\ell mn} t + im\phi}\right\}. \tag{3.29}$$

If $\mathrm{Re}\, k_+ < 0$, equivalently the superradiance condition (3.1) is satisfied, Eq. (3.29) indicates a flux escaping from the BH. Also, it can be shown from the conservation law of the stress-energy tensor that the satisfied superradiance condition ensures that the imaginary part of the eigenfrequencies, ω_I, is positive [168], resulting in the exponential growth of the bosonic field. Recall that now one can rewrite the coupling parameter (4.2.3) as $M\nu$ and the dynamics of a BH-cloud system is mostly described by this quantity. Particularly, in the non-relativistic limit, where the coupling parameter is small $(M\mu \ll 1)$, the field equations governing the bosonic fields reduce to those analogous to the Schrödinger equation for the hydrogen atom[5] [67], [73], [74], [168], [170], [184], [191]–[193]. The analytical expression of the complex eigenfrequencies Eq. (3.5) has been derived in this limit as follows

$$\omega_{\ell mn} \simeq \left\{1 - \frac{1}{2}\left(\frac{M\mu}{\ell + n + 1}\right)^2 + \mathcal{O}\left((M\mu)^4\right)\right\}\mu + i\,\frac{2\gamma r_+}{M}(m\Omega_H - \omega_R)(M\mu)^{4\ell+5}, \tag{3.30}$$

where γ is a numerical factor depending on n, ℓ, m. Again, the instability condition $\omega_I > 0$ reproduces the superrandiance condition Eq. (3.6). For the most unstable mode $\ell = m = 1, n = 0$, the small BH spin limit $(a/M \ll 1)$ leads to the growth rate

$$2\pi\omega_I \sim (0.07\,\mathrm{yr})^{-1}\left(\frac{a}{M}\right)\left(\frac{10M_\odot}{M}\right)\left(\frac{M\mu}{0.1}\right)^9. \tag{3.31}$$

Also, given the approximate hydrogenic spectrum of the system in the non-relativistic regime $(M\mu \ll 1)$, the radial function is expected to be written in terms of Laguerre polynomials [71] as

$$R_{\ell m}(\rho) \propto \rho^\ell \mathrm{e}^{-\rho/2} L_n^{2\ell+1}(\rho), \tag{3.32}$$

[5]One can find that the BH-cloud system has approximately hydrogenic energy levels and hence it is often referred to as "gravitational atom". In this analogy, the coupling parameter $M\mu$ exactly corresponds to the fine-structure constant.

where

$$\rho \equiv \frac{2M\mu^2}{\ell + n + 1} r. \tag{3.33}$$

Ref. [71] confirms that the approximate expression can be applied to numerical eigenfunctions up to $M\mu \lesssim 0.2$. Using Eq. (3.32), the eigenfunction's peak is located [68], [72] at

$$r_c \sim \frac{(\ell + n + 1)^2}{M\mu} \frac{1}{\mu} \sim \frac{1}{\mu}. \tag{3.34}$$

This implies that the bosonic cloud forms typically at $r_c \sim 1/\mu$, which is shown in Fig. 3.2.

The eigenfrequencies for general cases $M\mu \sim 1$ were numerically computed in [68], [168]. These numerical results indicate that the growth rate is significant typically when $M\mu \sim 0.5$, and that it scales with the increased spin parameter a or decreased indices such as ℓ, m. For a given unstable mode (fixed ℓ, m) and spin parameter a, a particular $M\mu$ yields the maximum growth rate ω_I. Especially, for extremal case $a \sim 1$, the growth rate reaches its maximum $\tau_{\text{inst}}^{-1} \sim 1.5 \times 10^{-7} (GM/c^3)^{-1}$ at $M\mu \approx 0.42$ [168].

3.2.3 Instability of massive vector fields

Similarly to the scalar case discussed above, we consider a real vector field minimally coupled with only gravity, A^α, whose system is described by the following action:

$$S = \int \mathrm{d}^4x \sqrt{-g} \left(\frac{R}{16\pi} - \frac{1}{4} F_{\alpha\beta} F^{\alpha\beta} - \frac{1}{2} \mu^2 A_\alpha A^\alpha \right), \tag{3.35}$$

where $F_{\alpha\beta} \equiv \nabla_\alpha A_\beta - \nabla_\alpha A_\beta$ is the field strength tensor. This action leads to the field equation that governs the evolution of massive vector fields, called the Proca equation:

$$\nabla_\alpha F^{\alpha\beta} = \mu^2 A^\beta. \tag{3.36}$$

By applying the operator ∇_β, it can be found that the vector field is necessarily in Lorenz gauge, which implies that the fields have three degrees of freedom, physically equivalent to polarizations.[6]

Unlike the Teukolsky equations for massive scalar fields, those for massive vector fields appeared to be inseparable until recently. Specifically, a set of partial differential equations for (r, θ) tends to remain coupled. Nevertheless, substantial efforts to solve the Proca equation have been made with some limits or approximations. For example, Refs. [184], [191] derived the solution in the slow-rotation ($a \ll M$) regime and Ref. [74] approximated a separable form focusing on the near-horizon and far-field

[6] This can be compared to the two polarizations of the photon.

regimes. Also, there have been different numerical approaches taken to derive the Proca solutions in the time domain [158], [183] and frequency domain [79].

Recently, Frolov *et al.* (we refer to as FKKS hereafter) [194] have made a remarkable discovery that using a specific ansatz inspired by Ref. [195], the equations governing the Proca fields can be separated on the Kerr-(A)dS-NUT spacetimes with arbitrary dimensions. In what follows, we provide a review of this approach, which reduces the problem to solving two decoupled differential equations and makes it computationally feasible to cover a broad parameter space. Taking an advantage of the separability, numerical computation has been performed to yield the field's growth rate for $S = \pm 1$ modes [194] and $S = 0$ mode [169] as well as GW radiation [171].

FKKS considers the Kerr spacetime in canonical coordinates $\{\tau \equiv t - a\phi, r, y = a\cos\theta, \phi = a/\phi\}$, where the metric takes the following form:

$$\mathrm{d}s^2 = -\frac{\Delta}{\Sigma}(\mathrm{d}\tau + y^2\,\mathrm{d}\psi)^2 + \frac{\Delta_y}{\Sigma}(\mathrm{d}\tau - r^2\,\mathrm{d}\phi)^2 + \frac{\Sigma}{\Delta}\mathrm{d}r^2 + \frac{\Sigma}{\Delta_y}\mathrm{d}y^2, \tag{3.37}$$

where Σ and Δ follow the definitions shown in Eq. (3.8) and $\Delta_y \equiv a^2 - y^2 = a^2\sin^2\theta$. Note that this metric admits Killing vectors $\Phi^\alpha_{(\tau)} = \partial^\alpha_\tau$ and $\Phi^\alpha_{(\psi)} = \partial^\alpha_\psi$ as well as a Killing-Yano tensor (or what is known as the principal tensor) $h_{\alpha\beta}$ such that $\nabla_\gamma h_{\alpha\beta} = g_{\gamma\alpha}\Phi^{(\tau)}_\beta - g_{\gamma\alpha}\Phi^{(\tau)}_\beta$. The separation ansatz introduced for Eq. (3.36) is

$$A^\alpha = B^{\alpha\beta}\nabla_\beta Z, \tag{3.38}$$

where $B^{\alpha\beta}$ is called the polarization tensor defined by

$$B^{\alpha\beta}(g_{\beta\gamma} + i\nu h_{\beta\gamma}) = \delta^\alpha_\gamma \tag{3.39}$$

with ν a separation constant as a function of the complex eigenfrequencies ω to be determined. Most importantly, a scalar function Z takes the multiplicative separated form, which reads

$$Z = R(r)S(\theta)\mathrm{e}^{-i\omega t + im\phi}, \tag{3.40}$$

using the Boyer-Lindquist coordinates.

FKKS proved that with this ansatz, the Proca equation (3.36) identically holds if the radial function, $R(r)$, and the angular function, $S(\theta)$, satisfy the two ordinary differential equations respectively such that

$$\frac{\mathrm{d}}{\mathrm{d}r}\left[\frac{\Delta}{q_r}\frac{\mathrm{d}R(r)}{\mathrm{d}r}\right] + \left[\frac{K_r^2}{q_r\Delta} + \frac{2-q_r}{q_r^2}\frac{\sigma}{\nu} - \frac{\mu^2}{\nu^2}\right]R(r) = 0 \tag{3.41}$$

$$\frac{1}{\sin\theta}\frac{\mathrm{d}}{\mathrm{d}\theta}\left[\frac{\sin\theta}{q_\theta}\frac{\mathrm{d}S(\theta)}{\mathrm{d}\theta}\right] - \left[\frac{K_\theta^2}{q_\theta\sin^2\theta} + \frac{2-q_\theta}{q_\theta^2}\frac{\sigma}{\mu} - \frac{m^2}{\mu^2}\right]S(\theta) = 0 \tag{3.42}$$

where

$$\begin{aligned} K_r &\equiv am_\phi - \left(a^2 + r^2\right)\omega, \quad & K_\theta &\equiv m_\phi - a\omega \sin^2\theta \\ q_r &\equiv 1 + \mu^2 r^2, & q_\theta &\equiv 1 - \mu^2 a^2 \cos^2\theta \\ \sigma &\equiv a\mu^2\left(m_\phi - a\omega\right) + \omega. \end{aligned} \tag{3.43}$$

In the massless limit ($\mu \to 0$), Eqs. (3.41) and (3.42) reduce to the Teukolsky equations for $s = \pm 1$ [188], [189], [196]. More thorough analysis of the Proca solution in other limits is discussed in Ref. [169].

To find the eigenfunction of Eq. (3.42), $S^{\nu}_{m\omega}(\theta)$, one expands it in terms of the Legendre polynomials $P^m_{\ell'}(\theta)$, namely

$$S^{\nu}_{m\omega}(\theta) = \sum_{\ell'=|m|}^{\infty} b_{\ell'} P^m_{\ell'}(\theta). \tag{3.44}$$

Substituting this ansatz into the angular equation (3.42) and projecting a specific ℓ mode by the integration $\int_{-1}^{1} \mathrm{d}\cos\theta P^{*m}_{\ell}(\theta)$, it reduces to solving the eigenvalue problem:

$$\sum_{\ell'=|m|}^{\infty} \mathcal{M}_{\ell\ell'} b_{\ell'} = 0. \tag{3.45}$$

For arbitrary ℓ's, the matrix $M_{\ell\ell'}$ reads

$$\begin{aligned} M_{\ell\ell'} =& \delta_{\ell\ell'}\left(\Lambda - \ell'\left(\ell'+1\right)\right) \\ &+ c^{(2)}_{\ell\ell'} a^2\left(\nu^2\ell'\left(\ell'+1\right) - 2\sigma\nu - \nu^2\Lambda + \gamma^2\right) \\ &- c^{(4)}_{\ell\ell'}\gamma^2 a^4\nu^2 - 2d^{(1)}_{\ell\ell'} a^2\nu^2 \end{aligned} \tag{3.46}$$

where the coefficients $c^{(2)}_{\ell\ell'}, c^{(4)}_{\ell\ell'}, d^{(1)}_{\ell\ell'}$ are given by

$$c^{(2)}_{\ell\ell'} \equiv \left\langle \ell m \left| \cos^2\theta \right| \ell' m \right\rangle = \frac{2\sqrt{\pi}}{3}\langle \ell, 0, \ell'\rangle + \frac{4}{3}\sqrt{\frac{\pi}{5}}\langle \ell, 2, \ell'\rangle \tag{3.47}$$

$$c^{(4)}_{\ell\ell'} \equiv \left\langle \ell m \left| \cos^4\theta \right| \ell' m \right\rangle = \frac{2\sqrt{\pi}}{5}\langle \ell, 0, \ell'\rangle + \frac{8}{7}\sqrt{\frac{\pi}{5}}\langle \ell, 2, \ell'\rangle + \frac{16\sqrt{\pi}}{105}\langle \ell, 4, \ell'\rangle \tag{3.48}$$

$$\begin{aligned} d^{(2)}_{\ell\ell'} &\equiv \left\langle \ell m \left| \sin\theta\cos\theta\frac{d}{d\theta} \right| \ell' m \right\rangle \\ &= \sqrt{\frac{4\pi}{3}}\left(\ell'\sqrt{\frac{(\ell'+1)^2 - m^2}{(2\ell'+1)(2\ell'+3)}}\langle \ell, 1, \ell'+1\rangle - (\ell'+1)\sqrt{\frac{\ell'^2 - m^2}{(2\ell'+1)(2\ell'-1)}}\langle \ell, 1, \ell'-1\rangle\right) \end{aligned} \tag{3.49}$$

with the definitions of

$$\left\langle \ell m | \hat{X} | \ell' m \right\rangle \equiv \int_{\Omega} P^{*m}_{\ell}\hat{X}P^m_{\ell'}\sin\theta\,\mathrm{d}\theta\,\mathrm{d}\phi, \tag{3.50}$$

and

$$\langle \ell_1, \ell_2, \ell_3\rangle \equiv (-1)^m\sqrt{\frac{(2\ell_1+1)(2\ell_2+1)(2\ell_3+1)}{4\pi}}\begin{pmatrix} \ell_1 & \ell_2 & \ell_3 \\ 0 & 0 & 0 \end{pmatrix}\begin{pmatrix} \ell_1 & \ell_2 & \ell_3 \\ -m & 0 & m \end{pmatrix} \tag{3.51}$$

using the usual Wigner 3-j symbol. Non-trivial solutions of Eq. (3.45) requires $\det\mathcal{M}_{\ell\ell'} = 0$, which yields the relation between ω and ν. In principle, eigenfuncions for the radial and angular equations (3.41) and (3.42), together with the condition of $\det\mathcal{M}_{\ell\ell'} = 0$, can be found numerically. Particularly, Ref. [169] investigated special solutions in the non-relativistic limit ($M\mu \ll 1$), considering the following three cases: For the parity-even $S = -1$ modes, ν takes the form of

$$\nu \to \frac{\mp\omega}{m - a\omega} \tag{3.52}$$

for any $m = \ell$ mode. The parity-odd $S = 0$ modes follow

$$\nu = \frac{1}{2a}\left(m + 1 - a\omega + \sqrt{(a\omega - m - 1)^2 + 4a\omega}\right). \tag{3.53}$$

Lastly, the eigenvalue for the $S = +1$ modes is derived from finding the middle root of the cubic

$$a\nu^3(m - a\omega) - \nu^2((m+1)(m+2) - a\omega(2m - a\omega)) + \omega\nu + \omega^2 = 0. \tag{3.54}$$

Additionally, similarly to the scalar case (see Eq. (3.30)), in the limit $M\mu \ll 1$ the Proca equations reduce to the Schrödinger-like equation [74] and hence the complex eigenfrequencies can be analytically given by

$$\frac{\omega}{\mu} \approx 1 - \frac{M^2\mu^2}{2n^2} + O\left((M\mu)^4\right) + i\, 2\gamma r_+(m\Omega_H - \omega_R)(M\mu)^{4|m|+4+2S}, \tag{3.55}$$

where $n \equiv |m| + \hat{n} + S + 1$ ($S = \{-1, 0, 1\}$ indicates the polarization state of the Proca fields as mentioned above and $\hat{n}$ is the overtone number) and a set of coefficients γ that depend on $m, \hat{n}, S$ can be found in Refs. [74], [79], [164]. This approximated frequency provides a reasonable initial guess to iteratively solve the radial and angular equations (3.41) and (3.42), together with the three eigenvalues (3.52), (3.53), the middle root of (3.54). As we will show in Chapter 4, for massive vector fields the instability of the second higher order mode ($m = 2$) can be as significant, which mostly results from systems with $M\mu \sim 1$ or beyond. In this range of $M\mu$ the analytical expression (3.55) does not hold any longer and hence, for accurate signal model of SGWB spectra, we adopt the following series expansion of ω_R in terms of $M\mu$:

$$\frac{\omega_R}{\mu} = 1 - \frac{(M\mu)^2}{2m^2} + \sum_{\alpha=4}^{10} c_\alpha^m (M\mu)^\alpha, \tag{3.56}$$

where we consider the most unstable mode $\hat{n} = 0, S = -1$ and the coefficients c_α^m and power indices α from 4 to 10 are summarized in Table 3.1. The listed values are used to saturated cloud energy and the frequencies of GW emission from the cloud.

Refs. [74], [184], [191] analytically verified that the instability timescale for the vector fields is generally much shorter than that for the scalar fields. In the limit $M\mu \ll 1$ the imaginary part of the complex frequency (3.55) can be rewritten [74] as

$$2\pi\omega_I \sim (7.3 \times 10^{-6}\,\mathrm{yr})^{-1}\left(\frac{a}{M}\right)\left(\frac{10M_\odot}{M}\right)\left(\frac{M\mu}{0.1}\right)^7, \tag{3.57}$$

$m\backslash M\mu$	4	5	6	7	8	9	10
1	−2.56	13.85	−97.65	349.53	−615.29	532.55	−183.08
2	−0.076	0.0071	0.029	−0.051	0.14	−0.12	0.034

Table 3.1: The fitted coefficients, c_α^m, defined in Eq. (3.56), of the higher order terms in ω_R for the $m = 1$ and $m = 2$ mode respectively.

which can be compared to the growth rate for the scalar fields, Eq. (3.31). Also, Refs. [169], [171], [194] computationally derived the growth rate for $m = 1$ modes with different S polarizations and consistently found that the $S = -1$ polarization is most unstable with the largest growth rate compared to $S = \{0, +1\}$. This numerical result is consistent with the implication from the analytical expression (3.55). This hierarchical difference in the instability timescale among the scalar and vector fields is physically due to the fact that the vector's unstable mode with $S = -1$ tends to spatially concentrate closest to the BH horizon and hence experience more efficient growth of the field energy.

The asymptotic behavior of the radial function $R(r)$ can be found by expanding the radial equation (3.41) at the horizon and spatial infinity respectively,

$$R(r) \sim \begin{cases} \mathrm{e}^{-ik_+ r_*}, & r \to r_+ \\ r^{(2\omega^2-\mu^2)M/\sqrt{\mu^2-\omega^2}}\mathrm{e}^{-\sqrt{\mu^2-\omega^2}r}, & r \to \infty \end{cases}, \tag{3.58}$$

which k_+ follows the same definition as the one used in Eq. (3.28) and r^* is the tortoise coordinates defined in Eq. (3.21). This ensures that the superradiance condition indeed realizes the outgoing field at the horizon, namely the energy/angular momentum extraction from a BH, and create a bound state that decays at infinity.

3.3 Gravitational-wave emission

Spacetime of a BH-cloud system can be fully described by the Einstein equations

$$G^{\alpha\beta} = 8\pi T^{\alpha\beta}, \tag{3.59}$$

where the stress-energy tensor on the right hand side reads

$$T^{\alpha\beta}(\Psi) = \Psi^{,\alpha}\Psi^{,\beta} + \frac{1}{2}g^{\alpha\beta}\left(\Psi_{,\gamma}\Psi^{,\gamma} + \mu^2\Psi^2\right) \tag{3.60}$$

for the real massive scalar fields and

$$T^{\alpha\beta}(A) = \mu^2 A^\alpha A^\beta + F^{\alpha\gamma}F^\beta_\gamma - \frac{1}{4}g^{\alpha\beta}\left(F_{\gamma\delta}F^{\gamma\delta} + 2\mu^2 A_\gamma A^\gamma\right) \tag{3.61}$$

for the real massive vector fields, respectively.

One could apply the quadrupole formula to compute the luminosity, but this is valid only in limited cases where the size of a GW source is sufficiently smaller than the GW wavelength and all the radiations are approximated to be coherent. However, it is not the case for the bosonic clouds, for which the spatial scale, typically $r_c \sim 1/\mu$, is comparable to the emitted GW wavelength $\sim 1/2\omega_R$ [71]. Therefore, it is more reasonable to make use of the more general theory of BH perturbation. Since gravitational perturbation can be treated as a massless tensor field, the Teukolsky formalism [188], [189] provides the complete prescription like the treatment applied for massive scalar fields. The gravitational perturbation on the Kerr background is represented as the Newman-Penrose scalar (NP scalar) $\psi_4 \equiv -C_{\alpha\beta\gamma\delta}n^\alpha m^{*\beta}n^\gamma m^{*\delta}$ [197], [198], where $C_{\alpha\beta\gamma\delta}$ is the Weyl tensor and

$$n^\alpha = \frac{1}{2\Sigma}\Big((r^2+a^2), -\Delta, 0, a\Big), \tag{3.62}$$

$$m^\alpha = \frac{\rho}{\sqrt{2}}(ia\sin\theta, 0, 1, i/\sin\theta), \tag{3.63}$$

are the Kinnersley null-tetrad found in Ref. [199], where ρ^* is a complex conjugate of $\rho = (r - ia\cos\theta)^{-1}$. The Teukolsky formalism for the tensor fields states that a new field defined as

$$\Phi \equiv \rho^{-4}\psi_4 \tag{3.64}$$

obeys the following master equation

$$\begin{aligned}
&-\left[\frac{(r^2+a^2)^2}{\Delta} - a^2\sin^2\theta\right]\frac{\partial^2\Phi}{\partial t^2} - \frac{4Mar}{\Delta}\frac{\partial^2\Phi}{\partial t\partial\phi} - \left[\frac{a^2}{\Delta} - \frac{1}{\sin^2\theta}\right]\frac{\partial^2\Phi}{\partial\phi^2} \\
&+\Delta^2\frac{\partial}{\partial r}\left(\Delta^{-1}\frac{\partial\Phi}{\partial r}\right) + \frac{1}{\sin\theta}\frac{\partial}{\partial\theta}\left(\sin\theta\frac{\partial\Phi}{\partial\theta}\right) - 4\left(\frac{a(r-M)}{\Delta} + \frac{i\cos\theta}{\sin^2\theta}\right)\frac{\partial\Phi}{\partial\phi} \\
&\qquad - 4\left(\frac{M(r^2-a^2)}{\Delta} - r - ia\cos\theta\right)\frac{\partial\Phi}{\partial t} - 2(2\cot^2\theta + 1)\Phi = 4\pi\Sigma\hat{T}(t, r, \Omega).
\end{aligned} \tag{3.65}$$

Here the source function $\hat{T}(t, r, \Omega)$ is evaluated through the transformation of $T_{\mu\nu}$ in the Einstein equation (3.59) and explicitly described in Ref. [199]. Similarly to the discussion in Chapter 3.2.2, the solution can be expanded in terms of the spheroidal harmonics of spin weight $s = -2$ as follows

$$\Phi = \sum_{\ell\tilde{m}}\int \mathrm{d}\tilde{\omega}' \mathrm{e}^{-i\tilde{\omega}'t + i\tilde{m}\phi}\, {}_{-2}S_{\ell\tilde{m}}(\theta)R_{\ell\tilde{m}\tilde{\omega}'}(r). \tag{3.66}$$

Substituting Eq. (3.66) into Eq. (3.65), one obtains two ordinary differential equations for the radial and angular components

$$\Delta^2\frac{\mathrm{d}}{\mathrm{d}r}\left(\Delta^{-1}\frac{\mathrm{d}R_{\ell\tilde{m}\tilde{\omega}'}}{\mathrm{d}r}\right) + \left(\frac{K^2 + 4i(r-M)K}{\Delta} - 8i\tilde{\omega}'r - a^2(\tilde{\omega}')^2 + 2a\tilde{m}\tilde{\omega}' + A_{\ell\tilde{m}}\right)R_{\ell\tilde{m}\tilde{\omega}'} = T_{\ell\tilde{m}\tilde{\omega}'}, \tag{3.67}$$

$$\frac{1}{\sin\theta}\frac{\mathrm{d}}{\mathrm{d}\theta}\left(\sin\theta\frac{\mathrm{d}\,{}_{-2}S_{\ell\tilde{m}}}{\mathrm{d}\theta}\right)+\left[a^2(\tilde{\omega}')^2\cos^2\theta-\frac{(\tilde{m}-2\cos\theta)^2}{\sin^2\theta}\right.$$
$$\left.+4a\tilde{\omega}'\cos\theta-2+A_{\ell\tilde{m}}\right]\,{}_{-2}S_{\ell\tilde{m}}=0, \quad (3.68)$$

where $K=(r^2+a^2)\tilde{\omega}'-\tilde{m}a$ and $A_{\ell\tilde{m}}$ is the eigenvalue of ${}_{-2}S_{\ell\tilde{m}}(\theta)$. The source term $T_{\ell\tilde{m}\tilde{\omega}'}$ is the projection of the source function $\hat{T}(t,r,\Omega)$, which is related to the stress-energy tensor of each scalar and vector fields respectively shown in Eqs. (3.60) and (3.61), onto the spheroidal harmonics. Therefore, it follows that

$$T_{\ell\tilde{m}\tilde{\omega}'}=2\int\frac{\mathrm{d}t}{\sqrt{2\pi}}\int_{S^2}d\Omega\,{}_{-2}\tilde{S}^*_{\ell\tilde{m}}\mathrm{e}^{i\tilde{\omega}'t-i\tilde{m}\phi}\frac{\hat{T}(t,r,\Omega)}{\rho^5\rho^*}. \quad (3.69)$$

Since Eq. (3.67) is an inhomogeneous (i.e. the source term $T_{\ell\tilde{m}\tilde{\omega}}$ is present) differential equation and categorized in a family of Sturm-Liouville equations, one can employ a Green's-function technique. The Green's function can be derived by connecting two independent solutions of the homogeneous version of Eq. (3.67) with each boundary condition imposed. See Appendix A for more discussion of solving an inhomogeneous Sturm–Liouville equation. Physically motivated boundary conditions are outgoing waves at the spatial infinity ($r\to\infty$) and ingoing waves at the event horizon ($r\to r_+$). Let the solution which satisfies each boundary condition be R^H and R_∞ respectively [174], [199] such that

$$R^H\to\begin{cases}\Delta^2\mathrm{e}^{-ikr^*} & (r^*\to-\infty),\\ r^3B_{\mathrm{out}}\mathrm{e}^{i\tilde{\omega}'r^*}+r^{-1}B_{\mathrm{in}}\mathrm{e}^{-i\tilde{\omega}'r^*} & (r^*\to\infty),\end{cases} \quad (3.70)$$

$$R^\infty\to\begin{cases}A_{\mathrm{out}}\mathrm{e}^{ikr^*}+\Delta^2A_{\mathrm{in}}\mathrm{e}^{-ikr^*} & (r^*\to-\infty),\\ r^3\mathrm{e}^{i\tilde{\omega}'r^*} & (r^*\to\infty),\end{cases} \quad (3.71)$$

where $k=\tilde{m}\Omega_H-\tilde{\omega}>0$, $A_{\mathrm{in/out}}, B_{\mathrm{in/out}}$ are constants and r^* is the tortoise coordinates defined in Eq. (3.21). Once the homogeneous solutions are found, the Green's function is constructed as

$$G(r^*,x^*)\begin{cases}\frac{R^\infty(x^*)}{W_l}R^H(r^*) & (-\infty<r^*<x^*),\\ \\ \frac{R^H(x^*)}{W_l}R^\infty(r^*) & (x^*<r^*<\infty).\end{cases} \quad (3.72)$$

W_l is so-called the Wronskian

$$W_l\equiv\frac{1}{\Delta}\left(R^\infty\frac{\mathrm{d}R^H}{\mathrm{d}r}-R^H\frac{\mathrm{d}R^\infty}{\mathrm{d}r}\right), \quad (3.73)$$

which is actually constant throughout r domain and can be found as $W_l=2i\tilde{\omega}'B_{\mathrm{in}}$ by plugging the asymptotic functional forms of Eqs. (3.70) and (3.71) into Eq. (3.73). Finally, the general solution of Eq. (3.67) is given by

$$R_{\ell\tilde{m}}=\frac{1}{W_l}\left(R^\infty\int_{r_+}^{r}\mathrm{d}x\frac{R^HT_{\ell\tilde{m}\tilde{\omega}'}}{\Delta^2}+R^H\int_{r}^{\infty}\mathrm{d}x\frac{R^\infty T_{\ell\tilde{m}\tilde{\omega}}}{\Delta^2}\right). \quad (3.74)$$

Since one is interested in gravitational radiation at infinity, the asymptotic solution

$$\lim_{r\to\infty} R_{\ell\tilde{m}}(r) = \frac{R^{\infty}}{W_l}\int_{r_+}^{\infty} \mathrm{d}r \frac{R^H T_{\ell\tilde{m}\tilde{\omega}'}}{\Delta^2} \tag{3.75}$$

$$= \frac{r^3 \mathrm{e}^{i\tilde{\omega}' r^*}}{2i\tilde{\omega}' B_{\mathrm{in}}}\int_{r_+}^{\infty} \mathrm{d}r \frac{R^H T_{\ell\tilde{m}\tilde{\omega}'}}{\Delta^2} \tag{3.76}$$

$$=: \delta(\tilde{\omega}' - \tilde{\omega})\tilde{Z}^{\infty}_{\ell\tilde{m}\tilde{\omega}'} r^3 \mathrm{e}^{i\tilde{\omega}' r^*} \tag{3.77}$$

needs to be computed. In the above expression, we assume that a bosonic field oscillating with the frequency of ω. Since $\hat{T}(t, r, \Omega)$ is proportional to the stress-energy tensor (contracted with tetrads given by Eqs. (3.62) and (3.63)), which is quadratic in the oscillating fields, it follows that $\hat{T} \propto \mathrm{Re}\{\mathrm{e}^{-i2\omega t + i2m\phi}\}$. This implies the respective relation for oscillation frequency and azimuthal index between the bosonic field and the NP scalar, $\tilde{\omega} = 2\omega, \tilde{m} = 2m$. Given the eigenfrequencies shown in Eqs. (3.30) and (3.55) respectively, perturbation of the bosonic field emits GWs with the nearly constant frequency $2\omega_R$. Plugging the radial function at infinity (3.77) into Eq. (3.66), together with the definition of Φ (3.64), the asymptotic behavior of the NP scalar ψ_4 takes the form

$$\psi_4^{\infty}(t, r, \theta, \phi) = \frac{1}{r}\sum_{\ell,\tilde{m}} \frac{\tilde{Z}^{\infty}_{\ell\tilde{m}\tilde{\omega}}}{\sqrt{2\pi}} \mathrm{e}^{i\tilde{\omega}(r_*-t)+i\tilde{m}\phi}\, {}_{-2}S_{\ell\tilde{m}\tilde{\omega}}(\theta). \tag{3.78}$$

In this expression, we ignore the time dependence of $\tilde{Z}^{\infty}_{\ell\tilde{m}\tilde{\omega}}$, in other words, the amplitude of the oscillating NP scalars is treated as stationary. As mentioned previously, this can be justified by the fact that the scalar's oscillating time scale, $1/2\omega_R$, is expected to be much shorter than the decay timescales, τ_{GW}.

At infinity the NP scalar encodes the second time derivatives of GW strains with the two independent polarizations $h_+, h_\times$

$$\psi_4 = \frac{1}{2}\left(\ddot{h}_+ - i\ddot{h}_\times\right). \tag{3.79}$$

Therefore, GW luminosity given by Eq. (1.27) reads

$$\frac{\mathrm{d}E_{\mathrm{GW}}}{\mathrm{d}t} = \int \mathrm{d}\Omega \frac{r^2}{16\pi}\left(\dot{h}_+^2 + \dot{h}_\times^2\right) = \frac{r^2}{16\pi}\int \mathrm{d}\Omega \left(\int 2\psi_4\, \mathrm{d}t\right)^2 \tag{3.80}$$

$$\to \frac{|\tilde{Z}^{\infty}_{\ell\tilde{m}\tilde{\omega}}|^2}{4\pi(2\omega_R)^2}, \tag{3.81}$$

where in the last expression we take an average over the oscillating time scale $1/\omega_R$ much shorter than the GW emission timescale and use the normalization of the spheroidal harmonics functions as follows

$$\int_0^{\pi} |{}_{-2}S_{\ell\tilde{m}}(\theta)|^2 \sin\theta d\theta = 2\pi. \tag{3.82}$$

Once the solution of the field equations (3.18) or (3.38) are given, one computes $\tilde{Z}^{\infty}_{\ell\tilde{m}\tilde{\omega}}$ through the expression of the stress-energy tensor for either type of the bosonic fields,

(3.60) or (3.61). Evaluating the total cloud energy using the time component of the stress-energy tensor T^t_t

$$M_S = \int T^t_t \sqrt{-g}\, \mathrm{d}r\, \mathrm{d}\Omega, \tag{3.83}$$

one can obtain the following proportionality of the approximated GW emission rate [68], [71], [73], [74]

$$\frac{\mathrm{d}E_{\mathrm{GW}}}{\mathrm{d}t} \approx \dot{\tilde{E}}_{\mathrm{GW}} \left(\frac{M_S^2}{M^2}\right). \tag{3.84}$$

In the non-relativistic limit $M\mu \ll 1$, $\dot{\tilde{E}}_{\mathrm{GW}}$ for the most unstable mode ($m = 1$) have been shown to follow different power-law dependences in terms of $M\mu$ for scalar [68], [71], [73] and vector [74] fields:

$$\dot{\tilde{E}}_{\mathrm{GW}} \propto \begin{cases} (M\mu)^{14} & \text{(scalar)} \\ \\ (M\mu)^{10} & \text{(vector).} \end{cases} \tag{3.85}$$

Particularly, from the scalar fields we adopt the expression given in Ref. [71] such that

$$\dot{\tilde{E}}_{\mathrm{GW}} = \frac{484 + 9\pi^2}{23040} (M\mu)^{14}. \tag{3.86}$$

This turns out to be still a good approximation when $M\mu \sim 1$ [174]. For the vector fields, similarly to the fields' oscillating frequencies ω_R, we consider the $m = 1, 2$ modes both and we note that there is non-negligible constribution from the regime $M\mu \geq 1$, in which the power-law expression (3.85) does not hold. Thus, we adopt the following polynomial functional form in the relativistic regime (namely, for $M\mu > 0.05$ if $m = 1$, and $\mu M > 0.67$ if $m = 2$)

$$\dot{\tilde{E}}^m_{\mathrm{GW}} = \sum_{\alpha=0}^{N_m} d^m_\alpha \, (M\mu)^\alpha \,, \tag{3.87}$$

where the respective coefficients are obtained by fitting to the numerical data of Ref. [171] and summarized in Table 3.2. We extrapolate the numerical-fitting results above to the non-relativistic limit with the following expressions

$$\begin{aligned} \dot{\tilde{E}}^{m=1}_{\mathrm{GW}} &= 1.3 \times 10^{-12} \left(\frac{M\mu}{0.05}\right)^{10}, && M\mu \leq 0.05, \\ \dot{\tilde{E}}^{m=2}_{\mathrm{GW}} &= \frac{(M\mu)^{14}}{1.0 \times 10^5} + 6.4 \times 10^{-4} (M\mu)^{16}, && M\mu \leq 0.67, \end{aligned} \tag{3.88}$$

where the exponent of the lowest order term in the respective expressions is set so that it is consistent with that of the analytic calculation in Ref. [74], and we fit the coefficients

against the numerical data of Ref. [171] up to $M\mu \approx 0.1$ for $m = 1$ and $M\mu \approx 0.7$ for $m = 2$. We avoid referring to the analytical expression from the literature even in non-relativistic limit because, based on the results in Ref. [74], we expect non-negligible corrections to the flatspace approximation. Nevertheless, we note that our predictions of SGWB are not strongly sensitive to the specifics of this extrapolation due to the strong suppression of the GW power in this regime.

Furthermore, one can estimate the emission timescale in $M\mu \ll 1$ regime,

$$\tau_{\rm GW} = \frac{M_S}{\mathrm{d}E_{\rm GW}/\,\mathrm{d}t} \tag{3.89}$$

$$\approx \begin{cases} 3.3\times10^{5}\ \mathrm{yr}\left(\frac{M_f}{10M_\odot}\right)\left(\frac{0.1}{M\mu}\right)^{14}\left(\frac{0.2M_f}{M_S}\right) & \text{(scalar)} \quad (3.90) \\ 6.0\times10^{-2}\ \mathrm{yr}\left(\frac{M_f}{10M_\odot}\right)\left(\frac{0.1}{M\mu}\right)^{10}\left(\frac{0.2M_f}{M_S}\right). & \text{(vector)} \quad (3.91) \end{cases}$$

We note that massive vector fields have several orders-of-magnitude shorter GW emission timescale, in other words larger GW luminosity, than scalar ones, similarly to the instability timescale. As will be shown in Section 4.3, this significant difference in the emission timescale makes a strong impact on our signal models of a SGWB.

3.4 Evolution of the system

The considerable difference in the timescales for scalar (vector) fields between Eqs. (3.31) and (3.90) (Eqs. (3.57) and (3.91)) suggests that the superradiant instability and subsequent GW emission can be analyzed separately as two independent steps. Therefore, once the superradiant instability is triggered, the bosonic fields grow exponentially without any dissipation and the BH continues to spin down until the superradiant condition Eq. (3.6) no longer holds. Subsequently, the GW emission dissipates the total energy of the boson clouds. Additionally, we approximate accretion effect onto a BH to be

$m\backslash\alpha$	0	1	2	3	4	5	6
1	-9.6×10^{-6}	−0.000064	0.018	−0.27	2.36	−12.8	41.5
2	−0.00014	−0.019	0.080	0.00011	1.00	−1.95	−9.31

$m\backslash\alpha$	7	8	9	10	11	12	13	14
1	−76.9	70.0	−15.9	−10.2	-	-	-	-
2	60.5	−165.1	275.5	−304.2	−224.6	−107.1	29.9	−3.72

Table 3.2: The coefficients, d^m_α, for the GW power ansatz in Eq. (3.87), fitted against the numerical data of Ref. [171]. Here, $N_{m=1} = 10$ and $N_{m=2} = 14$.

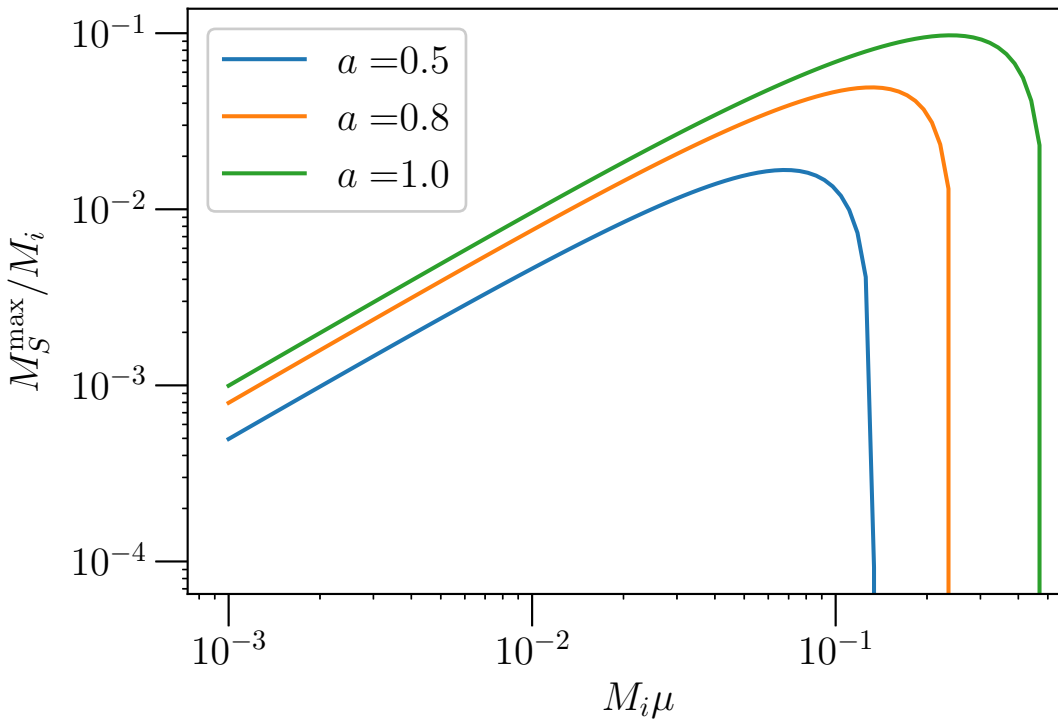

Figure 3.3: The maximum cloud energy obtained by Eq. (3.99) as a function of $M_i\mu$, considering only the most unstable ($m = 1$) mode. It follows that if $M\mu \sim 0.4$, a maximally spinning BH ($a = 1$) could deposit 10% of its energy into boson cloud through superradiant instability, which is broadly consistent with the more sophisticated analytical or numerical studies [158], [159]. Note that this figure allows for infinite time for the cloud to grow exponentially but practially this growth timescale tends to be much longer for $M\mu \sim 0.01$ or less, and hence less cloud energy can be deposited.

neglected as it is known that accreted matter does not significantly increase the initial spin of stellar mass BHs [200], although generally mass accretion onto a BH supplies angular momentum, which competes against the angular momentum extraction caused by the superradiant instability. In this prescription, the dynamics obey the following equations:

$$\begin{cases} \dot{M} = -\dot{M}_S \\ \dot{J} = -\dfrac{m}{\omega_R}\dot{M}_S \end{cases} \qquad (t \lesssim \tau_{\rm inst}) \tag{3.92}$$

$$\Downarrow$$

$$\begin{cases} \dot{M}_S = -\dot{E}_{\rm GW} \\ \dot{J}_S = -\dfrac{m}{\omega_R}\dot{E}_{\rm GW} \end{cases} \qquad (\tau_{\rm inst} \lesssim t \lesssim \tau_{\rm GW}). \tag{3.93}$$

Using Eq. (3.92), one can trace the transition of angular momentum between the initial and final states of a BH. Let the total mass and angular momentum of the BH at the initial and final state be $M_{i/f}$ and $J_{i/f}$ respectively. Integration of Eq. (3.92) over the

superradiance duration leads to the following consevation law,

$$J_f = \frac{m}{\omega_R}(M_f - M_i) + J_i. \tag{3.94}$$

Since the superradiance condition Eq. (3.6) becomes saturated at the final state, J_f can be expressed as follows

$$\omega_R = m\Omega_H = \frac{mJ_f}{2M^2(M + \sqrt{M^2 - (J_f/M)^2})} \tag{3.95}$$

$$\Rightarrow J_f = \frac{4mM_f^3\omega_R}{m^2 + 4M_f^2\omega_R^2}. \tag{3.96}$$

Equating Eq. (3.96) to Eq. (3.94), the BH mass of the final state, M_f, reads

$$M_f = \frac{m^3 - \sqrt{m^6 - 16m^2\omega_R(mM_i - \omega_R J_i)}}{8\omega_R^2(mM_i - \omega_R J_i)}. \tag{3.97}$$

Therefore, the total energy of the bosonic cloud can be written in terms of M_i and J_i, yielding

$$M_S^{\max} = M_i - M_f \tag{3.98}$$

$$= M_i - \frac{m^3 - \sqrt{m^6 - 16m^2\omega_R(mM_i - \omega_R J_i)}}{8\omega_R^2(mM_i - \omega_R J_i)}. \tag{3.99}$$

Fig. 3.3 shows the maximum cloud energy obtained by Eq. (3.99) as a function of $M_i\mu$, considering only the most unstable ($m = 1$) mode and different BH's initial spin, $a = J_i/M_i$. It follows that if $M\mu \sim 0.4$, a maximally spinning BH ($a = 1$) could deposit 10% of its energy into a boson cloud through superradiant instability, which is broadly consistent with the more sophisticated analytical or numerical studies [158], [159]. One should note that Fig. 3.3 allows for infinite time for the cloud to grow exponentially but practially this growth timescale tends to be much longer for $M\mu \sim 0.01$ or less than astrophysically relevant timescale, and hence less cloud energy can be deposited.

Once the superradiant instability halts, the GW emission evolves based on Eq. (3.93). Contrasted to the quasi-adiabatic approximation we adopt when discussing the evolution of BH scalar in the previous subsection, now let $M_S(t)$ encode time-dependence to construct the following differential equation

$$\dot{M}_S(t) = -\dot{\tilde{E}}_{\rm GW}\frac{M_S^2(t)}{M_f^2}, \tag{3.100}$$

where $\dot{\tilde{E}}_{\rm GW}$ is the dimensionless GW luminosity factor given by Eqs. (3.86) and (3.88). These are time-independent constants and hence Eq. (3.100) can be analytically solved, yielding

$$M_S(t) = \frac{M_S^{\max}}{1 + t/\tau_{\rm GW}} \tag{3.101}$$

with the GW emission timescale $\tau_{\rm GW}$ given in Eqs. (3.90) and (3.91) for scalar and vector fields respectively. Now one can evaluate the total GW energy emitted between the superradiance saturation and the present time as follows

$$E_{\rm GW} = \int_0^{\Delta t} {\rm d}t \frac{{\rm d}E_{\rm GW}}{{\rm d}t} = \int_0^{\Delta t} {\rm d}t \frac{M_S^{\rm max}\tau_{\rm GW}}{(t+\tau_{\rm GW})^2} \tag{3.102}$$

$$= \frac{M_S^{\rm max}\Delta t}{\Delta t + \tau_{\rm GW}}. \tag{3.103}$$

Here, the energy conservation law in Eq. (3.93) and Eq. (3.101) are used and the signal duration Δt is set to be the lifetime of BHs we consider, being typical $\Delta t \sim O(1)$ Gyr depending on their redshifts. Although, technically speaking, one needs to subtract the cloud's growth timescale from the BH's lifetime to compute the signal duration, the growth timescale is generally smaller than the GW emission timescale by a few orders of magnitude and hence the BH lifetime can be a reasonable proxy of overall signal duration.

Chapter 4

Stochastic Background Modeling

4.1 General formulation

As discussed in Chapter 2.1, for constructing our signal model, we assume: the SGWB is (a) isotropic, (b) unpolarized, (c) stationary and (d) Gaussian. The isotropic stochastic background is fully characterized by the dimensionless energy density of GWs per logarithmic frequency interval. For a range of astrophysical origins, this can be generally formulated as the integration of an energy spectrum from individual systems over their entire population,

$$\begin{aligned}\Omega_{\rm GW}(f) &\equiv \frac{1}{\rho_c}\frac{\mathrm{d}\rho_{\rm GW}}{\mathrm{d}\ln(f)} \\ &= \frac{f}{\rho_c}\int \mathrm{d}z \frac{\mathrm{d}t}{\mathrm{d}z}\int \mathrm{d}\boldsymbol{\theta} p(\boldsymbol{\theta}) R(z;\boldsymbol{\theta})\frac{\mathrm{d}E_s}{\mathrm{d}f_s}(\boldsymbol{\theta}).\end{aligned} \tag{4.1}$$

Here $R(z;\boldsymbol{\theta})$ is the event rate at which GW emission occurs per unit time in *source frame* per unit comoving volume, and $p(\boldsymbol{\theta})$ is the probability distribution of the source parameters $\boldsymbol{\theta}$, which involves assumptions one makes about a source population model. Regarding the SGWB originated from a superradiant instability, we consider the source parameters $\boldsymbol{\theta}$ as BH masses and their dimensionless *initial* spin parameter χ, which represents the BH spin before it starts to spin down due to the extraction of angular momentum during the instability.

The parameter distributions in Eq. (4.1) are determined by the BH population models, each of which will be discussed in the following sections, while the subtlety of the energy spectrum $\mathrm{d}E_s/\mathrm{d}f_s$ depends on types of bosonic fields one considers, scalar or vector, as discussed in the previous chapter. For either case of bosonic fields, individual sources emit GWs with nearly constant frequencies. Technically the GW signals are known to have a slight drift towards higher frequencies due to the cloud's binding energy increasing while the cloud loses its energy [177]. However, we note that the overall drift of the signal frequency is well within the width of each frequency bin that we will use for our analysis. Therefore the energy spectrum of signals from a single source can

be approximated as a delta function around its central frequency in source frame f_0,

$$\frac{\mathrm{d}E_\mathrm{s}}{\mathrm{d}f_s} \approx E_\mathrm{GW}\delta(f(1+z) - f_0). \tag{4.2}$$

Regarding $f_0 = \omega_R/\pi$, we consider only the leading term for scalar fields, namely $\omega_R \approx \mu$, whereas for vector fields we include the higher order terms shown in Eq. (3.56), whose coefficients are listed in Table. 3.1. Note that the source frame frequency f_s is related to the observed frequency f by a factor of the redshift: $f_s = (1+z)f$. The total radiated energy E_GW involves the GW emission timescale τ_GW, which follows a different power-law index of $M\mu$ between scalar and vector fields. (see Eqs. (3.90), (3.91)). Also we adopt the standard ΛCDM cosmology where the Hubble parameter is given by

$$H(z) = H_0\sqrt{\Omega_M(1+z)^3 + \Omega_\Lambda}. \tag{4.3}$$

Here H_0 is a Hubble constant and Ω_M, Ω_Λ are the dimensionless matter density and the dimensionless cosmological constant density, respectively. For these cosmological parameters, we adopt estimates derived from Planck [91], i.e. $H_0 = 68\,\mathrm{km\,s^{-1}Mpc^{-1}}$ and $\Omega_M = 1 - \Omega_\Lambda = 0.308$. Then $\mathrm{d}t/\mathrm{d}z$ reads as a function of redshift z,

$$\frac{\mathrm{d}t}{\mathrm{d}z} = \frac{1+z}{H_0}\sqrt{\Omega_M(1+z)^3 + \Omega_\Lambda}. \tag{4.4}$$

Since the background considered here is contributed only from unresolved component of the source population, we only integrate over the region of parameter space where predicted background spectra cannot be detected in a typical search for the individual source in question, namely a SNR less than 8 by searches for conventional CW sources or dedicated to boson cloud systems [177], [201]. Although we adopt semi-coherent analysis to compute representative SNR, only small patch of the parameter space could produce detectable signals and the specifics of SNR cutoff do not change the overall shape of the predicted spectra significantly.

4.2 Black hole population models

As can be seen from the formulation above, Eq. (4.1), not only the energy spectrum of each signal but also modeling the source population plays an important role in predicting the SGWB spectra. Specifically, we will need to assume a source number density and the mass and initial spin distributions of BHs coupled with ultra-light bosonic fields. Here, we consider two possible BH formation channels: (i) isolated extra-galactic BHs, and (ii) BBH merger remnants. We assume these channels independently contribute to the total GW energy density. As we will note below, our modeling of SGWB spectra depends on the details of the BH population models such as their mass function, spin distribution and star formation rate involved with each population, some of which have

not been strongly constrained yet. Although this thesis does not completely account for such astrophysical uncertainty, we will provide some assessment of potential impact of the uncertainty on the resultant SGWB spectra in Section 4.2.3.

Also note that we do not consider the galactic BH population (e.g. the one described in Ref. [179]), because our search method (described in Sec. 5) is optimized for a SGWB following a Gaussian distribution as well as an isotropic distribution on the sky. The signal emitted from galactic sources is expected to add a mostly non-Gaussian and anisotropically distributed component to the stochastic background.[1] This non-Gaussian component is typically removed during the of data conditioning process in the SGWB search pipeline we use [202]. Although an investigation for the specifics of this component is not the scope of this thesis, but it would be important to implement it into the pipeline for future work and the constraints we present here could be even more stringent.

4.2.1 Isolated black hole channel

Here we consider a population of extra-galactic isolated BHs born from core-collapse supernovae. For modeling the energy density spectrum, we accumulate the energy spectrum of a single source weighted by the BH formation rate over the age of the Universe, which yields from Eq. (4.1)

$$\Omega_{\rm GW}^{\rm iso}(f) = \frac{f}{\rho_c}\int \mathrm{d}z \frac{\mathrm{d}t}{\mathrm{d}z}\int \mathrm{d}M\,\mathrm{d}\chi p(\chi)\frac{\mathrm{d}\dot{n}}{\mathrm{d}M}\frac{\mathrm{d}E_s}{\mathrm{d}f_s}, \tag{4.5}$$

after marginalizing intrinsic source parameters. Here $p(\chi)$ is the probability density of a dimensionless spin parameter of a BH, $\chi = a/M$, and $\mathrm{d}\dot{n}/\mathrm{d}M$ is the BH formation rate as a density of BH mass M in the core-collapse supernovae model. Each term will be described in more detail in the following.

For the probability density of the natal BH spin χ, given little knowledge about the spin distribution at birth of isolated BHs[2], we assume a uniform distribution, being inspired by [70],

$$p(\chi) = \begin{cases} 0 & (\chi < \chi_{\rm ll}, \chi_{\rm ul} < \chi) \\ \frac{1}{\chi_{\rm ul}-\chi_{\rm ll}} & (\chi_{\rm ll} \leq \chi \leq \chi_{\rm ul}), \end{cases} \tag{4.6}$$

[1] We should also note that, for a given boson mass, the GW signals emitted by the galactic population would tend to lie in a very narrow frequency window around $f_0/(1+z)$[179] due to negligible redshift effect. On the other hand, the extra-galactic component should exhibit a broadband spectrum. Our search method is better suited for signals that emit in a broad range of frequencies.

[2] One can find some predictions for the natal BH spin distribution in Ref. [203] (see their Figs. 1 and 2). Nevertheless, we note that the BH spin distribution depends significantly on the model one assumes for the angular momentum transport in the progenitor stars.

where $\chi_{\rm ll}$ and $\chi_{\rm ul}$ are the lower and upper limit of the distribution, respectively. Since these lower/upper limits in the spin distribution are extremely uncertain, for simplicity when searching for this background, we will take into account this uncertainty by parametrizing the distribution in the following ways: (a) leave the lower limit $\chi_{\rm ll}$ as a free parameter, but fix $\chi_{\rm ul} = 1$; (b) leave the upper limit $\chi_{\rm ul}$ as a free parameter, but fix $\chi_{\rm ll} = 0$. In the remainder of the text, these will be denoted as the $\chi_{\rm ll}$ and $\chi_{\rm ul}$ parametrizations, respectively. In general, the first case allows for a larger amplitude of the background than the second case, since it ensures a population of BHs born with high-spin, from which it is possible to extract more energy through the superradiant instability. Different choices for these parametrizations can significantly affect the prediction of the background spectrum. Hence, as will be shown in Sec. 6, the choice of $p(\chi)$ parametrization one uses will significantly affect resultant constraints on boson masses when searching for such background in LIGO data.

The BH formation rate $\dot{n}(z, M)$ accounts for the number of BHs, with the mass M formed by direct core collapse of massive stars at a redshift z per unit comoving volume. Following its derivation described in Ref. [70], we consider the number of massive stars which will experience a supernova at the given z. For a given stellar-mass interval $\mathcal{M}_* \sim \mathcal{M}_* + \mathrm{d}\mathcal{M}_*$, the number of massive stars which enter the supernova phase at the given time t and form a BH can be derived as

$$\mathrm{d}\dot{n} = \psi\left(t - \tau(\mathcal{M}_*)\right) \frac{\xi(\mathcal{M}_*)\,\mathrm{d}\mathcal{M}_*}{\mathcal{M}_*}. \tag{4.7}$$

Here, $\tau(\cdot)$ is the lifetime function of a star with mass $\mathcal{M}_*$ based on [204], $\psi(t)$ is the SFR, as described in [205], takes the form of

$$\psi(z) = \nu \frac{a \exp(b(z - z_m))}{a - b + b\exp(a(z - z_m))}, \tag{4.8}$$

$$\text{where} \quad a = 2.2, b = 1.4, \nu = 0.24, z_m = 2.3. \tag{4.9}$$

Therefore, $\psi\left(t - \tau(\mathcal{M}_*)\right)$ denotes the star formation rate at the time of the progenitor's birth. One should note that $\xi(\mathcal{M}_*)$ is the initial mass function defined in terms of stellar mass fraction, which implies that $\xi(\mathcal{M}_*)\,\mathrm{d}\mathcal{M}_*$ provides the ratio of sum of the stellar masses in $[\mathcal{M}_* - \mathcal{M}_* + \mathrm{d}\mathcal{M}_*]$ to the total mass of the entire stellar population. Recall that there is the other definition of initial mass function (let it be $\phi(\mathcal{M}_*)$), which is commonly defined with regard to *the number fraction* of stars whose mass ranges between $\mathcal{M}_* \sim \mathcal{M}_* + \mathrm{d}\mathcal{M}_*$. We adopt Salpeter initial mass function [206], which follows $\phi(\mathcal{M}_*) \propto \mathcal{M}_*^{-2.35}$, in the range $\mathcal{M}_* \in [0.1 \sim 100]M_\odot$ so that

$$\xi(\mathcal{M}_*) = \frac{\mathcal{M}_*\phi(\mathcal{M}_*)}{\int_{0.1M_\odot}^{100M_\odot} \mathcal{M}_*\phi(\mathcal{M}_*)\,\mathrm{d}\mathcal{M}_*} = \frac{\mathcal{M}_*^{-1.35}}{\int_{0.1M_\odot}^{100M_\odot} \mathcal{M}_*^{-1.35}\,\mathrm{d}\mathcal{M}_*}. \tag{4.10}$$

To adapt the BH formation rate Eq. (4.7) into the formulation (4.5), we introduce a mapping function between a BH mass and its progenitor mass, namely $M = g(\mathcal{M}_*, Z)$,

and rewrite Eq. (4.7) as a density function with regard to BH mass M. It follows that

$$\frac{\mathrm{d}\dot{n}}{\mathrm{d}M} = \psi\left(t - \tau(\mathcal{M}'_*)\right) \frac{\xi(\mathcal{M}'_*)}{\mathcal{M}'_*} \left.\frac{\mathrm{d}\mathcal{M}_*}{\mathrm{d}M}\right|_{\mathcal{M}_*=\mathcal{M}'_*} \tag{4.11}$$

$$= \psi\left(t - \tau(\mathcal{M}'_*)\right) \frac{\xi(\mathcal{M}'_*)}{\mathcal{M}'_*} \left.\left(\frac{\mathrm{d}g(\mathcal{M}_*, Z)}{\mathrm{d}\mathcal{M}_*}\right)^{-1}\right|_{\mathcal{M}_*=\mathcal{M}'_*} \tag{4.12}$$

where the function $M = g(\mathcal{M}'_*, Z)$ depends on a core collapse model, for which we assume the delayed model of Ref. [207] and adopt a numerical fit provided therein, and on metalicity of the progenitor star. For the model of progenitor's metalicity, we adopt the evolution of cosmic metalicity given by Ref. [208], where the metalicity is evaluated as a function of redshift. Additionally, we apply the lower BH mass cutoff of $3M_\odot$ in $g(\mathcal{M}_*, Z)$. To sum up, the BH formation rate (see Eq. (4.12)) depends on the BH mass, M, and indirectly on redshift via the metalicity.

With the knowledge of the energy spectrum radiated from a single source, Eq. (4.2), one can compute the the energy density spectrum contributed from isolated BH populaton. As an example, Fig. 4.1 shows the energy density spectrum Eq. (4.5) for scalar fields with different masses. The each linestyle indicates different range of the initial spin distribution we assume, $\chi \in [0.8, 1][0.5, 1][0, 1][0, 0.5]$ respectively. As expected from the fact that faster spinning black possess more angular momentum and massive bosonic fields can extract and emit more energy with GWs during the superradiant instability, the magnitude of each spectrum shifts up for more optimistic spin distributions which are skewed towards high spin parameters. We note that this computation is mostly consistent with Fig. 2 of Ref. [70] except for the significant suppression seen from Fig. 4.1 in the case of $m_\mathrm{b} = 10^{-13}\,\mathrm{eV}$. [3]

The strong suppression of the background at $m_\mathrm{b} \approx 10^{-13}\,\mathrm{eV}$ can be explained in two regards. $M\mu$ effectively represents the coupling strength between ultra-light bosons and BHs and its typical value for a BH mass of interest $O(10\,\mathrm{M}_\odot)$ is

$$M\mu \to \frac{GMm_\mathrm{b}}{c\hbar} \approx 0.1 \frac{M}{50M_\odot} \frac{m_\mathrm{b}c^2}{10^{-12.5}\,\mathrm{eV}}. \tag{4.13}$$

This expression implies that in order for $M\mu$ to be $O(0.1)$ a given $M\mu$ the bosonic field of $m_\mathrm{b} = 10^{-13}\,\mathrm{eV}$ need to couple with isolated BHs as heavy as $150\,\mathrm{M}_\odot$, which is not as abundant as relatively light BHs such as $M \approx O(10\,\mathrm{M}_\odot)$. Even though the subpopulation of relatively light BHs can couple with such scalar fields, the GW emission timescale is rather long according to Eqs. (3.90) and (3.91) by many orders of magnitude. Hence, compared to the typical lifetime of those BHs, that is, the actual duration

[3] This disagreement is due to the difference in the upper limit of BH mass between this work and Ref. [70]. The BH formation rate computed for this work is purely analytic and does not produce BHs heavier than $60M_\odot$, while Ref. [70] employs a semi-analytic simulation to compute the rate and it produces a modest fraction of BHs with even around $\sim 70M_\odot$, which tend to strongly couple with lighter boson like $m_b \approx 10^{-13}\,\mathrm{eV}$ and contribute to the stochastic background with a higher amplitude.

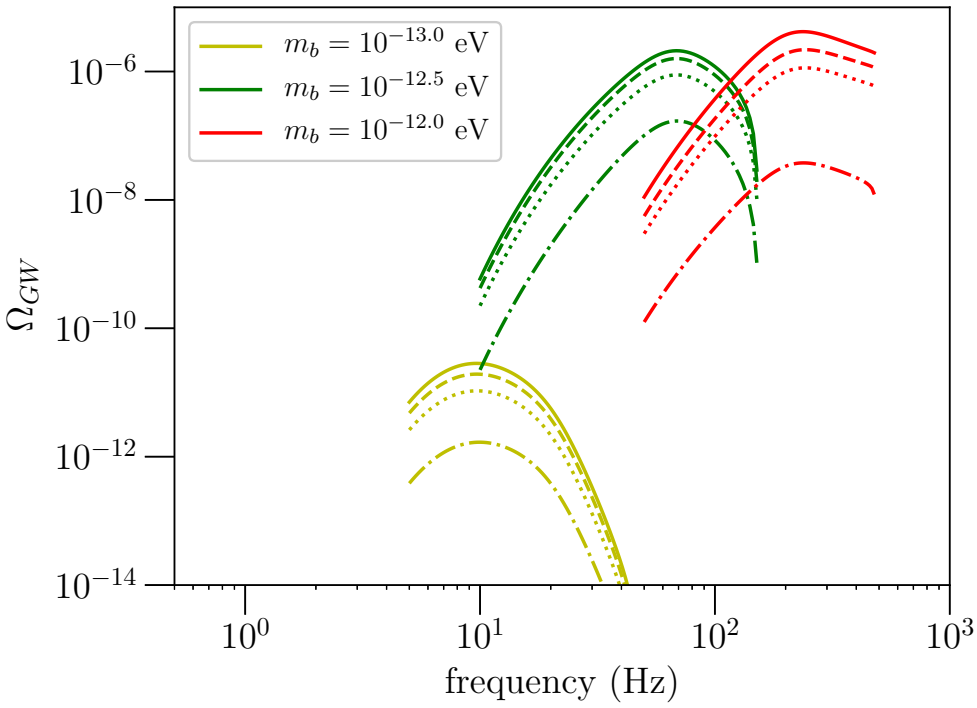

Figure 4.1: Energy density spectrum, $\Omega_{\rm GW}(f)$, predicted from scalar cloud model with difference spin distribution in the LIGO frequency band. The spectra with different colors are drawn for three choices of bosonic mass, $m_{\rm b}$. Also each linestyle corresponds to a uniform spin distribution with (from top to bottom) $\chi \in [0.8, 1], [0.5, 1], [0, 1], [0, 0.5]$.

of the GW emission, the signals can carry the energy at an extremely slow rate and only small fraction of the total cloud energy can be radiated away, leading to little contribution to the stochastic background. The same argument can be made for vector fields as well, but since the GW emission timescale is a lot shorter for vector fields (see Eq. (3.91)) at given $M\mu$, a similar suppression can be seen at even lighter vector fields $m_b \approx 10^{-13.5}$ eV, which is illustrated in Fig. 4.6.

4.2.2 Binary black hole merger remnants

Another BH formation channel we consider is BBH merger remnants. The expression of those background spectrum reads

$$\Omega_{\rm GW}^{\rm rem}(f) = \frac{f}{\rho_c}\int \mathrm{d}z \frac{\mathrm{d}t}{\mathrm{d}z} \times \int \mathrm{d}\boldsymbol{m}\,\mathrm{d}\chi\, p\,(\boldsymbol{m}) R_m(z;\boldsymbol{m}) p(\chi) \frac{\mathrm{d}E_s}{\mathrm{d}f_s}. \tag{4.14}$$

We label component masses of BBHs as $\boldsymbol{m}$, i.e. m_1 for the primary component and m_2 for the secondary component ($m_1 > m_2$ by definition) and define $\mathrm{d}\boldsymbol{m} \equiv \mathrm{d}m_1\,\mathrm{d}m_2$. $R_m(z;\boldsymbol{m})$ is the merger rate density of BBH systems per unit comoving volume for a given $\boldsymbol{m}$ and z. Contrasted to the uncertain natal spins of isolated BHs, one can physically constrain

$p(\chi)$ of BBH merger remnants population using the GW observation by advanced LIGO and Virgo [7], [21], [22], [24], [25], [27], [209]–[212] as well as several numerical simulations for BBH mergers with similar-mass [213]–[215]. In particular, most of the BBH observation using GWs suggest that, for a population of near-equal mass BHs that are non-rapidly spinning, the expected spin magnitude of final remnant BHs is approximately 0.7 [216]–[219]. Therefore, we assume the initial spin distribution such that,

$$p(\chi) = \delta(\chi - 0.7), \tag{4.15}$$

implying that all the remnant BHs initially have $\chi = 0.7$.

Following Ref. [132], we assume the BH mass distribution

$$p(m_1, m_2) \propto \frac{m_1^{-2.35}}{m_1 - 5M_\odot}, \tag{4.16}$$

with the constraints that $5M_\odot < m_1, m_2 < 95M_\odot$ and $m_1 + m_2 < 100M_\odot$. We adopt the following approximation for the mass of remnant BHs:

$$M \approx m_1 + m_2 - 5.7 \times 10^{-2} \frac{m_1 m_2}{m_1 + m_2}, \tag{4.17}$$

where the last term on the right hand side corresponds to the binding energy of the inner most stable orbit in a binary system to be subtracted [220].

For the merger rate density of BBHs, we adopt the prescription discussed in Refs. [131], [132] and model it as a convolution of the BH formation rate, $R_f(z; \boldsymbol{m})$ with the time delay distribution, $p(t_d)$, between the BBH formation and its merger such that

$$R_m(z; \boldsymbol{m}) = \int_{t_{\rm min}}^{t_{\rm max}} R_f(z_f; \boldsymbol{m}) p(t_d)\, {\rm d}t_d. \tag{4.18}$$

z_f denotes the redshift at the time of binary formation $t_f = t(z) - t_d$, in which $t(z)$ is the cosmic time at merger. Similarly to the model in Refs. [131], [132], [181], [182], we make the several assumptions as below: (i) we model the distribution $p(t_d)$ as the inverse of the time delay, namely $p(t_d) \propto 1/t_d$, defined over $t_d \in [t_{\rm min} - t_{\rm max}]$ ($t_{\rm min}$ is 50 Myr [131], [221] and $t_{\rm max}$ is the Hubble time [112], [221]–[223]), (ii) the formation rate of relatively light BBHs systems, where neither component mass is heavier than $30M_\odot$, is proportional to the SFR $\psi(z)$, (iii) we adopt the SFR consistent with the one used for the isolated BHs model (see [205]), (iv) massive binaries that have at least one of the two component masses heavier than $30M_\odot$ are not formed in a high metallicity environment such that $Z > Z_\odot/2$ ($Z_\odot$ is the solar metallicity), and the fraction of star formation for those binaries in a low-metalicity environment where $Z \leq Z_\odot/2$ can be accounted for by weighting the SFR with an efficiency factor $e(z)$ [224]. In other words,

$$R_f(z_f; \boldsymbol{m}) \propto \begin{cases} \psi(z_f) & \text{if } m_1, m_2 < 30M_\odot \\ e(z_f)\psi(z_f) & \text{otherwise.} \end{cases} \tag{4.19}$$

Along with the scaling in Eq. (4.19), we calibrate the merger rate using the BBH merger rate at the local Universe estimated from the observation by advanced LIGO and Virgo. Particularly, after marginalizing Eq. (4.18) over the component mass distribution $p(\boldsymbol{m})$, we adopt the rate estimate in Ref. [22] derived from the BH mass function with a power law distribution[4] 56 $\mathrm{Gpc}^{-3}\mathrm{yr}^{-1}$, which reads

$$\int p(\boldsymbol{m}) R_m(z=0;\boldsymbol{m})\,\mathrm{d}\boldsymbol{m} = 56\ \mathrm{Gpc}^{-3}\mathrm{yr}^{-1}. \tag{4.20}$$

While we assume the merger rate at the local Universe is exactly known, in principle this should be involved with uncertainty given by Poisson statistics, i.e. the 90% credible interval on the BBH merger rate, 9.7-101 $\mathrm{Gpc}^{-3}\mathrm{yr}^{-1}$ is given in Ref. [22]. Along with the assumptions we have made above, this uncertainty will lead to a systematic uncertainty in our modeling of the background spectrum from the BBH merger remnant channel, $\Omega_{\mathrm{GW}}^{\mathrm{rem}}(f)$. However, as we will show in the next subsection, the contribution from the BBH remnant channel is rather small compared to the isolated BH channel for the range of vector masses to which current GW detectors are sensitive. Therefore, we expect that these systematics do not significantly change the results from our injection studies, search and its implication, namely, constraints on the boson mass.

4.2.3 Total background model (channel comparison)

We treat the contributions from the two BH populations to the total background independently, in other words, one would observe the sum of these two components as the actual background spectrum in data,

$$\Omega_{\mathrm{GW}}(f) = \Omega_{\mathrm{GW}}^{\mathrm{iso}}(f) + \Omega_{\mathrm{GW}}^{\mathrm{rem}}(f), \tag{4.21}$$

where the superscript "iso" ("rem") indicates the component from the isolated BH (BBH merger remnant) population given by Eq. (4.5) (Eq. (4.14)). Figs. 4.2 and 4.3 show the comparison of background spectra between these two BH populations for each of massive scalar or vector fields. The different colors and linestyles represent different values of boson masses and BH populations respectively. In the figures, the spectra are also compared with power-law integrated curves [225] of advanced LIGO for O1+O2 and the design sensitivity (equivalent to O4) as well as the projected CBC background simulated in Ref. [132] with the extrapolation down to 5 Hz using a power-law spectrum Eq. (6.4).

The solid curves are the energy density spectra contributed from the isolated BH population where we assume a uniform distribution for the initial BH spin $\chi \in [0, 1]$. As

[4] During the writing of this thesis, LVC updated the BBH merger rate based on GWTC-2 [27], $\mathcal{R}_{\mathrm{BBH}} = 23.9\,\mathrm{Gpc}^{-3}\mathrm{yr}^{-1}$. Although this new estimate is not incorporated in the model we consider here, the update wouldn't affect the overall shape of the background spectrum significantly, as the component of the BBH remnant population is subdominant in most cases.

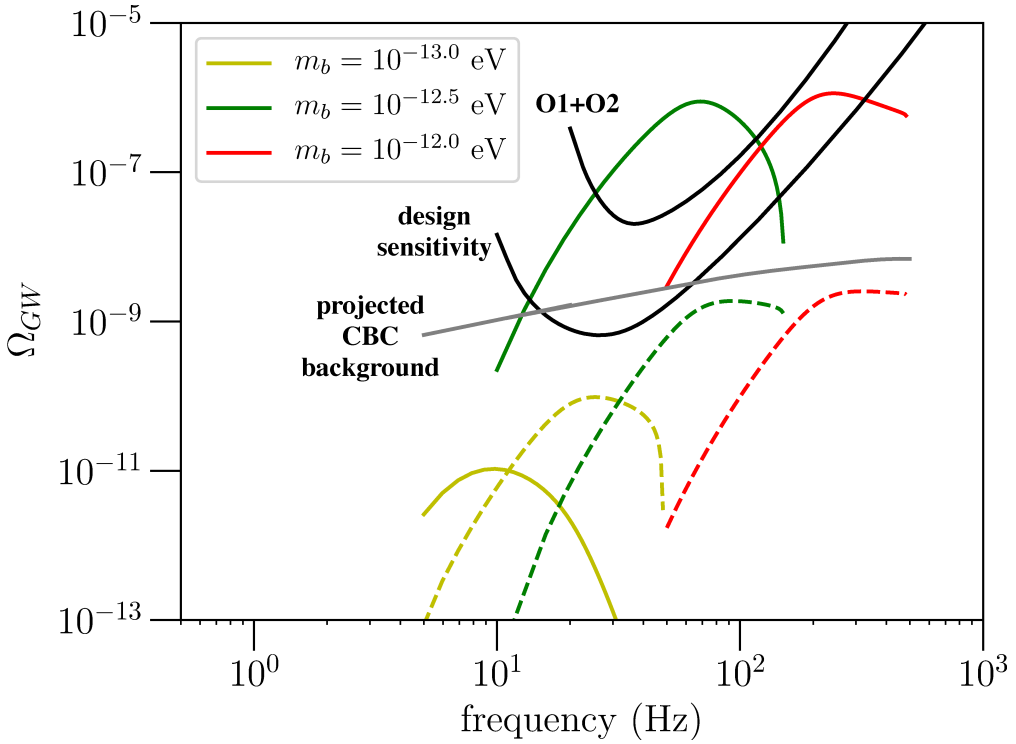

Figure 4.2: Energy density spectra produced from scalar cloud systems in the LIGO's frequency band, being plotted with the (2σ) power-law integrated curves [225] obtained using LIGO's O1 and O2 [84], and design sensitivity [226]. The isolated BH population model are shown by solid curves, where we assume a uniform distribution of $\chi \in [0, 1.0]$, while the BBH merger remnant population is represented by dashed curves. The gray line indicates the projected CBC background simulated in [132] with the extrapolation down to 5 Hz using a power-law spectrum Eq. (6.4).

shown in Fig. 4.1 and its relevant text, the spin distribution that contains highly spinning BHs would simply scale the overall spectrum. On the other hand, the dashed curves show the contribution from BBH merger remnant population. In our population model, generally speaking, the abundance of isolated BHs surpass the BBH merger rate by around four orders of magnitude. Therefore, the isolated BH population (solid curves) tend to dominate the background spectrum for the BBH merger remnant population (dashed curves), especially for scalar masses $\geq 10^{-12.5}$eV and for the entire range of vector mass shown in Fig. 4.3, corresponding to frequencies $\gtrsim$ 10 Hz. However, if scalar fields are relatively light, e.g. $m_b \sim 10^{-13}$eV, the SGWB from isolated BHs can be significantly reduced due to the fact that in our model of mass distribution [207], the core-collapse supernovae rarely produce BHs heavier than 50 $M_\odot$ to which scalar fields with such mass range is strongly coupled (see Eq.). In contrast, such heavy BHs can be readily be formed through the merger channel, and so the remnant BH component can be dominant in the background spectrum for this case. Since current GW detectors are mainly sensitive in the frequency range 10-100 Hz, the detectable SGWB from ultra-light bosons is expected to be mostly dominated by a component of the isolated BH population.

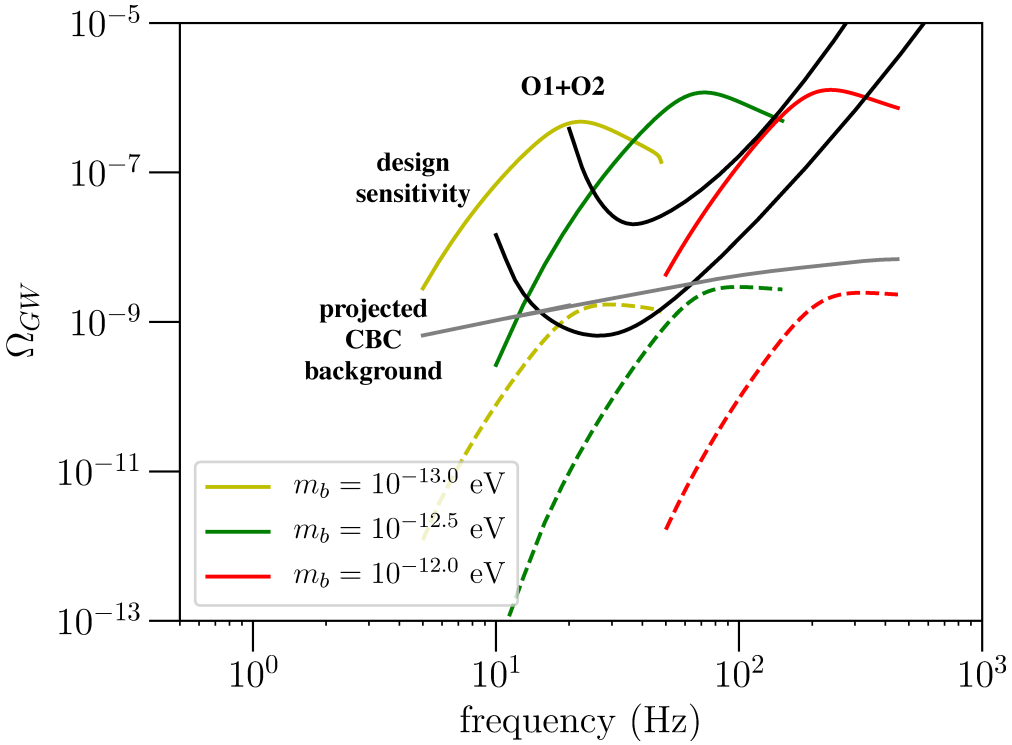

Figure 4.3: Energy density spectra produced from vector cloud systems in the LIGO's frequency band, being plotted with the (2σ) power-law integrated curves [225] obtained using LIGO's O1 and O2 [84], and design sensitivity [226]. The isolated BH population model are shown by solid curves, where we assume a uniform distribution of $\chi \in [0, 1.0]$, while the BBH merger remnant population is represented by dashed curves. The gray line indicates the projected CBC background simulated in [132] with the extrapolation down to 5 Hz using a power-law spectrum Eq. (6.4).

We note that the SGWB may dominate over the projected CBC background, approximating it as a power-law spectral model (see Ref. [132]), such that

$$\Omega_{\rm GW}^{\rm CBC}(f) = 1.8 \times 10^{-9} \left(\frac{f}{25{\rm Hz}}\right)^{2/3} . \tag{4.22}$$

Building up on this observation, as a part of our analysis study in Section 6, we also conduct a model selection test based on the Bayesian statistics in order to assess the possibility to distinguish between different signal models derived from the CBC population and the boson cloud model.

Lastly, we show an investigation to illustrate the impact of astrophysical uncertainty involved with the BH population models on the SGWB spectra. More specifically, while BH mass function and local BBH merger rate we adopt are motivated by the theoretical and observational constraints as described in Section 4.2, there are several models in the cosmic SFR. In Figs. 4.4 and 4.5, we show energy density spectra produced from scalar and vector cloud systems respectively, assuming different SFR models, for which we adopt the following four SFR examples: Hopkins *et. al.* 2006 (blue), Wilkins *et. al.* 2008 (yellow) and two models from Vigioni *et. al.* 2015 (green and red). Vigioni *et. al.* 2015 A/B represent different ways of calibrating the nominal SFR function, i.e. the model A calibrates it to the observational rate of the gamma-ray bursts [227] and is the model we use for our analysis, whereas the model B calibrates it to observations of the luminous galaxies [228], [229]. The contributions from the both BH populations are included under the assumption of isolated BH spin uniformly distributed over $\chi \in [0, 1.0]$. We find that over the boson mass range of interest, 10^{-13} eV to 10^{-12} eV, the SGWB spectrum predicted from the SFR model of Vigioni *et. al.* 2015 A lies between other SFR models, and hence the SGWB modeling we construct for the analysis is considered intermediate scenario among the astrophysical uncertainty.

4.3 Scalar-vector comparison

Fig. 4.6 also compares the background spectra for vector (in color) and scalar (gray) boson models. We note that the solid (dashed) curves in color represent the contribution from the isolated BH (BBH merger remnants) population, whereas the dash-dotted curves (the scalar field component) include both the two BH populations. For $m_b > 10^{-12.5}$ eV, the vector and scalar models predict almost the identical spectra because the GW emission timescale for both types of bosons in the mass range is sufficiently short (due to relatively large $M\mu$) and almost all the cloud energy is completely dissipated away. Also one can see that the scalar model for $10^{-12.5}$ eV (green curve) deviates from the vector model at higher frequencies. Since the signal duration is defined as BH lifetime, the energy emitted at such high frequencies is sourced from relatively

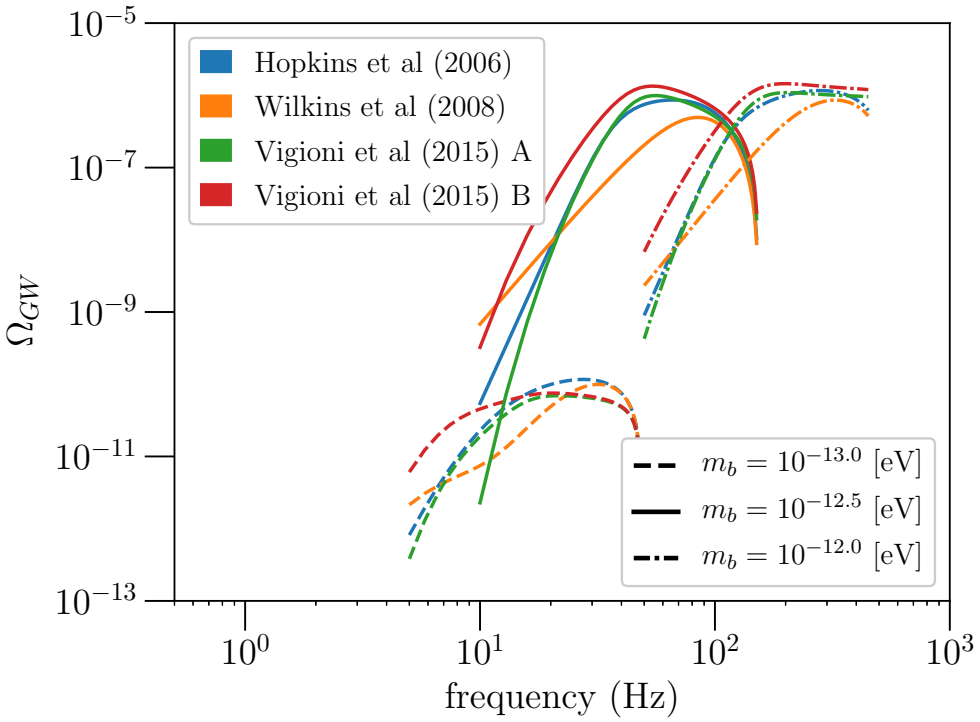

Figure 4.4: Energy density spectra produced from scalar cloud systems assuming different SFR models. Here, we adopt the following four SFR models: Hopkins *et. al.* 2006 (blue), Wilkins *et. al.* 2008 (yellow) and two models from Vigioni *et. al.* 2015 (green and red). Vigioni *et. al.* 2015 A/B represent different ways of calibrating the nominal SFR function, i.e. the model A calibrates it to the observational rate of the gamma-ray bursts [227] and the model B calibrates it to observations of the luminous galaxies [228], [229]. The different linestyles indicate the three scalar masses, 10^{-13} eV to 10^{-12} eV. The contributions from the both BH populations are included under the assumption of isolated BHs' spin uniformly distributed over $\chi \in [0, 1.0]$.

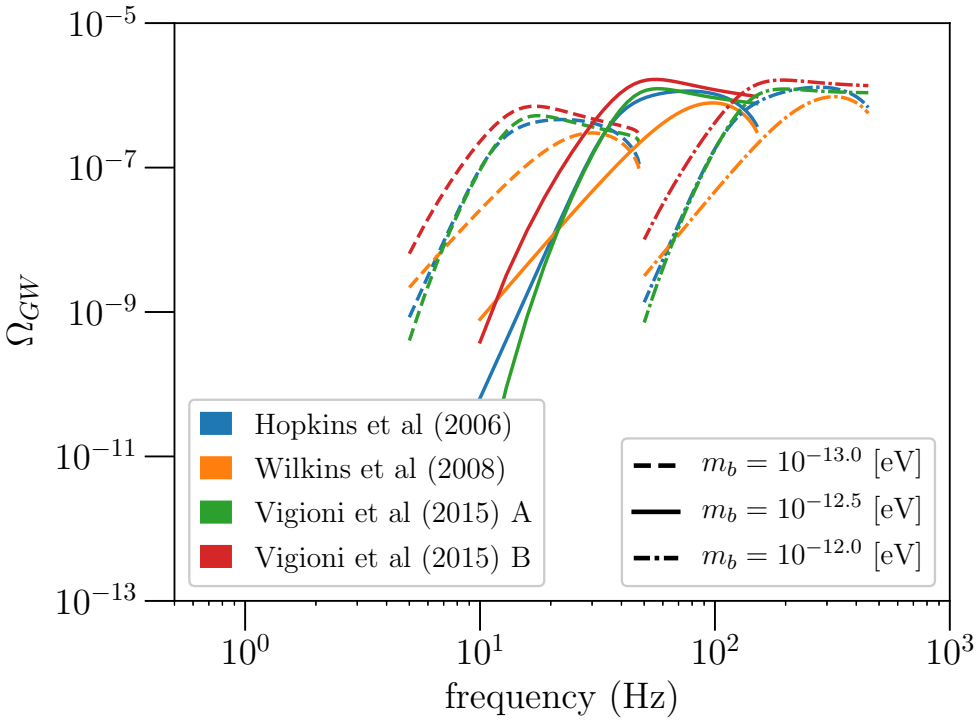

Figure 4.5: Energy density spectra produced from vector cloud systems assuming different SFR models. Here, we adopt the following four SFR models: Hopkins *et. al.* 2006 (blue), Wilkins *et. al.* 2008 (yellow) and two models from Vigioni *et. al.* 2015 (green and red). Vigioni *et. al.* 2015 A/B represent different ways of calibrating the nominal SFR function, i.e. the model A calibrates it to the observational rate of the gamma-ray bursts [227] and the model B calibrates it to observations of the luminous galaxies [228], [229]. The different linestyles indicate the three vector masses, 10^{-13} eV to 10^{-12} eV. The contributions from the both BH populations are included under the assumption of isolated BHs' spin uniformly distributed over $\chi \in [0, 1.0]$.

young BHs, which have shorter lifetime. Therefore, these BHs tend to suppress the energy emission for scalar bosons that have the longer emission timescale. For vector bosons, on the other hand, their shorter emission timescale makes it possible to exhaust the cloud energy even within the short BH lifetime. Lastly, for lighter masses, scalar fields produce much less energy than vector fields because of its longer emission timescale. Especially, for scalar masses of $m_b = 10^{-14}\,\mathrm{eV}$ and $10^{-13.5}\,\mathrm{eV}$, the background spectra do not even appear in the figure as their emission timescale is too long to emit the cloud energy during BH lifetime.

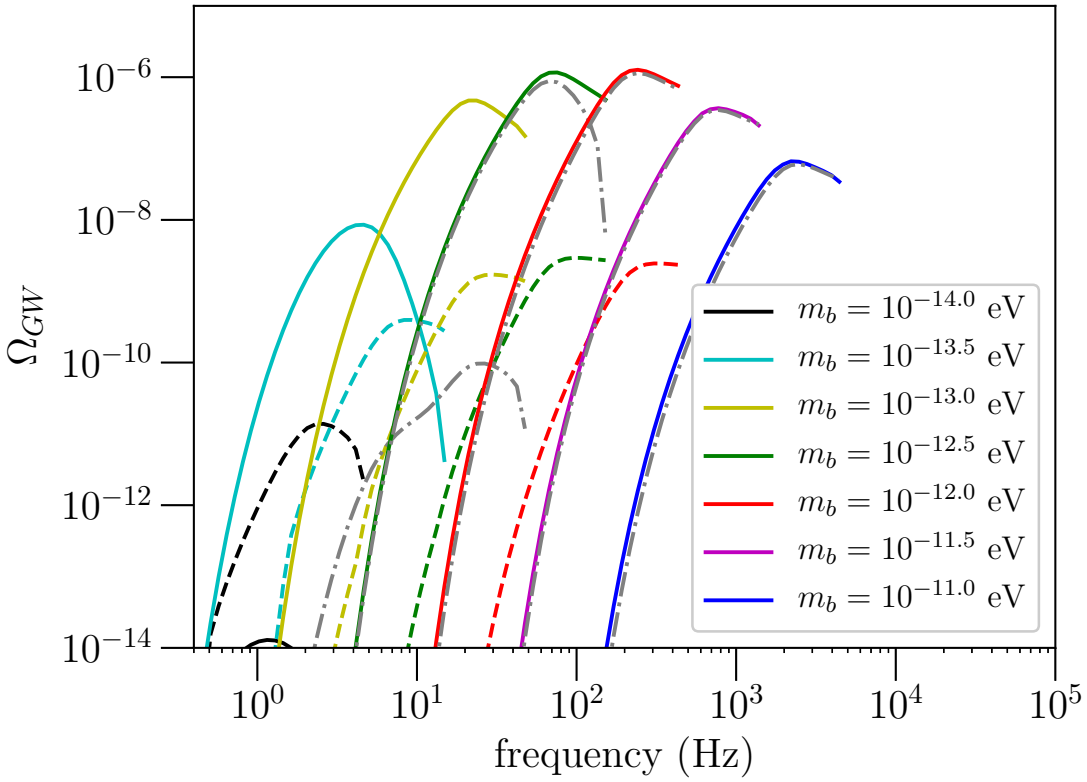

Figure 4.6: The comparison plot of energy density spectra between ultra-light scalar and vector fields. The solid curves in color represent the spectra produced from scalar fields through the isolated BH channel with an uniform distribution of $\chi \in [0, 1.0]$ and the dashed ones are through the BBH merger remnant channel. For comparison, the gray dashed-dot lines show the spectra produced from scalar boson including both of the two BH formation channels with the same BH mass range and spin distribution. Note that the spectra for scalar mass $m_b \geq 10^{-13.5}\,\mathrm{eV}$ are not shown in the figure as scalar fields with these masses emit GWs with a time scale much longer than typical BH lifetime. Also, the spectra of the BBH merger remnant channel for vector masses $m_b > 10^{-11.5}\,\mathrm{eV}$ (dashed lines in color) are strongly suppressed because these heavier vector bosons tend to couple with relatively lighter BHs such as $M_{\mathrm{BH}} < 10\,\mathrm{M}_\odot$.

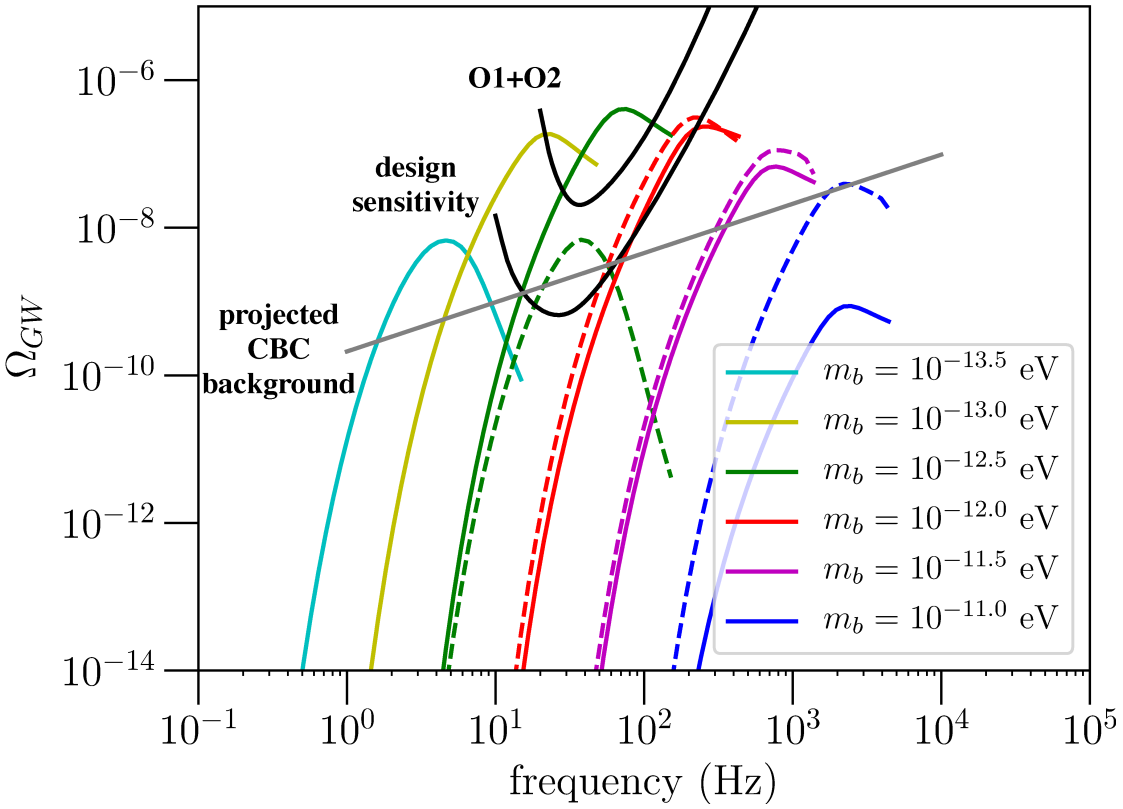

Figure 4.7: Energy density spectra produced from vector-cloud systems, comparing different GW emission modes. It is also plotted with the predicted CBC background and advanced LIGO power-law integrated curves similar to Figs. 4.2 and 4.3. The solid curves are the contribution from $m = 1$ mode for the isolated BH model with uniform distribution of $\chi \in [0, 0.8]$, whereas the dashed curves represent $m = 2$ mode.

4.4 Higher order mode

In general, superradiant instability occurs for different m modes of the unstable cloud. As shown in Eq. (3.55), the instability timescale for each mode differs typically by several orders of magnitudes and hence, the GW emission timescale correspondingly increase for higher modes. For the SGWB from ultra-light scalar fields, since the fundamental mode already has long emission timescale relative to the BH lifetime, the contribution of any higher modes to the total $\Omega_{\rm GW}(f)$ is expected to be negligible, and no such contribution is considered in Ref. [181]. Ultra-light vector fields, on the other hand, generally exhibit much quicker dynamics and the contribution from the higher modes could be non-negligible.

Fig. 4.7 shows the comparison between the energy density spectrum produced from $m = 1$ and 2 modes of the vector fields based on the isolated BH channel alone. One can see that the $m = 2$ mode tends to be dominant for relatively heavier masses. For a given m and BH mass range in our model, the critical BH spin increases with vector masses and reaches $\chi \approx 1$ for $m_b = 10^{-11}$ eV. The energy produced by instability scales

with the difference in the angular momentum of a BH between its initial and final states, $J_i - J_f$. For the $m = 1$ mode of those heavier vectors, this difference tends to be small or the initial BH spin can be lower than the critical value ($J_i < J_f$) and the instability does not even occur. Consequently, for such heavy vector bosons the contribution from the fundamental mode would be comparable or smaller than the $m = 2$ mode.

Chapter 5

Method

This chapter describes the statistical methodology we adopt for data analysis and a search for the boson cloud models. Generally speaking, statistical analysis encompasses two different approaches; frequentist statistics and Bayesian inference, each of which extracts conceptually different information from data. Frequentist statistics is meant to determine the probability of observing the data $\boldsymbol{d}$ under the null hypothesis labeled as H_0, $P(\boldsymbol{d}|H_0)$, whereas in a Bayesian inference the goal is to compute the probability of the hypothesis H being true conditioned by the observed data, namely the probability $P(H|\boldsymbol{d})$. Of these two approaches, this work has adopted Bayesian inference as many of the data-analysis researches in the field of GW astronomy has been tackled by use of Bayesian inference. [230] [231] [232]. Section 5.1 reviews the basics of Bayesian inference, based on [87], [230], [233]. In Section 5.2, we will apply the Bayesian framework to search for stochastic GW background following the pioneering work in Ref. [232].

5.1 Bayesian inference

The statistical analysis in a GW search mainly two-fold: parameter estimation and model selection between different hypotheses in light of the observed data (Section 5.1.2). The formalism of Bayesian inference deals with these problems by quantitatively representing the state of knowledge about a hypothesis H given data $\boldsymbol{d}$. The conditional probability of the hypothesis can be analyzed by Bayes' theorem, which states that

$$p(H|\boldsymbol{d}) = \frac{p(\boldsymbol{d}|H)p(H)}{p(\boldsymbol{d})}. \tag{5.1}$$

In this formula, $p(H|\boldsymbol{d})$ is the posterior probability of the hypothesis H being true for given data, $p(H)$ is the probability, called a prior, of the hypothesis H being true, one assumes or knows *a priori*, $p(\boldsymbol{d})$ is known as the evidence and acts as a normalizing constant, and $p(\boldsymbol{d}|H)$ is referred to as the likelihood, the probability to obtain $\boldsymbol{d}$ under the hypothesis H.

5.1.1 Parameter estimation

In practice, GW signals cannot be labeled only by its signal-present hypothesis H but rather characterized by a set of parameters $\boldsymbol{\theta} = [\theta_1, ..., \theta_N]$. In other words, one needs to not only detect a signal but also estimate the parameters the signal model involves. In the framework of Bayesian inference, that requires the posterior probability distribution defined in sub-hypothesis $H_{\boldsymbol{\theta}}$, that is, the signal characterized purely by $\boldsymbol{\theta}$ is present in the data. Therefore, parameter estimation is performed making use of Bayes' theorem discussed above, which can be extended to the sub-hypothesis $H_{\boldsymbol{\theta}}$ [230], [233],

$$p(H_{\boldsymbol{\theta}}|\boldsymbol{d}, H) = \frac{L(\boldsymbol{d}|H_{\boldsymbol{\theta}}, H)\pi(H_{\boldsymbol{\theta}}|H)}{Z(\boldsymbol{d}|H)}, \tag{5.2}$$

where $p(H_{\boldsymbol{\theta}}|\boldsymbol{d}, H)$ is the posterior probability on the multidimensional space, $L(\boldsymbol{d}|H_{\boldsymbol{\theta}}, H)$ is the likelihood, $\pi(H_{\boldsymbol{\theta}}|H)$ is the prior probability and $Z(\boldsymbol{d}|H)$ is the Bayesian evidence equivalent to the likelihood in Eq. (5.1). When one needs to only evaluate the posterior probability distribution of the given parameters, the evidence can be treated as the normalization constant and the posterior can be derived by rescaling the numerator of the right hand side of Eq. (5.2) without exactly evaluating these two functions. When inferring a specific parameter, let's say θ_1, from the multi-dimensional posterior distribution obtained above, one looks at the one-dimensional marginalized posterior of θ_1, which reads

$$p(\theta_1|\boldsymbol{d}, H) = \int p(H_{\boldsymbol{\theta}}|\boldsymbol{d}, H)\, \mathrm{d}\theta_2 ... \mathrm{d}\theta_N. \tag{5.3}$$

Using this probability distribution, one can estimate the parameter θ_1 by computing a credible interval at $\alpha\%$ level such that

$$\alpha = \int_{\theta_a}^{\theta_b} p(\theta_1|\boldsymbol{d}, H)\, \mathrm{d}\theta_1. \tag{5.4}$$

Note that given the confidence level α there remains a degree of freedom of where to choose the interval in a parameter space. It is customary to define it as a symmetric interval around the median or maximum of the posterior probability distribution.

5.1.2 Model selection

In the context of parameter estimation discussed above, one does not necessarily compute the evidence $p(\boldsymbol{d}|H)$ because it is taken as the normalizing factor which can be ignored for computing the posterior. On the other hand, the evidence actually plays an essential role in a situation where one needs to assess which model is more preferred over the other models based on the observed data.

Suppose that one observes the data $\boldsymbol{d}$ and tries to perform a model selection between H_0 and H_1. Relative probability of one model being more likely to explain the data

compared to the other is encoded by the odds ratio defined as

$$\frac{p(H_1|\boldsymbol{d})}{p(H_0|\boldsymbol{d})} = \frac{p(\boldsymbol{d}|H_1)\pi(H_1)}{p(\boldsymbol{d}|H_0)\pi(H_0)}, \tag{5.5}$$

where $p(\boldsymbol{d}|H_{0/1})$ is the evidence for each model respectively, and $\pi(H_1), \pi(H_0)$ are the prior probability of each hypothesis being true.

Due to the overall normalization of the posterior probability

$$\int p(H_{\boldsymbol{\theta}}|\boldsymbol{d}, H)\, \mathrm{d}^D\boldsymbol{\theta} = 1, \tag{5.6}$$

the Bayesian evidence can be expressed such that

$$Z(\boldsymbol{d}|H) = \int L(\boldsymbol{d}|H_{\boldsymbol{\theta}}, H)\pi(H_{\boldsymbol{\theta}}|H)\, \mathrm{d}^D\boldsymbol{\theta}. \tag{5.7}$$

This expression implements the idea that a model with fewer parameters tends to provide a larger evidence than one with more parameters, which is widely known as "Occam's razor". The practical issue that often rises here is that it is computationally challenging to perform a numerical integration (5.7) over the multi-dimensional grids (e.g. 15 dimensional parameter space for a typical CBC analysis), so there have been several efficient algorithms employing a Monte-Carlo sampling, one of which we will describe in the subsequent subsection.

5.2 Bayesian analysis for a stochastic background

Conventionally, the analysis for a SGWB has been conducted in the context of frequentist statistics as reviewed in Section 2.1, namely one computes the point estimate of SNR as detection statistics. For example, the isotropic SGWB search conducted by LVC [83], [84] produced upper limits on the reference amplitude Ω_α of a power-law spectrum such as

$$\Omega_{\mathrm{gw}}(f) = \Omega_\alpha \left(\frac{f}{f_*}\right)^\alpha \tag{5.8}$$

under several choices of the spectral index α. This procedure can only estimate the reference amplitude Ω_α since that is the parameter that can be directly derived by optimal filtering for fixed value of α. However, we do not always assume the power-law spectrum model and even if we do, it is not possible to simultaneously estimate multiple parameters: α and Ω_α. Subsequently, Ref. [232] introduced a Bayesian framework to provide a more general way of parameter estimation that can be used for an arbitrary $\Omega_{\mathrm{gw}}(f)$ model.

Building on this idea, we develop an analysis software to search for the SGWB signals from the superradiant instability. Fig. 5.1 is the flow chart between the LIGO

detectors and the output of our pipeline and shows that the developed pipeline consists of a sampling software and a SGWB model for which the likelihood function is evaluated, and produce output data. Regarding the SGWB model, we adopt the boson cloud model described in Section 4, although for a general use of the pipeline this model could be arbitrary, e.g. CBC background model. Also, it takes the cross-correlation estimator computed from two data stream of the LIGO detectors as an input data and runs the sampling software to construct a posterior distribution. As discussed in the above subsection, this way allows us to not only make an estimate on multiple parameters but also claim a detection and perform a model selection test. In what follows, we provide more specific formulation applied to this analysis.

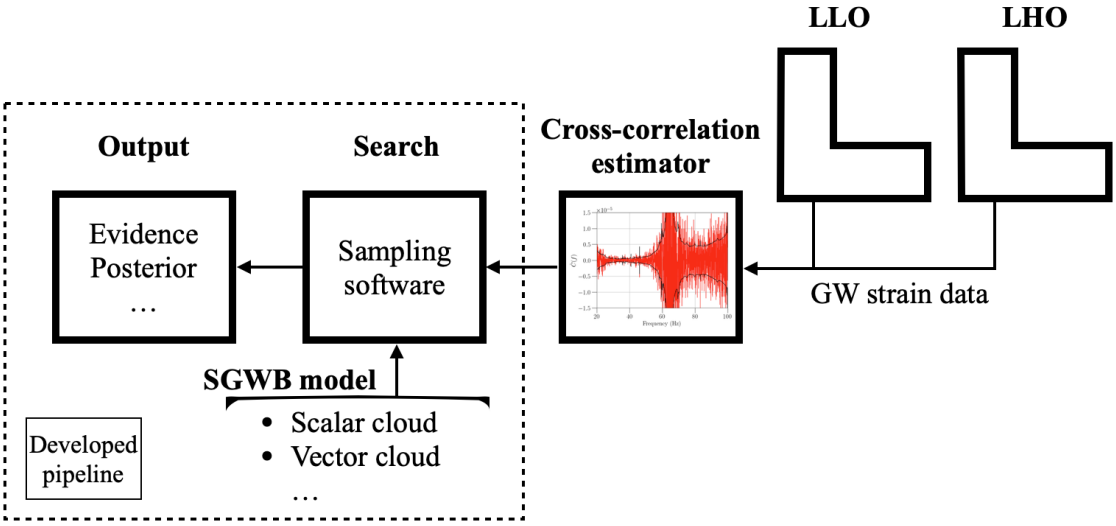

Figure 5.1: The schematic cartoon describing the entire data flow from the LIGO detectors [Hanford (LHO) and Livingston (LLO) observatories] the cross-correlation estimator and our developed pipeline.

5.2.1 Setup

Unlike the broadband estimator defined in Eq. (2.49), one can construct estimators for individual frequency bins from cross-correlation data [234]. Here, we define it as

$$\hat{Y}(f) \equiv \frac{20\pi^2}{3H_0^2} f^3 \tilde{s}_1^*(f)\tilde{s}_2(f), \tag{5.9}$$

which is normalized so that its mean is

$$\langle \hat{Y}(f) \rangle = \gamma(f)\Omega_{\rm gw}(f). \tag{5.10}$$

Then its variance reads

$$\sigma^2(f) = \frac{1}{2T\Delta f}\left(\frac{10\pi^2}{3H_0^2}\right)^2 f^6 P_1(f)P_2(f) \tag{5.11}$$

using the result of Eqs. (2.60) and (2.66) under the strong-signal approximation. [1]

The corresponding broadband estimator is derived from $\hat{Y}(f)$ and $\sigma^2(f)$ as follows

$$\hat{Y} \equiv \frac{\sum_f \hat{Y}(f)w(f)/\sigma^2(f)}{\sum_f w(f)/\sigma^2(f)}, \tag{5.14}$$

where $w(f)$ is a linear filter formed by hypothesized energy density spectrum $\Omega_m(f)$ so that

$$w(f) = \gamma(f)\Omega_m(f). \tag{5.15}$$

Once the broadband estimator is constructed, SNR can be computed similarly to Section 2.3,

$$\mathrm{SNR} = \frac{\langle\hat{Y}\rangle}{\sigma} \tag{5.16}$$

where

$$\langle\hat{Y}\rangle = \frac{\sum_f \gamma(f)\Omega_{\rm gw}(f)w(f)/\sigma^2(f)}{\sum_f w(f)/\sigma^2(f)} \tag{5.17}$$

$$\sigma^2 = \frac{\sum_f w^2(f)/\sigma^2(f)}{\left(\sum_f w(f)/\sigma^2(f)\right)^2}. \tag{5.18}$$

Here $\Omega_{\rm gw}(f)$ is a true background the observed data contains. Therefore, in the limit this can be written as

$$\mathrm{SNR} = \frac{\left(\langle\hat{Y}\rangle|\gamma(f)\Omega_m(f)\right)}{\sqrt{(\gamma(f)\Omega_m(f)|\gamma(f)\Omega_m(f))}}, \tag{5.19}$$

using the inner product

$$(A|B) \equiv \left(\frac{3H_0^2}{10\pi^2}\right)^2 2T\int_0^\infty \frac{\tilde{A}^*(f)\tilde{B}(f)}{f^6 P_1(f)P_2(f)}\,\mathrm{d}f. \tag{5.20}$$

[1] One should note that this estimator differs from the conventional one by a factor of $\gamma(f)$. This is due to its convenience in the context of a search for non-general-relativity polarization components, each of which has different $\gamma(f)$. For example, for the total energy density spectrum consisting of tensor, vector and scalar polarizations,

$$\Omega_{\rm gw}(f) = \Omega^T(f) + \Omega^V(f) + \Omega^S(f), \tag{5.12}$$

the estimator is constructed such that

$$\langle\hat{Y}(f)\rangle = \gamma_T(f)\Omega^T(f) + \gamma_V(f)\Omega^V(f) + \gamma_S(f)\Omega^S(f). \tag{5.13}$$

This decoupled linear expression among different polarizations makes it easier to perform Bayesian analysis. Nevertheless, GW polarizations are beyond the scope of this work, so hereafter the summation over different polarizations will be dropped for simplicity.

One can see that the expression Eq. (5.19) generalizes the definition of SNR to arbitrary signal model. From (5.19), when the hypothesized background exactly matches with the true background $w(f) = \gamma(f)\Omega_{\rm gw}(f)$, SNR is maximized to be

$$\mathrm{SNR}_{\rm opt} = \Big(\gamma(f)\Omega_{\rm gw}(f)|\gamma(f)\Omega_{\rm gw}(f)\Big), \tag{5.21}$$

which reproduces the conventional expression of optimal SNR (see Eq. (2.76)).

5.2.2 Model selection

As described in 5.1.2, model selection can be performed by an odds ratio

$$O^{\mathcal{A}}_{\mathcal{B}} = \frac{p(\mathcal{A}|\hat{Y})}{p(\mathcal{B}|\hat{Y})} = \frac{Z(\{\hat{Y}\}|\mathcal{A})}{Z(\{\hat{Y}\}|\mathcal{B})}\frac{\pi(\mathcal{A})}{\pi(\mathcal{B})} \approx \frac{Z(\{\hat{Y}\}|\mathcal{A})}{Z(\{\hat{Y}\}|\mathcal{B})} \tag{5.22}$$

where $Z(\{\hat{Y}\}|\mathcal{A}), Z(\{\hat{Y}\}|\mathcal{B})$ are the Bayesian evidence for the hypotheses $\mathcal{A}, \mathcal{B}$ respectively. Also $\pi(\mathcal{A})/\pi(\mathcal{B})$ is prior probability ratio between the two models, which we set as unity in this work as we do not prefer one model over the other *a priori*. Therefore, the odds ratio is fully characterized by the ratio of the Bayesian evidences, known as "Bayes factor" and in the subsequent chapter we will discuss the statistical preference between multiple hypotheses based on the Bayes factor. Also, following the convention found in [235], we set the Bayes factor of 8 as the threshold to prefer one model over the other. The evidence is given by

$$Z(\{\hat{Y}\}|\mathcal{A}) = \int L(\{\hat{Y}\}|\boldsymbol{\theta}_{\mathcal{A}}, \mathcal{A})\pi(\boldsymbol{\theta}_{\mathcal{A}}|\mathcal{A})\,\mathrm{d}^D\boldsymbol{\theta}_{\mathcal{A}}. \tag{5.23}$$

As mentioned previously, it is practical to perform Monte-Carlo sampling to carry out this integration. Specifically our pipeline adopts a `PYMULTINEST` package, which is a python wrapper of a nested sampling software `MULTINEST`. See Appendix. B for the details of the nested sampling algorithm. One needs to calculate the joint likelihood over frequency bins

$$L(\{\hat{Y}\}|\boldsymbol{\theta}_{\mathcal{A}}, \mathcal{A}) = \prod_f L(\hat{Y}(f)|\boldsymbol{\theta}_{\mathcal{A}}, \mathcal{A}), \tag{5.24}$$

where $L(\hat{Y}(f)|\boldsymbol{\theta}_{\mathcal{A}}, \mathcal{A})$ is the likelihood of a single measured $\hat{Y}(f)$ defined as

$$L(\hat{Y}(f)|\boldsymbol{\theta}_{\mathcal{A}}, \mathcal{A}) \equiv \frac{1}{\sqrt{2\pi\sigma^2(f)}}\exp\left(-\frac{\Big[\hat{Y}(f) - \gamma(f)\Omega_m(f;\boldsymbol{\theta}_{\mathcal{A}})\Big]^2}{2\sigma^2(f)}\right). \tag{5.25}$$

$\Omega_m(f;\boldsymbol{\theta}_{\mathcal{A}})$ is the energy density spectrum of hypothesis $\mathcal{A}$. In a complicated hypothesis that data contain several models $\Omega_i(f)$, the total energy density spectrum is expressed as the linear combination of those spectra

$$\Omega_m(f) = \sum_i \Omega_i(f). \tag{5.26}$$

From (5.24) and (5.25), it follows that

$$L(\{\hat{Y}\}|\theta_{\mathcal{A}},\mathcal{A}) = \left(\prod_f \frac{1}{\sqrt{2\pi\sigma^2(f)}}\right)\exp\left\{-\sum_f \frac{\left[\hat{Y}(f)-\gamma(f)\Omega_m(f;\boldsymbol{\theta}_{\mathcal{A}})\right]^2}{2\sigma^2(f)}\right\}. \tag{5.27}$$

Note that Eqs. (5.11) and (5.20) imply that the SNR (5.19) uniquely determines the broadband likelihood function as follows:

$$L(\{\hat{Y}\}|\theta_{\mathcal{A}},\mathcal{A}) \propto \exp\left\{\left(\langle\hat{Y}\rangle|\gamma(f)\Omega_m(f)\right)\right\} \tag{5.28}$$

$$= \mathrm{e}^{-\mathrm{SNR}}. \tag{5.29}$$

Here we take the assumed signal spectrum to be normalized so that

$$(\gamma(f)\Omega_m(f)|\gamma(f)\Omega_m(f)) = 1. \tag{5.30}$$

Eventually the obtained evidence is used to perform model selection between noise and signal hypotheses or between different signal models.

5.2.3 Parameter estimation

From the Bayes' theorem, the posterior distribution for a set of parameters $\boldsymbol{\theta}_{\mathcal{A}}$ under the hypothesis $\mathcal{A}$ is

$$p(\boldsymbol{\theta}_{\mathcal{A}}|\{\hat{Y}\},\mathcal{A}) = \frac{L(\{\hat{Y}\}|\boldsymbol{\theta}_{\mathcal{A}},\mathcal{A})\pi(\boldsymbol{\theta}_{\mathcal{A}}|\mathcal{A})}{Z(\{\hat{Y}\}|\mathcal{A})}. \tag{5.31}$$

Therefore, once the evidence is derived, posterior probability can be easily computed. Subsequently, the nested sampling algorithm generates a set of posterior samples and we use this set of posterior samples to estimate parameters in the boson cloud model.

Chapter 6

Results and Discussion

This chapter provides the main results of our studies involving software injections of background spectra predicted from the boson cloud models in Section. 4. Our pipeline is capable of injecting a theoretical background spectrum into synthesized Gaussian noise or real observed data and recovering the injected parameter values from their inferred posterior. Through this injection and recovery procedure, we assess the boson mass range that can be probed by the detection of the SGWB and the ability of model selection between the boson cloud models and fiducial CBC background model. Finally, Section. 6.5 provides the search results for the ultra-light bosons using the first and second advanced LIGO's observing runs.

6.1 Injection scheme and signal recovery

Figs. 4.2 and 4.3 illustrate that the background spectrum for the both scalar and vector bosons with the mass of $m_b \sim 10^{-13}$ eV could be detected by future or even current sensitivity of advanced LIGO. In order to assess this possibility quantitatively, we perform injection studies using the predicted background spectra of the boson cloud models.

Here we first discuss the overview of the injection scheme we adopted in our study, following the method in Ref. [181]. Particularly, when producing synthetic data for a given power spectrum density of GW detectors, one analytically computes the variance, $\sigma^2(f)$, of a cross-correlation estimator given by Eq. (5.11). A Gaussian noise is then synthesized based on the variance. The SGWB predicted from the boson cloud models is injected into this synthesized noise on the frequency domain. Thus, the cross-correlation estimator including an injected spectrum reads

$$\hat{C}_{\rm sim}(f) = \gamma_{\rm HL}(f)\Omega_{\rm inj}(f;\boldsymbol{\theta}_{\rm inj}) + \sigma(f)\hat{n}. \tag{6.1}$$

We consider only the advanced LIGO detector pair, i.e., the Hanford and Livingston detectors in our study for simplicity. $\gamma_{\rm HL}(f)$ is the overlap reduction function [236] for

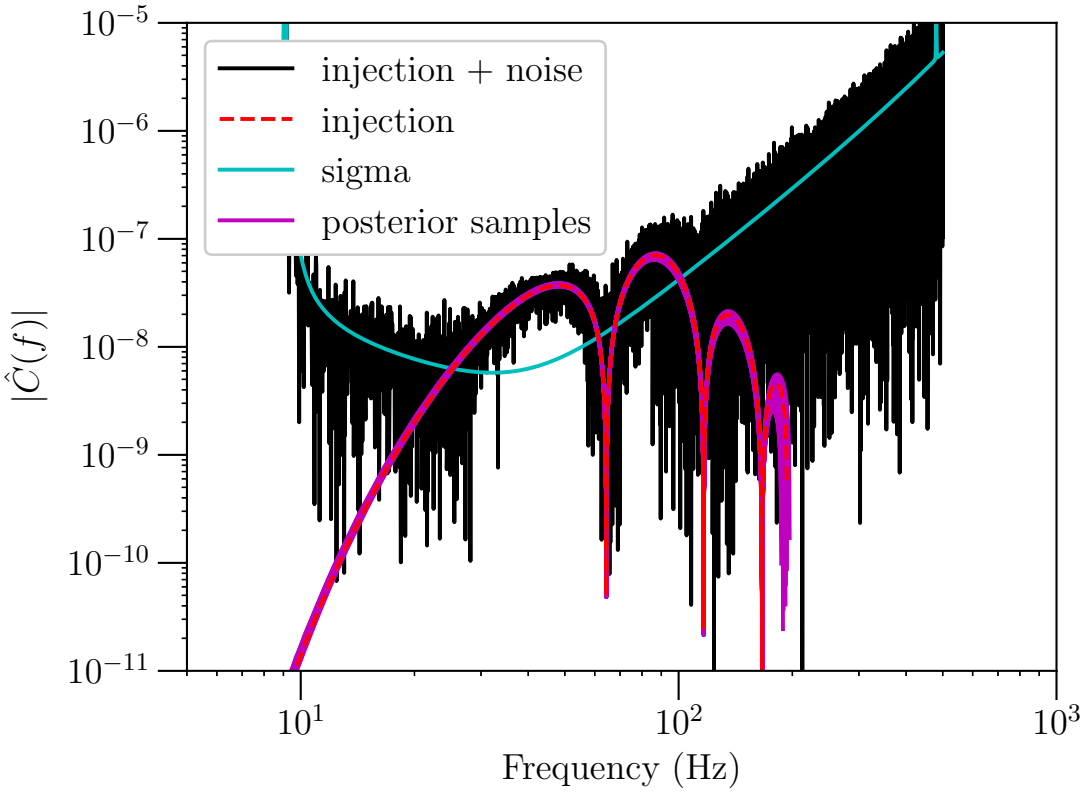

Figure 6.1: Cross-correlation estimator $\hat{C}_{\rm sim}(f)$ as a function of frequency (black), computed from a synthesized data with the simulated SGWB of superradiant instabilities of ultra-light scalar bosons injected. The cyan curve is 1-σ amplitude of $\hat{C}_{\rm sim}(f)$ derived from the design sensitivity assuming three years of observation. The red dashed line represents the injected background spectrum. This injection has SNR $\sim$ 145 and corresponds to the scalar cloud model with $m_{\rm b} = 4 \times 10^{-13}$ eV and $\chi_{\rm ul} = 0.8$. The magenta region is an ensemble of $\Omega_{\rm GW}$ of the scalar cloud model evaluated with 100 samples randomly drawn from the inferred posterior.

the baseline that consists of the two detectors, $\boldsymbol{\theta}_{\rm inj}$ is a set of the parameters characterizing a boson cloud model, from which the injected background spectrum $\Omega_{\rm inj}(f; \boldsymbol{\theta}_{\rm inj})$ is constructed. $\hat{n}$ is a random variable drawn from a normal distribution.

Figs. 6.1 and 6.2 are examples of the cross-correlation estimator $\hat{C}_{\rm sim}(f)$ plotted from 9 Hz to 500 Hz with an injection of a background spectrum computed for scalar and vector cloud models. The cyan lines are the standard deviation, $\sigma(f)$, which simulates 3-year observation of the advanced LIGO detectors with its projected design sensitivity (see Figs. 6.1 and 6.2). The red dashed line in each figure show the injected background spectrum, which has the expected SNR $\sim$ 145 (scalar boson model) and 20 (vector boson model) with an injected boson mass of $m_b = 4 \times 10^{-13}$ eV and 4.6×10^{-13} eV, respectively. In the both cases, we assume an uniform distribution from 0 to 0.8 (namely, $\chi_{\rm ll} = 0, \chi_{\rm ul} = 0.8$) for BH an initial spin in the isolated BH population.

To infer the model parameters $\boldsymbol{\theta}_{\rm inj}$, the simulated cross-correlation estimator (the black curve in the Figs. 6.1 and 6.2) is used to evaluate the likelihood. Our pipeline

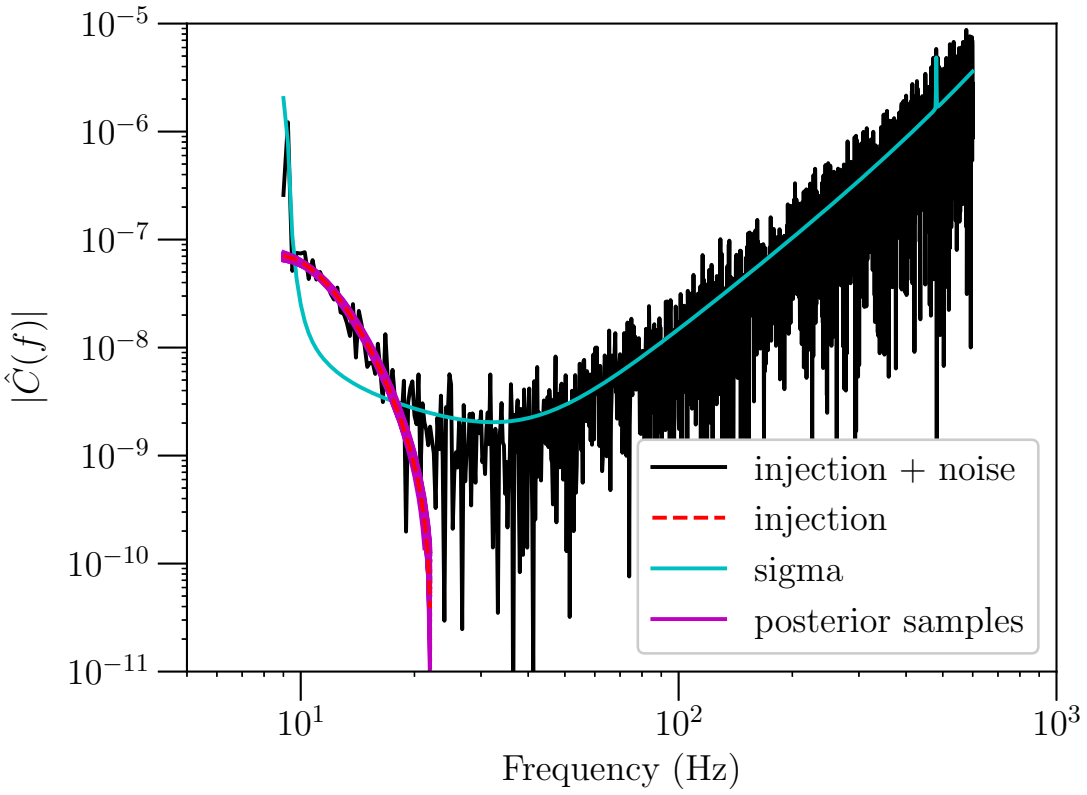

Figure 6.2: Cross-correlation estimator $\hat{C}_{\rm sim}(f)$ as a function of frequency (black), computed from a synthesized data with the simulated SGWB of superradiant instabilities of ultra-light vector bosons injected. The cyan curve is 1-σ amplitude of $\hat{C}_{\rm sim}(f)$ derived from the design sensitivity assuming three years of observation. The red dashed line represents the injected background spectrum. This injection has SNR ~ 145 and corresponds to the vector cloud model with $m_{\rm b} = 4 \times 10^{-13}$ eV and $\chi_{\rm ul} = 0.8$. The magenta region is an ensemble of $\Omega_{\rm GW}$ of the vector cloud model evaluated with 100 samples randomly drawn from the inferred posterior.

package adopts the nested sampling algorithm implemented through `PyMultiNest` and explore the parameter space defined by the model parameters $\boldsymbol{\theta}$ to construct a Bayesian posterior. The magenta region in each of Figs. 6.1 and 6.2 represents an ensemble of background spectra of each model evaluated with 100 sets of the model parameters randomly drawn from the inferred posterior whose detail is discussed in the following paragraphs. We note that the simulated estimator the expected variance of noise data or the injected spectrum where it is above the noise variance and that the drawn posterior sample correspond to the spectra lying mostly near the injection. Therefore, these figures illustrate that the simulated estimator properly reflects the injected background and the inferred posterior produce samples consistent with the injections.

Figs. 6.3 and 6.4 show the resulting Bayesian posteriors estimated from the simulated observations of the injections shown in Figs. 6.1 and 6.2. For the both cases, we adopt $\chi_{\rm ul}$ parametrization of an initial spin distribution in the isolated BH population. In this parameterization, the upper limit of the distribution $\chi_{\rm ul}$ is set as a free parameter to estimate, while the lower limit $\chi_{\rm ll}$ is fixed to be 0, being consistent with the injections. We adopt a log-uniform prior for m_b across the range 10^{-14} eV to 10^{-11} eV and a uniform prior of $\chi_{\rm ul}$ between 0 and 1 for both types of scalar and vector cloud model. Each blue dot represents a sample of the posterior distribution and the two contours indicate 2 and 3-σ credible region, respectively. The star markers pinpoint the true parameter set of each injection, which lies within the contours respectively. The log bayes factor estimated for these recovered injections are approximately 2800 (scalar boson model) and 500 (vector boson model), which are roughly consistent with the expected SNRs. These figures illustrate that the analysis pipeline can infer the parameters of a loud injection to the precision of $O(1)\%$. Appendix C provides the result of our statistical test conducted for the parameter estimation consistency.

6.2 Sensitive range of boson masses

To evaluate the boson mass range we can potentially probe through a detection of the boson cloud SGWB, we make 500 injections, following the procedure in Section. 6.1, and compute their Bayes factors between the signal and noise hypotheses. For every injection, we assume an uniform distribution from 0 to 0.8 (namely, $\chi_{\rm ul} = 0.8$ in the $\chi_{\rm ul}$ parameterization) for an BH initial spin in the isolated BH population. The injected m_b values are log-uniformly drawn from the range 10^{-14} eV to 10^{-11} eV.

For the injection recovery under the signal hypothesis, $\mathcal{S}$, being consistent with the injections, we adopt $\chi_{\rm ul}$ parameterization. The data are also analyzed under the noise hypothesis, $\mathcal{N}$, and, assuming the equal prior probability for each hypothesis, the Bayes

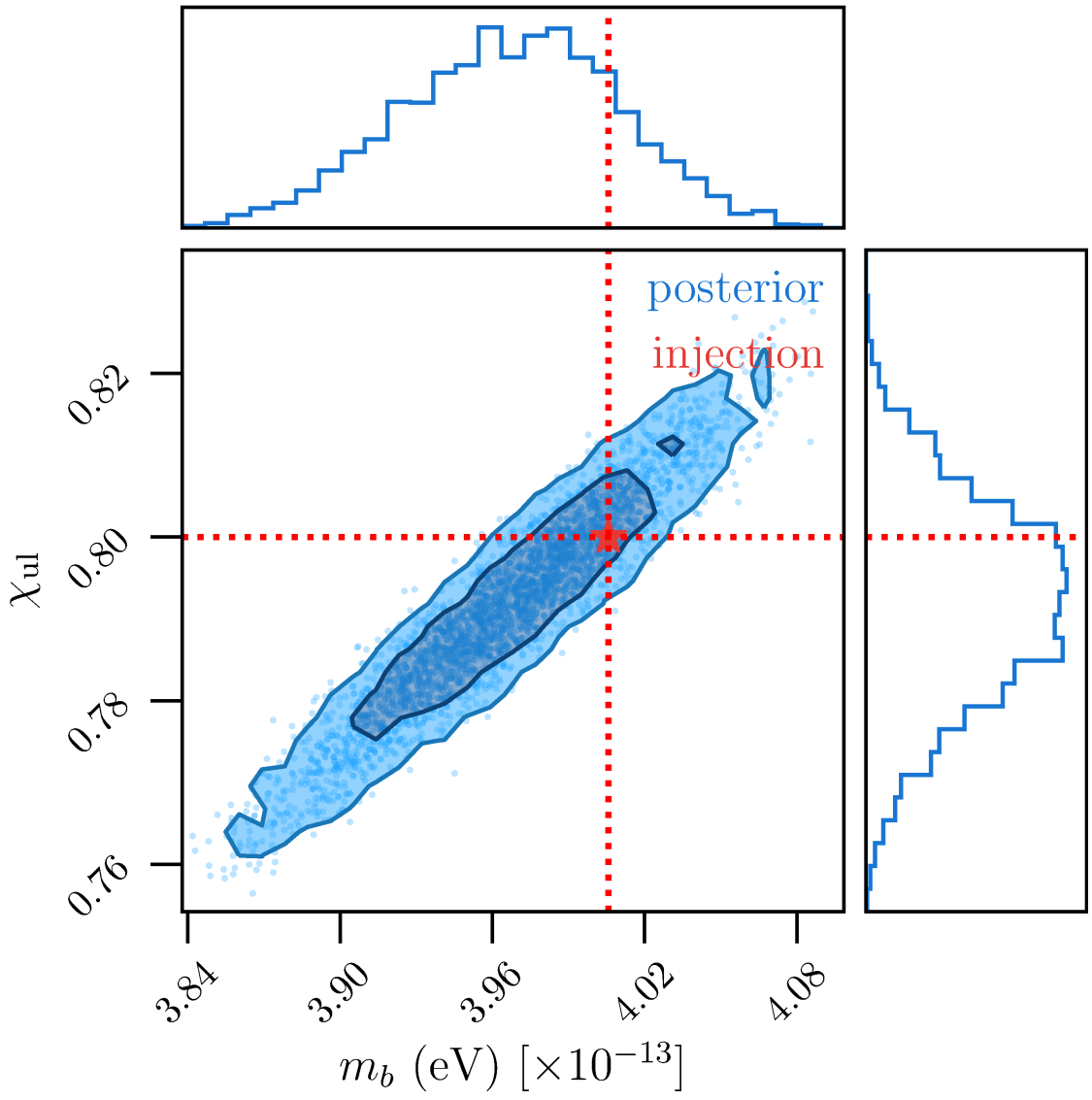

Figure 6.3: Posterior samples recovered for the injection of scalar cloud model $\Omega_{\rm inj}(f;\boldsymbol{\theta})$ shown in Fig. 6.1. We adopt a uniform prior for m_b across the range 10^{-13} eV to 10^{-12} eV and a uniform prior for $\chi_{\rm ul}$ between 0 and 1. Each blue dot represents a sample of the posterior distribution and the two contours indicate 2 and 3-σ credible region. The star marker pinpoints the true parameter set of each injection, which lies within the contour. The log bayes factor estimated for these recovered injections are approximately 2800.

factor is defined as

$$\ln \mathcal{O}_{\mathrm{N}}^{\mathrm{SIG}} \equiv \ln \left\{ \frac{Z(\{\hat{C}_{\mathrm{inj}}\}|\mathcal{S})}{Z(\{\hat{C}_{\mathrm{inj}}\}|\mathcal{N})} \frac{p(\mathcal{S})}{p(\mathcal{N})} \right\} = \ln \left\{ \frac{Z(\{\hat{C}_{\mathrm{inj}}\}|\mathcal{S})}{Z(\{\hat{C}_{\mathrm{inj}}\}|\mathcal{N})} \right\}. \tag{6.2}$$

We repeat this procedure for each injection and plot in Figs. 6.5 and 6.6 the Bayes factor for the injections as a function of injected boson mass values. As mentioned previously, we define the injections above a log Bayes factor of 8 as detected and indicate the threshold in each the two figures with a red horizontal line. The m_b range in which a log Bayes factor for the injections is larger than 8 can be interpreted as the sensitive range of boson masses, which is around 1.8×10^{-13} eV to 7.5×10^{-13} eV for scalar bosons and 0.4×10^{-13} eV to 9.4×10^{-13} eV for vector bosons. The range for vector bosons is wider than that for scalar bosons because the predicted background spectrum for $m_b \sim 10^{-13}$ eV in the vector boson cloud model is enhanced significantly due to their shorter emission timescale compared to scalar bosons. Also, note that the sensitive mass range actually depends on spin parameter χ_{ul}, e.g. $\chi_{\mathrm{ul}} = 0.8$ in our study. Since larger χ_{ul} simply shifts up the spectrum amplitude overall, that leads to a wider detectable range of boson masses for a larger χ_{ul}.

6.3 Model selection study

As can be seen in Fig. 4.7, the SGWB signal from the boson cloud model can dominate over that from the projected CBC background for some parameter space of boson masses and BH spins. Given the boson mass in the detectable range it would be likely to detect the SGWB from *both* the boson cloud and CBC models. Thus, the next question to address is "Given a detected SGWB signal, can we distinguish these two models from one another?" In the following, we evaluate the capability to distinguish the models based on the Bayesian framework in Section 6.3.

While in the previous subsection we assess the detectability of each boson cloud signal alone, we consider a signal model that consists of the components from both the boson cloud (BC) and the projected CBC background, which reads

$$\Omega_{\mathrm{inj}}(f;\boldsymbol{\theta}) = \Omega_{\mathrm{inj}}^{\mathrm{BC}}(f;\boldsymbol{\theta}) + \Omega_{\mathrm{inj}}^{\mathrm{CBC}}(f). \tag{6.3}$$

$\Omega_{\mathrm{inj}}^{\mathrm{BC}}(f;\boldsymbol{\theta})$ is the background due to boson clouds under the χ_{ul} parametrization given by Eq. (4.21), and $\Omega_{\mathrm{inj}}^{\mathrm{CBC}}(f)$ is the fixed CBC background approximated as a power-law spectrum such that

$$\Omega_{\mathrm{GW}}^{\mathrm{CBC}}(f) = 1.8 \times 10^{-9} \left(\frac{f}{25\mathrm{Hz}} \right)^{2/3}, \tag{6.4}$$

as inferred from Ref. [132]. Note that, assuming the design sensitivity of advanced LIGO with three-year observation, $\Omega_{\mathrm{inj}}^{\mathrm{CBC}}(f)$ alone can be detected with a log Bayes

factor of 8.8 for a CBC-only hypothesis against a noise hypothesis, corresponding to an SNR of 5.5.

Using a simulation of the combined background spectrum expressed in Eq. (6.3), we analyze synthesized data based on two different models: a CBC-only model and a joint BC and CBC model (BC+CBC). For signal recovery, we parametrize the CBC background with a power-law index and an amplitude at the reference frequency 25Hz, which reads[1],

$$\Omega_{\rm rec}^{\rm CBC}(f;\Omega_0,\alpha) \equiv \Omega_0 \left(\frac{f}{25{\rm Hz}}\right)^{\alpha}. \tag{6.5}$$

Also, a prior for Ω_0 (or α) is set to be a log-unifor (uniform) distribution in the range of $[10^{-10} - 10^{-17}]([-5 - 5])$ respectively, while the priors for m_b and $\chi_{\rm ul}$ are identical to those described in Section 6.1. Table 6.1 summarizes the sets of parameters we consider for each signal model in this study.

Models	CBC-only	VC+CBC
Parameters	Ω_0, α	$m_b, \chi_{\rm ul}, \Omega_0, \alpha$

Table 6.1: Parameters in each recovered background model.

While the scalar cloud model we consider here includes both the isolated BH and BBH remnant populations, the vector cloud model ignores the latter channel for for the computational convenience. Since the BBH remnant channel is subdominant for vector boson masses of interest (see Fig. 4.6) and below the projected CBC background, we do not expect the inclusion of the additional channel would change the results significantly. Being consistent with the injected signal, we adopt the $\chi_{\rm ul}$ parametrization for $p(\chi)$.

As a measure of signal signature for boson clouds compared to CBC population, for every injection we compute a log Bayes factor (BF) between the two hypotheses, $\ln \mathcal{O}^{\rm BC}_{\rm CBC}$. The larger Bayes factors would imply that the observed data are better fit into the BC+CBC model and suggests the signature of the SGWB from boson clouds with statistical significance. We repeat this computation, varying injected $(m_b, \chi_{\rm ul})$ values until we explore a grid over the entire prior space. Figs. 6.7 and 6.8 are a gray-scale maps of a log Bayes factor for scalar and vector cloud model, respectively, with two contours of ln(BF) = 8 (magenta) and 0 (cyan). The two figures indicate that, over the parameter space inside the magenta contour, one can confidently claim the detection of each boson cloud background even in the presence of the CBC background. Similarly to

[1]We note that although Eq. (6.5) is generally called a "power-law spectrum model", not a simulated CBC background, Refs. [237], [238] show that with the current sensitivity of GW detectors the systematic error potentially caused by this bias is below the statistical error and hence would not affect the detectability of the background.

the detectability of the boson cloud background alone discussed in the Section. 6.2, the parameter space where the vector cloud background is detectable is larger, especially down to $m_b \sim 10^{-13}$ eV, than the scalar cloud model.

6.4 Search for the BBH merger remnant component

Figs. 4.6 and 4.7 imply that at the LIGO's design sensitivity the merger BBH remnant alone might be detectable. Even if not detected, we would be able to place more robust constraints on boson masses compared to the case where the isolated BH population is included in the signal model. Given the observational constraints on the local BBH merger rate and BBH mass function, the BBH merger remnant population suffer less from astrophysical uncertainties compared to the isolated BH population model involving the BH formation rate and the initial spin distribution. To assess this possibility, similar simulations using the LIGO's design sensitivity with and without an injection are performed to search for the BBH remnant component alone. With the injection of the SGWB for $m_b = 10^{-13}$ eV, we found the injection with the Bayes factor of 10.4, and hence we could claim that the SGWB from the BBH population is barely detected. Fig. 6.9 represents the 1-D posterior distribution for the vector mass, which consistently recovered the injected vector. On the other hand, without the injection we exclude the vector mass of 4×10^{-14} eV to 5×10^{-13} eV at the 95% confidence level. Although due to a computational challenge we leave the model selection test between the BBH merger remnant component and CBC background model as future work, these results indicate that we will potentially be able to make more robust detection or constraint on the vector mass by probing the BBH remnant signal model.

6.5 Advanced LIGO's O1+O2 analysis

We present the results of a search for a SGWB based on each boson cloud model using the cross-correlation estimators obtained from O1 and O2 of advanced LIGO. LIGO conducted O1 from September 18, 2015 15: 00 UTC to January 12, 2016 16: 00 UTC and O2 from 16: 00: 00 UTC on November 30, 2016 to 22: 00: 00 UTC on August 25, 2017. Only the two LIGO detectors operated during O1, while in O2 Virgo detector started collecting data from August 2017 apart from the LIGO detectors. However, given the shorter duration of Virgo's operation and its subdominant sensitivity, the Virgo detector hardly contributes to the overall SGWB search. Therefore, following the approach taken in the LVC's O2 SGWB analysis [84], [86] we do not include its observed data in this analysis.

For both O1 and O2, the cross-correlation estimators were computed from the Fourier transform of segments with a duration of 192 s weighted by 50% Hann windows and af-

terward six adjacent frequency bins were combined to obtain the frequency resolution of $1/32$ Hz over the frequency range of 20-1726 Hz. In the process of computing the estimators, time segments are removed from the dataset when the detectors were operating in an unstable configuration or when known GW signals were detected. Additionally, non-stationary noise is removed based on the method described in the supplement of Ref. [239]. As a result, these cuts remove 35% of the coincident time between the two LIGO detectors for O1 and 16% for O2, leading to the total coincident livetime of 29 (99) days for O1 (O2), respectively [83], [84].

The cross-correlation estimators are publicly available in the data product given at Ref. [240]. The search and parameter estimation are performed following the same procedure as the injection study described in Sections 6.2 and 6.3. Since an independent cross-correlation spectrum is provided from each observing run, the joint likelihood function one needs to evaluate is the direct product of O1 and O2 likelihood functions, such that

$$L(\hat{C}_{\rm O1}, \hat{C}_{\rm O2}|\boldsymbol{\theta}, \mathcal{H}_{\rm VC}) = L(\hat{C}_{\rm O1}|\boldsymbol{\theta}, \mathcal{H}_{\rm VC}) L(\hat{C}_{\rm O2}|\boldsymbol{\theta}, \mathcal{H}_{\rm VC}). \tag{6.6}$$

Each likelihood in the right hand side follows the definition of Eq. (5.24).

The same prior as used in the previous injection studies is chosen for boson mass m_b in each of the searches, and we adopt two different parametrizations for BH initial spin distribution, namely $\chi_{\rm ul}$ and $\chi_{\rm ll}$ parametrizations. Remember that for $\chi_{\rm ul}$ parametrization, we fix $\chi_{\rm ll}$ as 0 and vary $\chi_{\rm ul}$, and $\chi_{\rm ll}$ parametrization fixes $\chi_{\rm ul}$ as 1 and varies $\chi_{\rm ll}$. Unlike the previous injection studies, the vector cloud model includes the contribution from the CBC remnant population. However, the SGWB predicted from the population alone is well below the O1+O2 sensitivity curve and it is expected that the addition of the BBH remnant component in the BH populations wouldn't impact the search results significantly.

6.5.1 Search results and boson mass constraints

We summarize the Bayes factors obtained from each search with different configurations in Table 6.2 and there is no strong evidence of a SGWB signal for either of the boson cloud models. The null results of these searches allow us to place constraints on the two dimensional space of m_b and $\chi_{\rm ul,ll}$ using the inferred posterior. In what follows, we define the boson mass constraints at the 95% confidence level for a given range of the spin parameter as the mass range completely outside (i.e. its lower bound is given by the maximum of the lower part of the contour, while its upper bound is given by the minimum of the higher part the contour.) the 95% contour in the two-dimensional posterior distribution inferred from the analysis.

In Figs. 6.11 and 6.12, we present the posteriors produced from the scalar boson search under the $\chi_{\rm ul}$ and $\chi_{\rm ll}$ parametrizations, respectively. Fig. 6.11 indicates that, for

	χ_{ul}	χ_{ll}
scalar cloud	0.14	-1.36
vector cloud	-0.06	-0.51

Table 6.2: Bayes factor of each boson cloud model against noise model. The columns represent different ways of parametrize the initial BH spin distribution.

the χ_{ul} case, the two-dimensional posterior distribution disfavors the parameter space where χ_{ul} higher than 0.6 and $m_b \approx 10^{-13}\,\mathrm{eV}$. More specifically, we set $\chi_{\mathrm{ul}} = 0.8$ as a fiducial value, finding the scalar mass constraint of $2 \times 10^{-13}\,\mathrm{eV}$ to $4 \times 10^{-13}\,\mathrm{eV}$. m_b posterior does not indicate a strong confidence level. In contrast, the posterior distribution in Fig. 6.12 exhibits more stringent constraints where the scalar mass of $m_b = 2.4 \times 10^{-13}\,\mathrm{eV}$ to $5.2 \times 10^{-13}\,\mathrm{eV}$ is disfavored regardless of χ_{ll}. This result is consistent with Fig. 4.2, which suggests that the search on LIGO's O1 and O2 data is most sensitive to the scalar boson mass of $m_b \sim 10^{-12.5}\,\mathrm{eV}$ as well as the fact that χ_{ll} parametrization generally tends to have faster spinning BH populations and leads to larger amplitude of a predicted spectrum than χ_{ul} one. The apparent peak in the marginalized one dimensional posteriors for m_b of Fig. 6.11 is consistent with noise fluctuation and this behavior goes away in a simulated search using synthesized Gaussian noise, which is described in the next subsection. Also note that the parameter space that is ruled out here is larger than the search performed on O1 data alone described in Ref. [181]. This is attributed to the sensitivity improvement of LIGO's data due to the more sensitive detector noise and extended observation time.

For the vector cloud search, the inferred posteriors for the two different parametrizations are shown in Figs. 6.13 and 6.14. According to Fig. 6.13, the posterior disfavors the vector mass around $m_b \sim 10^{-13}\,\mathrm{eV}$ as long as the spin parameter higher than 0.2 in χ_{ul} parametrization. For $\chi_{\mathrm{ul}} = 0.8$, we find the vector mass constraints of $0.9 \times 10^{-13}\,\mathrm{eV}$ to $5.1 \times 10^{-13}\,\mathrm{eV}$. On the other hand, in the χ_{ll} parametrization, the mass range $0.8 \times 10^{-13}\,\mathrm{eV}$ to $6.5 \times 10^{-13}\,\mathrm{eV}$ is excluded regardless of spin lower bound χ_{ll}. (See the 1-D marginalized posterior of m_b in Fig. 6.14) This can be understood by Fig. 4.7, where the vector boson mass only around $10^{-13.5}\,\mathrm{eV}$ can be detected by the O1+O2 power-law integrated curve. A qualitative difference in this result between each spin parametrization is consistent with what is seen in the scalar cloud search. We note that this is the first constraint for vector boson mass given by the SGWB search.

6.5.2 Robustness of the constraints

It is important to ask how robust the boson mass constraints above are against noise fluctuation. Also, one can see from the posterior distributions for the χ_{ul} case (Figs. 6.11

and 6.13) that the posterior samples cluster in one region of the parameter space near the 95% contour, yielding the apparent peak in each 1D boson mass posterior. It would be natural to wonder if these features imply something physical. To answer these questions, we provide a follow-up study that investigates the behavior caused by noise fluctuation. We conduct a similar search for the boson cloud models, but using synthesized noise data instead of LIGO's real data.

To ensure the same detector sensitivity, we make use of the variance of the cross-correlation estimator computed for LIGO's O1 or O2, based on Eq. (5.11). We synthesize noise data by drawing the estimator from a Gaussian distribution with the LIGO's O1 or O2 variance at each frequency bin. Following the same analysis procedure, we produce the posterior results for all of the four search configurations shown in Table 6.2. Figs. 6.16 and 6.18 show the posterior results with $\chi_{\rm ul}$ parametrization for scalar and vector cloud models, respectively. The contour in the both posteriors is varied due to different realization of noise. More quantitatively, we find the mock constraints to be 2.0×10^{-13} eV to 8.4×10^{-13} eV for the scalar case and 7.7×10^{-14} eV to 8.3×10^{-13} eV for the vector case, which can be compared to 2.0×10^{-13} eV to 4.0×10^{-13} eV (9.6×10^{-14} eV to 5.1×10^{-13} eV) for the scalar (vector) case in the real search. In other words, given the specific noise realization, the constraints can become wider by a factor of 1.5-2 in the logarithmic scale. We also note that another realization could shrink the constraints potentially to the same degree. Therefore, especially for the scalar's $\chi_{\rm ul}$ case, we conclude that the obtained constraints might not be significant enough to be robust against noise fluctuation. Additionally, it is noticeable that the posterior samples appear to cluster differently from the real search results. Therefore, we note that the sample clustering in Figs. 6.11 and 6.13 is simply due to the specific noise realization of the real data we used.

On the other hand, Figs. 6.17 and 6.19 represent the mock posterior results given by $\chi_{\rm ul}$ parametrization for scalar and vector cloud models, respectively. The contour in either of the posteriors does not appear to be strongly affected by different noise realization. The mock constraints we obtained are 2.5×10^{-13} eV to 6.6×10^{-13} eV for the scalar case and 0.8×10^{-14} eV to 8.3×10^{-13} eV for the vector case. Comparing these values to those given by the real search, namely 2.4×10^{-13} eV to 5.2×10^{-13} eV (0.8×10^{-13} eV to 6.5×10^{-13} eV) for the scalar (vector) case, we find that the mock constraints are wider only by a factor of ~ 1.1, leading to the conclusion that the boson mass constraints with $\chi_{\rm ll}$ parametrization are relatively robust against noise fluctuation. This difference in the constraint's robustness between the two spin parametrizations is due to the fact that in $\chi_{\rm ll}$ parametrization the SGWB amplitude can sharply increase up to well above the LIGO's sensitivity curve at some mass scale regardless of $\chi_{\rm ll}$, and hence, the boundary of the detectable range is determined mostly by the critical scale rather than detail of given data.

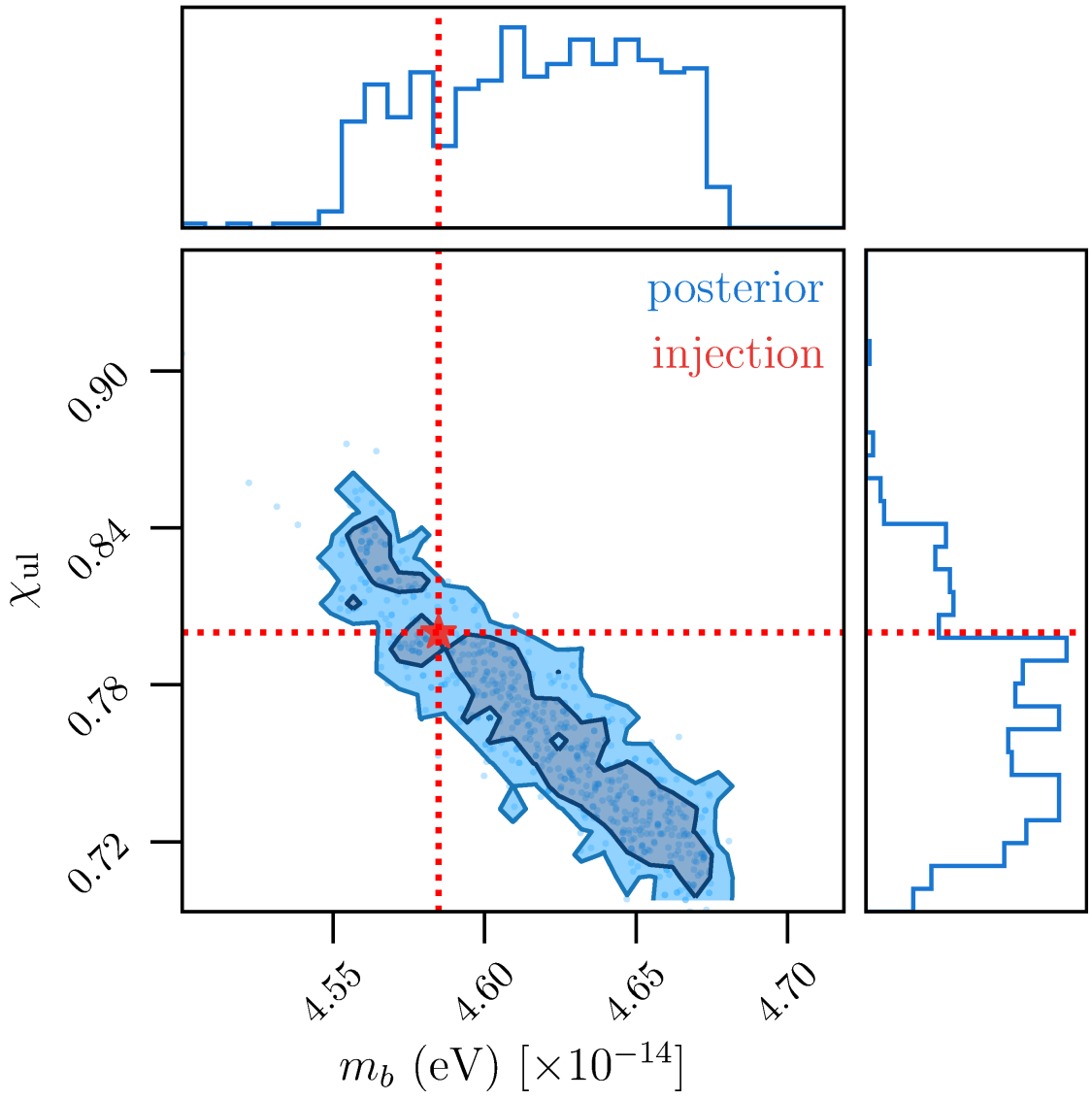

Figure 6.4: Posterior samples recovered for the injection of vector cloud model $\Omega_{\rm inj}(f;\boldsymbol{\theta})$ shown in Fig. 6.2. We adopt a log-uniform prior for m_b across the range 10^{-14} eV to 10^{-11} eV and a uniform prior for $\chi_{\rm ul}$ between 0 and 1. Each blue dot represents a sample of the posterior distribution and the two contours indicate 2 and 3-σ credible region, respectively. The star marker pinpoints the true parameter set of the injection, which lies within the contour. The log bayes factor estimated for this injection is approximately 500.

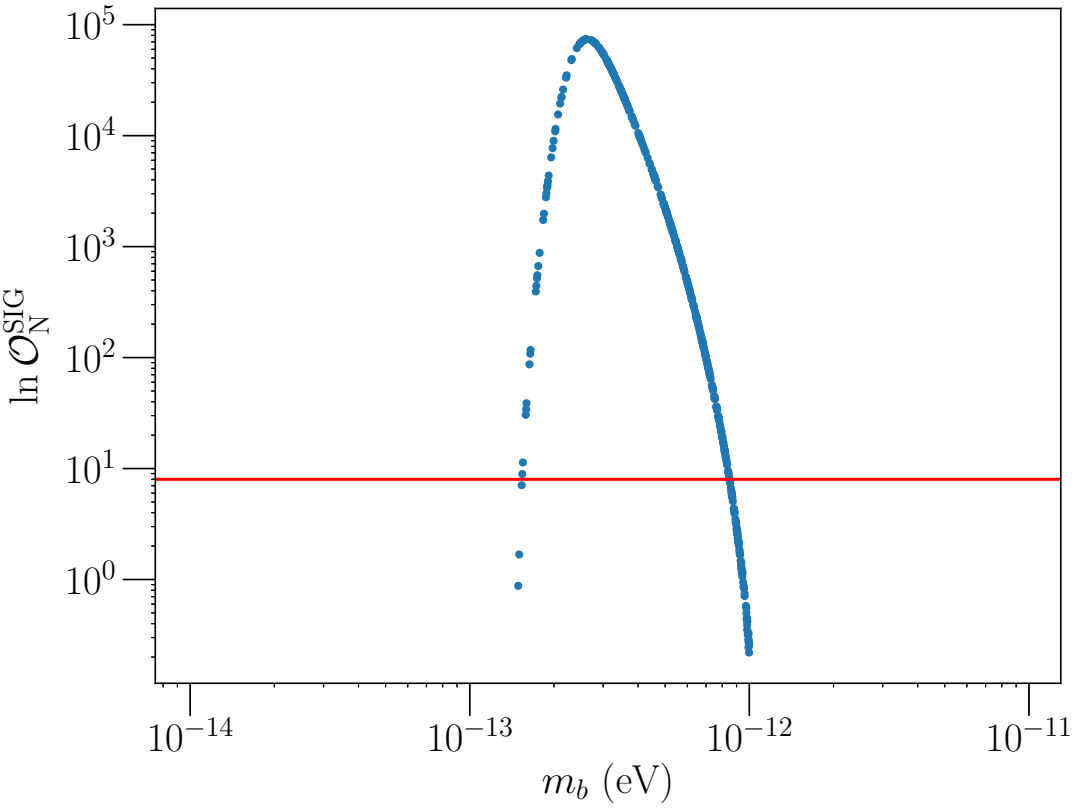

Figure 6.5: Bayes factor of the recovered injection as a function of injected m_b[eV] values. For every injection, we assume an uniform distribution from 0 to 0.8 (namely, $\chi_{\rm ul} = 0.8$ in the $\chi_{\rm ul}$ parameterization) for BH an initial spin in the isolated BH population. The red horizontal line shows our detection criteria of $\ln \mathcal{O}_{\rm N}^{\rm SIG} = 8$.

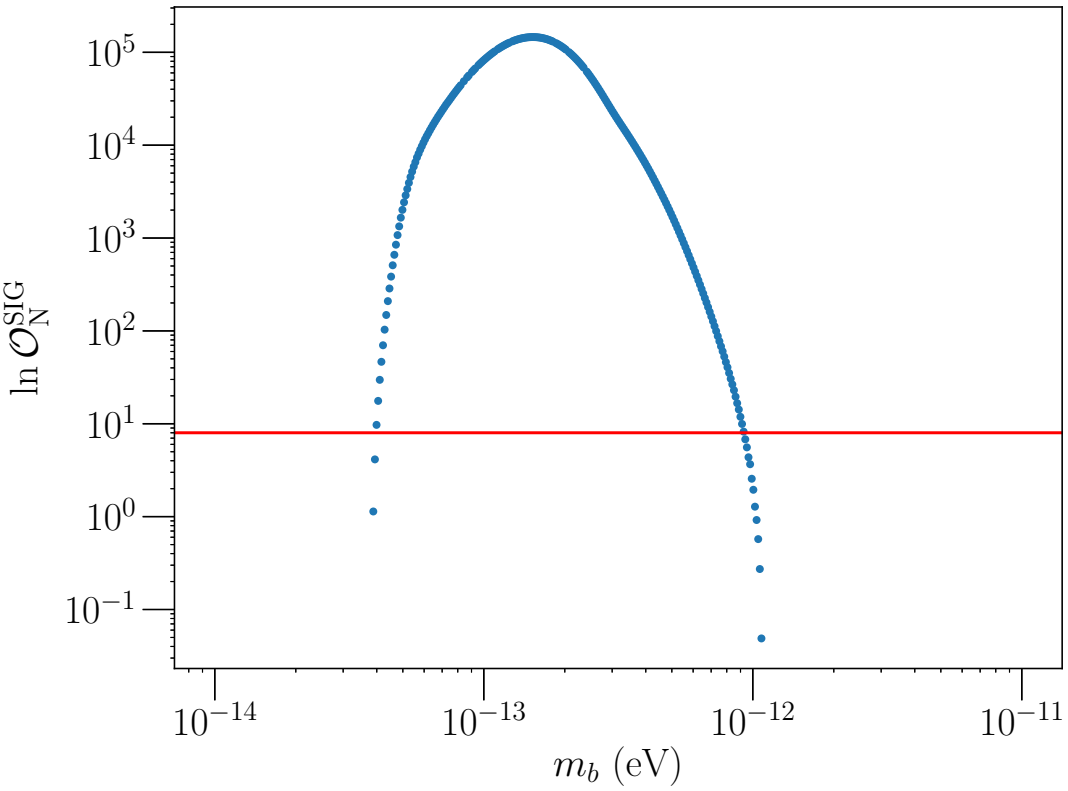

Figure 6.6: Bayes factor of the recovered injection as a function of injected m_b[eV] values. For every injection, we assume an uniform distribution from 0 to 0.8 (namely, $\chi_{\rm ul} = 0.8$ in the $\chi_{\rm ul}$ parameterization) for BH an initial spin in the isolated BH population. The red horizontal line shows our detection criteria of $\ln \mathcal{O}_{\rm N}^{\rm SIG} = 8$.

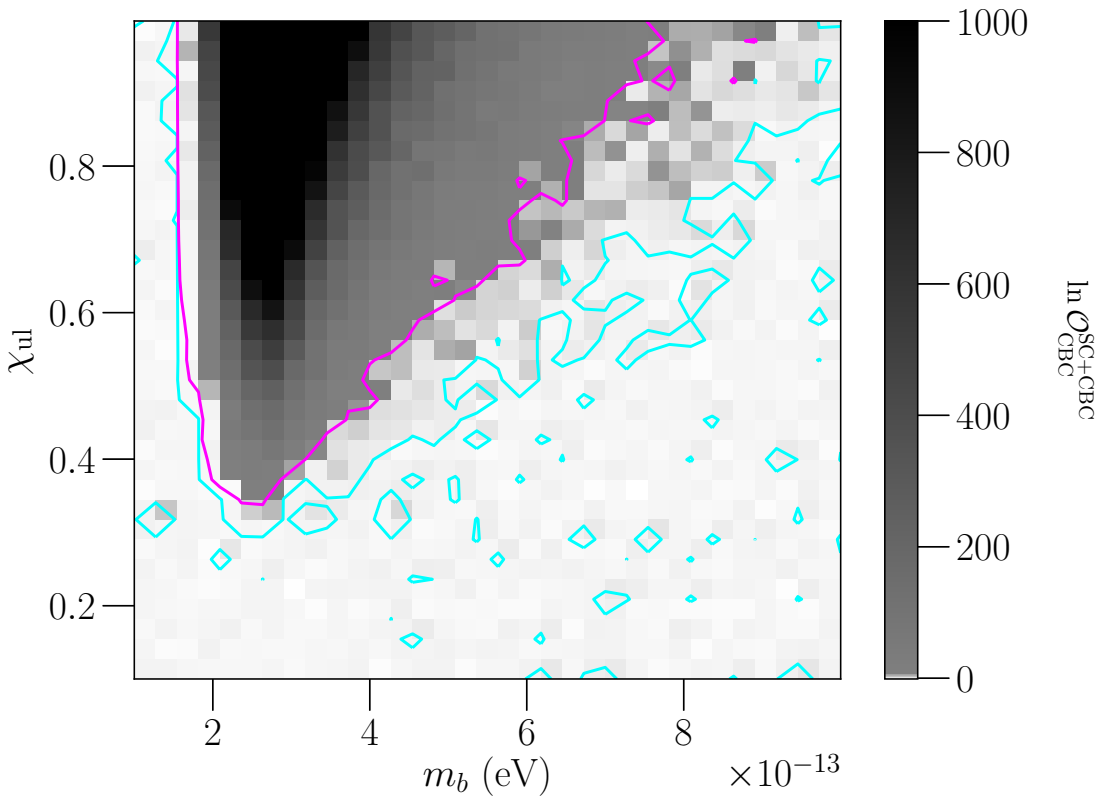

Figure 6.7: Grey scale map of bayes factor between CBC-only and the joint scalar cloud +CBC models with two contours of ln(BF) = 8 (magenta) and 0 (cyan). The parameter space inside the magenta contour indicates where one can claim the signature of the scalar cloud background in the presence of the CBC background.

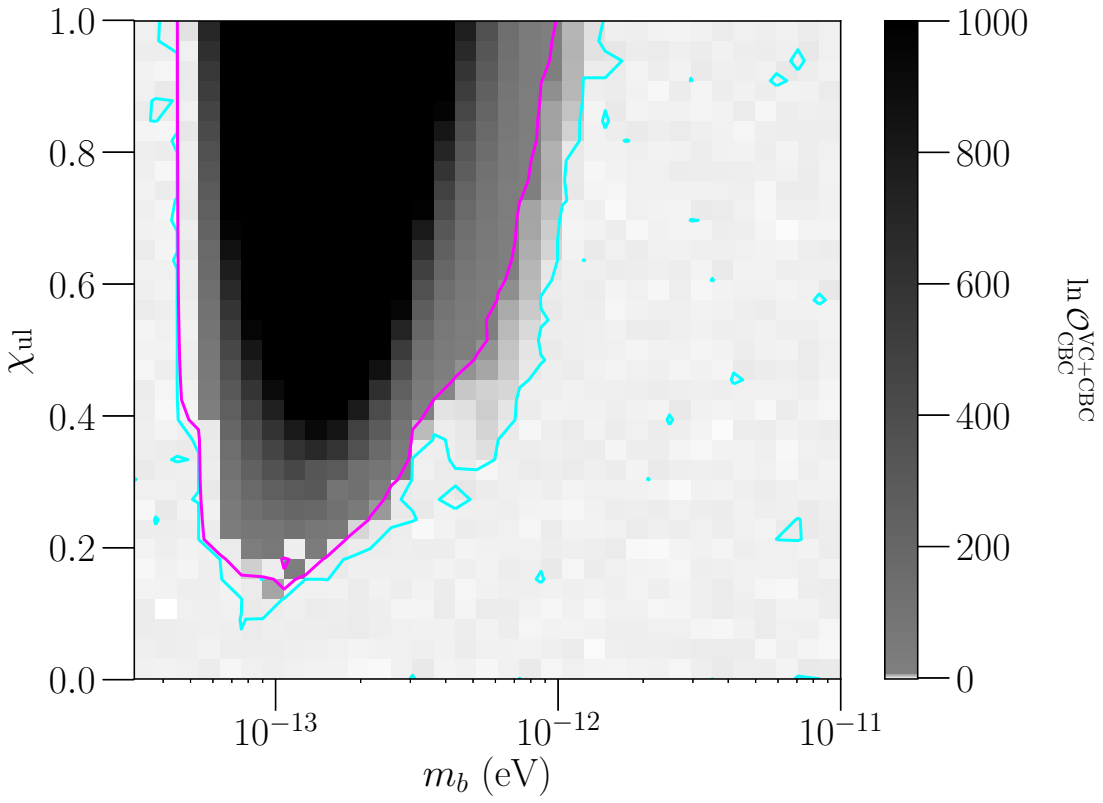

Figure 6.8: Grey scale map of bayes factor between CBC-only and the joint vector cloud +CBC models with two contours of ln(BF) = 8 (magenta) and 0 (cyan). The parameter space inside the magenta contour indicates where one can claim the signature of the vector cloud background in the presence of the CBC background.

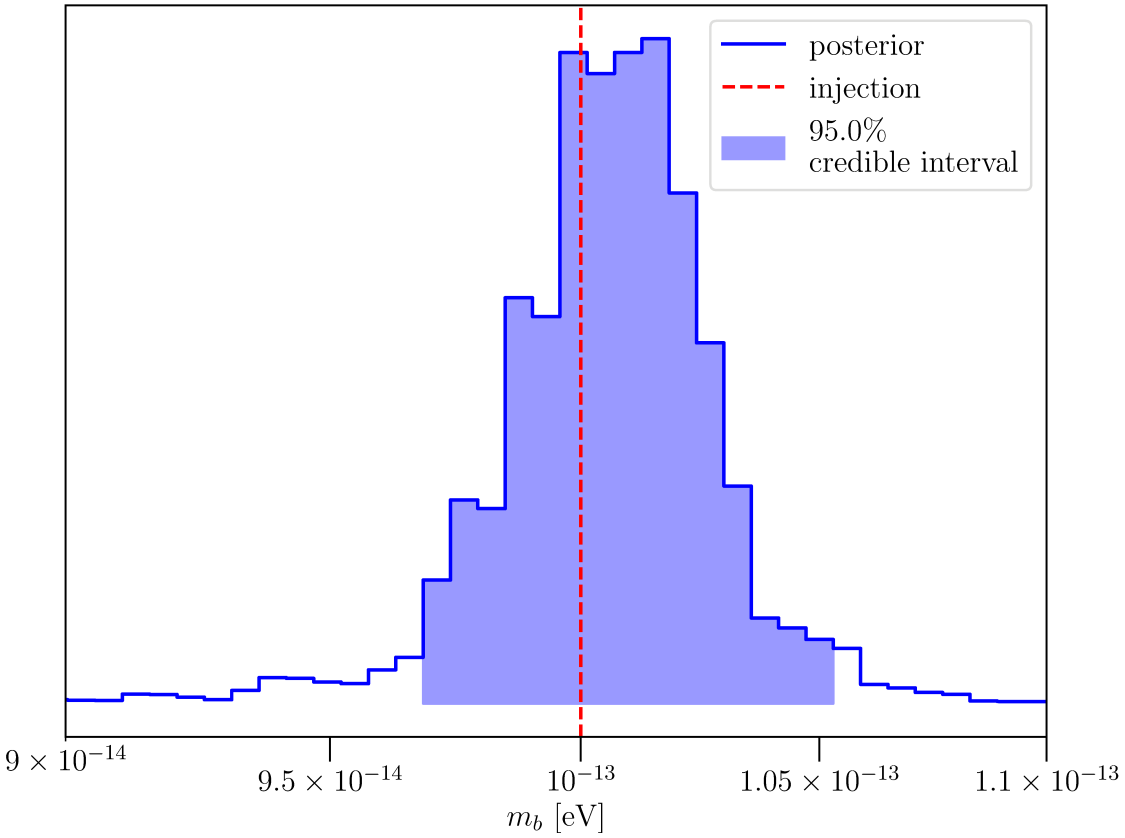

Figure 6.9: 1-D posterior distribution for the vector boson mass m_b when searching for the BBH merger remnant component with an injection using synthesized noise of the LIGO's design sensitivity. The red dashed line indicates the injected vector mass value. The shaded region is the 95% credible interval counted around the maximum posterior probability sample.

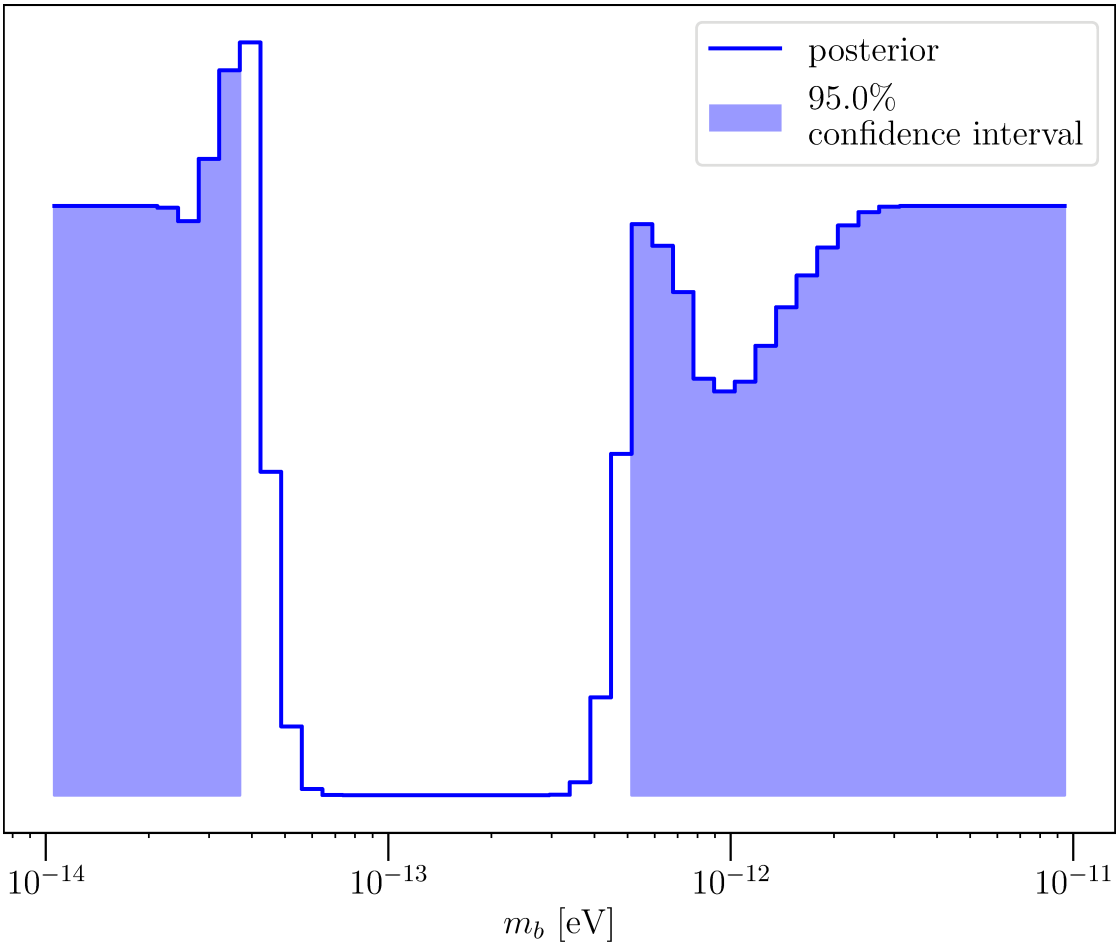

Figure 6.10: 1-D posterior distribution with regard to the vector boson mass m_b when searching for the BBH merger remnant component without any injection using synthesized noise of the LIGO's design sensitivity. The shaded region is the 95% credible interval counted around the minimum posterior probability sample.

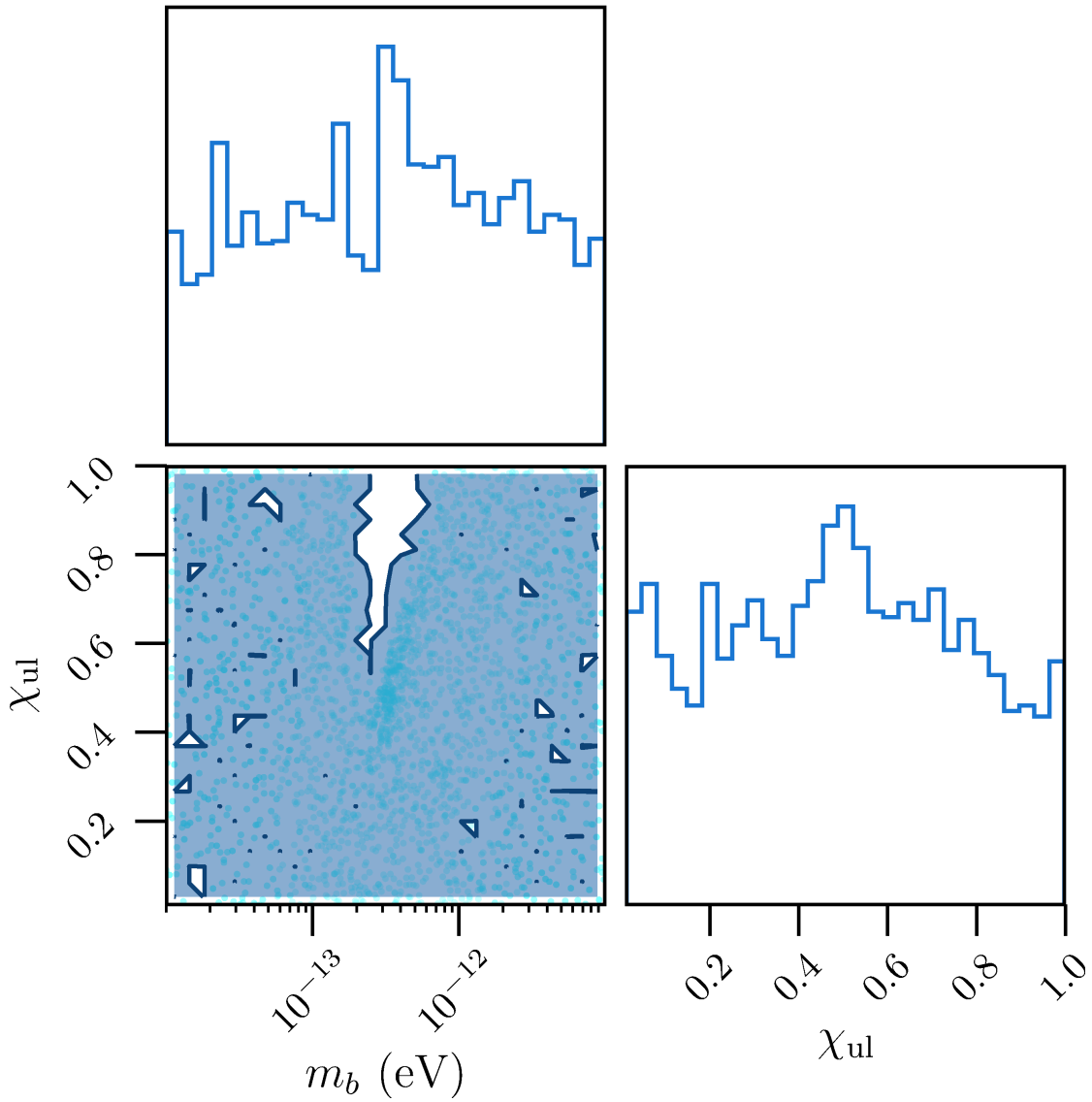

Figure 6.11: 2-D posterior result of the advanced LIGO's O1+O2 search for scalar cloud model, recovering with $\chi_{\rm ul}$. The contour on the two-dimensional posterior represents the 95% confidence level limit.

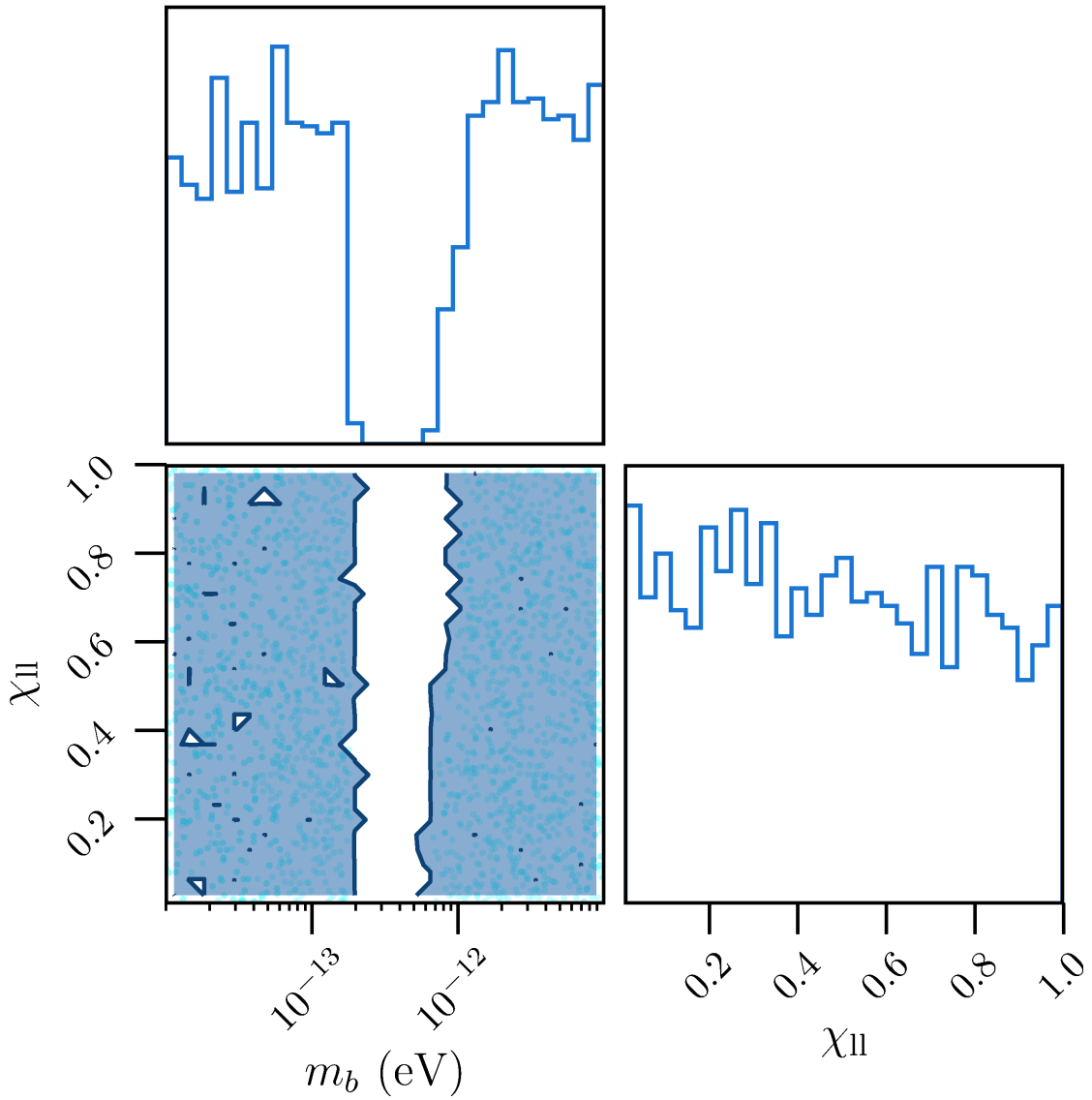

Figure 6.12: 2-D posterior result of the advanced LIGO's O1+O2 search for scalar cloud model, recovering with $\chi_{\rm ll}$. The contour on the two-dimensional posterior represents the 95% confidence level limit.

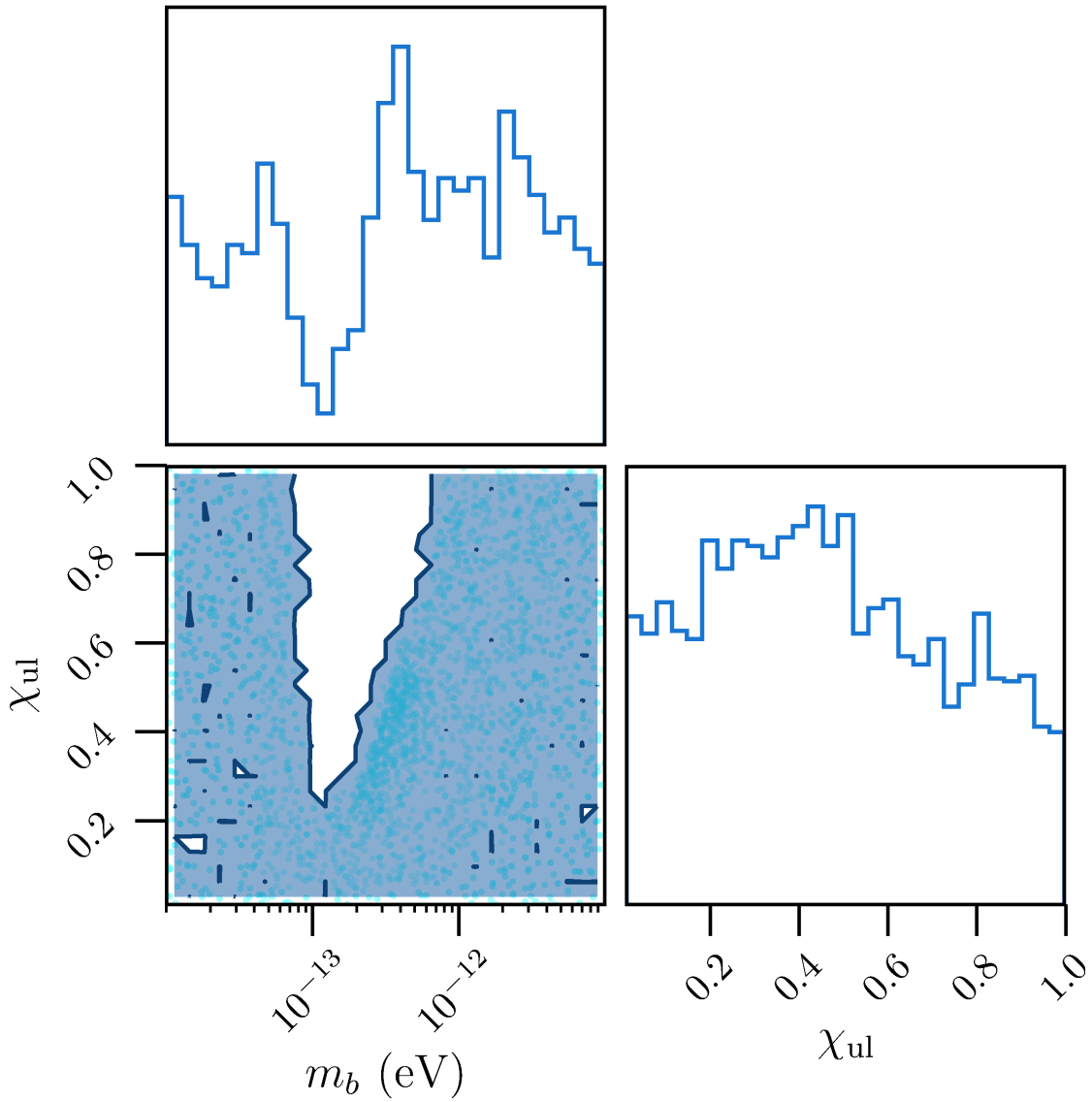

Figure 6.13: 2-D posterior result of the advanced LIGO's O1+O2 search for vector cloud model, recovering with $\chi_{\rm ul}$. The contour on the two-dimensional posterior represents the 95% confidence level limit.

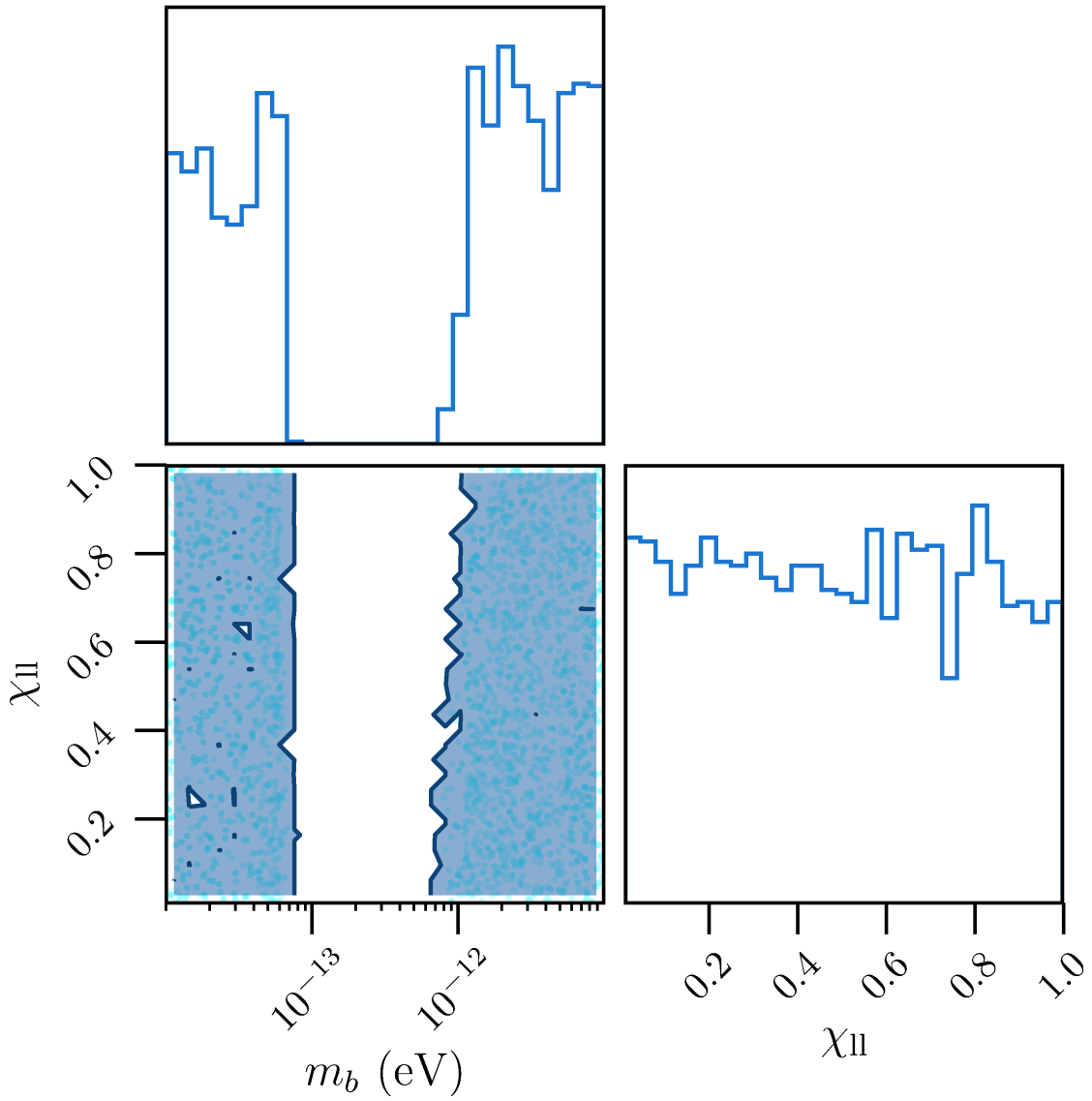

Figure 6.14: 2-D posterior result of the advanced LIGO's O1+O2 search for vector cloud model, recovering with χ_{ll}. The contour on the two-dimensional posterior represents the 95% confidence level limit.

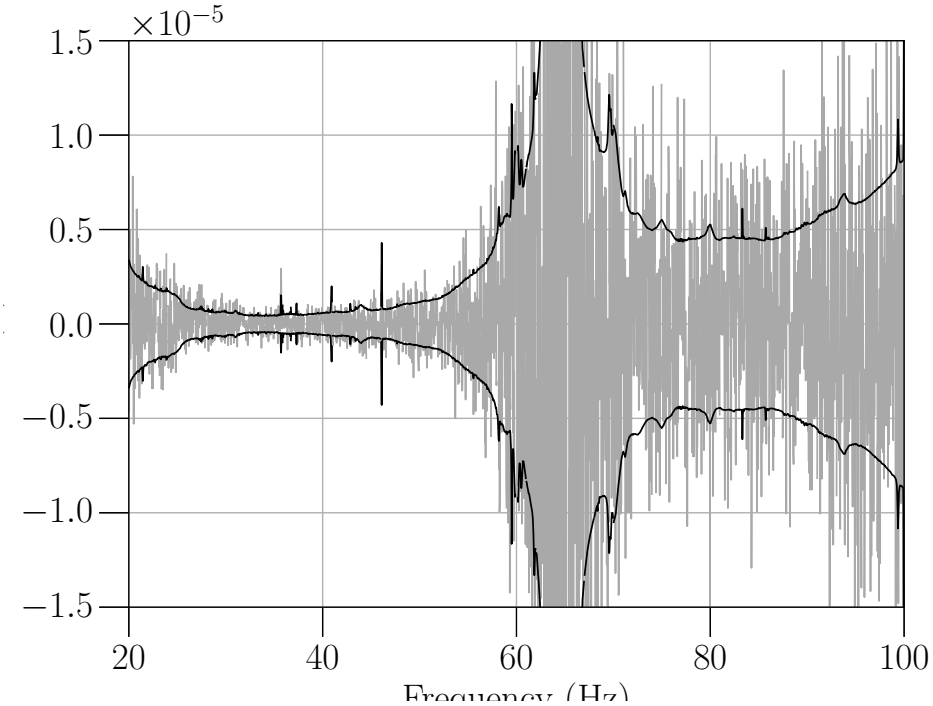

Figure 6.15: Synthetic LIGO's O2 cross-correlation estimator used for the follow-up study. The light grey curve represent the synthesized point estimates at each frequency bin and the black curve is the standard deviation symmetric around zero taken from Ref. [240]. Similarly, an O1 estimator is mimicked using the O1's variance [240].

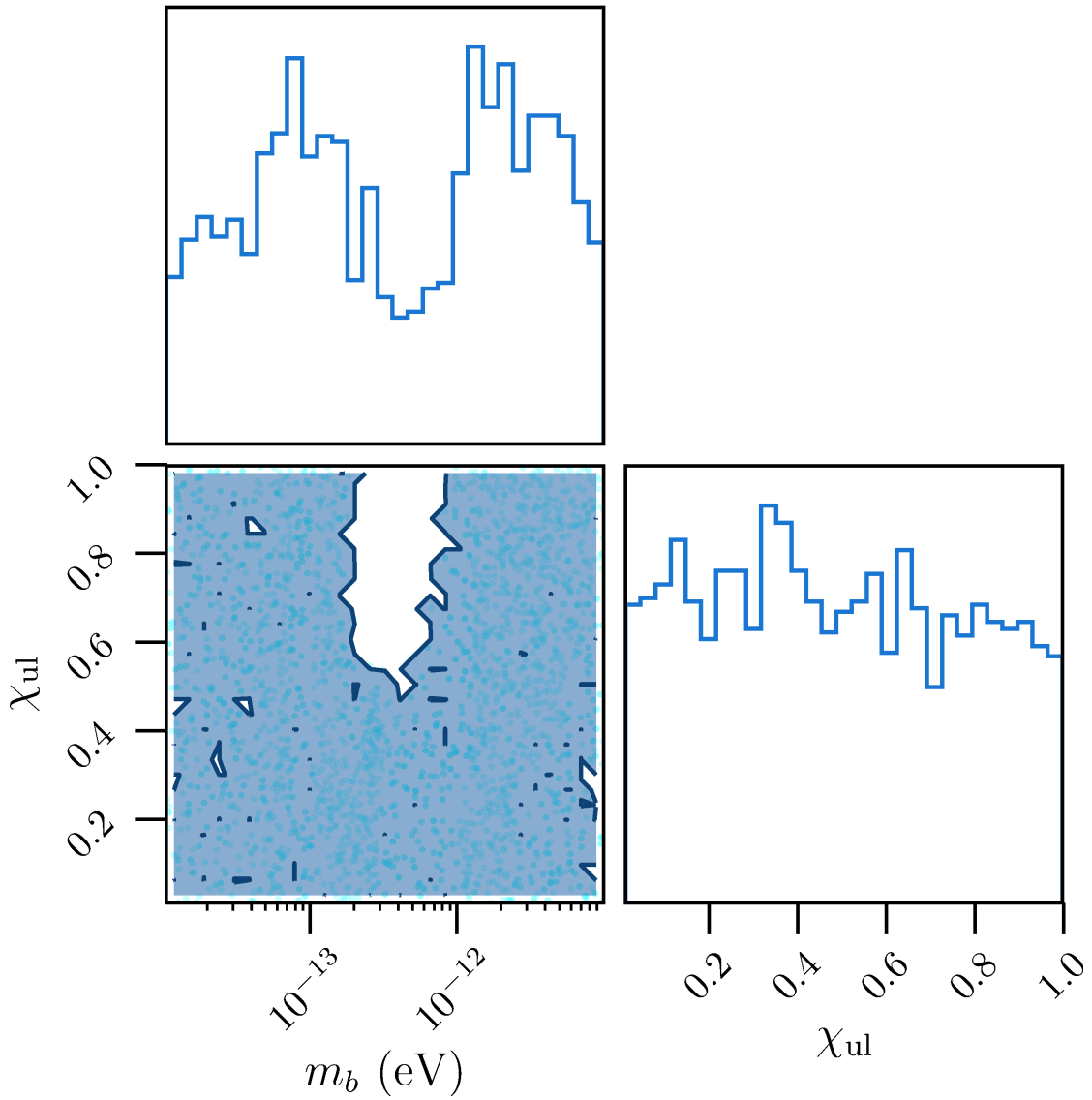

Figure 6.16: 2-D posterior result of a follow-up study using fake data for the advanced LIGO's O1+O2 search for scalar cloud model, recovering with $\chi_{\rm ul}$. The contour on the two-dimensional posterior represents the 95% confidence level limit.

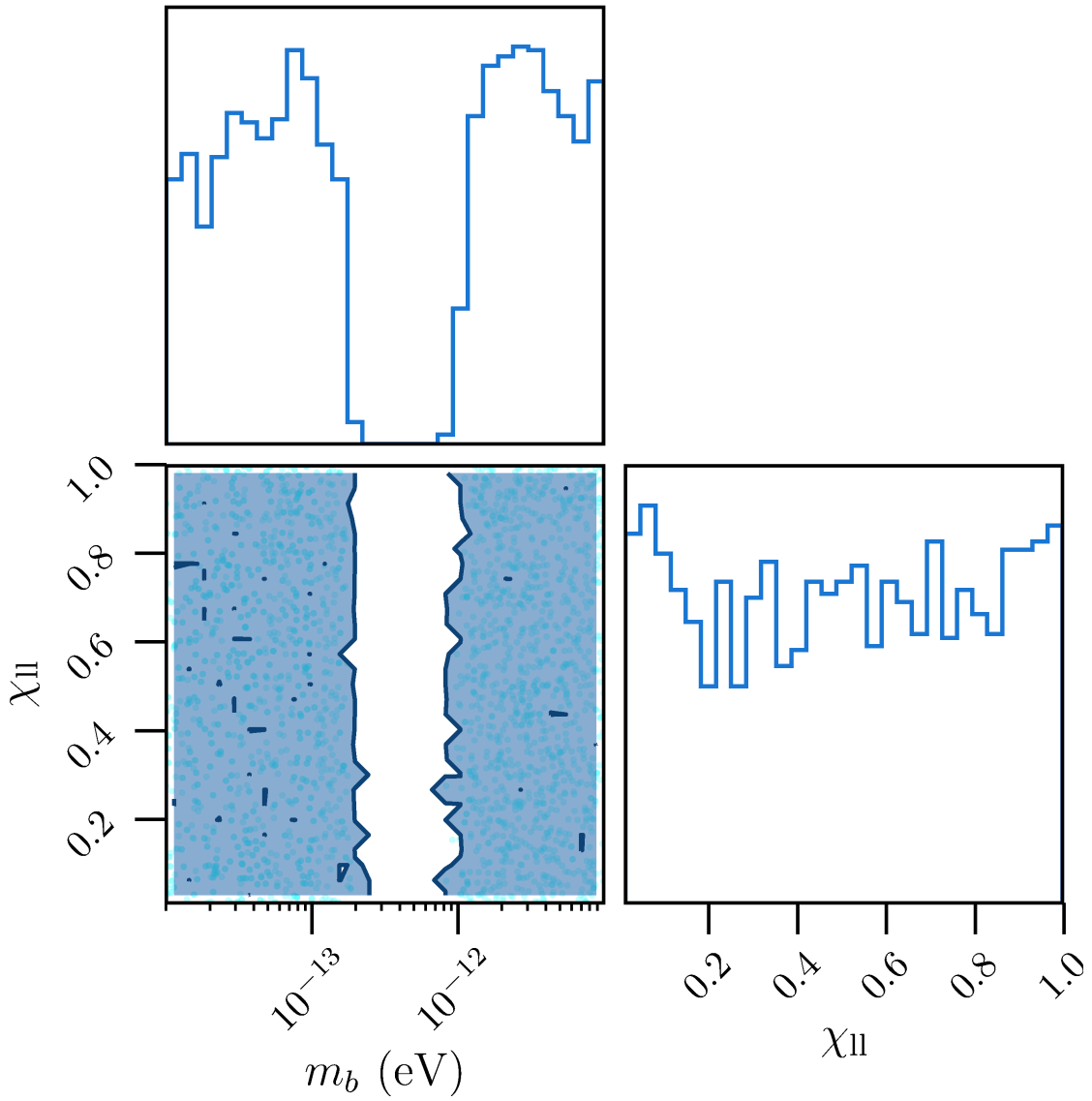

Figure 6.17: 2-D posterior result of a follow-up study using fake data for the advanced LIGO's O1+O2 search for scalar cloud model, recovering with $\chi_{\rm ll}$. The contour on the two-dimensional posterior represents the 95% confidence level limit.

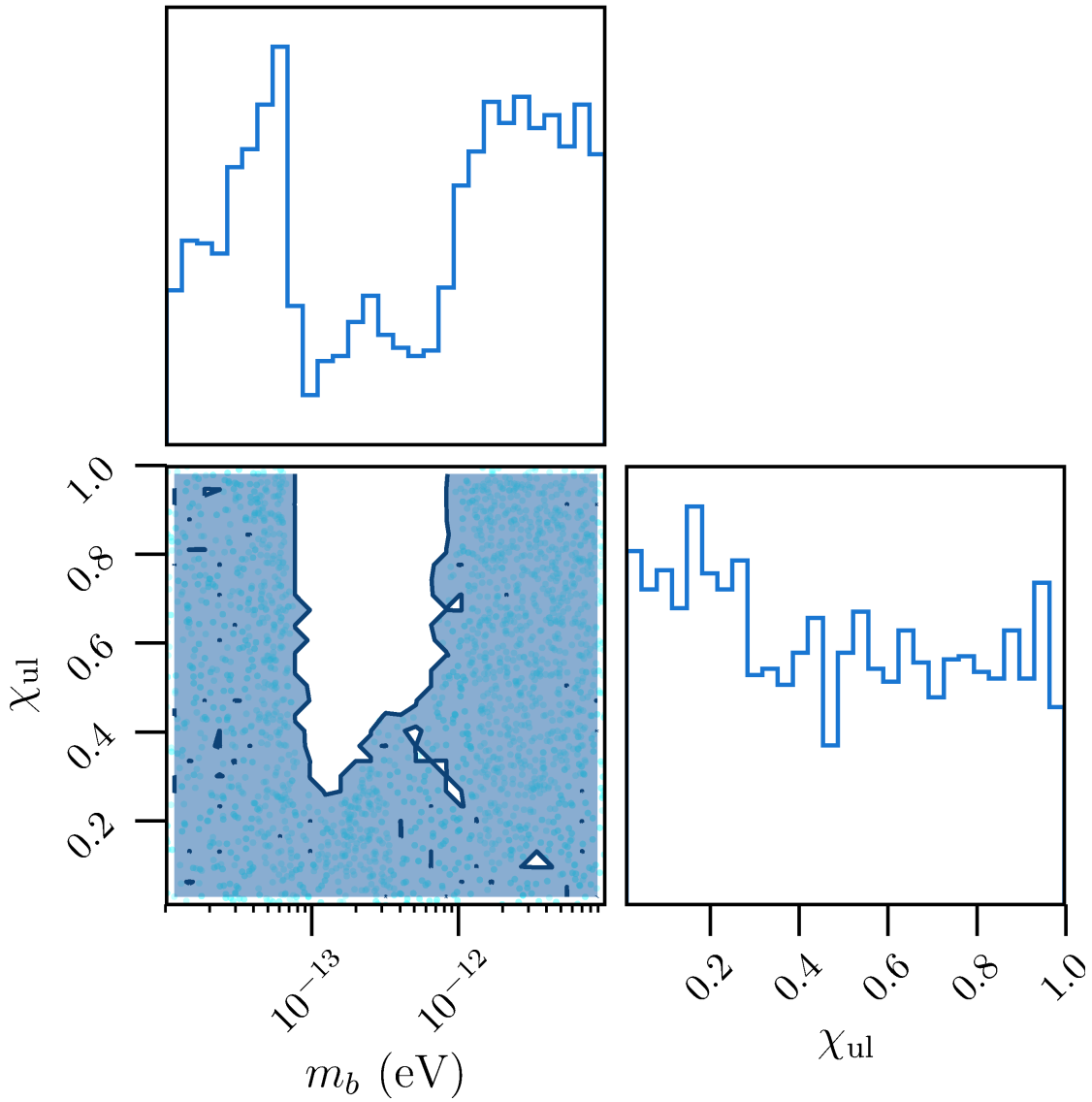

Figure 6.18: 2-D posterior result of a follow-up study using fake data for the advanced LIGO's O1+O2 search for vector cloud model, recovering with $\chi_{\rm ul}$. The contour on the two-dimensional posterior represents the 95% confidence level limit.

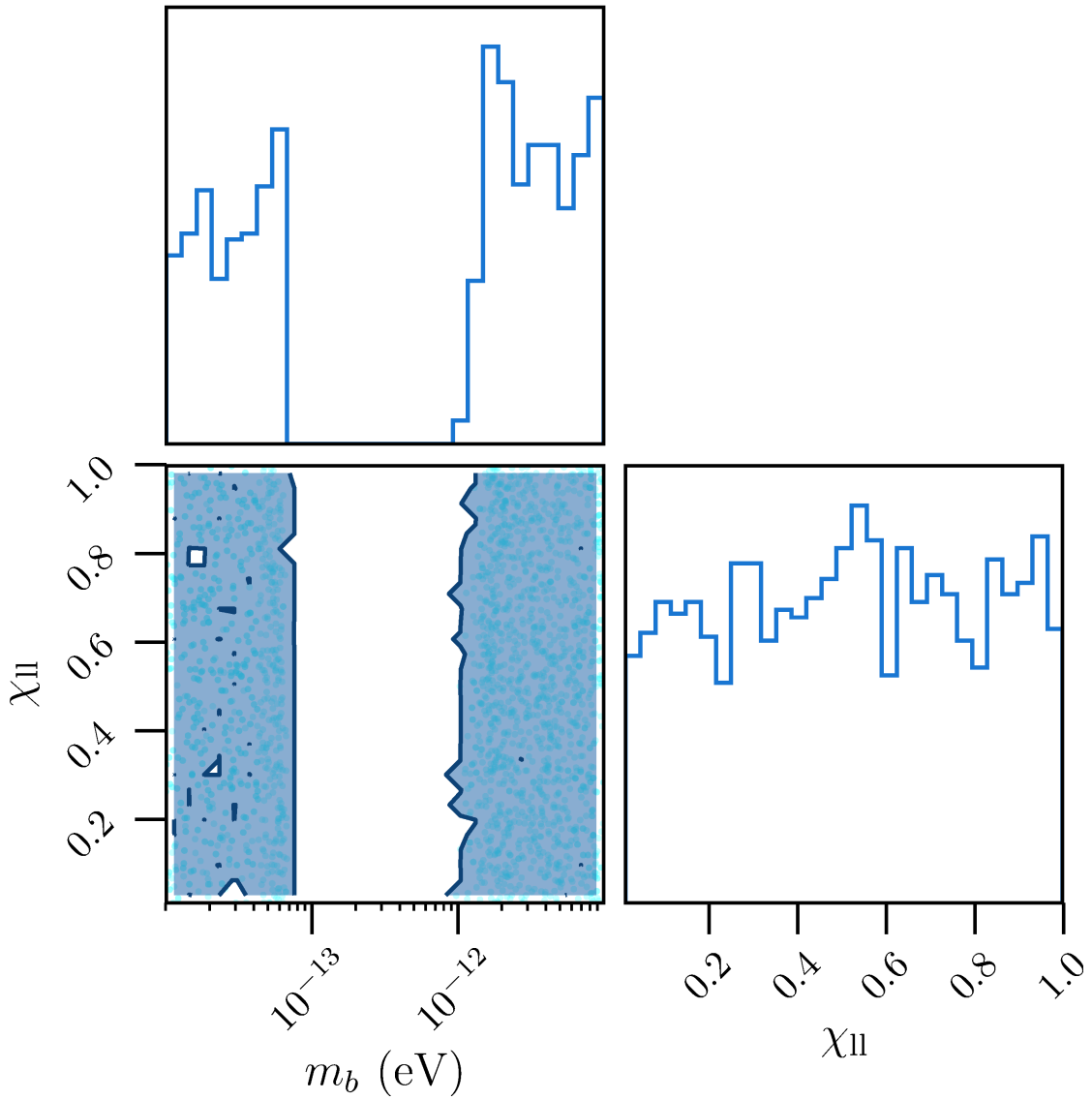

Figure 6.19: 2-D posterior result of a follow-up study using fake data for the advanced LIGO's O1+O2 search for vector cloud model, recovering with $\chi_{\rm ll}$. The contour on the two-dimensional posterior represents the 95% confidence level limit.

Chapter 7

Conclusion

This thesis presents modeling of the predicted SGWB spectrum for both models of the minimally-coupled massive scalar and vector bosons and the search results of such SGWB model using advanced LIGO. Based on the unstable behavior of the two types of bosonic fields, which is discussed in Chapter. 3, we note that whole dynamical timescale for the vector field is several order-of-magnitude shorter than that for the scalar field. See Eqs. (3.31) and (3.57) for instability timescale and Eqs. (3.90) and (3.91) for GW emission timescale. In chapter 4, we calculated the SGWB spectra predicted from these boson cloud models and found that the significant difference in the GW emission timescale leads to the enhancement of the background amplitude for the vector model with the mass $\sim 10^{-13}$ eV. Interestingly, assuming the isolated BHs and BBH merger remnant as the entire BH population, we identified a range of the boson masses that yields potentially detectable SGWB signal even with the current sensitivity of advanced LIGO, which implies our capability to place a meaningful constraint on the boson masses using a null result of the SGWB search. Furthermore, we included a higher-order mode ($m = 2$) in the SGWB model of the vector cloud and found that for relatively heavy vector bosons, e.g. $m_b \sim 10^{-11}$ eV, the $m = 2$ mode can be dominant over the fundamental mode ($m = 1$). We infer that this is due to the fact that, for the $m = 1$ mode of such heavy vectors, the change in the angular momentum during the instability tends to be small or the initial BH spin can be lower than the critical value ($J_i < J_f$) and the instability might not even occur.

We implemented the SGWB models of the BH superradiance induced by such bosonic fields into a Bayesian-based search pipeline. In order to assess the pipeline's performance, several injection tests were performed. From individual injection recoveries, Figs. 6.3 and 6.4 confirmed that our pipeline can accurately infer the injected parameters for both scalar and vector cloud models. We also computed a Bayes factor for multiple injections to construct a detectability curve as a function of each boson mass. Our study suggests that the search pipeline can be sensitive to scalar mass of around 1.8×10^{-13} eV to 7.5×10^{-13} eV and to vector mass of 0.4×10^{-13} eV to 9.4×10^{-13} eV,

respectively. Considering a more realistic situation where a SGWB from the expected CBC population and from a boson cloud model both are present in data, we performed a model-selection test with injections of the both models and varying the injected parameters for the boson cloud model so that we can explore a parameter space where the predicted SGWB signal from the boson cloud model can be separated from the CBC background. The 2D colormaps of the Bayes factor between the two models shown in Figs.6.7 and 6.8 indicate that we can distinguish the boson cloud SGWB with even a modestly spinning BH population at around 3×10^{-13} eV(1×10^{-13} eV) for the scalar (vector) cloud model.

Lastly, we conducted a search for this kind of SGWB from each scalar and vector cloud model using the data from advanced LIGO's O1 and O2. We adopted two different parametrizations for BH spin distribution: one takes the lower limit ($\chi_{\rm ll}$) of the distribution as a free parameter, whereas the other varies its upper limit ($\chi_{\rm ul}$). For either parameterization, we do not find any strong evidence of such SGWB signal for scalar or vector cloud model. This allows us to place the following constraints on each boson mass: for the pessimistic case, at $\chi_{\rm ul} = 0.8$ we exclude scalar mass of 2.0×10^{-13} eV to 4.0×10^{-13} eV and similarly vector mass of 0.9×10^{-13} eV to 5.1×10^{-13} eV (see Figs. 6.11 and 6.13). On the other hand, for the optimistic case, scalar mass of $m_b = 2.4 \times 10^{-13}$ eV to 5.2×10^{-13} eV and vector bosons mass of $m_b = 0.8 \times 10^{-13}$ eV to 6.5×10^{-13} eV are disfavored regardless of spin lower bound $\chi_{\rm ll}$ at a 95% confidence level (see Figs. 6.12 and 6.14). Fig. 7.1 illustrates the scalar and vector mass constraints we obtained using LIGO's O1 and O2 data in the optimistic scenario, compared to several other observations placing the upper limit of the boson-photon coupling constant for given boson masses. Among the vast range of possible boson mass scale, we can constrain only a narrow window of the boson masses, however, those masses are disfavored regardless of the coupling constant as the superradiant instability does not involve any photon coupling. We would like to highlight that these are the first constraints made on the boson masses based on a rigorous SGWB search.

In Figs. 4.4 and 4.5, we find that our SGWB modeling considers an intermediate scenario in terms of the SFR models intrinsic to the BH populations. As future work, we aim to incorporate effects of such astrophysical uncertainty as well as other factors, e.g. a BH mass function and the initial spin distribution for the isolated BH population. Also, the local merger rate used to model the SGWB spectrum from the BBH remnant population need to be updated given the lowered rate estimate shown in the latest GW catalog [27]. From a theoretical point of view, this thesis only considered a minimally-coupled ultra-light boson particle without possible non-gravitational couplings to other Standard Model particles, as well as any self-interactions beyond the mass term. Although our results can be valid for any massive bosonic field that involves such interactions being negligible compared to the gravitational interaction with the BH,

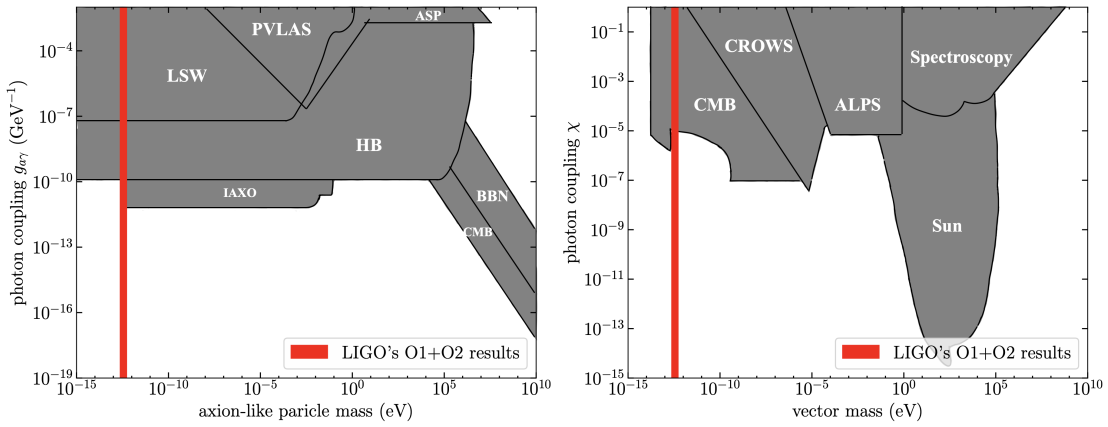

Figure 7.1: Comparison of the boson mass constraints obtained from LIGO's O1+O2 search ($\chi_{\rm ll}$ parametrization) with those from other observations in terms of a boson-photon coupling constant (see Eqs.(1.49) and (1.50)), which are reproduced from Ref. [55] and [241] for the scalar and the vector respectively. The red region on each panel represents the scalar or vector mass constraint we obtained at 95% confidence level, using LIGO's O1 and O2 data.

large non-gravitational interactions could affect the evolution of the superradiant instability. For example, it has been shown that ultra-light scalar fields with self-interactions [68], [242], [243] and photon couplings [244]–[246] can halt the superradiant instability, and effectively increase the instability timescale [247], [248]. The impact of such interactions has been investigated less for massive vector fields and it would be necessary to study these circumstances in more detail in the future. In any case, as current ground-based GW detectors such as advanced LIGO and Virgo improve their sensitivity for future observing runs, this framework can be used to place even stronger constraints on the existence of such boson particles.

Appendix A

Sturm-Liouville equations

In the discussion of gravitational radiation from a BH-cloud system, we find that the radial component of a NP scalar follows an inhomogeneous Sturm-Liouville equation shown in Eq. (3.67). We briefly review the Green's-function technique to generally solve such a equation and provide the derivation of a Green's function solution.

A.1 Green's-function technique

Suppose a function $u(t)$ defined over the interval $(-\infty, \infty)$ follows an inhomogeneous Sturm–Liouville equation given by a linear operator such that

$$\mathcal{L}[u(t)] = \frac{\mathrm{d}}{\mathrm{d}t}\left[p(t)\frac{\mathrm{d}u(t)}{\mathrm{d}t}\right] - q(t)u(t) = f(t). \tag{A.1}$$

Here one needs to solve the above equation under some boundary conditions, e.g. in our case motivated boundary conditions are outgoing waves at the spatial infinity ($r^* \to \infty$) and ingoing waves at the event horizon ($r^* \to -\infty$), where r^* is the tortoise coordinates defined in Eq. (3.21). Then we define the Green's-function solution, $G(t, \xi)$, as follows:

$$\mathcal{L}[G(t, \xi)] = \delta(t - \xi). \tag{A.2}$$

Multiplying the source term $f(t)$ on the right hand of Eq. (A.1) and integrating over ξ yields

$$\int_{-\infty}^{\infty} \mathcal{L}G(t, \xi) f(\xi)\, \mathrm{d}\xi = \mathcal{L}\left[\int_{-\infty}^{\infty} G(t, \xi) f(\xi)\, \mathrm{d}\xi\right] = \int_{-\infty}^{\infty} f(\xi)\delta(t - \xi)\, \mathrm{d}\xi = f(t). \tag{A.3}$$

Comparing this equation with Eq. (A.1), it follows that

$$u(t) = \int_{-\infty}^{\infty} G(t, \xi) f(\xi)\, \mathrm{d}\xi. \tag{A.4}$$

Therefore, one needs to find the Green's function solution in order to solve for $u(t)$.

A.2 The derivation of a Green's fucntion

A Green's function for Eq. (A.1) can be found by connecting a solution for the homogeneous Sturm–Liouville equation, $\mathcal{L}[\tilde{u}(t)] = 0$ at each boundary. Let the two homogeneous solutions be $\tilde{u}_1(t)$ and $\tilde{u}_2(t)$ at the boundaries $t \to \pm\infty$, respectively[1] and the Green's function $G(t,\xi)$ is given by

$$G(t,\xi) = \begin{cases} A(\xi)\tilde{u}_1(t) & (a \le t < \xi) \\ B(\xi)\tilde{u}_2(t) & (\xi < t \le b) \end{cases}, \tag{A.5}$$

where by definition $G(t,\xi)$ satisfies the boundary conditions. Also, one requires $G(t,\xi)$ to be continuous at $t = \xi$ and hence

$$A(\xi)\tilde{u}_1(\xi) = B(\xi)\tilde{u}_2(\xi). \tag{A.6}$$

In addition, integrating either side of Eq. (A.2) over $[\xi - 0, \xi + 0]$, which yields

$$\int_{\xi-0}^{\xi+0} \frac{\mathrm{d}}{\mathrm{d}t}\left[p(t)\frac{\mathrm{d}u(t)}{\mathrm{d}t}\right]\mathrm{d}t - \int_{\xi-0}^{\xi+0} q(t)u(t)\,\mathrm{d}t = \int_{\xi-0}^{\xi+0} \delta(t-\xi)\,\mathrm{d}t \tag{A.7}$$

$$\Rightarrow \left[p(t)\frac{\mathrm{d}}{\mathrm{d}t}G(t,\xi)\right]_{\xi-0}^{\xi+0} = 1, \tag{A.8}$$

one can find the relation between the first derivative of $G(t,\xi)$:

$$\left(\frac{\mathrm{d}G}{\mathrm{d}t}\right)_{t=\xi+0} - \left(\frac{\mathrm{d}G}{\mathrm{d}t}\right)_{t=\xi-0} = -A(\xi)\tilde{u}_1'(\xi) + B(\xi)\tilde{u}_2'(\xi) \tag{A.9}$$

$$= \frac{1}{p(\xi)}. \tag{A.10}$$

From Eqs. (A.6) and (A.10), one can explicitly derive $A(\xi), B(\xi)$:

$$\begin{aligned} A(\xi) &= -\frac{\tilde{u}_2(\xi)}{p(\xi)\left(\tilde{u}_1(\xi)\tilde{u}_2'(\xi) - \tilde{u}_2(\xi)\tilde{u}_1'(\xi)\right)} = -\frac{\tilde{u}_2(\xi)}{p(\xi)w(\xi)}, \\ B(\xi) &= -\frac{\tilde{u}_1(\xi)}{p(\xi)\left(\tilde{u}_2(\xi)\tilde{u}_1'(\xi) - \tilde{u}_1(\xi)\tilde{u}_2'(\xi)\right)} = -\frac{\tilde{u}_1(\xi)}{p(\xi)w(\xi)}, \end{aligned} \tag{A.11}$$

where $\Delta(\xi)$ is, corresponding to Eq. (3.73), a Wronskian given by the determinant of a coefficient matrix

$$w(\xi) = \begin{vmatrix} \tilde{u}_1(\xi) & \tilde{u}_2(\xi) \\ \tilde{u}_1'(\xi) & \tilde{u}_2'(\xi) \end{vmatrix} = \tilde{u}_1(\xi)\tilde{u}_2'(\xi) - \tilde{u}_2(\xi)\tilde{u}_1'(\xi). \tag{A.12}$$

Eventually, one substitutes each coefficient, $A(\xi)$ and $B(\xi)$ into Eq. (A.5) and derives the solution $u(t)$ from Eq. (A.4). Specifically, one can associate each term that appears in the above discussion with the following terms mentioned in Chapter 3.3:

$$\begin{aligned} &\tilde{u}_1(\xi) \to R_H(r^*), \quad p(\xi)w(\xi) \to W_l, \\ &\tilde{u}_2(\xi) \to R_\infty(r^*), \qquad f(t) \to \frac{T_{\ell\tilde{m}\tilde{\omega}}}{\Delta^2}, \end{aligned} \tag{A.13}$$

leading to the solution for the radial component of the NP scalar shown in Eq. (3.74).

[1] These solutions correspod to R_H, R_∞ in Chapter 3.3.

Appendix B

Nested sampling

The sampling procedure implemented in `MULTINEST` software, which we use for our SGWB analysis is built upon a nested sampling algorithm. As mentioned in Section 5.1, the Bayesian evidence evaluation Eq. (5.7) involves a multi-dimensional integration and its intensive computational cost is one of the largest hurdles to overcome in order to perform a model selection. Several techniques of calculating evidence have been investigated extensively [249] [250] [251], although each of them is more or less still inefficient or restricted to some special cases. Nested sampling [252] is a Monte-Carlo-based method to efficiently calculate the evidence. Here we cover basics of the nested sampling and the detailed implimentation of `MULTINEST` can be found in Ref. [233].

In this algorithm of [252], new samples are drawn from an elliptical bound around only the posterior peak at each iteration.

Nested sampling evaluates the evidence thorough transformation from the multi-dimensional integration (5.7) to a one-dimensional integral. The prior volume X is defined by

$$\mathrm{d}X \equiv \pi(\boldsymbol{\theta})\mathrm{d}^D\boldsymbol{\theta} \tag{B.1}$$

such that

$$X(\lambda) \equiv \int_{L(\boldsymbol{\theta})>\lambda} \pi(\boldsymbol{\theta})\mathrm{d}^D\boldsymbol{\theta}. \tag{B.2}$$

Here a likelihood function is given by $\mathcal{L}(\boldsymbol{\theta}) \equiv p(H_{\boldsymbol{\theta}}|\boldsymbol{s}, H)$ and the multi-dimensional integral runs over the region of parameter space encompassed with the iso-likelihood contour $\mathcal{L}(\boldsymbol{\theta}) = \lambda$. In other words, $X(\lambda)$ can be interpreted as the fraction of a prior space over the parameter space which produces the likelihood value smaller than λ. From (B.1) and (5.7), it follows that

$$Z = \int_0^1 L(X)\mathrm{d}X, \tag{B.3}$$

where $L(X)$ is defined as the inverse function of $X(\lambda)$ and returns the minimal likelihood in the prior domain specified by X. One can note that $L(X)$ is a monotonically decreasing

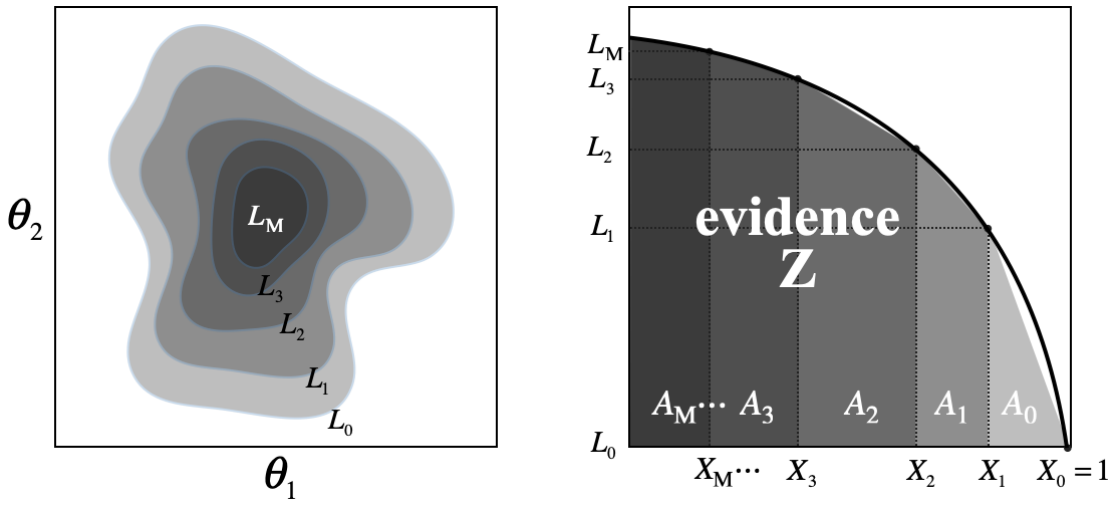

Figure B.1: (Left): Cartoon illustration of a two-dimensional likelihood distribution as a function of θ_1 and θ_2. (Right) Corresponding $L(X)$ with binned the prior volume, X_i. Each gray scale of a X_i bin in the two figures correspond with each other.

function of X. If one takes X_i as M series of decreasing values, i.e. decreasing prior volumes, so that

$$0 < X_M < \cdots < X_2 < X_2 < X_0 = 1, \tag{B.4}$$

$L(X)$ accordingly produces a series of increasing likelihood values towards the maximum of the multi-dimensional posterior. Fig. B.1 depicts an cartoon illustration of a two-dimensional posterior distribution and its $L(X)$ function. As Eq. (B.3) indicates, the total area below the black solid curve shown in the right panel of Fig. B.1 is equivalent to the evidence. The integration in Eq. (B.3) can be geometrically approximated as

$$Z = \int_0^1 L(X)\mathrm{d}X \approx \sum_i A_i \tag{B.5}$$

$$= \sum_{i=1}^{M} \frac{1}{2} \left(L(X_i) + L(X_{i-1})\right) \Delta X_i \tag{B.6}$$

$$= \sum_{i=0}^{M} L(X_i) w_i, \tag{B.7}$$

where A_i is the area of a trapezoid in a binned prior volume, each of which has a different gray scale in Fig. B.1 and $\Delta X_i = X_{i-1} - X_i$, $w_i = (X_{i-1} - X_{i+1})/2$ except $w_0 = (X_0 - X_1)/2$. The summation (B.5) suggests that one needs to add up every trapezoid until M-th sampling iteration at which the user-defined precision is satisfied.

The detail of sampling procedure is described below. First of all, N "active" samples are uniformly drawn from the full prior $\pi(\boldsymbol{\theta})$ volume, so $X_0 = 1$. Now one needs to explore on the contour of $L - X$ plane inwards in X correspondingly upwards in L. Next after sorting the samples in order of their likelihood, the lowest one L_0 is discarded

(treated as an inactive sample) and replaced with a new sample uniformly drawn subject to the constraint $L > L^*(= L_0)$. Finally, the sample with the lowest likelihood in the new active set is selected and its likelihood is set to be a new L^*. The essential issue here is how efficiently a new sample can be drawn without bias satisfying the constraint $L > L_*$. This procedure is iterated likewise, so at subsequent iterations the number of inactive samples will be increased one by one and the prior volume obeying the constraint $L > L^*$ will keep reducing. One can note that since the samples are randomly distributed, the degree to which the newly constrained prior volume is reduced is actually random variable. Furthermore, the shrinkage of the evolving prior volume at each iteration, donated as $t_i = X_i/X_{i-1}$, is found to follow the following probability distribution [1],

$$P(t) = Nt^{N-1}. \tag{B.8}$$

Under this probability distribution, one can derive the expectation value of $\log t$

$$\mathrm{E}[\log t] = \int_0^1 (\log t) N t^{N-1} \mathrm{d}t \tag{B.9}$$

$$= N\left(\left[\log t \frac{t^N}{N}\right]_0^1 - \int_0^1 \frac{t^N}{N}\mathrm{d}t\right) \tag{B.10}$$

$$= -\frac{1}{N}, \tag{B.11}$$

and its variance

$$\sigma^2[\log t] = \mathrm{E}\left[(\log t)^2\right] - \mathrm{E}[\log t]^2 \tag{B.12}$$

$$= N\left(\left[(\log t)^2 \frac{t^N}{N}\right]_0^1 - \int_0^1 \left(2\frac{\log t}{t}\right)\frac{t^N}{N}\mathrm{d}t\right) - \frac{1}{N^2} \tag{B.13}$$

$$= -2\left(\left[(\log t)\frac{t^N}{N}\right]_0^1 - \int_0^1 \frac{t^N}{N}\mathrm{d}t\right) - \frac{1}{N^2} \tag{B.14}$$

$$= \frac{2}{N^2} - \frac{1}{N^2} = \frac{1}{N^2}. \tag{B.15}$$

At k-th iteration, the new constraint X^* can be written as

$$X^* = X_k = \prod_{i=1}^{k} t_i. \tag{B.16}$$

Each logarithmic shrinkage ratio is independently distributed, so after k-th iteration

$$\log X_k = -\frac{k}{N} \pm \frac{\sqrt{k}}{N}, \tag{B.17}$$

[1] This formula can be derived in a straightforward manner. Suppose that N active samples are uniformly distributed within $[0 < t < 1]$ because $X_i^{\forall} < X^*$ and that the sample with the lowest likelihood turns out to be associated with the prior volume of $t'X^*$. Now the remaining $N-1$ samples are supposed to be independently packed within $[0 < t < t']$, the probability of that happening is t'^{N-1}. Also the case should be counted N times, so totally $P(t') = Nt'^{N-1}$

or equivalently

$$X_k \approx \mathrm{e}^{\frac{k}{N}}. \tag{B.18}$$

The procedure above will be terminated when the approximate evaluation (B.3) becomes complete to pre-specified precision. Finally, this approximation is finalized by adding the contribution from the remaining N active samples

$$\Delta Z = \sum_{j=1}^{N} L(X_{M+j})\bar{w}, \tag{B.19}$$

where $\bar{w} = X_M/N$. Overall uncertainty on the calculated evidence can be estimated by considering the relative entropy of the full series of samples [253].

Appendix C

Consistency of the parameter estimation

We describe our assessment of the statistical consistency for the parameter estimation conducted by our analysis pipeline using `PyMultiNest`. Specifically, a probability-probability plot (p-p plot) is produced based on 500 injection recoveries. We follow the injection procedure described in Chapter 6.1 using a simulated SGWB signal of the scalar cloud model and Gaussian noise synthesized by the observed $\sigma(f)$ spectrum of advanced LIGO's O1 data. The p-value for each injected scalar mass, m_b, is computed from the marginalized posterior for m_b such that for i-th injection, p-value is given by

$$p_i \equiv \int_{m_0}^{m_b^*} p(m_b)\, \mathrm{d}m_b, \tag{C.1}$$

where $p(m_b)$ represents the marginalized posterior of m_b, m_b^* is the injected value and m_0 the lower bound of the prior space. Among the 500 injections with each p-value, we calculate the fraction of injections whose p-values is smaller then a given threshold p_i, and then plot it as a function of the threshold. Statistically consistent posteriors are supposed to yield p_i's following a uniform distribution over [0-1] and hence , the fraction of injections with p-values smaller than a given threshold p_i is expected to be p_i. In other words, a pp-plot for such samples should have a series of samples aligned with the diagonal in the plot. We show the pp-plot derived from our set of injections in Fig. C.1, which implies that posterior distributions our pipeline produce are statistically consistent within the 95% credible error depicted as the gray shadow. We also highlight that depending on a signal amplitude of the injections, a credible region produced from each posterior can be interpreted in two ways: for loud injections, a pipeline yields a good estimate of parameter distribution likely to be clustered near its true value, whereas if the injection is too weak for the pipeline to detect, the credible region rather indicates the allowed parameter region. Despite these distinctions, we observe that the orange curve in Fig. C.1 overall stays within the error region. Therefore, we conclude that

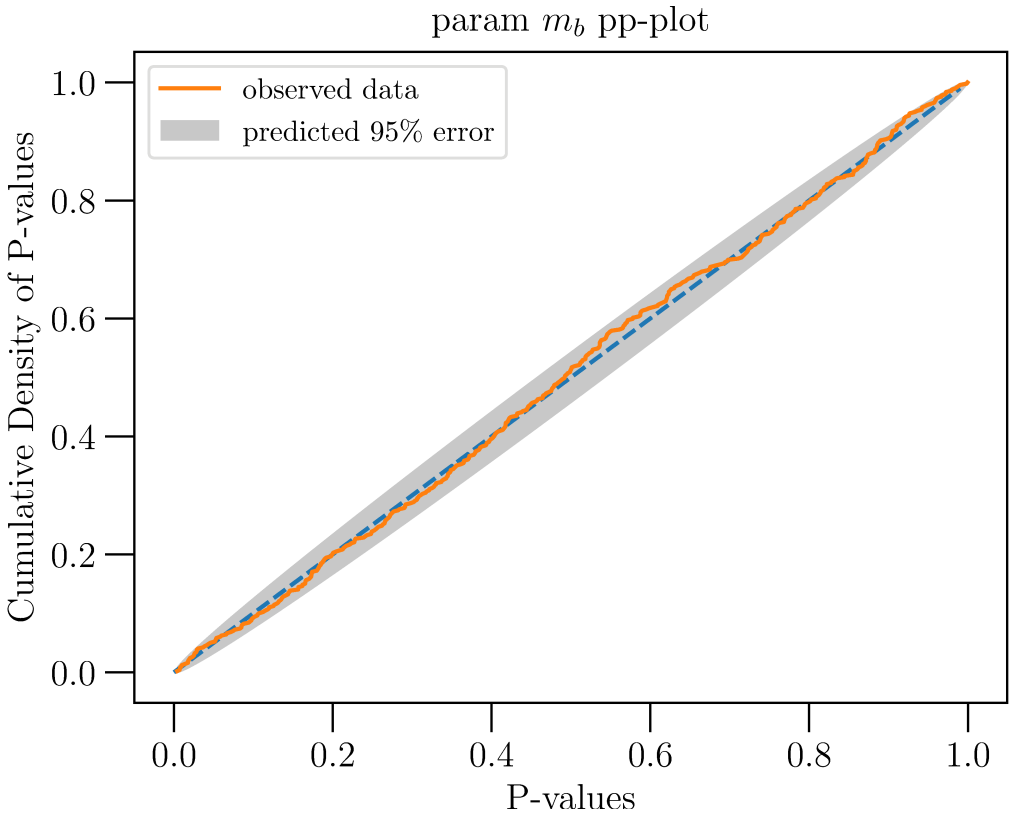

Figure C.1: P-p plot obtained by 500 injections into synthesized noise with advanced LIGO's O1 sensitivity. Each point represents one p-value threshold derived from a injection into different O1 noise realizations. The gray shadow is the 95% credible error region predicted by statistical fluctuation from the ideal diagonal

our pipeline is capable of recover the parameter distribution of given injections in a statistically consistent manner regardless of the injections' SNR.

Acknowledgements

First of all, I would like to deeply thank my Ph.D. advisor, Kipp Cannon, for his patience and mentorship to guide me through everything, from how to use `vim` to a scientific mentality a scientist needs to have. Additionally, to my collaborators, Richard Brito, Thomas Callister, William East, Andrew Matas, Patrick Meyers and Nils Siemonsen, thank you for substantial effort, fruitful discussion and instruction to put my papers together.

I want show my gratitude to my colleagues in RESCEU, and it has been such inspirational and motivating experiences to work in a great environment. Also I would like to thank a great amount of support from administrative staff in RESCEU: Sayuri Nagano, Reiko Sugiyama and Chiyo Ueda.

Finally, I would like to give many (and many) thanks to my family: my dad, mom, Sara, Lulu for their tremendous support throughout my long journey. I owe what I am today truly to them. In particular, to my dad, the best example of researchers I know of, I wish I could have shown my degree before you passed.

My research was also supported by a Grant-in-Aid from the Japan Society for the Promotion of Science (JSPS KAKENHI Grant Number JP18J21709) throughout my Ph.D. program.

Bibliography

[1] S. G. Turyshev, "Experimental tests of general relativity," *Annual Review of Nuclear and Particle Science*, vol. 58, no. 1, pp. 207–248, 2008. eprint: https://doi.org/10.1146/annurev.nucl.58.020807.111839.

[2] E. Berti *et al.*, "Testing general relativity with present and future astrophysical observations," *Classical and Quantum Gravity*, vol. 32, no. 24, p. 243 001, Dec. 2015.

[3] A. Einstein, "Naherungsweise Integration der Feldgleichungen der Gravitation. (German) [Approximate integration of the field equations of gravitation]," German, pp. 688–696, 1916.

[4] A. Einstein, "Die Feldgleichungen der Gravitation. (German) [The field equations of gravitation]," German, pp. 844–847, 1915.

[5] R. A. Hulse and J. H. Taylor, "Discovery of a pulsar in a binary system.," *Astrophys. J. Lett.*, vol. 195, pp. L51–L53, Jan. 1975.

[6] J. Weber", "Gravitational radiation," *Physical Review Letters*, vol. 18, no. 13, pp. 498–501, 1967.

[7] "Observation of gravitational waves from a binary black hole merger," *Physical Review Letters*, vol. 116, no. 6, 2016.

[8] T. Kinugawa, K. Inayoshi, K. Hotokezaka, D. Nakauchi, and T. Nakamura, "Possible indirect confirmation of the existence of Pop III massive stars by gravitational wave," *Monthly Notices of the Royal Astronomical Society*, vol. 442, no. 4, pp. 2963–2992, Jun. 2014, ISSN: 0035-8711. eprint: https://academic.oup.com/mnras/article-pdf/442/4/2963/4158785/stu1022.pdf.

[9] T. Kinugawa, A. Miyamoto, N. Kanda, and T. Nakamura, "The detection rate of inspiral and quasi-normal modes of Population III binary black holes which can confirm or refute the general relativity in the strong gravity region," *Monthly Notices of the Royal Astronomical Society*, vol. 456, no. 1, pp. 1093–1114, Dec. 2015, ISSN: 0035-8711. eprint: https://academic.oup.com/mnras/article-pdf/456/1/1093/3657599/stv2624.pdf.

[10] S. Sigurdsson and L. Hernquist, "Primordial black holes in globular clusters," *Nature*, vol. 364, 423 EP -, Jul. 1993.

[11] M. Sasaki, T. Suyama, T. Tanaka, and S. Yokoyama, "Primordial black hole scenario for the gravitational-wave event gw150914," *Phys. Rev. Lett.*, vol. 117, p. 061 101, 6 Aug. 2016.

[12] "Gw170817: Observation of gravitational waves from a binary neutron star inspiral," *Physical Review Letters*, vol. 119, no. 16, 2017.

[13] B. P. Abbott *et al.*, "Gravitational waves and gamma-rays from a binary neutron star merger: Gw170817 and grb 170817a," *The Astrophysical Journal Letters*, vol. 848, no. 2, p. L13, 2017.

[14] B. D. Metzger, G. Martinez-Pinedo, S. Darbha, E. Quataert, A. Arcones, D. Kasen, R. Thomas, P. Nugent, I. V. Panov, and N. T. Zinner, "Electromagnetic counterparts of compact object mergers powered by the radioactive decay of r-process nuclei," *Monthly Notices of the Royal Astronomical Society*, vol. 406, no. 4, pp. 2650–2662, Aug. 2010, ISSN: 0035-8711. eprint: https://academic.oup.com/mnras/article-pdf/406/4/2650/3356185/mnras0406-2650.pdf.

[15] D. Kasen, N. Badnell, and J. Barnes, "Opacities and Spectra of the r-process Ejecta from Neutron Star Mergers," *Astrophys. J.*, vol. 774, p. 25, 2013. arXiv: 1303.5788 [astro-ph.HE].

[16] M. Tanaka and K. Hotokezaka, "Radiative Transfer Simulations of Neutron Star Merger Ejecta," *Astrophys. J.*, vol. 775, no. 2, 113, p. 113, Oct. 2013. arXiv: 1306.3742 [astro-ph.HE].

[17] B. P. Abbott *et al.*, "Multi-messenger observations of a binary neutron star merger," *The Astrophysical Journal*, vol. 848, no. 2, p. L12, Oct. 2017.

[18] B. P. Abbott *et al.*, "Gw170817: Measurements of neutron star radii and equation of state," *Phys. Rev. Lett.*, vol. 121, p. 161 101, 16 Oct. 2018.

[19] B. P. Abbott *et al.*, "Tests of general relativity with gw170817," *Phys. Rev. Lett.*, vol. 123, p. 011 102, 1 Jul. 2019.

[20] B. P. Abbott *et al.*, "A gravitational-wave standard siren measurement of the hubble constant," *Nature*, vol. 551, no. 7678, pp. 85–88, 2017.

[21] B. P. Abbott *et al.*, "Binary black hole mergers in the first advanced ligo observing run," *Phys. Rev. X*, vol. 6, p. 041 015, 4 Oct. 2016.

[22] "Gwtc-1: A gravitational-wave transient catalog of compact binary mergers observed by ligo and virgo during the first and second observing runs," *Physical Review X*, vol. 9, no. 3, 2019.

[23] R. Abbott *et al.*, "GWTC-2: Compact Binary Coalescences Observed by LIGO and Virgo During the First Half of the Third Observing Run," Oct. 2020. arXiv: 2010.14527 [gr-qc].

[24] R. Abbott *et al.*, "GW190412: Observation of a Binary-Black-Hole Coalescence with Asymmetric Masses," *Phys. Rev. D*, vol. 102, no. 4, p. 043 015, 2020. arXiv: 2004.08342 [astro-ph.HE].

[25] R. Abbott *et al.*, "GW190521: A Binary Black Hole Merger with a Total Mass of 150 M," *Phys. Rev. Lett.*, vol. 125, no. 10, p. 101 102, 2020. arXiv: 2009.01075 [gr-qc].

[26] R. Abbott *et al.*, "GW190814: Gravitational Waves from the Coalescence of a 23 Solar Mass Black Hole with a 2.6 Solar Mass Compact Object," *Astrophys. J. Lett.*, vol. 896, no. 2, p. L44, 2020. arXiv: 2006.12611 [astro-ph.HE].

[27] R. Abbott *et al.*, "Population Properties of Compact Objects from the Second LIGO-Virgo Gravitational-Wave Transient Catalog," Oct. 2020. arXiv: 2010.14533 [astro-ph.HE].

[28] M. Punturo *et al.*, "The einstein telescope: A third-generation gravitational wave observatory," *Classical and Quantum Gravity*, vol. 27, no. 19, p. 194 002, Sep. 2010.

[29] D. Reitze, R. X. Adhikari, S. Ballmer, B. Barish, L. Barsotti, G. Billingsley, D. A. Brown, Y. Chen, D. Coyne, R. Eisenstein, M. Evans, P. Fritschel, E. D. Hall, A. Lazzarini, G. Lovelace, J. Read, B. S. Sathyaprakash, D. Shoemaker, J. Smith, C. Torrie, S. Vitale, R. Weiss, C. Wipf, and M. Zucker, *Cosmic explorer: The u.s. contribution to gravitational-wave astronomy beyond ligo*, 2019. arXiv: 1907.04833 [astro-ph.IM].

[30] P. Amaro-Seoane *et al.*, *Laser interferometer space antenna*, 2017. arXiv: 1702.00786 [astro-ph.IM].

[31] N. Seto, S. Kawamura, and T. Nakamura, "Possibility of direct measurement of the acceleration of the universe using 0.1 hz band laser interferometer gravitational wave antenna in space," *Phys. Rev. Lett.*, vol. 87, p. 221 103, 22 Nov. 2001.

[32] S. Kawamura *et al.*, *Current status of space gravitational wave antenna decigo and b-decigo*, 2020. arXiv: 2006.13545 [gr-qc].

[33] M. Armano *et al.*, "Sub-femto-g free fall for space-based gravitational wave observatories: Lisa pathfinder results," *Phys. Rev. Lett.*, vol. 116, p. 231 101, 23 Jun. 2016.

[34] G. Desvignes *et al.*, "High-precision timing of 42 millisecond pulsars with the European Pulsar Timing Array," *Monthly Notices of the Royal Astronomical Society*, vol. 458, no. 3, pp. 3341–3380, Mar. 2016, ISSN: 0035-8711. eprint: https://academic.oup.com/mnras/article-pdf/458/3/3341/8006796/stw483.pdf.

[35] M. Kerr, D. J. Reardon, G. Hobbs, R. M. Shannon, R. N. Manchester, S. Dai, C. J. Russell, S. Zhang, W. van Straten, S. Osowski, and et al., "The parkes pulsar timing array project: Second data release," *Publications of the Astronomical Society of Australia*, vol. 37, e020, 2020.

[36] S. Ransom, A. Brazier, S. Chatterjee, T. Cohen, J. M. Cordes, M. E. DeCesar, P. B. Demorest, J. S. Hazboun, M. T. Lam, R. S. Lynch, M. A. McLaughlin, S. M. Ransom, X. Siemens, S. R. Taylor, and S. J. Vigeland, "The nanograv program for gravitational waves and fundamental physics," *Bulletin of the AAS*, vol. 51, no. 7, Sep. 30, 2019, https://baas.aas.org/pub/2020n7i195.

[37] Z. Arzoumanian *et al.*, *The nanograv 12.5-year data set: Search for an isotropic stochastic gravitational-wave background*, 2020. arXiv: 2009.04496 [astro-ph.HE].

[38] P. A. R. Ade *et al.*, "Constraints on primordial gravitational waves using planck, wmap, and new bicep2/keck observations through the 2015 season," *Phys. Rev. Lett.*, vol. 121, p. 221 301, 22 Nov. 2018.

[39] B. P. Abbott *et al.*, "Advanced LIGO," *Class. Quant. Grav.*, vol. 32, no. 7, p. 074 001, Mar. 2015.

[40] *Ligo-t2000012*, https://dcc.ligo.org/LIGO-T2000012/public.

[41] B. P. Abbott *et al.*, "Prospects for observing and localizing gravitational-wave transients with advanced LIGO, advanced virgo and KAGRA," *Living Reviews in Relativity*, vol. 23, no. 1, Sep. 2020.

[42] L. Roszkowski, E. M. Sessolo, and S. Trojanowski, "WIMP dark matter candidates and searches-current status and future prospects," *Reports on Progress in Physics*, vol. 81, no. 6, p. 066 201, May 2018.

[43] R. D. Peccei and H. R. Quinn, "Cp conservation in the presence of pseudoparticles," *Phys. Rev. Lett.*, vol. 38, pp. 1440–1443, 25 Jun. 1977.

[44] J. E. Kim and G. Carosi, "Axions and the strong cp problem," *Rev. Mod. Phys.*, vol. 82, pp. 557–601, 1 Mar. 2010.

[45] R. D. Peccei, "The strong cp problem and axions," in *Axions: Theory, Cosmology, and Experimental Searches*, M. Kuster, G. Raffelt, and B. Beltran, Eds. Berlin, Heidelberg: Springer Berlin Heidelberg, 2008, pp. 3–17, ISBN: 978-3-540-73518-2.

[46] P. Sikivie, "Axion cosmology," in *Axions: Theory, Cosmology, and Experimental Searches*, M. Kuster, G. Raffelt, and B. Beltran, Eds. Berlin, Heidelberg: Springer Berlin Heidelberg, 2008, pp. 19–50, ISBN: 978-3-540-73518-2.

[47] A. Arvanitaki, S. Dimopoulos, S. Dubovsky, N. Kaloper, and J. March-Russell, "String axiverse," *Phys. Rev. D*, vol. 81, no. 12, 2010.

[48] B. Acharya and C. Pongkitivanichkul, "The axiverse induced dark radiation problem," *Journal of High Energy Physics*, vol. 2016, no. 4, p. 9, 2016.

[49] A. Ringwald, *Exploring the role of axions and other wisps in the dark universe*, 2012. arXiv: 1210.5081 [hep-ph].

[50] J. Redondo and A. Ringwald, "Light shining through walls," *Contemporary Physics*, vol. 52, no. 3, pp. 211–236, 2011. eprint: https://doi.org/10.1080/00107514.2011.563516.

[51] A. Ringwald, "Searching for axions and ALPs from string theory," *Journal of Physics: Conference Series*, vol. 485, p. 012 013, Mar. 2014.

[52] G. Carosi, A. Friedland, M. Giannotti, M. J. Pivovaroff, J. Ruz, and J. K. Vogel, *Probing the axion-photon coupling: Phenomenological and experimental perspectives. a snowmass white paper*, 2013. arXiv: 1309.7035 [hep-ph].

[53] D. J. Marsh, "Axion cosmology," *Physics Reports*, vol. 643, pp. 1–79, 2016, Axion cosmology, ISSN: 0370-1573.

[54] "Preface," in *Particle Dark Matter: Observations, Models and Searches*. Cambridge University Press, 2010, pp. xvii–xix.

[55] G. Sigl, *Astroparticle Physics: Theory and Phenomenology*, ser. Atlantis Studies in Astroparticle Physics and Cosmology. Atlantis Press, 2017, vol. 1, ISBN: 978-94-6239-242-7, 978-94-6239-243-4.

[56] M. Goodsell, J. Jaeckel, J. Redondo, and A. Ringwald, "Naturally light hidden photons in LARGE volume string compactifications," *Journal of High Energy Physics*, vol. 2009, no. 11, pp. 027–027, Nov. 2009.

[57] F. Bossi, S. Giovannella, P. Santangelo, and B. Sciascia, Eds., *Proceedings, Dark Forces at Accelerators (DARK2012): Frascati, Italy, October 16-19, 2012*, vol. 56, 2012, pp. 1–283.

[58] J. Preskill, M. B. Wise, and F. Wilczek, "Cosmology of the invisible axion," *Physics Letters B*, vol. 120, no. 1, pp. 127–132, 1983, ISSN: 0370-2693.

[59] L. Abbott and P. Sikivie, "A cosmological bound on the invisible axion," *Physics Letters B*, vol. 120, no. 1, pp. 133–136, 1983, ISSN: 0370-2693.

[60] M. Dine and W. Fischler, "The not-so-harmless axion," *Physics Letters B*, vol. 120, no. 1, pp. 137–141, 1983, ISSN: 0370-2693.

[61] D. H. Weinberg, J. S. Bullock, F. Governato, R. Kuzio de Naray, and A. H. G. Peter, "Cold dark matter: Controversies on small scales," *Proceedings of the National Academy of Sciences*, vol. 112, no. 40, pp. 12 249–12 255, 2015, ISSN: 0027-8424. eprint: https://www.pnas.org/content/112/40/12249.full.pdf.

[62] E. Brinks and W. J. G. de Blok, "The core-cusp problem," *Advances in Astronomy*, vol. 2010, p. 789 293, 2010.

[63] H.-Y. Schive, T. Chiueh, and T. Broadhurst, "Cosmic structure as the quantum interference of a coherent dark wave," *Nature Physics*, vol. 10, no. 7, pp. 496–499, 2014.

[64] B. Schwabe, J. C. Niemeyer, and J. F. Engels, "Simulations of solitonic core mergers in ultralight axion dark matter cosmologies," *Phys. Rev. D*, vol. 94, p. 043 513, 4 Aug. 2016.

[65] H.-Y. Schive, M.-H. Liao, T.-P. Woo, S.-K. Wong, T. Chiueh, T. Broadhurst, and W.-Y. P. Hwang, "Understanding the core-halo relation of quantum wave dark matter from 3d simulations," *Phys. Rev. Lett.*, vol. 113, p. 261 302, 26 Dec. 2014.

[66] J. Veltmaat and J. C. Niemeyer, "Cosmological particle-in-cell simulations with ultralight axion dark matter," *Phys. Rev. D*, vol. 94, p. 123 523, 12 Dec. 2016.

[67] R. Brito, V. Cardoso, and P. Pani, "Superradiance," Jan. 2015. eprint: 1501.06570.

[68] A. Arvanitaki", "Exploring the string axiverse with precision black hole physics," *Physical Review D*, vol. 83, no. 4, 2011.

[69] A. Arvanitaki, M. Baryakhtar, S. Dimopoulos, S. Dubovsky, and R. Lasenby, "Black hole mergers and the qcd axion at advanced ligo," *Phys. Rev. D*, vol. 95, no. 4, 2017.

[70] R. Brito", "Stochastic and resolvable gravitational waves from ultralight bosons," *Physical Review Letters*, vol. 119, no. 13, 2017.

[71] R. Brito, V. Cardoso, and P. Pani, "Black holes as particle detectors: Evolution of superradiant instabilities," *Classical and Quantum Gravity*, vol. 32, no. 13, p. 134 001, 2015.

[72] H. KODAMA and H. YOSHINO, "Axiverse and black hole," *International Journal of Modern Physics: Conference Series*, vol. 07, pp. 84–115, 2012. eprint: http://www.worldscientific.com/doi/pdf/10.1142/S2010194512004199.

[73] H. Yoshino and H. Kodama, "Gravitational radiation from an axion cloud around a black hole: Superradiant phase," *Progress of Theoretical and Experimental Physics*, vol. 2014, no. 4, 043E02, 2014. eprint: /oup/backfile/content_public/journal/ptep/2014/4/10.1093_ptep_ptu029/4/ptu029.pdf.

[74] M. Baryakhtar, R. Lasenby, and M. Teo, "Black Hole Superradiance Signatures of Ultralight Vectors," *Phys. Rev. D*, vol. 96, no. 3, p. 035 019, 2017. arXiv: 1704.05081 [hep-ph].

[75] A. Pierce, K. Riles, and Y. Zhao, "Searching for dark photon dark matter with gravitational-wave detectors," *Phys. Rev. Lett.*, vol. 121, p. 061 102, 6 Aug. 2018.

[76] H.-K. Guo, K. Riles, F.-W. Yang, and Y. Zhao, "Searching for dark photon dark matter in ligo o1 data," *Communications Physics*, vol. 2, no. 1, p. 155, 2019.

[77] A. L. Miller, P. Astone, G. Bruno, S. Clesse, S. D'Antonio, A. Depasse, F. D. Lillo, S. Frasca, I. L. Rosa, P. Leaci, CristianoPalomba, O. J. Piccinni, L. Pierini, L. Rei, and A. Tanasijczuk, *Adapting a semi-coherent method to directly detect dark photon dark matter interacting with gravitational-wave interferometers*, 2020. arXiv: 2010.01925 [astro-ph.IM].

[78] Y. Michimura, T. Fujita, S. Morisaki, H. Nakatsuka, and I. Obata, "Ultralight vector dark matter search with auxiliary length channels of gravitational wave detectors," *Phys. Rev. D*, vol. 102, p. 102 001, 10 Nov. 2020.

[79] V. Cardoso, O. J. Dias, G. S. Hartnett, M. Middleton, P. Pani, and J. E. Santos, "Constraining the mass of dark photons and axion-like particles through black-hole superradiance," *Journal of Cosmology and Astroparticle Physics*, vol. 2018, no. 03, pp. 043–043, Mar. 2018.

[80] B. Allen, "The stochastic gravity-wave background: Sources and detection," *"Relativistic gravitation and gravitational radiation", J.-A. Marck, J.-P. Lasota. (Proceedings, Les Houches School of Physics: Astrophysical Sources of Gravitational Radiation), Cambridge Contemporary Astrophysics, 1997, pages 373-417*, eprint: gr-qc/9604033.

[81] B. Allen and J. D. Romano, "Detecting a stochastic background of gravitational radiation: Signal processing strategies and sensitivities," *Phys. Rev. D*, vol. 59, p. 102 001, 10 Mar. 1999.

[82] N. Christensen, "Stochastic Gravitational Wave Backgrounds," *Rept. Prog. Phys.*, vol. 82, no. 1, p. 016 903, 2019. arXiv: 1811.08797 [gr-qc].

[83] B. P. Abbott *et al.*, "Upper limits on the stochastic gravitational-wave background from advanced ligo's first observing run," *Phys. Rev. Lett.*, vol. 118, p. 121 101, 12 Mar. 2017.

[84] B. P. Abbott *et al.*, "Search for the isotropic stochastic background using data from advanced ligo's second observing run," *Phys. Rev. D*, vol. 100, p. 061 101, 6 Sep. 2019.

[85] B. P. Abbott *et al.*, "Directional limits on persistent gravitational waves from advanced ligo's first observing run," *Phys. Rev. Lett.*, vol. 118, p. 121 102, 12 Mar. 2017.

[86] "Directional limits on persistent gravitational waves using data from advanced ligo's first two observing runs," *Physical Review D*, vol. 100, no. 6, 2019.

[87] J. Creighton and W. Anderson, *Gravitational-Wave Physics and Astronomy: An Introduction to Theory, Experiment and Data Analysis*, ser. Wiley Series in Cosmology. Wiley, 2012, ISBN: 9783527636044.

[88] A. A. Penzias and R. W. Wilson, "A Measurement of Excess Antenna Temperature at 4080 Mc/s.," *Astrophys. J.*, vol. 142, pp. 419–421, Jul. 1965.

[89] G. F. Smoot, C. L. Bennett, A. Kogut, E. L. Wright, J. Aymon, N. W. Boggess, E. S. Cheng, G. de Amici, S. Gulkis, M. G. Hauser, G. Hinshaw, P. D. Jackson, M. Janssen, E. Kaita, T. Kelsall, P. Keegstra, C. Lineweaver, K. Loewenstein, P. Lubin, J. Mather, S. S. Meyer, S. H. Moseley, T. Murdock, L. Rokke, R. F. Silverberg, L. Tenorio, R. Weiss, and D. T. Wilkinson, "Structure in the COBE Differential Microwave Radiometer First-Year Maps," *Astrophys. J. Lett.*, vol. 396, p. L1, Sep. 1992.

[90] G. Hinshaw, D. Larson, E. Komatsu, D. N. Spergel, C. L. Bennett, J. Dunkley, M. R. Nolta, M. Halpern, R. S. Hill, N. Odegard, L. Page, K. M. Smith, J. L. Weiland, B. Gold, N. Jarosik, A. Kogut, M. Limon, S. S. Meyer, G. S. Tucker, E. Wollack, and E. L. Wright, "Nine-year Wilkinson Microwave Anisotropy Probe (WMAP) Observations: Cosmological Parameter Results," *ASTROPHYS. J. SUPPL. S.*, vol. 208, no. 2, 19, p. 19, Oct. 2013. arXiv: 1212.5226 [astro-ph.CO].

[91] P. A. R. Ade *et al.*, "Planck 2015 results - xiii. cosmological parameters," *Astro. Astrophys.*, vol. 594, A13, 2016.

[92] A. H. Guth, "Inflationary universe: A possible solution to the horizon and flatness problems," *Phys. Rev. D*, vol. 23, pp. 347–356, 2 Jan. 1981.

[93] A. Vilenkin, "Cosmic strings and domain walls," *Physics Reports*, vol. 121, no. 5, pp. 263–315, 1985, ISSN: 0370-1573.

[94] R. Jeannerot, "How generic is cosmic string formation in supersymmetric grand unified theories," *Physical Review D*, vol. 68, no. 10, 2003.

[95] M. Sakellariadou, "Cosmic superstrings," *Philosophical Transactions of the Royal Society A: Mathematical, Physical and Engineering Sciences*, vol. 366, no. 1877, pp. 2881–2894, Jun. 2008.

[96] M. G. Jackson, N. T. Jones, and J. Polchinski, "Collisions of cosmic f- and d-strings," *Journal of High Energy Physics*, vol. 2005, no. 10, pp. 013–013, Oct. 2005.

[97] T. Damour and A. Vilenkin, "Gravitational wave bursts from cosmic strings," *Phys. Rev. Lett.*, vol. 85, pp. 3761–3764, 18 Oct. 2000.

[98] T. Damour and A. Vilenkin, "Gravitational wave bursts from cusps and kinks on cosmic strings," *Phys. Rev. D*, vol. 64, p. 064 008, 6 Aug. 2001.

[99] T. Damour and A. Vilenkin, "Gravitational radiation from cosmic (super)strings: Bursts, stochastic background, and observational windows," *Phys. Rev. D*, vol. 71, p. 063 510, 6 Mar. 2005.

[100] S. Henrot-Versille *et al.*, "Improved constraint on the primordial gravitational-wave density using recent cosmological data and its impact on cosmic string models," *Classical and Quantum Gravity*, vol. 32, no. 4, p. 045 003, Jan. 2015.

[101] B. P. Abbott *et al.*, "All-sky search for short gravitational-wave bursts in the second advanced ligo and advanced virgo run," *Phys. Rev. D*, vol. 100, p. 024 017, 2 Jul. 2019.

[102] M. D'Onofrio and K. Rummukainen, "Standard model cross-over on the lattice," *Phys. Rev. D*, vol. 93, p. 025 003, 2 Jan. 2016.

[103] S. Iso, P. D. Serpico, and K. Shimada, "Qcd-electroweak first-order phase transition in a supercooled universe," *Phys. Rev. Lett.*, vol. 119, p. 141 301, 14 Oct. 2017.

[104] D. E. Morrissey and M. J. Ramsey-Musolf, "Electroweak baryogenesis," *New Journal of Physics*, vol. 14, no. 12, p. 125 003, Dec. 2012.

[105] C. Caprini, M. Hindmarsh, S. Huber, T. Konstandin, J. Kozaczuk, G. Nardini, J. M. No, A. Petiteau, P. Schwaller, G. Servant, and D. J. Weir, "Science with the space-based interferometer eLISA. II: Gravitational waves from cosmological phase transitions," *Journal of Cosmology and Astroparticle Physics*, vol. 2016, no. 04, pp. 001–001, Apr. 2016.

[106] M. Hindmarsh, S. J. Huber, K. Rummukainen, and D. J. Weir, "Gravitational waves from the sound of a first order phase transition," *Phys. Rev. Lett.*, vol. 112, p. 041 301, 4 Jan. 2014.

[107] M. Hindmarsh, S. J. Huber, K. Rummukainen, and D. J. Weir, "Numerical simulations of acoustically generated gravitational waves at a first order phase transition," *Phys. Rev. D*, vol. 92, p. 123 009, 12 Dec. 2015.

[108] C. Caprini, R. Durrer, and G. Servant, "The stochastic gravitational wave background from turbulence and magnetic fields generated by a first-order phase transition," *Journal of Cosmology and Astroparticle Physics*, vol. 2009, no. 12, pp. 024–024, Dec. 2009.

[109] M. Kamionkowski, A. Kosowsky, and M. S. Turner, "Gravitational radiation from first-order phase transitions," *Phys. Rev. D*, vol. 49, pp. 2837–2851, 6 Mar. 1994.

[110] N. Bartolo *et al.*, "Science with the space-based interferometer LISA. IV: Probing inflation with gravitational waves," *Journal of Cosmology and Astroparticle Physics*, vol. 2016, no. 12, pp. 026–026, Dec. 2016.

[111] K. Belczynski, R. Perna, T. Bulik, V. Kalogera, N. Ivanova, and D. Q. Lamb, "A study of compact object mergers as short gamma-ray burst progenitors," *The Astrophysical Journal*, vol. 648, no. 2, p. 1110, 2006.

[112] M. Dominik, K. Belczynski, C. Fryer, D. E. Holz, E. Berti, T. Bulik, I. Mandel, and R. O'Shaughnessy, "Double compact objects. i. the significance of the common envelope on merger rates," *Astrophys. J.*, vol. 759, no. 1, p. 52, 2012.

[113] K. Belczynski, D. E. Holz, T. Bulik, and R. O'Shaughnessy, "The first gravitational-wave source from the isolated evolution of two stars in the 40–100 solar mass range," *Nature*, vol. 534, 512 EP -, Jun. 2016.

[114] B. S. Sathyaprakash and S. V. Dhurandhar, "Choice of filters for the detection of gravitational waves from coalescing binaries," *Phys. Rev. D*, vol. 44, pp. 3819–3834, 12 Dec. 1991.

[115] C. Cutler and É. E. Flanagan, "Gravitational waves from merging compact binaries: How accurately can one extract the binary's parameters from the inspiral waveform?" *Phys. Rev. D*, vol. 49, pp. 2658–2697, 6 Mar. 1994.

[116] E. Poisson and C. M. Will, "Gravitational waves from inspiraling compact binaries: Parameter estimation using second-post-newtonian waveforms," *Phys. Rev. D*, vol. 52, pp. 848–855, 2 Jul. 1995.

[117] C. L. Rodriguez, M. Zevin, C. Pankow, V. Kalogera, and F. A. Rasio, "Illuminating black hole binary formation channels with spins in advanced ligo," *The Astrophysical Journal Letters*, vol. 832, no. 1, p. L2, 2016.

[118] C. L. Rodriguez, S. Chatterjee, and F. A. Rasio, "Binary black hole mergers from globular clusters: Masses, merger rates, and the impact of stellar evolution," *Phys. Rev. D*, vol. 93, p. 084 029, 8 Apr. 2016.

[119] M. J. Benacquista and J. M. B. Downing, "Relativistic binaries in globular clusters," *Living Reviews in Relativity*, vol. 16, no. 1, p. 4, 2013.

[120] C. Talbot and E. Thrane, "Determining the population properties of spinning black holes," *Phys. Rev. D*, vol. 96, p. 023 012, 2 Jul. 2017.

[121] M. Zevin, C. Pankow, C. L. Rodriguez, L. Sampson, E. Chase, V. Kalogera, and F. A. Rasio, "Constraining formation models of binary black holes with gravitational-wave observations," *The Astrophysical Journal*, vol. 846, no. 1, p. 82, Sep. 2017.

[122] M. Zevin, J. Samsing, C. Rodriguez, C.-J. Haster, and E. Ramirez-Ruiz, "Eccentric black hole mergers in dense star clusters: The role of binary-binary encounters," *The Astrophysical Journal*, vol. 871, no. 1, p. 91, Jan. 2019.

[123] C. L. Rodriguez, P. Amaro-Seoane, S. Chatterjee, K. Kremer, F. A. Rasio, J. Samsing, C. S. Ye, and M. Zevin, "Post-newtonian dynamics in dense star clusters: Formation, masses, and merger rates of highly-eccentric black hole binaries," *Phys. Rev. D*, vol. 98, p. 123 005, 12 Dec. 2018.

[124] L. Gondan and B. Kocsis, "Measurement accuracy of inspiraling eccentric neutron star and black hole binaries using gravitational waves," *The Astrophysical Journal*, vol. 871, no. 2, p. 178, Jan. 2019.

[125] J. Samsing and D. J. D'Orazio, "Black Hole Mergers From Globular Clusters Observable by LISA I: Eccentric Sources Originating From Relativistic N-body Dynamics," *Monthly Notices of the Royal Astronomical Society*, vol. 481, no. 4, pp. 5445–5450, Aug. 2018, ISSN: 0035-8711. eprint: https://academic.oup.com/mnras/article-pdf/481/4/5445/26075165/sty2334.pdf.

[126] S. Vitale, R. Lynch, R. Sturani, and P. Graff, "Use of gravitational waves to probe the formation channels of compact binaries," *Classical and Quantum Gravity*, vol. 34, no. 3, 03LT01, Jan. 2017.

[127] W. M. Farr, S. Stevenson, M. C. Miller, I. Mandel, B. Farr, and A. Vecchio, "Distinguishing spin-aligned and isotropic black hole populations with gravitational waves," *Nature*, vol. 548, no. 7668, pp. 426–429, 2017.

[128] B. Farr, D. E. Holz, and W. M. Farr, "Using spin to understand the formation of LIGO and virgo's black holes," *The Astrophysical Journal*, vol. 854, no. 1, p. L9, Feb. 2018.

[129] D. Wysocki, J. Lange, and R. O'Shaughnessy, "Reconstructing phenomenological distributions of compact binaries via gravitational wave observations," *Phys. Rev. D*, vol. 100, p. 043 012, 4 Aug. 2019.

[130] S. Fairhurst, R. Green, M. Hannam, and C. Hoy, "When will we observe binary black holes precessing?" *arXiv preprint arXiv:1908.00555*, 2019.

[131] B. P. Abbott *et al.*, "Gw150914: Implications for the stochastic gravitational-wave background from binary black holes," *Phys. Rev. Lett.*, vol. 116, no. 13, 2016.

[132] B. P. Abbott *et al.*, "Gw170817: Implications for the stochastic gravitational-wave background from compact binary coalescences," Oct. 2017. eprint: 1710.05837.

[133] M. R. Adams and N. J. Cornish, "Detecting a stochastic gravitational wave background in the presence of a galactic foreground and instrument noise," *Phys. Rev. D*, vol. 89, p. 022 001, 2 Jan. 2014.

[134] Nelemans, G., Yungelson, L. R., and Portegies Zwart, S. F., "The gravitational wave signal from the galactic disk population of binaries containing two compact objects," *A&A*, vol. 375, no. 3, pp. 890–898, 2001.

[135] A. J. Farmer and E. S. Phinney, "The gravitational wave background from cosmological compact binaries," *MON. NOT. R. ASTRON. SOC.*, vol. 346, no. 4, pp. 1197–1214, Dec. 2003. arXiv: astro-ph/0304393 [astro-ph].

[136] M. R. Adams and N. J. Cornish, "Discriminating between a stochastic gravitational wave background and instrument noise," *Phys. Rev. D*, vol. 82, p. 022 002, 2 Jul. 2010.

[137] M. Remazeilles, J. Delabrouille, and J.-F. Cardoso, "CMB and SZ effect separation with constrained Internal Linear Combinations," *Monthly Notices of the Royal Astronomical Society*, vol. 410, no. 4, pp. 2481–2487, Jan. 2011, ISSN: 0035-8711. eprint: https://academic.oup.com/mnras/article-pdf/410/4/2481/18703080/mnras0410-2481.pdf.

[138] Planck Collaboration, Akrami, Y., *et al.*, "Planck 2018 results - iv. diffuse component separation," *A&A*, vol. 641, A4, 2020.

[139] R. Umstätter, N. Christensen, M. Hendry, R. Meyer, V. Simha, J. Veitch, S. Vigeland, and G. Woan, "Bayesian modeling of source confusion in lisa data," *Phys. Rev. D*, vol. 72, p. 022 001, 2 Jul. 2005.

[140] R. Umstatter, N. Christensen, M. Hendry, R. Meyer, V. Simha, J. Veitch, S. Vigeland, and G. Woan, "LISA source confusion: Identification and characterization of signals," *Classical and Quantum Gravity*, vol. 22, no. 18, S901–S911, Aug. 2005.

[141] J. Crowder and N. J. Cornish, "Extracting galactic binary signals from the first round of mock LISA data challenges," *Classical and Quantum Gravity*, vol. 24, no. 19, S575–S585, Sep. 2007.

[142] A. Stroeer and J. Veitch, "Bayesian approach to the study of white dwarf binaries in lisa data: The application of a reversible jump markov chain monte carlo method," *Phys. Rev. D*, vol. 80, p. 064 032, 6 Sep. 2009.

[143] A. Stroeer, J. Veitch, C. Rover, E. Bloomer, J. Clark, N. Christensen, M. Hendry, C. Messenger, R. Meyer, M. Pitkin, J. Toher, R. Umstatter, A. Vecchio, and G. Woan, "Inference on white dwarf binary systems using the first round mock LISA data challenges data sets," *Classical and Quantum Gravity*, vol. 24, no. 19, S541–S549, Sep. 2007.

[144] W. Dehnen and J. Binney, "Mass models of the Milky Way," *Monthly Notices of the Royal Astronomical Society*, vol. 294, no. 3, pp. 429–438, Mar. 1998, ISSN: 0035-8711. eprint: https://academic.oup.com/mnras/article-pdf/294/3/429/4063697/294-3-429.pdf.

[145] P. J. McMillan, "Mass models of the Milky Way," *MON. NOT. R. ASTRON. SOC.*, vol. 414, no. 3, pp. 2446–2457, Jul. 2011. arXiv: 1102.4340 [astro-ph.GA].

[146] Gaia Collaboration, Brown, A. G. A., *et al.*, "Gaia data release 1 - summary of the astrometric, photometric, and survey properties," *A&A*, vol. 595, A2, 2016.

[147] Gaia Collaboration, Brown, A. G. A., *et al.*, "Gaia data release 2 - summary of the contents and survey properties," *A&A*, vol. 616, A1, 2018.

[148] M. Kilic, N. C. Hambly, P. Bergeron, C. Genest-Beaulieu, and N. Rowell, "Gaia reveals evidence for merged white dwarfs," *Monthly Notices of the Royal Astronomical Society: Letters*, vol. 479, no. 1, pp. L113–L117, Jun. 2018, ISSN: 1745-3925. eprint: https://academic.oup.com/mnrasl/article-pdf/479/1/L113/25145783/sly110.pdf.

[149] R. Abbott *et al.*, "Gravitational-wave constraints on the equatorial ellipticity of millisecond pulsars," *The Astrophysical Journal*, vol. 902, no. 1, p. L21, Oct. 2020.

[150] V. Ferrari, S. Matarrese, and R. Schneider, "Stochastic background of gravitational waves generated by a cosmological population of young, rapidly rotating neutron stars," *MON. NOT. R. ASTRON. SOC.*, vol. 303, no. 2, pp. 258–264, Feb. 1999. arXiv: astro-ph/9806357 [astro-ph].

[151] Q. Cheng, Y.-W. Yu, and X.-P. Zheng, "Stochastic gravitational wave background from magnetic deformation of newly born magnetars," *Monthly Notices of the Royal Astronomical Society*, vol. 454, no. 3, pp. 2299–2304, Oct. 2015, ISSN: 0035-8711. eprint: https://academic.oup.com/mnras/article-pdf/454/3/2299/4032913/stv2127.pdf.

[152] Q. Cheng, S.-N. Zhang, and X.-P. Zheng, "Stochastic gravitational wave background from newly born massive magnetars: The role of a dense matter equation of state," *Phys. Rev. D*, vol. 95, p. 083 003, 8 Apr. 2017.

[153] D. Talukder, E. Thrane, S. Bose, and T. Regimbau, "Measuring neutron-star ellipticity with measurements of the stochastic gravitational-wave background," *Phys. Rev. D*, vol. 89, p. 123 008, 12 Jun. 2014.

[154] R. Penrose, "Gravitational Collapse: the Role of General Relativity," *Nuovo Cimento Rivista Serie*, vol. 1, 1969.

[155] I. ZEL'DOVICH, "Amplification of cylindrical electromagnetic waves reflected from a rotating body," *Soviet Physics-JETP*, vol. 35, pp. 1085–1087, 1972.

[156] W. H. PRESS and S. A. TEUKOLSKY, "Floating orbits, superradiant scattering and the black-hole bomb," *Nature*, vol. 238, 211 EP -, Jul. 1972.

[157] B. R. Iyer", "Note on the absence of massive fermion superradiance from a kerr black hole," *Physical Review D*, vol. 18, no. 12, pp. 4799–4801, 1978.

[158] W. E. East and F. Pretorius, "Superradiant instability and backreaction of massive vector fields around kerr black holes," *Physical Review Letters*, vol. 119, no. 4, 2017.

[159] C. A. R. Herdeiro and E. Radu, "Dynamical formation of kerr black holes with synchronized hair: An analytic model," *Phys. Rev. Lett.*, vol. 119, p. 261 101, 26 Dec. 2017.

[160] H. Davoudiasl and P. B. Denton, "Ultralight boson dark matter and event horizon telescope observations of m87," *Phys. Rev. Lett.*, vol. 123, p. 021 102, 2 Jul. 2019.

[161] N. Fernandez, A. Ghalsasi, and S. Profumo, *Superradiance and the spins of black holes from ligo and x-ray binaries*, 2019. arXiv: 1911.07862 [hep-ph].

[162] K. K. Y. Ng, O. A. Hannuksela, S. Vitale, and T. G. F. Li, *Searching for ultralight bosons within spin measurements of a population of binary black hole mergers*, 2020. arXiv: 1908.02312 [gr-qc].

[163] K. K. Y. Ng, S. Vitale, O. A. Hannuksela, and T. G. F. Li, *Constraints on ultralight scalar bosons within black hole spin measurements from ligo-virgo's gwtc-2*, 2020. arXiv: 2011.06010 [gr-qc].

[164] D. Baumann, H. S. Chia, and R. A. Porto, "Probing ultralight bosons with binary black holes," *Phys. Rev. D*, vol. 99, p. 044 001, 4 Feb. 2019.

[165] J. Zhang and H. Yang, "Gravitational floating orbits around hairy black holes," *Phys. Rev. D*, vol. 99, p. 064 018, 6 Mar. 2019.

[166] E. Berti, R. Brito, C. F. B. Macedo, G. Raposo, and J. L. Rosa, "Ultralight boson cloud depletion in binary systems," *Phys. Rev. D*, vol. 99, p. 104 039, 10 May 2019.

[167] J. Zhang and H. Yang, "Dynamic signatures of black hole binaries with superradiant clouds," *Phys. Rev. D*, vol. 101, p. 043 020, 4 Feb. 2020.

[168] S. R. Dolan", "Instability of the massive klein-gordon field on the kerr spacetime," *Physical Review D*, vol. 76, no. 8, 2007.

[169] S. R. Dolan, "Instability of the Proca field on Kerr spacetime," *Phys. Rev.*, vol. D98, no. 10, p. 104 006, 2018. arXiv: 1806.01604 [gr-qc].

[170] S. Detweiler, "Klein-gordon equation and rotating black holes," *Phys. Rev. D*, vol. 22, pp. 2323–2326, 10 Nov. 1980.

[171] N. Siemonsen and W. E. East, "Gravitational wave signatures of ultralight vector bosons from black hole superradiance," *Phys. Rev. D*, vol. 101, no. 2, p. 024 019, 2020. arXiv: 1910.09476 [gr-qc].

[172] T. J. Zouros and D. M. Eardley, "Instabilities of massive scalar perturbations of a rotating black hole," *Annals of Physics*, vol. 118, no. 1, pp. 139–155, 1979, ISSN: 0003-4916.

[173] S. Ghosh, E. Berti, R. Brito, and M. Richartz, "Follow-up signals from superradiant instabilities of black hole merger remnants," *Phys. Rev. D*, vol. 99, no. 10, p. 104 030, 2019. arXiv: 1812.01620 [gr-qc].

[174] R. Brito", "Gravitational wave searches for ultralight bosons with ligo and lisa," *Physical Review D*, vol. 96, no. 6, 2017.

[175] S. D'Antonio, C. Palomba, P. Astone, S. Frasca, G. Intini, I. La Rosa, P. Leaci, S. Mastrogiovanni, A. Miller, F. Muciaccia, O. J. Piccinni, and A. Singhal, "Semicoherent analysis method to search for continuous gravitational waves emitted by ultralight boson clouds around spinning black holes," *Phys. Rev. D*, vol. 98, p. 103 017, 10 Nov. 2018.

[176] C. Palomba, S. D'Antonio, P. Astone, S. Frasca, G. Intini, I. La Rosa, P. Leaci, S. Mastrogiovanni, A. L. Miller, F. Muciaccia, O. J. Piccinni, L. Rei, and F. Simula, "Direct constraints on the ultralight boson mass from searches of continuous gravitational waves," *Phys. Rev. Lett.*, vol. 123, p. 171 101, 17 Oct. 2019.

[177] M. Isi, L. Sun, R. Brito, and A. Melatos, "Directed searches for gravitational waves from ultralight bosons," *Phys. Rev. D*, vol. 99, p. 084 042, 8 Apr. 2019.

[178] L. Sun, R. Brito, and M. Isi, "Search for ultralight bosons in cygnus x-1 with advanced ligo," *Phys. Rev. D*, vol. 101, p. 063 020, 6 Mar. 2020.

[179] S. J. Zhu, M. Baryakhtar, M. A. Papa, D. Tsuna, N. Kawanaka, and H.-B. Eggenstein, "Characterizing the continuous gravitational-wave signal from boson clouds around galactic isolated black holes," *Phys. Rev. D*, vol. 102, p. 063 020, 6 Sep. 2020.

[180] X.-L. Fan and Y. Chen, "Stochastic gravitational-wave background from spin loss of black holes," *Phys. Rev. D*, vol. 98, no. 4, 2018.

[181] L. Tsukada, T. Callister, A. Matas, and P. Meyers, "First search for a stochastic gravitational-wave background from ultralight bosons," *Phys. Rev. D*, vol. 99, p. 103 015, 10 May 2019.

[182] L. Tsukada, R. Brito, W. E. East, and N. Siemonsen, *Modeling and searching for a stochastic gravitational-wave background from ultralight vector bosons*, 2020. arXiv: 2011.06995 [astro-ph.HE].

[183] W. E. East", "Superradiant instability of massive vector fields around spinning black holes in the relativistic regime," *Physical Review D*, vol. 96, no. 2, 2017.

[184] P. Pani, "Black-hole bombs and photon-mass bounds," *Physical Review Letters*, vol. 109, no. 13, 2012.

[185] R. Brito", "Massive spin-2 fields on black hole spacetimes: Instability of the schwarzschild and kerr solutions and bounds on the graviton mass," *Physical Review D*, vol. 88, no. 2, 2013.

[186] R. Brito, S. Grillo, and P. Pani, "Black Hole Superradiant Instability from Ultralight Spin-2 Fields," *Phys. Rev. Lett.*, vol. 124, no. 21, p. 211 101, 2020. arXiv: 2002.04055 [gr-qc].

[187] D. L. Wiltshire, M. Visser, and S. M. Scott, *The Kerr spacetime: Rotating black holes in general relativity.* Cambridge University Press, 2009.

[188] S. A. Teukolsky, "Perturbations of a Rotating Black Hole. I. Fundamental Equations for Gravitational, Electromagnetic, and Neutrino-Field Perturbations," *The Astrophysical Journal*, vol. 185, pp. 635–648, Oct. 1973.

[189] W. H. Press and S. A. Teukolsky, "Perturbations of a Rotating Black Hole. II. Dynamical Stability of the Kerr Metric," *The Astrophysical Journal*, vol. 185, pp. 649–674, Oct. 1973.

[190] E. Berti", "Eigenvalues and eigenfunctions of spin-weighted spheroidal harmonics in four and higher dimensions," *Physical Review D*, vol. 73, no. 2, 2006.

[191] P. Pani, V. Cardoso, L. Gualtieri, E. Berti, and A. Ishibashi, "Perturbations of slowly rotating black holes: Massive vector fields in the kerr metric," *Phys. Rev. D*, vol. 86, p. 104 017, 10 Nov. 2012.

[192] J. G. Rosa and S. R. Dolan, "Massive vector fields on the schwarzschild spacetime: Quasinormal modes and bound states," *Phys. Rev. D*, vol. 85, p. 044 043, 4 Feb. 2012.

[193] S. Endlich and R. Penco, "A modern approach to superradiance," *Journal of High Energy Physics*, vol. 2017, no. 5, May 2017.

[194] V. P. Frolov, P. Krtous, D. Kubiznak, and J. E. Santos, "Massive Vector Fields in Rotating Black-Hole Spacetimes: Separability and Quasinormal Modes," *Phys. Rev. Lett.*, vol. 120, p. 231 103, 2018. arXiv: 1804.00030 [hep-th].

[195] O. Lunin, "Maxwell's equations in the myers-perry geometry," *Journal of High Energy Physics*, vol. 2017, no. 12, Dec. 2017, ISSN: 1029-8479.

[196] S. A. Teukolsky", "Rotating black holes: Separable wave equations for gravitational and electromagnetic perturbations," *Physical Review Letters*, vol. 29, no. 16, pp. 1114–1118, 1972.

[197] E. Newman and R. Penrose, "An approach to gravitational radiation by a method of spin coefficients," *Journal of Mathematical Physics*, vol. 3, no. 3, pp. 566–578, 1962. eprint: https://doi.org/10.1063/1.1724257.

[198] E. Newman and R. Penrose, "Errata: An approach to gravitational radiation by a method of spin coefficients," *Journal of Mathematical Physics*, vol. 4, no. 7, pp. 998–998, 1963. eprint: https://doi.org/10.1063/1.1704025.

[199] M. Sasaki and H. Tagoshi, "Analytic black hole perturbation approach to gravitational radiation," *Living Reviews in Relativity*, vol. 6, no. 1, p. 6, Nov. 2003, ISSN: 1433-8351.

[200] A. R. King and U. Kolb, "The evolution of black hole mass and angular momentum," *Monthly Notices of the Royal Astronomical Society*, vol. 305, no. 3, pp. 654–660, 1999. eprint: /oup/backfile/content_public/journal/mnras/305/3/10.1046/j.1365-8711.1999.02482.x/2/305-3-654.pdf.

[201] S. D'Antonio *et al.*, "A semi-coherent analysis method to search for continuous gravitational waves emitted by ultra-light boson clouds around spinning black holes," *LIGO-P1800247*, 2018.

[202] "Identification and mitigation of narrow spectral artifacts that degrade searches for persistent gravitational waves in the first two observing runs of advanced ligo," *Physical Review D*, vol. 97, no. 8, 2018.

[203] K. Belczynski *et al.*, "Evolutionary roads leading to low effective spins, high black hole masses, and O1/O2 rates for LIGO/Virgo binary black holes," *Astron. Astrophys.*, vol. 636, A104, 2020. arXiv: 1706.07053 [astro-ph.HE].

[204] Schaerer, D., "On the properties of massive population iii stars and metal-free stellar populations," *A&A*, vol. 382, no. 1, pp. 28–42, 2002.

[205] E. Vangioni, K. A. Olive, T. Prestegard, J. Silk, P. Petitjean, and V. Mandic, "The impact of star formation and gamma-ray burst rates at high redshift on cosmic chemical evolution and reionization," *Monthly Notices of the Royal Astronomical Society*, vol. 447, no. 3, pp. 2575–2587, 2015. eprint: /oup/backfile/content_public/journal/mnras/447/3/10.1093_mnras_stu2600/3/stu2600.pdf.

[206] E. E. Salpeter, "The Luminosity Function and Stellar Evolution.," *The Astrophysical Journal*, vol. 121, p. 161, Jan. 1955.

[207] C. L. Fryer, K. Belczynski, G. Wiktorowicz, M. Dominik, V. Kalogera, and D. E. Holz, "Compact remnant mass function: Dependence on the explosion mechanism and metallicity," *The Astrophysical Journal*, vol. 749, no. 1, p. 91, 2012.

[208] X. Ma, P. F. Hopkins, C.-A. Faucher-Giguere, N. Zolman, A. L. Muratov, D. Keres, and E. Quataert, "The origin and evolution of the galaxy mass-metallicity relation," *Monthly Notices of the Royal Astronomical Society*, vol. 456, no. 2, pp. 2140–2156, Dec. 2015.

[209] "Gw151226: Observation of gravitational waves from a 22-solar-mass binary black hole coalescence," *Physical Review Letters*, vol. 116, no. 24, 2016.

[210] "Gw170104: Observation of a 50-solar-mass binary black hole coalescence at redshift 0.2," *Physical Review Letters*, vol. 118, no. 22, 2017.

[211] B. P. Abbott *et al.*, "Gw170608: Observation of a 19-solar-mass binary black hole coalescence," Nov. 2017. eprint: 1711.05578.

[212] "Gw170814: A three-detector observation of gravitational waves from a binary black hole coalescence," *Physical Review Letters*, vol. 119, no. 14, 2017.

[213] J. A. Gonzalez, "Maximum kick from nonspinning black-hole binary inspiral," *Phys. Rev. Lett.*, vol. 98, no. 9, 2007.

[214] E. Berti, "Inspiral, merger, and ringdown of unequal mass black hole binaries: A multipolar analysis," *Phys. Rev. D*, vol. 76, no. 6, 2007.

[215] L. Rezzolla, E. N. Dorband, C. Reisswig, P. Diener, D. Pollney, E. Schnetter, and B. Szilagyi, "Spin diagrams for equal-mass black hole binaries with aligned spins," *Astrophys. J.*, vol. 679, no. 2, p. 1422, 2008.

[216] M. Fishbach, D. E. Holz, and B. Farr, "Are ligo's black holes made from smaller black holes?" *The Astrophysical Journal*, vol. 840, no. 2, p. L24, May 2017.

[217] D. Gerosa, "Are merging black holes born from stellar collapse or previous mergers?" *Physical Review D*, vol. 95, no. 12, 2017.

[218] Z. Doctor, D. Wysocki, R. O'Shaughnessy, D. E. Holz, and B. Farr, "Black hole coagulation: Modeling hierarchical mergers in black hole populations," *The Astrophysical Journal*, vol. 893, no. 1, p. 35, Apr. 2020.

[219] C. Kimball, C. Talbot, C. P. L. Berry, M. Carney, M. Zevin, E. Thrane, and V. Kalogera, "Black hole genealogy: Identifying hierarchical mergers with gravitational waves," *The Astrophysical Journal*, vol. 900, no. 2, p. 177, Sep. 2020.

[220] M. Maggiore, *Gravitational Waves. Vol. 1: Theory and Experiments*, ser. Oxford Master Series in Physics. Oxford University Press, 2007, ISBN: 9780198570745, 9780198520740.

[221] M. Dominik, K. Belczynski, C. Fryer, D. E. Holz, E. Berti, T. Bulik, I. Mandel, and R. O'Shaughnessy, "Double compact objects. ii. cosmological merger rates," *Astrophys. J.*, vol. 779, no. 1, p. 72, 2013.

[222] E. Nakar, "Short-hard gamma-ray bursts," *Physics Reports*, vol. 442, no. 1, pp. 166–236, 2007, The Hans Bethe Centennial Volume 1906-2006, ISSN: 0370-1573.

[223] R. O'Shaughnessy, K. Belczynski, and V. Kalogera, "Short gamma-ray bursts and binary mergers in spiral and elliptical galaxies: Redshift distribution and hosts," *Astrophys. J.*, vol. 675, no. 1, p. 566, 2008.

[224] P. Madau and M. Dickinson, "Cosmic star-formation history," *Annual Review of Astronomy and Astrophysics*, vol. 52, no. 1, pp. 415–486, Aug. 2014, ISSN: 1545-4282.

[225] E. Thrane, "Sensitivity curves for searches for gravitational-wave backgrounds," *Phys. Rev. D*, vol. 88, no. 12, 2013.

[226] LIGO-G1800243, https://dcc.ligo.org/LIGO-G1800243/public.

[227] M. D. Kistler, H. Yuksel, and A. M. Hopkins, "The Cosmic Star Formation Rate from the Faintest Galaxies in the Unobservable Universe," *arXiv e-prints*, arXiv:1305.1630, arXiv:1305.1630, May 2013. arXiv: 1305.1630 [astro-ph.CO].

[228] P. S. Behroozi and J. Silk, "A SIMPLE TECHNIQUE FOR PREDICTING HIGH-REDSHIFT GALAXY EVOLUTION," *The Astrophysical Journal*, vol. 799, no. 1, p. 32, Jan. 2015.

[229] R. J. Bouwens, G. D. Illingworth, P. A. Oesch, M. Trenti, I. Labbé, L. Bradley, M. Carollo, P. G. van Dokkum, V. Gonzalez, B. Holwerda, M. Franx, L. Spitler, R. Smit, and D. Magee, "UV Luminosity Functions at Redshifts z ~ 4 to z ~ 10: 10,000 Galaxies from HST Legacy Fields," *The Astrophysical Journal*, vol. 803, no. 1, 34, p. 34, Apr. 2015. arXiv: 1403.4295 [astro-ph.CO].

[230] J. Veitch *et al.*, "Parameter estimation for compact binaries with ground-based gravitational-wave observations using the lalinference software library," *Phys. Rev. D*, vol. 91, p. 042 003, 4 Feb. 2015.

[231] B. P. Abbott *et al.*, "Gw150914: First results from the search for binary black hole coalescence with advanced ligo," *Phys. Rev. D*, vol. 93, p. 122 003, 12 Jun. 2016.

[232] V. Mandic, E. Thrane, S. Giampanis, and T. Regimbau, "Parameter estimation in searches for the stochastic gravitational-wave background," *Phys. Rev. Lett.*, vol. 109, p. 171 102, 17 Oct. 2012.

[233] F. Feroz, M. P. Hobson, and M. Bridges, "Multinest: An efficient and robust bayesian inference tool for cosmology and particle physics," *Monthly Notices of the Royal Astronomical Society*, vol. 398, no. 4, pp. 1601–1614, 2009. eprint: /oup/backfile/content_public/journal/mnras/398/4/10.1111/j.1365-2966.2009.14548.x/2/mnras0398-1601.pdf.

[234] J. Aasi *et al.*, "Searching for stochastic gravitational waves using data from the two colocated ligo hanford detectors," *Phys. Rev. D*, vol. 91, p. 022 003, 2 Jan. 2015.

[235] H. Jeffreys, *Theory of Probability*, Third. Oxford, England: Oxford, 1961.

[236] E. E. Flanagan, "Sensitivity of the laser interferometer gravitational wave observatory to a stochastic background, and its dependence on the detector orientations," *Phys. Rev. D*, vol. 48, no. 6, pp. 2389–2407, 1993.

[237] T. Callister, L. Sammut, S. Qiu, I. Mandel, and E. Thrane, "Limits of astrophysics with gravitational-wave backgrounds," *Phys. Rev. X*, vol. 6, p. 031 018, 3 Aug. 2016.

[238] A. Saffer and K. Yagi, "Parameter estimation for tests of general relativity with the astrophysical stochastic gravitational wave background," *Physical Review D*, vol. 102, no. 2, 2020.

[239] B. P. Abbott, R. Abbott, Acernese ‡, *et al.*, "An upper limit on the stochastic gravitational-wave background of cosmological origin," *Nature*, vol. 460, no. 7258, pp. 990–994, 2009.

[240] *Ligo-t1900058*, https://dcc.ligo.org/LIGO-T1900058/public.

[241] J. Jaeckel, *A force beyond the standard model - status of the quest for hidden photons*, 2013. arXiv: 1303.1821 [hep-ph].

[242] H. Yoshino and H. Kodama, "Bosenova Collapse of Axion Cloud around a Rotating Black Hole:" *Progress of Theoretical Physics*, vol. 128, no. 1, pp. 153–190, Jul. 2012, ISSN: 0033-068X. eprint: https://academic.oup.com/ptp/article-pdf/128/1/153/5197059/128-1-153.pdf.

[243] H. Yoshino and H. Kodama, "The bosenova and axiverse," *Classical and Quantum Gravity*, vol. 32, no. 21, p. 214 001, Oct. 2015.

[244] J. G. Rosa and T. W. Kephart, "Stimulated axion decay in superradiant clouds around primordial black holes," *Phys. Rev. Lett.*, vol. 120, p. 231 102, 23 Jun. 2018.

[245] M. Bo škovi ć, R. Brito, V. Cardoso, T. Ikeda, and H. Witek, "Axionic instabilities and new black hole solutions," *Phys. Rev. D*, vol. 99, p. 035 006, 3 Feb. 2019.

[246] T. Ikeda, R. Brito, and V. Cardoso, "Blasts of light from axions," *Phys. Rev. Lett.*, vol. 122, p. 081 101, 8 Feb. 2019.

[247] H. Fukuda and K. Nakayama, "Aspects of nonlinear effect on black hole superradiance," *Journal of High Energy Physics*, vol. 2020, no. 1, p. 128, 2020.

[248] A. Mathur, S. Rajendran, and E. H. Tanin, "Clockwork mechanism to remove superradiance limits," *Phys. Rev. D*, vol. 102, p. 055 015, 5 Sep. 2020.

[249] K. S. Riedel, "Numerical bayesian methods applied to signal processing," *Technometrics*, vol. 39, no. 1, pp. 106–106, 1997. eprint: http://amstat.tandfonline.com/doi/pdf/10.1080/00401706.1997.10485453.

[250] M. P. Hobson, S. L. Bridle, and O. Lahav, "Combining cosmological data sets: Hyperparameters and bayesian evidence," *Monthly Notices of the Royal Astronomical Society*, vol. 335, no. 2, pp. 377–388, 2002.

[251] R. Trotta, "Applications of bayesian model selection to cosmological parameters," *Monthly Notices of the Royal Astronomical Society*, vol. 378, no. 1, pp. 72–82, 2007.

[252] J. Skilling, "Nested sampling," *AIP Conference Proceedings*, vol. 735, no. 1, pp. 395–405, 2004. eprint: http://aip.scitation.org/doi/pdf/10.1063/1.1835238.

[253] F. Feroz and M. P. Hobson, "Multimodal nested sampling: an efficient and robust alternative to Markov Chain Monte Carlo methods for astronomical data analyses," *Monthly Notices of the Royal Astronomical Society*, vol. 384, pp. 449–463, Feb. 2008. arXiv: 0704.3704.